

How do bubble-bubble and bubble-conduit interactions affect gas mass transport in a magmatic conduit?

Matthew Thomas Roscoe

BSc Physics (University of Lancaster, 2013)

MSc Volcanology and Geological Hazards (University of Lancaster, 2014)

This thesis is submitted in partial fulfilment of the requirements for the degree of
Doctor of Philosophy

August 2023

Declaration

I declare that this work is my own, and has not been submitted in substantially the same form for the award of a higher degree elsewhere. To date, no parts of this thesis have been submitted to, or published in, scientific journals.

Matthew Roscoe

August 2023

“The surface of the earth is the shore of the cosmic ocean.

On this shore we’ve learnt most of what we know.

Recently we’ve waded a little way out, maybe ankle deep,

and the water seems inviting.

Some part of our being knows this is where we came from.

We long to return.

And we can, because the cosmos is also within us.

We are made of star stuff.

We are a way for the cosmos to know itself.”

Carl Sagan

Cosmos

Episode 1: The Shores of the Cosmic Ocean

Abstract

As magma ascends, the bubbles that develop within it affect eruption style and, thus, understanding the possible configuration of bubbles in volcanic systems ultimately helps in mitigating volcanic hazard. While conduit models exist to describe the development of gas bubbles in basaltic systems, these do not take into consideration the effect of bubbles acting as groups on length scales comparable to multiple bubble diameters, nor do they consider the impact of non-vertical magma conduits. These effects were explored using a series of analogue experiments to identify and begin to quantify bubble grouping behaviour in a viscous liquid and the effect of inclining the constraining walls of a gas bubble-viscous liquid system. The main findings were that 1) bubbles have a tendency to self-organise into groups of greater bubble number density, 2) groups of bubbles act together such that their rise speed is typically 2-5 times greater than the buoyant rise speed of individual bubbles, 3) bubble interactions tend to result in vertical size stratification, and 4) the inclination of a conduit radically alters the spatial distribution across the width of the conduit even at low ($<5^\circ$) inclinations. The onset of group behaviour appears to occur when the separation distance of the bubbles is less than five bubble diameters. In systems with slowly rising magma, the increased bubble rise speed may result in the surface manifestation (eruption) of a magma injection occurring several days earlier than what would have previously been expected from existing conduit models. There was sufficient evidence to conclude that, in slow rising, low viscosity, magmas, the effect of bubble-bubble interactions have a notable impact on the gas mass transport and may form part of explanatory models of cyclical eruptive behaviour in low viscosity magmatic systems. The impact of inclination on the rise speed of bubbles and cyclical behaviour was inconclusive. Future magma conduit models should take into consideration the effects of group behaviour once additional experimentation has facilitated a rigorous numerical model to describe these effects across a broad parameter space.

Acknowledgements

To my supervisors, Mike, Steve and Hugh for the innumerable meetings, corrections and pieces of advice and encouragement over the years. Without your guidance, support and advice, this work could never have happened.

To my family for encouragement and support over the years. In particular, to my father for insightful conversations over the years to probe my work and facilitate a deeper understanding.

To my many friends from all corners of the Earth for taking an interest in what I have been working on and giving me so many (perhaps too many?!) opportunities to relax and do something fun. There are quite simply too many to name, as you number in the hundreds, but you have all helped in some small way.

To all of my LEC colleagues, and in particular my office colleagues for continued support and advice. Especially Chris Kneale: I shall miss our lunchtime backgammon games and repeatedly advising me on the best way to eat an elephant.

To Graeme Sinclair for the many long chats we had about the PhD life, music, life in general, and for the valuable experiences you shared about your fieldwork and the advice you gave in the last few weeks and days of writing this thesis. To Nathan, for showing me the ropes when I first started on this adventure having no idea where to begin.

To my fellow volcanology PhD students at Lancaster: Nathan, Graeme, Antonio Anson, Duncan, Bryce, Holly and Ellen. It has always been of great benefit to discuss academic and practical problems with you all.

To my current and past band members: Kieran, Mark, Alex, Matt, Leth, and Bob. Thank you for the support, understanding that I'm not necessarily always free to practice and the laughs in the rehearsal room and on stage.

To my A-level geography teacher, Lorraine Heyworth. If it were not for your enthusiasm while teaching us about volcanoes, I almost certainly would not have expressed an interest in the subject towards the end of my undergraduate degree and would never have gone down this path and this work would never have existed without the passion you so clearly showed for volcanology.

Finally, to the band “Katla.” for being (probably) the only volcanologically inspired artists of the many artists that have accompanied my work over the last four years. My work may not specifically concern the band’s namesake, but the physics is universal.

“Fjöll, holt og hóla
í húminu fann
bak við mín augnlök
og hjartað þar brann
Staður sem slíkur
má sorgina geyma
en hvert sem ég rata
þá á ég þar heima”
Katla. – Hyldýpi (2018)

I thank you all.

Table of Contents

1.	Introduction.....	1
1.1.	Thesis Structure.....	2
2.	Literature Review.....	3
2.1.	Eruption Styles.....	3
2.1.1.	Quiescent Degassing.....	3
2.1.2.	Hawaiian Eruptions.....	4
2.1.3.	Strombolian Eruptions.....	4
2.2.	Properties of Magma.....	5
2.2.1.	Chemical composition.....	5
2.2.2.	Physical Parameters.....	6
2.2.3.	Solubility of Volatiles.....	7
2.2.3.1.	Influence of Pressure.....	7
2.2.3.2.	Influence of Temperature.....	8
2.2.3.3.	Influence of Chemical Composition.....	9
2.2.4.	Rheological Models of Magma.....	10
2.3.	Properties of Bubbles.....	11
2.3.1.	Nucleation Criteria.....	11
2.3.2.	Bubble Growth.....	13
2.3.3.	Dimensionless Numbers.....	14
2.3.3.1.	Reynolds Number.....	14
2.3.3.2.	Eötvös Number.....	14
2.3.3.3.	Morton Number.....	15
2.3.3.4.	Froude Number.....	15
2.3.3.5.	Kapitsa Number.....	15
2.3.4.	Shape Regime.....	16
2.4.	Conduit Models.....	18
2.4.1.	Rise Speed Dependent (RSD) Model.....	18
2.4.2.	Collapsing Foam Model.....	19
2.4.3.	Model Limitations.....	20
2.5.	Models of Bubble Motion.....	21
2.5.1.	Single Bubbles.....	21
2.5.2.	Pairs of Bubbles.....	22
2.5.3.	Bubble Groups.....	25
2.6.	Analogues with Sedimentation.....	29

2.6.1.	Hindered Settling.....	29
2.6.2.	Particle Clustering	33
3.	Methods.....	34
3.1.	Requirements.....	34
3.2.	Methods Development	35
3.2.1.	Equipment Characteristics	35
3.2.2.	Bubble Characteristics	36
3.2.3.	Injections	37
3.2.3.1.	Injection Control	38
3.2.3.2.	Air	39
3.2.3.3.	1-Propanol.....	40
3.2.3.4.	Methanol	40
3.2.3.5.	Diethyl Ether	41
3.2.3.6.	Air and Silicone Oil	41
3.3.	Experimental Configuration	42
3.3.1.	Experimental Tube.....	43
3.3.2.	Base Plate	44
3.3.3.	Solenoid Valve	44
3.3.4.	Pressure.....	44
3.4.	Experimental Procedure for Data Acquisition	45
3.4.1.	Camera Specifications	46
3.4.2.	Camera Placement	46
3.4.3.	Camera Operation.....	48
3.4.4.	Lighting	48
3.4.5.	Sample Preparation.....	50
3.5.	Data Analysis	51
3.5.1.	Bubble Selection.....	51
3.5.2.	Image Processing.....	52
3.5.3.	Bubble Speed Measurement	52
3.5.4.	Stokes' Law and Hadamard-Rybczynski Model	53
3.5.5.	Uncertainty	55
4.	Silicone Oil Characterisation	57
4.1.	Density	57
4.2.	Viscosity.....	58
4.2.1.	Equipment.....	58
4.2.2.	Spheres.....	60

4.2.3.	Method.....	61
4.2.4.	Falling Ball Viscometry Results.....	62
4.3.	Compressibility	63
4.4.	Thermal Expansion	64
4.5.	Volatile Content	64
4.6.	Optical Distortions	65
4.8.	Summary	76
5.	Bubbles in Pseudo-infinite Fluids.....	78
5.1.	Injection.....	78
5.2.	General Bubble Behaviour	79
5.3.	Single Bubbles.....	79
5.3.1.	Summary of Single Bubbles	83
5.4.	Bubbles of Significantly Differing Size	84
5.5.	Group Behaviour.....	89
5.5.1.	Group Formation	91
5.5.2.	Pairs of Similar Sized Bubbles	93
5.5.3.	Coalescence	94
5.5.4.	Dilute Columns.....	95
5.5.5.	Dense Groups	100
5.5.6.	Group Breakups.....	108
5.6.	Summary	110
6.	Bubbles in Vertical Constrained Tubes	113
6.1.	Single Bubbles.....	113
6.2.	Dilute Groups	118
6.3.	Dense Groups	123
6.4.	Other Features	126
6.5.	Summary	127
7.	Bubbles in Inclined Tubes	130
7.1.	General Features of Behaviour.....	130
7.2.	Single Bubbles.....	132
7.3.	Dilute Groups	133
7.3.1.	Bubble Driven Convection	135
7.4.	Dense Groups	136
7.4.1.	Dense Group Breakups	137
7.5.	Other Features	139
7.6.	Summary	139

8.	Discussion	140
8.1.	Evaluation of Experimental Results	140
8.1.1.	Bubbles Interactions Increase Rise Speed	140
8.1.2.	Formation of Groups.....	140
8.1.3.	Bubbles Travel Faster in Most Configurations.....	142
8.1.4.	Bubble Induced Convection	143
8.1.5.	Shallow Inclinations Altered Flow Configuration.....	143
8.1.6.	Returns Flows were Slow and/or Wide	144
8.1.7.	Coalescence was Rare.....	146
8.1.8.	Size Stratification.....	147
8.1.9.	Short Scale Heterogeneities were Unavoidable.....	149
8.1.10.	Dense Groups	151
8.2.	Volcanic Context of Experimental Results	154
8.2.1.	Experimental Limitations	157
8.2.1.1.	Role of Crystals.....	157
8.2.1.2.	Non-Newtonian Effects.....	157
8.2.1.3.	Non-linear Tubes.....	158
8.2.1.4.	Long-Term Behaviours	158
8.2.1.5.	Persistent Nucleation Caused by Rising Magma	158
8.2.2.	Future Work.....	159
8.3.	Application of Results to Volcanic Cases	160
8.3.1.	Convection within a Magma Conduit.....	160
8.3.2.	Gas Puffing Rate.....	163
8.3.3.	Gas Pistoning	164
9.	Conclusion	166
10.	Appendices.....	168
10.1.	Residual and Statistical Information.....	168
10.1.1.	Pseudo-infinite Single.....	168
10.1.2.	Pseudo-Infinite Dilute.....	169
10.1.3.	Pseudo-infinite Dense	170
10.1.4.	Constrained Single.....	171
10.1.5.	Constrained Dilute	172
10.1.6.	Constrained Dense	173
10.1.7.	Inclined Single	174
10.1.8.	Inclined Dilute	175
10.1.9.	Inclined Dense	176

10.2. Location of Data.....	177
11. References.....	178

List of Figures

Figure 2.1: Variations in SO₂ flux (shown in red) over time at the Halema'uma'u lava later in July 2017. From Patrick et al. (2019).	4
Figure 2.2: Diagram of magma classifications based on SiO₂, NaO₂ and K₂O content (Le Bas et al., 1986).	6
Figure 2.3: The solubility of H₂O and CO₂ for rhyolitic and basaltic magmas at two temperatures (Wallace & Anderson, 2000)	8
Figure 2.4: Variations in H₂O solubility in haplogranitic melts and albite (Holtz et al., 1991). The filled triangles are Holtz et al. (1991) experimental results and the open triangles are from Hamilton and Oxtoby (1986).	9
Figure 2.5: A linear relation is demonstrated between Π and CO₂ solubility at a range of pressures and temperatures (Dixon, 1997).	10
Figure 2.6: Balance of dimensionless numbers and their effects on the shape of a single bubble rising in an unhindered gravitational motion. From Clift et al. (1978).	17
Figure 2.7: The relative speed in a bubble pair as a function of their relative separation in an air-H₂O system, where R is the actual separation and a is the bubble diameter. \dot{R} is the magnitude of the rate of change of bubble separation. U_{∞} is the buoyant rise speed of the bubbles, which is not the same as the nomenclature used elsewhere in this thesis. Adapted from Figure 5 in van Wijngaarden (1993).	24
Figure 2.8: Variation of lift coefficient on the lower of two bubbles in a bubble pair as a function of their separation angle. Figure 17 from Kusuno et al. (2019), where θ is defined as the angle between the horizontal direction and the centreline of the two bubbles.	25
Figure 2.9: Probability density function of bubbles travelling at different speeds for a variety of gas volume fractions. For higher gas volume fractions, the modal value decreases and the width of the distribution increases. From Zenit et al. (2001).	27
Figure 2.10: Measured bubble velocity of homogeneous (~1 mm) nitrogen bubbles in H₂O as a function of gas volume fraction. The open circle is for a single bubble in isolation, while the open diamond is for bubbles in highly dilute suspensions (both indicating an increase in $du_b/d\alpha$ between $\alpha = 0$ and $\alpha \approx 0.005$ compared to all other values of α shown. The dashed, dash-dotted and dotted lines represent model estimates using Equation 2.23 for $A = 20$, $A = 10$ and $A = A(\alpha)$ respectively. $A(\alpha)$ is obtained from a fit of velocity variance measurements. Adapted from Zenit et al. (2001).	28
Figure 2.11: Diagram showing a cylindrical column of fluid with radius R flowing past a stationary sphere with radius a at a flow rate of V_0. The plane XX' is the horizontal plane going through the centre of the sphere. From Oliver (1960).	30
Figure 2.12: Relative settling velocity against the solid volume fraction. Data from multiple experiments are shown and demonstrate that the equation for relative settling velocity describes the experimental results well. Adapted from Oliver (1960).	32
Figure 3.1: A cross section diagram of simplest form of the experimental apparatus, excluding the modifications to introduce bubbles into the base of the tube. A column of silicone oil within a glass tube can be subjected to partial vacuum conditions using the vacuum pump.	36

Figure 3.2: This configuration of equipment facilitates the injection of oil mixtures using a solenoid valve to control the timing of the injection. This setup forms the basis of all the main experiments.	39
Figure 3.3: Diagram of the final experimental design.	43
Figure 3.4: Demonstration of the effect that the fluorescent lighting and black cardboard screen have on the visibility of bubbles (examples circled in red). With the lighting and screen in (b), even very small bubbles are clearly distinguished, whereas without it, as in (a), even large bubbles are difficult to observe.	49
Figure 3.5: A top-down view of how three cameras might be set up for an experiment. The direction of view of the TOP camera is perpendicular to the LOW and MID cameras' direction of view.	50
Figure 3.6: Viscosity as a function of temperature for Wacker AK silicone fluids of viscosity greater than or equal to 0.1 Pa s relative to the viscosity at 25 °C. Although this was a different compound than AS 100, in the absence of data for AS 100, the data for AK 100 is taken to be a suitable proxy. Image from the Wacker Silicone Fluid AK data sheet (Wacker, nd.)	54
Figure 4.1: Summary of the experimental setup for falling ball viscometry, not drawn to scale. Note that the oil was almost colourless but is represented by a pale tan colour here for visual clarity.	59
Figure 4.2: Sample image from a falling ball viscometry experiment. A 1 mm Delrin sphere was falling through the viscometer. The two vertical white lines near the centre of the tube were reflections of the fluorescent strip lighting used to illuminate the experiment.	59
Figure 4.3: Example images from the optical characterisation of 1 mm Delrin spheres showing the different surface textures. In (a), the ball had a rough surface texture which may have affected the fall speed through the oil. In (b), the ball appeared to have a smooth surface texture and appeared to have a uniform shape. Scale labels were in millimetres, with the smallest subdivisions being 0.1 mm.	61
Figure 4.4: Measured viscosity for different sphere diameters.	63
Figure 4.5: Experimental setup for determining optical distortions. The silicone oil has been shaded a pale tan colour here for visual clarity.	66
Figure 4.6: Images showing the ruler (a) and the same ruler in the same place, but submerged in oil inside of a glass tube (b).	67
Figure 4.7: Characterisation of horizontal optical distortions in an 80 mm tube. The missing data for "Air, Glass, Oil" between -2 mm and +1 mm was due to reflections on the glass rendering the scale unreadable (Figure 4.6(b)).	67
Figure 4.8: Characterisations of optical distortions in a 40 mm tube.	68
Figure 4.9: Quadratic fit of the central part of the measured distortion ratios of the 80 mm tube.	70
Figure 4.10: Residual between the modelled and observed height:width ratios against the modelled height:width ratio. In all cases, the experimental uncertainty was greater than the magnitude of the residual.	73
Figure 4.11: Shape regime plot for bubbles in the pseudo-infinite tube. The black line indicates the limit of spherical bubbles such that bubbles below the line were in the spherical regime. The curve was determined empirically from the boundary between spherical and non-spherical bubbles shown in Figure 2.2. Note that both the horizontal and vertical scales are logarithmic.	74
Figure 4.12: Shape regime plot for the bubbles in the constrained tube experiments.	75

Figure 4.13: Shape regime plot for the bubbles in the inclined tube experiments. .	76
Figure 5.1: Measured versus theoretical rise speed for single bubbles. The black line marks where theoretical and measured values are equal, so results falling on this line represent values where the Hadamard-Rybczynski model accurately describes those bubbles' motion.	80
Figure 5.2: An example of the motion of a bubble in a pseudo-infinite experiment from RUN15_LOW3 PS1. The green line represents vertical speed, the black dashed line shows the total speed, the red line shows measured horizontal speed, the blue line represents the theoretical speed as described by the Hadamard-Rybczynski model, with the blue dashed line indicating the uncertainty values.....	82
Figure 5.3: A bubble (RUN06_MID PS13) travelling through pseudo-infinite fluid. As with Figure 5.2, there was very close agreement with the Hadamard-Rybczynski model and no evidence of notable lateral motion.	82
Figure 5.4: A single bubble (RUN06_MID PS12) travelling through a pseudo-infinite fluid. As with Figures 5.2 and 5.3, there was very close agreement with the Hadamard-Rybczynski model and no evidence of notable lateral motion.....	83
Figure 5.5: A large bubble (approximately 5 mm tall) interacting with many smaller bubbles at varying separation distances. (a) An extended line of very small ($\ll 1$ mm diameter) bubbles was left in the wake of a very large bubble (~ 50 mm diameter) at the start of experiment (not shown). These bubbles were still rising in the wake of that bubble, but were moving much slower than the larger bubble below. In (b), the larger bubble was at the same height as the lower portion of the stream of bubbles. A significant bend in what was originally a near straight line of bubbles was observed. This was due to the passage of the larger bubble. In (c) a similar effect was seen, however the bubble stream was further away from the larger bubble and so the effect was much reduced. Similarly, in (d) the effect was barely visible. The time interval between each frame shown was 0.4 seconds.....	85
Figure 5.6: Example images of two interactions between a small bubble and a much larger bubble from RUN03_LOW3. The bubble circled in red is RUN03_LOW3 PS1 (Figure 5.7) and the bubble circled in green is RUN03_LOW3 PS3 (Figure 5.8).....	86
Figure 5.7: The measured versus theoretical rise speed of a small bubble (RUN03_LOW3 PS1) interacted with a much larger bubble which subtended and then overtook the smaller bubble. The gaps in the data were from frames where the smaller bubble were not clearly visible on the image, so data were not collected. ..	87
Figure 5.8: A further example of a small bubble (RUN03_LOW3 PS3) interacting with a larger one. The deceleration of this bubble is not shown as it moved out of the field of view of the camera.....	87
Figure 5.9: The excess height gained by nine smaller bubbles interacting with a much larger bubble. The data gaps are where the bubbles were not visible. The increase in speed for RUN02_NEWLOW1 bubbles was due to another large bubble passing through the tube and interacting with those bubbles.	89
Figure 5.10: A sample image from RUN10_MID showing two examples of a dilute column. The cluster of between the two boxes had a bubble number density too great to be considered a dilute grouping, however it also would not have been considered a dense group as this cluster was transient and did not maintain a high bubble number density for a sufficient length of time in order to take measurements.....	90

Figure 5.11: Three examples of dense groups from RUN2_LOW2. The direction of motion in this image was right to left. The majority of the bubbles not circled would be considered as being part of dilute groups...... 91

Figure 5.12: Demonstration of preferential formation of groupings of bubbles. In (a) and (b) the larger dense grouping of bubbles can be seen (highlighted in green) breaking apart and becoming less dense. In (c) and (d) a small but dense group of around ten bubbles forms (highlighted in red). The time interval between each frame shown here was 1.2 s. The static round feature in the centre-left of the images was a hole in the tube wall that was repaired with epoxy. Three height markers can be seen which were 10 cm apart and indicated the heights of 0.5 m, 0.6 m, and 0.7 m above the base plate...... 92

Figure 5.13: Photograph of the lower portion of the experimental tube, showing that the apparatus obscured the observation of the early behaviour of the bubbles (a) and a highly distorted image of the injection needle (b)...... 93

Figure 5.14: Example of two pairs of bubbles in a pseudo-infinite tube in RUN07_LOW. Touching pairs of bubbles was an uncommon type of interaction and observing two instances of it at the same time occurred only once, shown here...... 94

Figure 5.15: Theoretical versus measured rise speed for bubbles in the dilute column. The black line indicates where the theoretical and measured values are equal...... 95

Figure 5.16: An example of the movement of a small bubble through a dilute column of other bubbles of similar volume, from RUN06_MID PS4. The gap in the data at approximately frame 30 was due to another bubble briefly obscuring the one being measured. The Hadamard-Rybczynski model was used to obtain the calculated value for the bubble’s speed, with the minimum and maximum values (dashed blue lines) calculated using the upper and lower bounds from the experimental uncertainty in the bubble’s size...... 97

Figure 5.17: Measured and theoretical rise speeds of RUN06_MID PS5. The gap in the data were frames where the bubble was not clearly visible. 98

Figure 5.18: Images from the video RUN06_MID with bubble PS5 highlighted at the centre of the red circles. The frame numbers correspond to the frame from the first measurement (and therefore Figure 5.17), as measurements did not start on the first frame of the video, but rather the 19th frame as the bubble was not in the field of view of the camera for the first 18 frames...... 99

Figure 5.19: Theoretical versus Measured speeds of 30 bubbles in dense groups in the pseudo-infinite tube...... 100

Figure 5.20: Sample images from the two slowest moving bubbles measured in dense groups (a and b) and the two fastest moving bubbles in dense groups (c and d), the measured bubbles were at the centre of the red circles. In these images, the direction of motion was from right to left. 102

Figure 5.21: Measured rise speed against initial group size for 18 dense groups. The two groups examined in further detail are circles in red and green. These colours correspond to the same groups in Figure 5.22...... 103

Figure 5.22: The progression of the two dense groups from RUN09_LOW. Both groups were only measured between Frames 120 and 150, with the earlier frames provided for additional context. The larger group, circled in red, was formed of three smaller groups, which consolidated into one larger group at around Frame 120, whereas the smaller group, circled in green, travelled through the

column of bubbles trailing behind the larger group. As the time interval between each frame was 0.04 s, there was an interval duration of 1.2 s between each of the frames shown here.....	104
Figure 5.23: Ascent of two dense groups through the experimental tube from RUN08_LOW. The smaller group is circled in red and the larger group circles in green. The smaller group observation duration was from Frame 50 to Frame 175 whereas the larger group only formed as one single group in Frame 150, so the observations began on that frame. The blue circles show the constituent groups that later combined to form the larger group circled in green. The time interval between each frame was 0.04 s, and an interval duration of 1.0 s separating the frames shown here.....	105
Figure 5.24: Instantaneous speeds of two dense groups from RUN08_LOW. The smaller group (circled in red in Figure 5.23) was observed to change shape across the observation period which coincides with a reduction in speed. The “Large Group” data correspond to the large group circled in green in Figure 5.23.	107
Figure 5.25: The distance from the initial position of the centre of ten dense groups. The black dashed line is a straight reference line to illustrate that most of these groups decelerated over time. The observations ended when the groups were judged to be breaking up, or if they left the field of view of the camera.....	109
Figure 5.26: Height to width ratio of 17 dense groups as they began to break apart. All but one (RUN08_LOWb, shown as the group circled in green in Figure 5.23) became flatter and wider, as shown by the reduction in this ratio over time. The frame numbers refer to each specific video, so cannot be compared between experimental runs.....	109
Figure 5.27: Change in volume of 17 groups as they began to break apart. In all cases shown here, the volume of the groups increased, even if the increase was small in some cases, most of these groups increased in volume by a factor of 1.5-3. The frame number refers to each specific video, so were not comparable between groups, but demonstrate the duration of time that elapsed between the measurement.....	110
Figure 6.1: Theoretical and measured rise speeds for single bubbles in a constrained tube. As in Chapter 5, the black line represents the points where measured speed and theoretical speed are equal.....	113
Figure 6.2: Inter-frame measured speed and theoretical speed of bubble RUN18_LOW PS1. The plot was cropped to more clearly show the detail in the lower speed values as a large bubble passed through the experimental tube which increased the speed of the RUN18_LOW PS1 bubble between frames 160 and 180 to a maximum of 62.2 mm s⁻¹.....	115
Figure 6.3: Inter-frame measured speed and theoretical speeds of bubble RUN19_LOW1 PS1. Extreme values have been cropped to show detail in the smaller values. The maximum measured speed was 65.6 mm s⁻¹, achieved in Frame 216.....	115
Figure 6.4: Excess height of the bubble RUN19_LOW1 PS1 (this was the same bubble as Figure 6.3). The injection of oil into the base of the apparatus began on frame 148 and ended at approximately frame 190. The increases in height around frames 210 and 355 were due to interactions with large bubbles.....	117
Figure 6.5: Theoretical versus measured speeds for bubbles in dilute columns. In all cases, the bubbles travelled approximately twice as fast as the Hadamard-Rybczynski equation predicted for their volume, indicating strong group	

behaviour. The linear fit shows a constant speed increase of approximately 2.5 mm s^{-1} in the measured values, as well as a gradient of 0.654 ± 0.007 indicating that larger bubbles rose disproportionately faster than expected under the Hadamard-Rybczynski model.....	119
Figure 6.6: Comparison between dilute groups in the constrained tube and the pseudo-infinite tube. Aside from two areas of increased number density in Frame 1, there was a relatively (compared to (c) and (d)) uniform bubble number density within the column of bubbles and a similar bubble number density in (b), and the shape of the column of bubbles did not vary greatly across the time period. Whereas in (c), the bubble number density was not consistent across the group and as the group developed into what is seen in (d), the group spread laterally, further changing the bubble number density. Note that for the Pseudo-infinite images, the images were flipped horizontally so that the direction of motion in all four images was from left to right. The field of view for (a) and (b) was approximately 10 cm, whereas the field of view for (c) and (d) was approximately 20 cm.....	121
Figure 6.7: The variation in speed over time of RUN17_LOW4 PS6 across an 8-second observation period. While there was some variation across this time, it typically travelled at $10 \pm 2 \text{ mm s}^{-1}$, representing a more consistent speed than in Figures 5.15 and 5.16 (which were for Pseudo-infinite RUN06_MID) in the pseudo-infinite case.....	122
Figure 6.8: Theoretical and measured rise speeds for selected bubbles in dense groups. A very weak positive correlation was shown between the measured and theoretical rise speeds.....	124
Figure 6.9: Two dense groups. (a) and (b) show a dense group in the constrained experiment while (c) and (d) show a constrained group in the pseudo-infinite experiment. The field of view in (a) and (b) was approximately 10 cm whereas the field of view in (c) and (d) was approximately 20 cm. The dense group in (c) has a larger estimated volume than the group in (a), despite appearing to be smaller in the image.....	125
Figure 7.1: Example of typical bubble behaviour in an inclined tube (internal diameter of 40 mm). This image was from 11.56 s in video RUN07_LOW. Note that the camera was not aligned perfectly vertically, and was approximately 2° from vertical, making the tube inclination in the image appear greater than 4.3°	131
Figure 7.2: Theoretical and measured rise speeds for single bubbles in an inclined tube.....	133
Figure 7.3: Theoretical and measured rise speeds for bubbles in dilute groups in an inclined tube.....	134
Figure 7.4: Theoretical versus measured rise speed for dense groups in an inclined tube.....	137
Figure 7.5: Images from RUN06_LOW1 demonstrating the breakup of a dense group.....	138
Figure 7.6: An example of the breakup of two dense groups from RUN07_LOW1.....	138
Figure 8.1: Sketch plot of how the vertical velocity of the oil, v , may vary with distance from the centre of the tube (marked as 0) across a tube with radius R when a column of bubbles (small grey circles) rises through the centre of the tube. Due to the conservation of momentum, the integral of v with respect to the distance from the central axis evaluated between $-R$ and R must equal zero, unless the surface of the oil is rising. Not drawn to scale.....	145

Figure 8.2: Sketch plot of the expected velocity of oil of an inclined tube in the direction of the tube walls. The direction of acceleration due to gravity, g, is shown. Not drawn to scale.	146
Figure 8.3: Cross section sketch of a dense group showing the internal motion of bubbles within the group which may cause the observed toroidal motion of bubbles within the group, in the frame of reference of that group. The black lines show the motion of the oil around the group, while the grey arrows indicate the observed motion of bubbles within the group. Not drawn to scale.	152
Figure 8.4: Sketch demonstrating how the oil may flow through the group in dilute groups (a) or around a dense group (b). Note that the flow lines of the oil are in the frame of reference of the group itself rather than relative to the tube walls. Not drawn to scale.....	153
Figure 8.5: Map of different flow patterns characterised by Froude and Kapitza numbers. In the inset images, orange denotes the liquid while white denotes gas bubbles, the red, orange, green and blue squares show the regimes of experiments performed by Pioli et al. (2017) while the large red cross shows the approximate regime of the experiments presented in Chapters 5, 6 and 7. From Figure 1 of Pioli et al. (2017).....	162
Figure 10.1: Residual between theoretical and measured rise speed against theoretical rise speed for single bubbles in the Pseudo-infinite tube. The red line denotes where the residual is equal to zero.	168
Figure 10.2: Residual between theoretical and measured rise speed against theoretical rise speed for bubbles in dilute groups in the Pseudo-infinite tube.	169
Figure 10.3: Residual between theoretical and measured rise speed against theoretical rise speed for bubbles in dense groups in the Pseudo-infinite tube.	170
Figure 10.4: Residual between theoretical and measured rise speed against theoretical rise speed for single bubbles in the Constrained tube.....	171
Figure 10.5: Residual between theoretical and measured rise speed against theoretical rise speed for bubbles in dilute groups in the Constrained tube.....	172
Figure 10.6: Residual between theoretical and measured rise speed against theoretical rise speed for bubbles in dense groups in the Constrained tube.....	173
Figure 10.7: Residual between theoretical and measured rise speed against theoretical rise speed for single bubbles in the Inclined tube.....	174
Figure 10.8: Residual between theoretical and measured rise speed against theoretical rise speed for bubbles in dilute groups in the Inclined tube.....	175
Figure 10.9: Residual between theoretical and measured rise speed against theoretical rise speed for bubbles in dense groups in the Inclined tube.	176

List of Tables

Table 2.1: Selection of common magmas, their liquidus temperatures and melt viscosities at liquidus at a pressure of 0.1 MPa (Spera, 2000)	7
Table 2.2: Model parameters for a general basaltic system to examine the most probable bubble shape regime.....	18
Table 4.1: Breakdown of the measurements for determination of H₂O and oil density. Uncertainties in mass are calculated using standard deviation of repeated measurements. Uncertainty in oil density was from propagation of the relative uncertainty in oil mass (shown to be normally distributed from a Kolmogorov-Smirnov test for normality), and the precision value of the graduated cylinder.....	57
Table 4.2: Summary of the size and density data for the four types of spheres used in the falling ball viscometry experiments. The uncertainty in diameter was based on the standard deviation of ten measurements. Uncertainty in density was calculated from the uncertainty in diameter and the precision of the weighing scale. The optical values shown here are after an adjustment to account for the parallax effect.....	60
Table 4.3: Summary of the volatile extraction experiment. The uncertainty in the weight measurements was based on the variation observed in repeat measurements. Given the sensitivity of the weighing scale, the variation could be explained by local air currents.....	65
Table 4.4: Summary of the average number of pixels per millimetre for the non-extreme values for different tubes.....	68
Table 4.5: Observed ratio of bubble height to bubble width. Intermediate calculations and position data are in the supplemental data (Section 10.2).....	71
Table 4.6: Observed and measured ratios between the height and width of bubbles.	72
Table 4.7: Summary of the findings of this chapter, the measured results were the results to be used for the analysis of data in the main experiments.....	77
Table 10.1: Tests for normality for single bubbles in the Pseudo-infinite tube.	168
Table 10.2: Theoretical-Measured correlation and Theoretical-Residual correlation for single bubbles in the Pseudo-infinite tube. The theoretical, measured and residual values were all normally distributed, so Pearson's R is used.....	169
Table 10.3: Tests for normality for bubbles in dilute groups in the Pseudo-infinite tube.....	169
Table 10.4: Theoretical-Measured correlation and Theoretical-Residual correlation for bubbles in dilute groups in the Pseudo-infinite tube. The theoretical, measured and residual values were all normally distributed, so Pearson's R is used.	169
Table 10.5: Tests for normality for bubbles in dense groups in the Pseudo-infinite tube.....	170
Table 10.6: Theoretical-Measured correlation and Theoretical-Residual correlation for bubbles in dense groups in the Pseudo-infinite tube. The theoretical, measured and residual values were all normally distributed, so Pearson's R is used.	170
Table 10.7: Tests for normality for single bubbles in the Constrained tube.....	171
Table 10.8: Theoretical-Measured correlation and Theoretical-Residual correlation for single bubbles in the Constrained tube. The theoretical, measured and residual values were all normally distributed, so Pearson's R is used.	171
Table 10.9: Tests for normality for bubbles in dilute groups in the Constrained tube.....	172

Table 10.10: Theoretical-Measured correlation and Theoretical-Residual correlation for bubbles in dilute groups in the Constrained tube. The theoretical, measured and residual values were all normally distributed, so Pearson's R is used.	172
Table 10.11: Tests for normality for bubbles in dense groups in the Constrained tube.	173
Table 10.12: Theoretical-Measured correlation and Theoretical-Residual correlation for bubbles in dense groups in the Constrained tube. The theoretical, measured and residual values were all normally distributed, so Pearson's R is used.	173
Table 10.13: Tests for normality for single bubbles in the Inclined tube.	174
Table 10.14: Theoretical-Measured correlation and Theoretical-Residual correlation for single bubbles in the Inclined tube. The theoretical, measured and residual values were all normally distributed, so Pearson's R is used.	174
Table 10.15: Tests for normality for bubbles in dilute groups in the Inclined tube.	175
Table 10.16: Theoretical-Measured correlation and Theoretical-Residual correlation for bubbles in dilute groups in the Inclined tube. The theoretical, measured and residual values were all normally distributed, so Pearson's R is used.	175
Table 10.17: Tests for normality for bubbles in dense groups in the Inclined tube.	176
Table 10.18: Theoretical-Measured correlation and Theoretical-Residual correlation for bubbles in dense groups in the Inclined tube. The theoretical, measured and residual values were all normally distributed, so Pearson's R is used.	176

1. Introduction

The understanding and management of the threat posed by volcanic activity remains a challenge for society. By better understanding the physical processes within the volcanic system it is possible to make more accurate and timely forecasts of activity. In low viscosity (on the order of tens to hundreds of Pa s) basaltic systems, the configuration of bubbles in the magma upon eruption (e.g. a very large gas slug or many small and dispersed small bubbles) upon eruption is critical to the eruption style (Parfitt & Wilson, 1994). While an understanding of how different configurations of bubbles affect surface activity, subsurface processes are not fully understood, and current monitoring is not always sufficient to issue suitable warnings. For example, the unusually large eruptions at Stromboli in July and August 2019 were not expected based on readings from real-time monitoring (INGV, 2019a; INGV 2019b), indicating that current observations alone are insufficient to anticipate some eruptions, particularly paroxysmal eruptions. Conduit models are based on an understanding of possible subsurface processes but, different models are used to represent different ranges of physical processes and, individually, may only be applicable to specific types of volcano rather than provide a generalised description covering all processes (e.g. Burton et al., 2007). Furthermore, models often consider vertical magma conduits, whereas measurements indicate highly inclined conduits in some volcanic systems. Preliminary analogue experimental studies, prior to those described in Chapter 3, indicated the possibility of small gas bubbles in viscous liquids interacting with each other and with the constraining walls to alter their ascent rate and create spatial variations in bubble number density. Additionally, it was observed in preliminary experiments that even shallow inclinations (less than 5° from vertical) can change the spatial configuration of bubbles in the liquid substantially, which is an effect not considered in current conduit models. The role of inter-relationships between gas bubbles in a magma has not been completely described by previously published conduit models (e.g. Parfitt & Wilson, 1994; Parfitt, 2004; Vergnolle & Jaupart, 1986; Jaupart & Vergnolle, 1988). As such, the following chapters examine experimentally how ascending bubbles interact with each other and with constraining walls, thus, changing their ascent speed and spatial configurations beyond what would be otherwise assumed in existing models.

It is proposed that the interactions between bubbles and other bubbles, or bubbles with conduit walls, and more broadly, heterogeneities in bubble number density

distribution across a tube or conduit, have a notable impact on the ascent rate and spatial configuration of bubbles, leading to variations in eruption styles compared to those expected from an interaction-free model.

1.1. Thesis Structure

Chapter 2 recaps the present understanding of the relevant physical properties of magma and gas bubbles, and some of the present conduit models and existing models for the ascent of bubbles and groups of bubbles. Chapter 3 details the laboratory method used to investigate bubble interactions, which was based on silicone oil as a magma analogue. Characterisation of the physical properties of the silicone oil is described in Chapter 4. Additionally, Chapter 4 demonstrates that the bubbles measured in the following chapters can be considered valid candidate bubbles for the theoretical modelling of their rise speed under the assumption of them being spherical and without interactions with the tube walls and other bubbles. Chapters 5-7: Chapter 5 presents observations of small bubbles in a pseudo-infinite fluid (where the bubbles were sufficiently far from the constraining walls that the walls were not expected to influence the bubble behaviour). Chapter 6 presents similar experiments, but where the tube diameter was sufficiently narrow that the walls of the tube were expected to affect gas bubble ascent. Chapter 7 presents results from experiments in which the experimental tube was inclined. Chapter 8 evaluates the relevance of the analogue experimental results for understanding magmatic system, highlights limitations of the experimental apparatus and technique, and discusses the implications of the findings on present understanding on gas mass transport processes in basaltic magmatic systems. Chapter 9 concludes the thesis with the main findings. Chapter 10 (Appendices) contains residual plots, details of statistical analyses and information about the online repository of raw data.

2. Literature Review

2.1. Eruption Styles

In volcanic systems, the gas content within the magma is a fundamental control on the style of eruption (Jaupart, 1996) and so understanding the way in which gas travels through a volcanic conduit necessarily aids understanding of the eruptive process. Whilst many possible styles of volcanic activity exist, there are only a small number that are of immediate relevance to the aims of the work presented in subsequent chapters. The subsequent sections identify three different types of behaviour, these are notable members on a continuous scale of varying gas bubble sizes and distributions.

2.1.1. Quiescent Degassing

Although quiescent, or passive, degassing is not an eruption style, it is a relevant volcanic activity between eruptions as it characterises non-eruptive behaviour, from which the gas flux during eruptive behaviour can be compared. For example, the gas mass flux of SO₂ at Kilauea in July 2017 was measured to vary temporally as different types of activity occurred at the Halema'uma'u lava lake. In periods where no spattering occurred, the SO₂ flux was measured to be approximately 10 kg s⁻¹, rising to peaks of over 100 kg s⁻¹ at times when spattering occurred (Figure 2.1) (Patrick et al., 2019). Additionally, SO₂ flux at Stromboli has indicated quiescent degassing is responsible for gas mass fluxes of 2.3 kg s⁻¹ (Burton et al., 2007), which accounts for the majority of the SO₂ flux at Stromboli, as single explosive events release 15-40 kg of SO₂ per explosion, which accounts for only 3-8 % of the daily SO₂ flux (Mori & Burton, 2009). At Etna, quiescent degassing is thought to account for over 80 % of the gas mass budget, as less than 20 % of the rising magma, from which the gas exsolves, eventually erupts (Allard, 1997). The spatial configuration of gas bubbles immediately below the surface during quiescent degassing has been suggested to be characterised by many small bubbles or slugs (larger bubbles formed from coalesced smaller bubbles) (James et al., 2009). The transition from bubbles in this configuration to that which induces explosive eruptive activity is important in understanding the possible eruption styles as a result of rising magma.

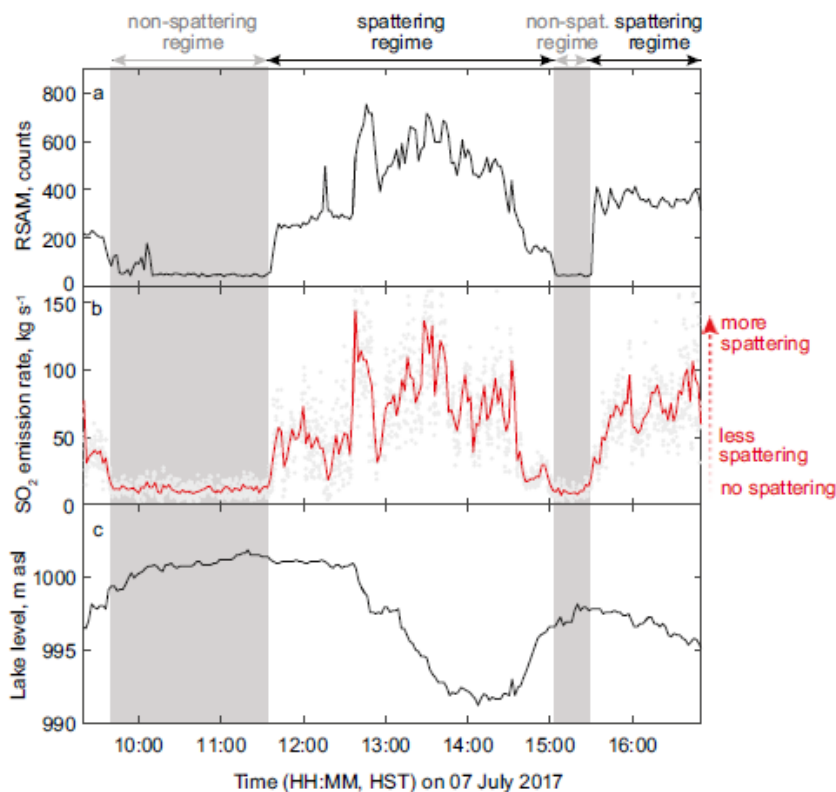


Figure 2.1: Variations in SO₂ flux (shown in red) over time at the Halema'uma'u lava later in July 2017. From Patrick et al. (2019).

2.1.2. Hawaiian Eruptions

Hawaiian style eruptions are characterised as constant eruption (over several hours or even days) of gas-rich magma in the form of fire fountains, which may attain heights of 500 m and mass fluxes over 10^6 kg s^{-1} (Parfitt et al., 1995; Gonnermann & Manga, 2013; Houghton & Gonnermann, 2008). It is thought that gas bubbles prior to eruption are distributed as many small bubbles because, when the rise speed of the magma is sufficiently fast ($> 1 \text{ m s}^{-1}$) (Parfitt & Wilson, 1995), coalescence of gas bubbles is insufficient to produce the large bubbles that would cause discrete explosive events (Section 2.1.3). The transition from this, Hawaiian, behaviour to more impulsive, Strombolian, style eruptions is thought to be connected to the ascent rate of magma, as slower moving magma allows a greater amount of time for bubbles to coalesce into larger bubbles, which cause more impulsive and discrete eruptions (Parfitt & Wilson, 1995).

2.1.3. Strombolian Eruptions

Strombolian activity is characterised by small (compared to, for example, Plinian eruptions), cyclical explosions (Gurioli et al., 2013; Chouet et al., 1974;

Blackburn et al., 1976). The explosions are widely accepted to be the surface manifestation of very large gas bubbles (slugs) (James et al., 2009), requiring significant coalescence of smaller bubbles to occur. Photoballistic analysis of the explosions suggest the mass of gas in these bubbles can be greater than 100 kg (Chouet et al., 1974). Geochemical analysis of the gas emitted during Strombolian eruptions at Stromboli has indicated that the formation of the slugs occurs at a depth of approximately 3 km below the surface, with suggestions that the coalescence is the result of discontinuities in the morphology of the constraining walls of the magma (Burton et al., 2007; Jaupart & Vergnolle, 1988; Jaupart & Vergnolle, 1989). The depth noted is specific to Stromboli, but the mechanism that the model utilises may not be. This model, and the Hawaiian model are compared in Section 2.4.

2.2. Properties of Magma

2.2.1. Chemical composition

Magma is typically composed of a few major compounds and many minor compounds. Major compounds include SiO_2 , Al_2O_3 , FeO , Fe_2O_3 , CaO , MgO , and Na_2O while minor compounds include K_2O , TiO_2 , MnO , and P_2O_5 (Rogers & Hawkesworth, 2000). In particular, the balance of silicone dioxide (SiO_2) to sodium oxide (Na_2O) and potassium oxide (K_2O) is often considered as a useful differentiation between types of magma (Figure 2.2).

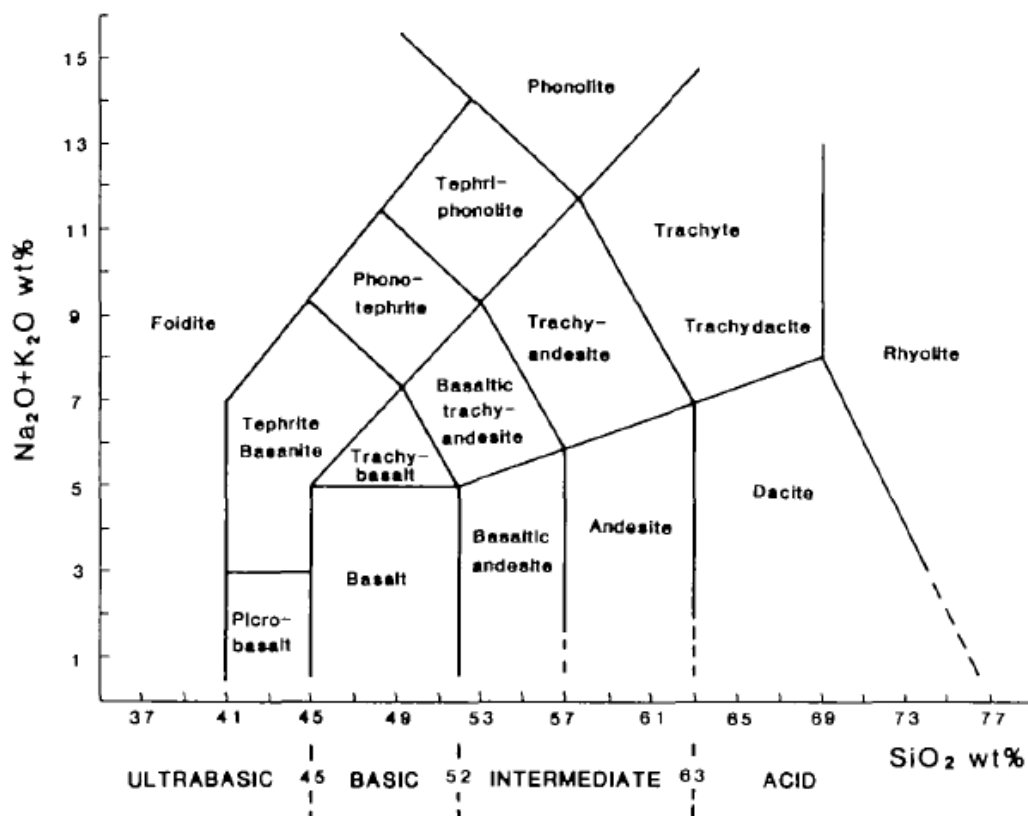


Figure 2.2: Diagram of magma classifications based on SiO_2 , Na_2O and K_2O content (Le Bas et al., 1986).

Basaltic magmas, which are of principal concern in this body of work, have typical compositions of 45-52 % by weight SiO_2 (hereafter denoted as wt. %) and <5 wt. % $\text{SiO}_2 + \text{K}_2\text{O}$. The chemical composition is one of several factors affecting the physical properties of the magma.

2.2.2. Physical Parameters

The principal physical parameter governing degassing of magma processes is its viscosity. Magma viscosity may vary by several orders of magnitude and is predominantly affected by the chemical composition, volatile content, crystal content and temperature of the magma. In the context of magma, a volatile is a compound with a low boiling point which can dissolve in and exsolve from magma to form a gas phase.

Table 2.1: Selection of common magmas, their liquidus temperatures and melt viscosities at liquidus at a pressure of 0.1 MPa (Spera, 2000)

Magma Type	Liquidus Temperature / °C	Melt Viscosity / Pa s
Rhyolitic (completely degassed)	900	1.2×10^{10}
Rhyolitic (2 wt. % H ₂ O)	900	5×10^5
Basaltic	1200	30

The liquidus temperature is defined as the “temperature below which a molten compound begins to crystallize” (Jeanloz, 2000) and as such, it is the temperature at which a magma ceases to be a homogeneous melt phase.

Table 2.1 shows that there are 9 orders of magnitude difference between the viscosities of the magma resulting from comparatively small changes in temperature and the chemical composition of the magma (a reduction of 300 °C, an increase in SiO₂ of approximately 20 % and removing all H₂O). There is a very large change in viscosity (5 orders of magnitude) between rhyolitic magma containing 2 wt. % H₂O and completely degassed rhyolitic magma. Magma viscosity, and its effect on magma degassing, strongly influences eruption style (Pistone et al., 2015; Jaupart, 1996), therefore, understanding the solubility of volatiles, nucleation of bubbles, the separation of the gas and liquid phases and how gas travels in magma are important aspects in understanding volcanic risks. Understanding how volatile species move from being a dissolved volatile, to gas bubbles and then the path taken by those bubbles as they ascend towards the surface, is vital in aiding the understanding of differing volcanic eruption styles.

2.2.3. Solubility of Volatiles

The distribution of gas within a conduit is a major factor in influencing eruption style (Jaupart, 1996). As a volatile-bearing magma ascends, dissolved volatile species will exsolve to form gas bubbles when their solubility limit is reached. The main factors which affect solubility of volatiles in magma are pressure, temperature, and chemical composition of the magma.

2.2.3.1. Influence of Pressure

Pressure is the primary factor influencing volatile solubility (Gonnermann & Manga, 2012). While pressure decreases, the solubility of both CO₂ and H₂O decreases in a non-linear manner (Figure 2.3). At zero gauge pressure, solubility of CO₂ and H₂O is almost zero which implies that, given the correct conditions, magma could completely degas. On Earth, subaerial eruptions occur at atmospheric pressure

(approximately 0.1 MPa). Pressure within Earth increases with depth according to the lithostatic pressure equation, assuming a constant gravitational field (Equation 2.1) (Landau & Lifshitz, 1966)

$$P = \rho gh + c \quad (2.1)$$

where ρ is rock density, g is acceleration due to gravity, h is depth and c is the pressure at zero depth (i.e. atmospheric pressure). Pressure affects solubility and the dominant parameter governing pressure variations in a magmatic setting is depth.

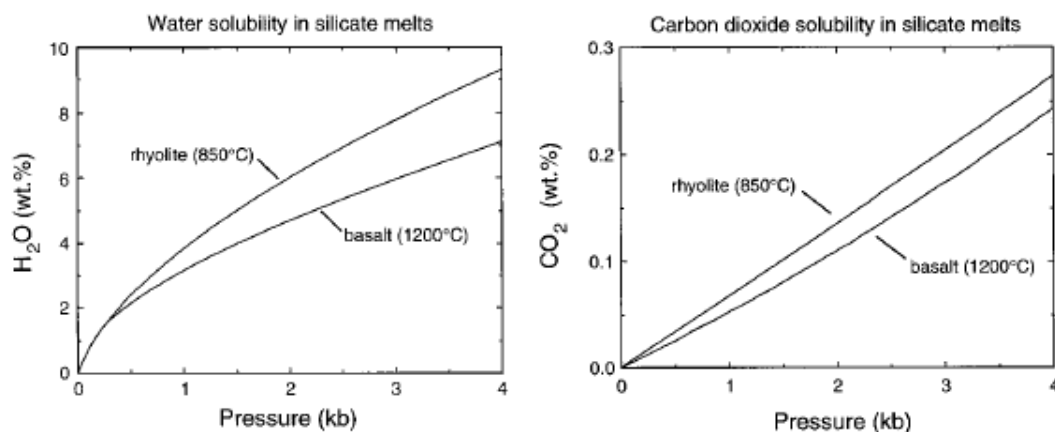


Figure 2.3: The solubility of H₂O and CO₂ for rhyolitic and basaltic magmas at two temperatures (Wallace & Anderson, 2000)

Due to the difference in temperature that is typical between basaltic and rhyolitic magmas, both H₂O and CO₂ generally have lower solubility in basaltic magma than in rhyolitic magma at high pressure (Figure 2.3). Additionally, H₂O is more soluble than CO₂ at a given pressure.

However, at approximately 0.5 kbar (50 MPa, approximately 2 km depth for a rock density of 2,500 kg m⁻³), the solubility of H₂O in basalt and rhyolite become similar, indicating that at depths less than ~2 km, temperature alone does not strongly influence any observed differences in solubility between the two magma types.

2.2.3.2. Influence of Temperature

A secondary physical factor which affects the solubility of volatiles is temperature. There is no detectable change in solubility as a function of temperature for CO₂ in basaltic magma at 1 GPa and 1.5 GPa (Pan et al., 1991). However, there is a negative correlation between temperature and H₂O solubility in rhyolitic melt at 200 MPa, indicating that the solubility of volatiles at lower depths is partially dependent on temperature (Figure 2.4)

(Holtz et al., 1992). Relative to variations in solubility due to pressure, variations in solubility due to temperature are considered negligible for the purposes of this work.

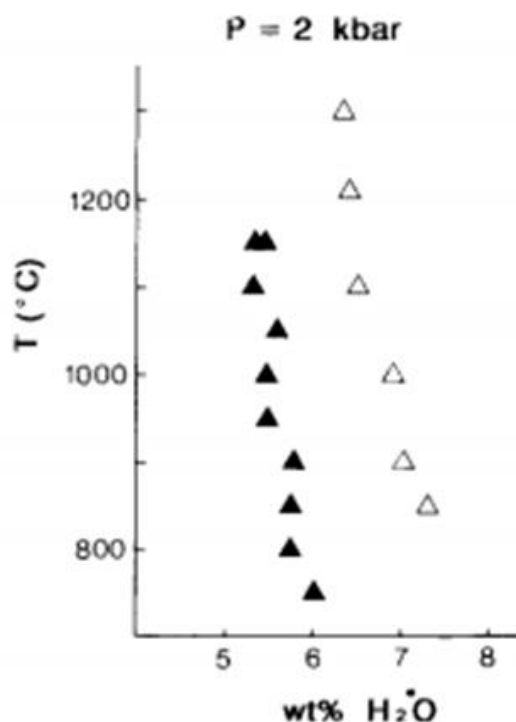


Figure 2.4: Variations in H₂O solubility in haplogranitic melts and albite (Holtz et al., 1991). The filled triangles are Holtz et al. (1991) experimental results and the open triangles are from Hamilton and Oxtoby (1986).

2.2.3.3. Influence of Chemical Composition

The solubility of CO₂ and H₂O is partly controlled by the content of minor volatiles (Dixon, 1997). The compositional parameter Π is used to describe the combined effect of the molar proportions of Si⁴⁺, Al³⁺, Ca²⁺, K⁺, Na⁺, Mg²⁺ and Fe²⁺ ions, which are the cations affecting the solubility of CO₂ and H₂O (Equation 2.2) (Dixon, 1997).

$$\Pi = -6.50(\text{Si}^{4+} + \text{Al}^{3+}) + 20.17(\text{Ca}^{2+} + 0.8\text{K}^{+} + 0.7\text{Na}^{+} + 0.4\text{Mg}^{2+} + 0.4\text{Fe}^{2+}) \quad (2.2)$$

The solubility of CO₂ in a melt is linearly dependent on Π and the parametrisation of Π holds over a range of temperatures and pressures (Figure 2.5) (Dixon, 1997).

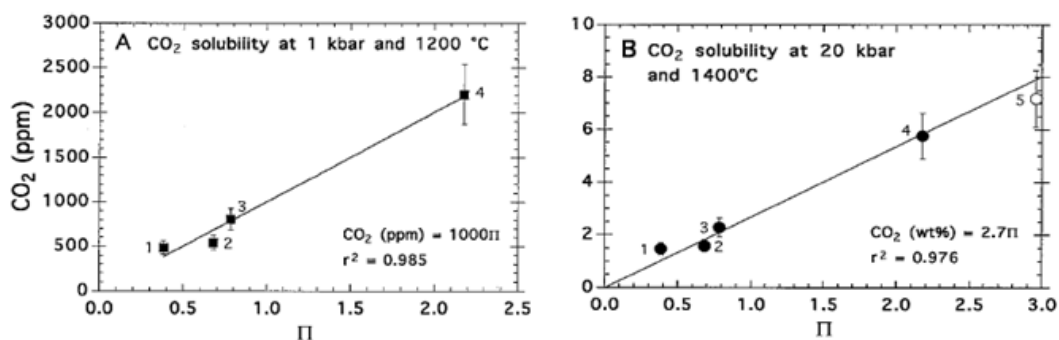


Figure 2.5: A linear relation is demonstrated between Π and CO_2 solubility at a range of pressures and temperatures (Dixon, 1997).

2.2.4. Rheological Models of Magma

The rheology of magma affects the rise speed of bubbles through magma, and affects how the magma responds to the application of stress (for example, the shear stress generated between an upward moving column of magma and the static conduit walls). Magma rheology is principally influenced by chemical composition, volatile content, temperature, gas volume fraction, gas bubble size, crystal volume fraction, crystal shape and strain rate (Gonnerman & Manga, 2007).

Different models exist to model different types of magma, different areas of the conduit and may use simplified models to approximate the magma's properties when appropriate. For example, a homogeneous melt at great depth with an absence of bubbles and crystals may be described using a one phase fluid rheological model. However, the magma just prior to eruption contains bubbles, crystals and melt and would be more appropriately described by a three-phase fluid model. Some rheological models focus on the influence of one or two parameters rather than comprehensively examining all possible parameters.

In Newtonian fluids, such as H_2O , the shear stress and resultant strain rate are directly proportional to each other via the viscosity of the fluid.

$$\tau = \eta \dot{\gamma} \quad (2.3)$$

where τ is the shear stress of the fluid, η is the viscosity of the fluid and $\dot{\gamma}$ is the resultant strain rate of the fluid caused by the stress τ . Assumption of Newtonian rheology has been found to adequately explain the morphology of Soufrière lava (Huppert et al., 1982). Additionally, a Newtonian approximation for lava flows at high temperatures has been shown to be appropriate for Etnean lava flows (Tallarico & Dragoni, 1999).

Alternatively, considering magma or lava as a Herschel-Bulkley fluid (Equation 2.4) can be an effective model and relatively simple to use due to a low number of variables (Castruccio et al., 2010; Castruccio et al., 2014; Cimarelli et al., 2011; Okumura et al., 2013; Mueller et al., 2010; Mueller et al., 2011). The Herschel-Bulkley equation is defined as

$$\tau = \tau_0 + K\dot{\gamma}^n \quad (2.4)$$

where τ_0 is the yield strength of the fluid (the minimum force required to deform the fluid), K is the consistency and n is the flow index (Mueller et al., 2010). The flow index, n , determines if the fluid responds linearly to an applied force. When $n > 1$, the fluid is shear thickening whereas when $0 < n < 1$, the fluid is shear thinning. When $n = 1$, the fluid responds linearly to an applied force. The consistency, K , of the fluid is analogous to the viscosity of a Newtonian fluid and has dimension of [pressure][time]ⁿ, so when $n = 1$ and $\tau_0 = 0$, the Newtonian model is recovered.

2.3. Properties of Bubbles

2.3.1. Nucleation Criteria

The solubility of volatiles reduces as magma rises through the Earth due to reduction in pressure. Rising magma carrying dissolved volatiles will reach a particular depth at which their concentration exceeds their solubility within the magma, causing the magma to become supersaturated. At a certain level of supersaturation, it is possible for bubbles to nucleate homogeneously. Homogeneous nucleation is nucleation without the aid of any nucleation points, in contrast to heterogeneous nucleation, where preferential nucleation sites, for example crystals, aid in the nucleation of bubbles. For a stable bubble to form, the radius of the bubble nucleus must be sufficient for the change in Gibbs free energy ($\Delta G = 4\pi\sigma r^3 - (4\pi/3)\Delta g_v R^3$, where Δg_v is the energy density difference between the dissolved and gaseous states) to achieve its local maximum, ΔG^* (Taqieddin et al., 2018). ΔG^* can be expressed as a function of the surface tension of the bubble and supersaturation pressure (Equation 2.5) (Sparks, 1978).

$$\Delta G^* = \frac{16\sigma^3}{3(\Delta P)^2} \quad (2.5)$$

where σ is the bubble-melt interfacial tension (surface tension of the bubble) and ΔP is the difference in pressure between the vapour pressure of the dissolved volatile and the pressure at the wall of the bubble (supersaturation pressure). As ΔP increases, a lower free

energy is required to form stable bubbles. Similarly, the lower the surface tension, the more likely it is that a bubble will nucleate in a given region (Sparks, 1978).

The nucleation rate can be characterised by the number of nucleation events per unit volume per unit time to describe the overall amount of nucleation within a body of magma. A nucleation rate, J , of $1 \text{ cm}^{-3} \text{ s}^{-1}$ (rates below this are not easily measured experimentally) would require a critical supersaturation pressure, ΔP^* , of

$$\Delta P^* = 100 \left(\frac{\sigma^3}{1.6T} \right)^{0.5} \quad (2.6)$$

where T is absolute temperature (Swanger & Rhines, 1972). A higher surface tension requires a higher supersaturation pressure to sustain the same nucleation rate and a higher temperature requires a lower supersaturation pressure to yield the same nucleation rate. It is, however, possible to induce nucleation at lower pressures by altering the effective surface tension, σ , through the inclusion of crystals or other inhomogeneities in the magma (Hurwitz & Navon, 1994; Mangan et al., 2004).

For a typical basaltic magma, it is not trivial to determine a typical depth at which different volatile species exsolve as the formation of a stable nucleus may happen whenever a volatile is saturated due to a change in solubility arising from the decompression of magma as it rises (Figure 2.3). The nucleation rate, J , varies according to a number of factors, including the existing volatile concentration, crystal content, temperature, bubble-melt interfacial tension and diffusivity of the volatile species (Equation 2.7) (Shea, 2017).

$$J = J_0 \exp \left(- \frac{16\pi\sigma^3}{3k_B T (P_B^* - P_M)^2} \varphi \right) \quad (2.7)$$

$$J_0 = \frac{2n_0^2 D_g V_g}{a_0} \sqrt{\frac{\sigma}{k_B T}} \quad (2.8)$$

$$\varphi = \frac{(2 - \cos \theta)(1 + \cos \theta)^2}{4} \quad (2.9)$$

Here, P_B^* is the internal pressure of the bubble nucleus, P_M is the melt pressure, φ is a term that describes the type of nucleation occurring ($\varphi = 1$ for homogeneous nucleations and $0 < \varphi < 1$ for heterogeneous nucleation in the magma), n_0 is the concentration of volatile molecules per volume of melt, D_g is the diffusivity of the volatile at the bubble-melt interface, V_g is the volume of a volatile molecule in the melt, a_0 is the separation distance between volatile molecules in the melt, k_B is the Boltzmann constant

and θ is the contact angle between the bubble interface and crystal surfaces if the nucleation is heterogeneous (if the nucleation is homogeneous then $\varphi = 1$) (Shea, 2017).

2.3.2. Bubble Growth

Once bubbles nucleate, there are a number of processes through which they can grow, which include decompressive growth, diffusive growth and coalescence.

Decompressive growth is the expansion of bubbles due to changes in ambient pressure as the magma rises. Under the assumption of an ideal gas, pressure multiplied by volume is a constant, so halving the ambient pressure (for example, halving the distance to the surface, assuming that atmospheric pressure is negligible) would allow for a bubble to double in volume. For spherical bubbles, doubling the volume results in an increase of diameter by a factor of $2^{1/3}$.

Diffusive growth is bubble growth due to additional volatile molecules entering the bubble. The volatile molecules move towards the vicinity of a bubble through diffusion as the region of melt immediately adjacent to the bubble wall is depleted of volatiles and so a concentration gradient exists which allows diffusion to occur (Sparks et al., 1994). When equilibrium is achieved between the concentration of the volatile species within the bubble and the surrounding melt, diffusive growth can no longer occur as there is no concentration gradient. It is possible to model diffusive bubble growth of a bubble with radius r using a parabolic growth law as a function of time and diffusion coefficient (Equation 2.10) (Sparks, 1978; Scriven, 1959; Blower et al., 2003).

$$r = 2\beta\sqrt{(Dt)} \quad (2.10)$$

where r is the bubble radius, β is a dimensionless empirical constant, D is the diffusion coefficient and t is time; after Scriven (1959). While this method is common, it is not usable over long time scales as in the parabolic model, bubbles will grow indefinitely whereas in reality, diffusive growth ends when there is no longer a concentration gradient between the bubble and surrounding melt. In some circumstances a linear growth law is more appropriate (Blower et al., 2001b), however again, this may only apply over a limited time scale as eventually equilibrium is achieved between the bubble and the melt and the maximum volume due to diffusion is achieved. Numerical simulations of diffusive bubble growth in basaltic magmas indicate that the maximum volume is achieved in less than a few thousand seconds, but normally within tens or hundreds of seconds (Prousevitch et al., 1993). Higher volatile concentrations result in faster growth rates and larger maximum bubble sizes (up to 2 mm radius for a 5 wt. % volatile compared to 0.7 mm in approximately 100 s for 1 wt. %). In systems of equally spaced bubbles, a

greater inter-bubble spacing requires a longer time to achieve equilibrium, but the bubbles' maximum size is much greater. For example, when the bubble separation is 100 times that of the radius, an equilibrium size of 0.7 mm is achieved in 45 s whereas when the spacing is 1000 times the final bubble radius of 7 mm is achieved in 4455 s.

Coalescence occurs as the liquid film between two bubbles drains (either through gravitational or capillary forces). In magmatic systems, the timescale for film drainage is partially dependent on the radii of the bubbles, however for radii up to 1 mm, the timescale of coalescence for basaltic magma (model parameters set to a viscosity of 100 Pa s, temperature of 1150 °C and volatile content of 1 wt. % of H₂O) was calculated to be approximately 10 seconds once bubbles are touching (Nguyen et al., 2013).

2.3.3. Dimensionless Numbers

Dimensionless numbers are indicators of similarity between two systems which may have very different length scales and materials. The dimensionless numbers relevant to the systems discussed in subsequent sections are the ratios of inertial, viscous, gravitation and surface tension forces.

2.3.3.1. Reynolds Number

The Reynolds number (Re) measures the balance of inertial and viscous forces for an object moving in a liquid (or alternatively, a liquid moving around a static object) and is defined as

$$\text{Re} = \frac{\rho u L}{\eta} \quad (2.11)$$

where ρ is the density of the liquid, u is a characteristic speed of the system in question, L is a characteristic length scale of the system and η is the viscosity of the liquid. In the case of bubbles in a magmatic or analogue system, the characteristic speed and length scales would be the bubble speed and diameter respectively. The Reynolds number is one of three dimensionless numbers used to define the shape regime of a bubble or droplet (Clift et al., 1978).

2.3.3.2. Eötvös Number

The Eötvös number (Eo), also referred to as the Bond number in some literature, is the ratio between gravitational and surface tension forces (James et al., 2013) and is one of the three dimensionless numbers used to define the shape of a bubble or droplet (Section 2.3.5). It is defined as

$$Eo = \frac{\rho g D^2}{\sigma} \quad (2.12)$$

where g is acceleration due to gravity, D is bubble diameter and σ is the interfacial tension between the bubble and the liquid.

2.3.3.3. Morton Number

The Morton number (Mo) is the third dimensionless number used to define the shape regime of a bubble or droplet. It measures the ratio between viscous and surface tension forces (James et al., 2013) and is defined as

$$Mo = \frac{g\eta^4}{\rho\sigma^3} \quad (2.13)$$

Note that the Morton number is independent of bubble size or speed and so is common to all gas-liquid systems where the density, viscosity and interfacial tension are the same.

2.3.3.4. Froude Number

The Froude number (Fr) represents the ratio of inertial to gravitational forces (Pioli et al., 2017) and when examining the properties of a group of bubbles rising through a fluid, the Froude number is defined as

$$Fr = \frac{u_{sg}}{\sqrt{gD_H}} \quad (2.14)$$

where u_{sg} is the superficial gas velocity, taken as the ratio between the gas volume flow rate and the cross-sectional area of the conduit and D_H is the hydraulic diameter of the group of bubbles, which is the equivalent diameter of the group if it were completely spherical (Pioli et al., 2017).

2.3.3.5. Kapitsa Number

The Kapitsa number represents the ratio between surface tension and inertial forces and is defined as

$$Ka = \left(\frac{g\eta^4\Delta\rho}{p_l\sigma^3} \right)^{0.25} \quad (2.15)$$

where $\Delta\rho$ is the density difference between the bubble and the liquid and p_l is the density of the liquid (Pioli et al., 2017). In systems where the gas density is much lower than the liquid density, the Kapitsa number can be taken as

$$\text{Ka} = \left(\frac{g\eta^4}{\sigma^3} \right)^{0.25} \quad (2.16)$$

because $\frac{\Delta\rho}{\rho_l} \approx 1$.

2.3.4. Shape Regime

One of the requirements of the Hadamard-Rybczynski model (Section 2.5.1) is that the objects modelled using it are spherical. Bubbles not subject to external forces are spherical when the Reynolds number, Morton number and Eötvös numbers fall within particular ranges of values (Figure 2.6).

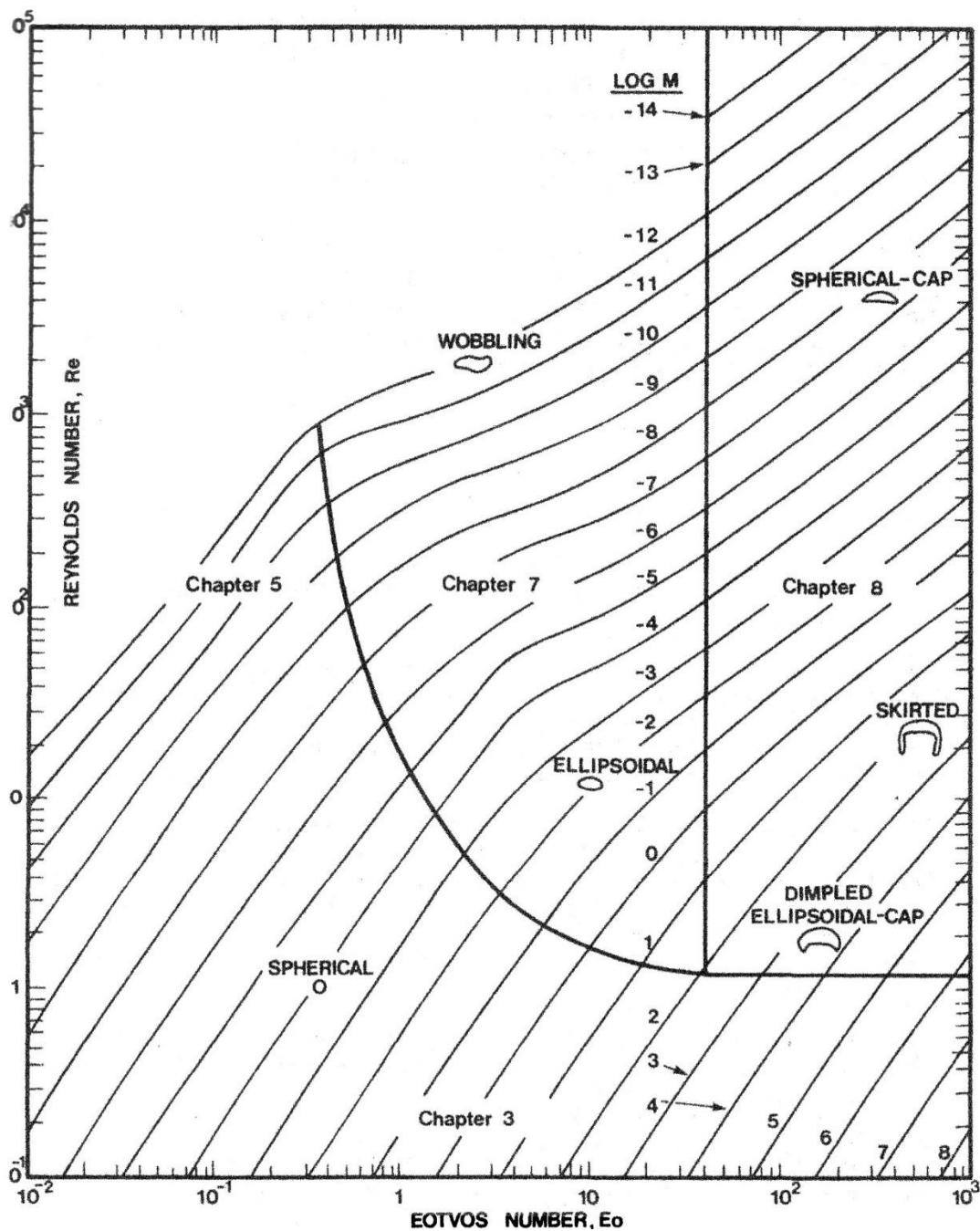


Figure 2.6: Balance of dimensionless numbers and their effects on the shape of a single bubble rising in an unimpeded gravitational motion. From Clift et al. (1978).

It is possible to determine some (upper estimate) values for these dimensionless numbers in a basaltic magmatic system using the parameters from Table 2.2.

Table 2.2: Model parameters for a general basaltic system to examine the most probable bubble shape regime.

Quantity	Value	Unit	Source
Bubble diameter	10^{-3}	m	(approximation)
Gas density	0	kg m^{-3}	(approximation)
Liquid density	2600	kg m^{-3}	Spera (2000)
Liquid viscosity	30	Pa s	Spera (2000)
Surface tension	0.05-0.3	N m^{-1}	Gonnermann and Manga (2013)
Acceleration due to gravity	10	m s^{-2}	(approximation)

Using the Hadamard-Rybczynski equation (Section 2.5.1), a theoretical rise speed of $1.4 \times 10^{-3} \text{ m s}^{-1}$ was calculated, from which a Reynolds number of 1.2×10^{-4} was obtained (using the lowest surface tension in Table 2.2 to maximise Re). Additionally, $Eo = 0.09$ to 0.5 and $\log(Mo) = 5$ to 7 depending on the surface tension value used. The region on the Re against Eo plot indicated by these calculations is off the scale of Figure 2.6, however the Eötvös and Reynolds numbers both indicate values that are well within the spherical regime. As such, it is appropriate to consider bubbles in lower viscosity magmatic systems with diameters less than 1 mm to be spherical. Bubbles with a diameter of 5 mm in otherwise identical conditions would have a Reynolds number of 1.06 and Eötvös number of 12.8, resulting in the shape of the bubble approximately straddling the spherical, ellipsoidal and dimpled-ellipsoidal cap regimes, and where deformation of the bubbles could be expected, as surface tension no longer dominates the shape of the bubble (Amaya-Bower & Lee, 2010; Manga & Stone, 1994).

2.4. Conduit Models

It has been established that degassing plays a crucial role in the style of volcanic eruptions. A number of models exist which aim to provide explanatory and predictive insights into degassing processes.

2.4.1. Rise Speed Dependent (RSD) Model

The RSD model provides an explanation for the transition from effusive to explosive regimes through the consequences of changes in magma rise speed. In the RSD model, volatiles exsolve into bubbles as the magma rises and are buoyant within the surrounding magma. The speed of the rising magma provides a time constraint on how far a bubble may travel relative to the parcel of magma within which it exsolved prior to eruption. A slowly rising ($< 1 \text{ m s}^{-1}$) magma will yield bubbles which ascend rapidly compared to the magma, whereas a faster rising ($> 1 \text{ m s}^{-1}$) magma yields bubbles which do not have great

opportunity to rise far. In a case where magma is moving quickly there is less chance for bubble coalescence or time for diffusive growth of bubbles than when the magma ascent is slow. As the magma rises, diffusion and decompressive growth of bubbles cause the gas volume fraction to become sufficiently large for fragmentation to take place. Fragmentation of the magma allows for faster rise speeds and this can lead to relatively fast ($\sim 100 \text{ m s}^{-1}$) ejection speeds at the vent (Wilson & Head, 1981). The RSD model does not account for very highly explosive behaviour (i.e. Plinian style eruptions).

Strombolian style eruptions can be accounted for by slowly rising magma as it becomes possible for large bubbles to form, then rise quickly and coalesce with smaller bubbles above them. Additionally, the cyclic behaviour of Strombolian eruptions, may be controlled by repeated cooling and rupturing of a high viscosity layer at the top of a conduit (Wilson, 1980; Gaudin et al., 2017). If large gas bubbles, formed due to slowly rising magma, arrive at the top of the conduit frequently enough, the high viscosity layer is not able to cool completely, and the gas bubbles continue to travel upwards. On the other hand, if the gas bubbles are arriving infrequently, then the skin may cool and become rheologically stiffened. In this instance it may take more than one bubble in order to produce the required force to break through the high viscosity layer and erupt. In this instance, the resulting eruption would be more violent (Parfitt, 2004).

2.4.2. Collapsing Foam Model

The collapsing foam posits that the formation of very large gas slugs occurs at depth when a trapped collection of many bubbles form into a foam, which eventually collapses into a single, much larger, bubble and ascends through the conduit (Parfitt, 2004). Vergnolle & Jaupart (1986) note that the gas volume to erupted melt volume ratio at Stromboli was found to be 1.8×10^4 and 1.2×10^5 for two explosions (Chouet et al., 1974) and the gas:particle mass ratio varied between 2.5 and 16. Chouet et al. (1974) concluded that either additional volatile content is contaminating the eruptions at Stromboli or that some mechanism is concentrating the volatiles. Vergnolle & Jaupart (1986) reasoned that the latter explanation was correct and that the gas must be separated from the melt.

Vergnolle & Jaupart (1986) also noted that coalescence in a conduit alone is insufficient to produce sufficiently large bubbles (of the order of 10 cm to 1 m) to produce Strombolian explosions. It was also suggested that coalescence may only occur between bubbles of different sizes, as bubbles of the same size would rise at the same speed and so never come into contact with each other. Additionally, turbulent effects and bubble deformation would mean that bubbles of different sizes approaching each other may not necessarily coalesce. Therefore, close bubble packing (a gas volume fraction exceeding

0.7) would be required, and the relative motion of the bubbles must be slow to avoid turbulent effects and excessive deformation. It was suggested that if these conditions were met in a magma chamber, then large bubbles (> 10 cm diameter) could be formed in order to produce Strombolian style explosions. Analogue experiments demonstrated that the mechanism proposed is plausible (Jaupart & Vergnolle, 1988). These experiments also showed that viscosity of the liquid phase controlled the style of the eruption. At low viscosities, a single large gas bubble formed from the collapse of the foam, which ascended through the conduit in an annular flow (a jet of gas surrounded on all sides by a thin layer of liquid coating the walls of the conduit) which resulted in a sustained fountain-like eruption. At higher viscosities, several bubbles were formed from the foam collapse, which were smaller than the bubbles in the lower viscosity experiments. These bubbles rose discretely and produced minor explosive activity upon eruption. These two modes of eruption were interpreted as explanatory mechanisms for both Hawaiian and Strombolian styles of eruption in the collapsing foam model where viscosity, rather than the magma rise speed, was the principal control on the eruption style.

2.4.3. Model Limitations

The collapsing foam model is unable to provide an explanation for Strombolian activity in conduits where there is not a suitable discontinuity in order to produce foams, whereas the RSD model does not account for these types of discontinuities existing at all. Additionally, the collapsing foam model is unable to account for the coalescence of bubbles in slowly rising magmas.

The RSD model does not appear to be able to account for heightened concentrations of CO₂ in explosions at Etna (up to 60 % of the erupted gases) (Tazieff, 1970), which implies that an undescribed mechanism is capable of concentrating CO₂ such that it forms the majority of the gas within the erupted bubble, but this mechanism does not also apply to other volatile species, such as H₂O which would typically account for a greater proportion of the total volatile content at depth due to its much higher solubility at comparable pressures (Figure 2.3).

Neither model is able to account for all possible conduit geometries, so there remains a need for a more generalised understanding of how bubbles move and interact within magma conduits.

2.5. Models of Bubble Motion

Bubble rise speed has been observed experimentally to vary depending on whether the bubble is rising in isolation, near to another bubble, or as part of a large network of bubbles.

2.5.1. Single Bubbles

While the speed of a solid sphere in a stagnant fluid is well described by Stokes' Law at low (<1) Reynolds numbers, a bubble rising through fluid is not well described because the assumption of a no-slip boundary condition does not apply between two fluids (Clift et al., 1978). The lack of a no-slip boundary causes rotation of gas within the bubble, affecting the rise speed of that bubble. To accommodate this, the boundary conditions are modified to account for the balance of normal and shear stresses at the interface. However, small bubbles are an exception as surface contaminations alter the role of surface tension on the internal motion of gas in a bubble such that Stokes' law describes the observed motion (Bond & Newton, 1928; Ervik & Bjørklund, 2018). For larger, spherical, bubbles without surface contaminants, the Hadamard-Rybczynski equation provides an accurate description of the rise speed of bubbles as a function of their size, and has been shown to be effective in previous experiments (Ervik & Bjørklund, 2018; Hornyak & Weinberg, 1984). The Hadamard-Rybczynski model is based on a spherical bubble with no contaminants and where the Reynolds number of the system is low, the creeping flow assumption can be made such that

$$E^4\psi = E^4\psi_p = 0 \quad (2.17)$$

where ψ is the Stokes stream function of the liquid phase, ψ_p is the Stokes stream function of the bubble's internal rotation and E^4 is the E^2 operator applied twice where

$$E^2 = \frac{\partial^2}{\partial r^2} + \frac{1}{r^2} \frac{\partial^2}{\partial \theta^2} - \frac{\cot \theta}{r^2} \frac{\partial}{\partial \theta} \quad (2.18)$$

where r and θ refer to positions in spherical polar coordinates (Clift et al, 1978). The flow within the bubble, ψ_p , is computed to be non-zero and results in a terminal velocity U_T according to the Hadamard-Rybczynski equation, given as a function of the bubble radius, a , gas-liquid density difference, $\Delta\rho$, acceleration due to gravity, g , liquid viscosity, η , and bubble (gas) viscosity, κ (Equation 2.19).

$$U_T = \frac{2}{3} \frac{g a^2 \Delta\rho}{\eta} \left(\frac{1 + \kappa}{2 + 3\kappa} \right) \quad (2.19)$$

When gas viscosity is very low, and bubble diameter, d , used instead of radius, the equation simplifies to the form of Stokes' Law, but with calculated velocities 1.5 times larger (Equation 2.20).

$$U_T = \frac{1}{12} \frac{gd^2\Delta\rho}{\eta} \quad (2.20)$$

The Hadamard-Rybczynski equation provides the theoretical description of the expected rise speed of spherical bubbles in the experiments presented in the following chapters. It is, however, only valid for spherical bubbles. As bubbles increase in size, the balance of inertial, viscous and tension forces changes, which facilitates a change in the shape of bubbles (Figure 2.6). An equation which allows for the description of bubbles across different shape regimes has been proposed by Park et al. (2017) (Equation 2.21).

$$U_T = \frac{1}{\sqrt{\frac{144\mu_L^2}{g^2\rho_L^2d_e^4} + \frac{\mu_L^{4/3}}{0.14425^2g^{5/3}\rho_L^{4/3}d_e^3} + \frac{1}{\frac{2.14\sigma_L}{\rho_L d_e} + 0.505gd_e}}} \quad (2.21)$$

where U_T is the rise speed of the bubble (spherical or non-spherical), μ_L is the viscosity of the liquid, g is acceleration due to gravity, ρ_L is the liquid density, d_e is the volume equivalent diameter of the bubble and σ_L is the surface tension between the gas and bubble. The Park et al. (2017) model may be used for bubbles which are not spherical, but are of interest experimentally.

2.5.2. Pairs of Bubbles

The simplest example of bubble-bubble interactions is the two-bubble system. A model describing the interactions may include a number of parameters, such as the relative size and position of the two bubbles in a given fluid. When bubbles of the same size rise at the same height as each other (i.e. they only have lateral separation), the interaction between them varies depending on the size and separation of those bubbles. In experiments on bubbles which were sufficiently large to be deformed by the flow field of the other bubble, bubble separation has been observed to vary in the manner of a simple harmonic oscillator (Huang et al., 2019). The oscillatory behaviour has been interpreted to be caused by vortex counteraction and wake merging effects (Huang et al., 2019). The phenomena of bubble attraction and repulsion has been described as a function of the bubbles' Reynolds number and dimensionless separation distance, S (the ratio between the bubbles' diameter and separation distance), such that below a critical value of $S(\text{Re})$, the bubble interaction is repulsive, whereas above that value, the interaction is attractive (Legendre et al., 2003). The change from a repulsive regime to an attractive regime has been described to occur at approximately $30 < \text{Re} < 100$ for $2.25 < S < 10$ (Legendre et al., 2003), as well as $\text{Re} < 17$ for $S \approx 3.5$ (Yu et al., 2011). These results are inconsistent with each other, but both suggest that for when S is of the order of magnitude

10^0 , then the transition between repulsive and attractive regimes occurs when Re has an order of magnitude less than 10^2 . In some experiments, bubbles in pairs were observed to bounce off each other without coalescing (van Wijngaarden, 1993; van Wijngaarden, 1998), such that in pure H_2O , coalescence was rarely observed. The oscillatory behaviour is caused by attractive and repulsive forces varying with lateral separation. When the bubbles exceed a critical separation distance, bubbles are attracted through the Venturi effect, however when the bubble separation reduces, the vorticity of each bubble increases the pressure between the bubbles, repelling them (Hallez & Legendre, 2011; Legendre et al., 2003). As bubbles ascend near each other, the non-uniform pressure field experienced by each bubble in a pair, the bubbles deform asymmetrically to the vertical direction, generating a lateral lift force (van Wijngaarden, 1998). The attraction-repulsion cycles have been experimentally observed to occur at least five times between a given pair of bubbles; however, viscous effects prevent further lateral motion significant beyond approximately five or six oscillations in air- H_2O systems, although this is a function of the fluid viscosity (van Wijngaarden, 1993).

The relative horizontal velocity of two bubbles, during attraction, can be described as a function of their relative separation distance (their actual distance divided by the bubble diameter) and as their separation decreases, the relative speed between them increases (Figure 2.7). The maximum relative speed between bubbles has been calculated to be 0.43 times their buoyant rise speed if they were rising separately (van Wijngaarden, 1993) (Figure 2.7).

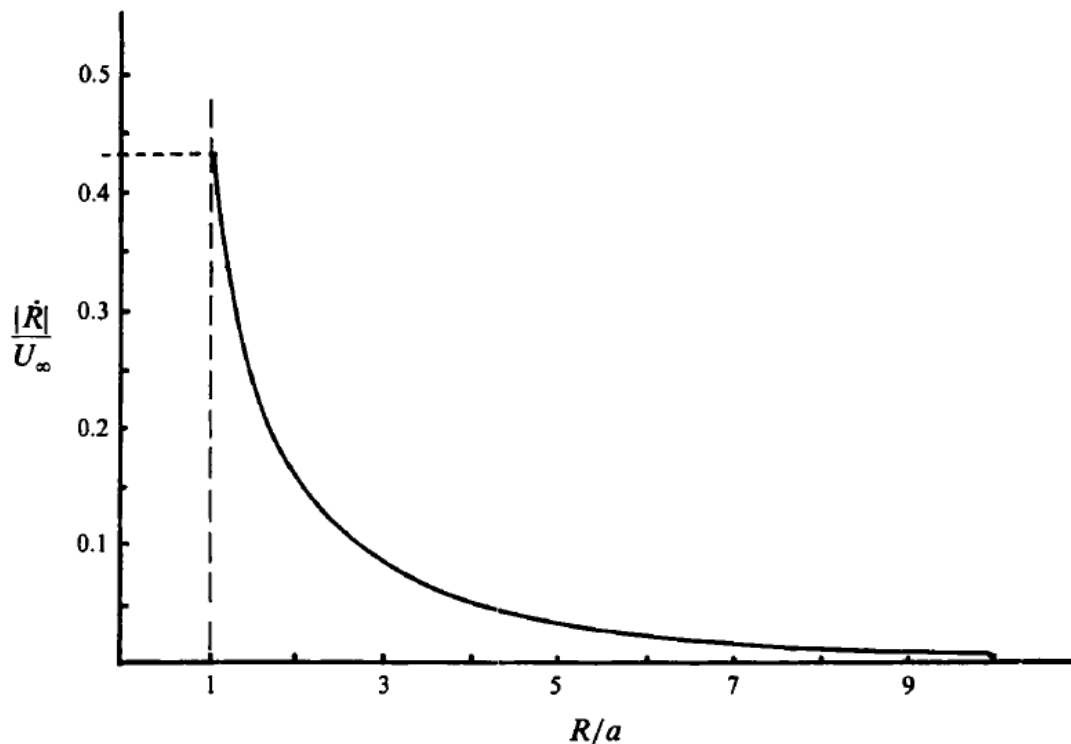


Figure 2.7: The relative speed in a bubble pair as a function of their relative separation in an air-H₂O system, where R is the actual separation and a is the bubble diameter. $|\dot{R}|$ is the magnitude of the rate of change of bubble separation. U_∞ is the buoyant rise speed of the bubbles, which is not the same as the nomenclature used elsewhere in this thesis. Adapted from Figure 5 in van Wijngaarden (1993).

The relative direction of the bubbles may be described by the angle, θ , between the vertical (or horizontal) direction and the line between the centre of the two bubbles. In some literature, when $\theta = 0^\circ$, the bubbles have only vertical separation and no lateral separation, and when $\theta = 90^\circ$, the bubbles have the same height, but are only separated laterally (for example, van Wijngaarden, 1993), whereas other literature uses the opposite convention (for example, Hallez & Legendre, 2011) such that side-by-side bubbles have $\theta = 0^\circ$ and $\theta = 90^\circ$ for vertically aligned bubbles. In a low Reynolds number experiment ($Re < 20$) for bubbles that were only vertically separated, the trailing bubble accelerated towards the leading bubble (Kusuno et al., 2019), despite the bubbles having similar sizes (the ratio of their diameters was greater than 0.95).

The variation of θ between 0° and 90° and for a given separation distance causes the interaction behaviours to vary considerably. For example, for a given bubble separation distance, there is a non-zero lift interaction force acting on the lower of the two bubbles, which varies with θ and Reynolds number (Figure 2.8).

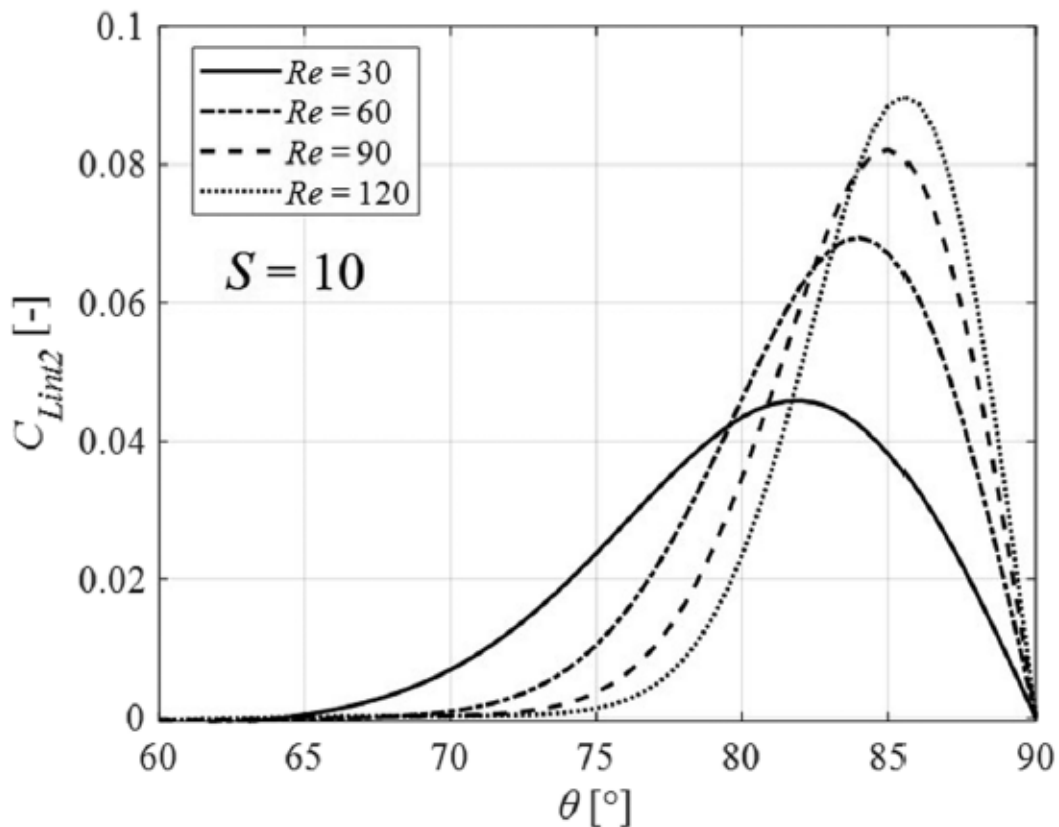


Figure 2.8: Variation of lift coefficient on the lower of two bubbles in a bubble pair as a function of their separation angle. Figure 17 from Kusuno et al. (2019), where θ is defined as the angle between the horizontal direction and the centreline of the two bubbles.

As Reynolds number decreases, the magnitude of the lift coefficient decreases, and its maximum occurs at angles further from vertical bubble alignment. The Reynolds numbers of bubbles in Chapters 5, 6 and 7 are lower than those of many previous studies, so the magnitude of the lift effect may be much lower, but not necessarily zero. When bubble separation decreases, the value of θ may vary and the rate of change of θ may increase. Thus, the effect of horizontal lift on a pair of bubbles is not necessarily constant, specifically such that at large separations, the time taken for the trailing bubble to appreciably move laterally is greater than at smaller separations (Kusuno et al., 2019).

2.5.3. Bubble Groups

A description of the effect on bubble rise of many bubbles travelling in close proximity is non-trivial due to the lack of general analytic solutions to the Navier-Stokes equation and the difficulty of solving generic n-body problems. Attempts have been made to characterise the group effect as a function of the gas volume fraction, Reynolds number and Weber number. The Weber number, We , is a measure of the relative strength of the

inertial and surface tension forces acting on a bubble defined as $We = \rho u^2 D / \sigma$ where ρ is the liquid density, u is the speed of the bubble, D is the diameter of the bubble, and σ is the surface tension of the bubble (Day et al., 2012). Within a group of monodisperse bubbles in a finite cuboid container for low Weber number ($O(10^0)$) and high Reynolds number ($O(10^2)$) with gas volume fraction α , and a buoyant rise speed (for a single bubble in isolation) of U_∞ , an expression for the bubble rise speed, based on the equivalent problem for solid particles is

$$u_b = U_\infty (1 - \alpha)^n \quad (2.22)$$

where n is an experimentally determined constant (Zenit et al., 2001; Richardson & Zaki, 1954; Manga, 1996). The experiments conducted by Zenit et al. (2001) used nitrogen bubbles of approximately 1 mm diameter in H_2O , giving a Reynolds number of approximately 500 for each bubble in isolation. Group behaviour decreased bubble velocities relative to U_∞ as α increased. However, the reduction in speed was not consistent among all bubbles studied (Figure 2.9). With increasing gas volume fraction, the modal value decreased while the width of the distribution increased, indicating that the bubbles generally travelled at lower speeds, but the variance in the speed increased with gas volume fraction.

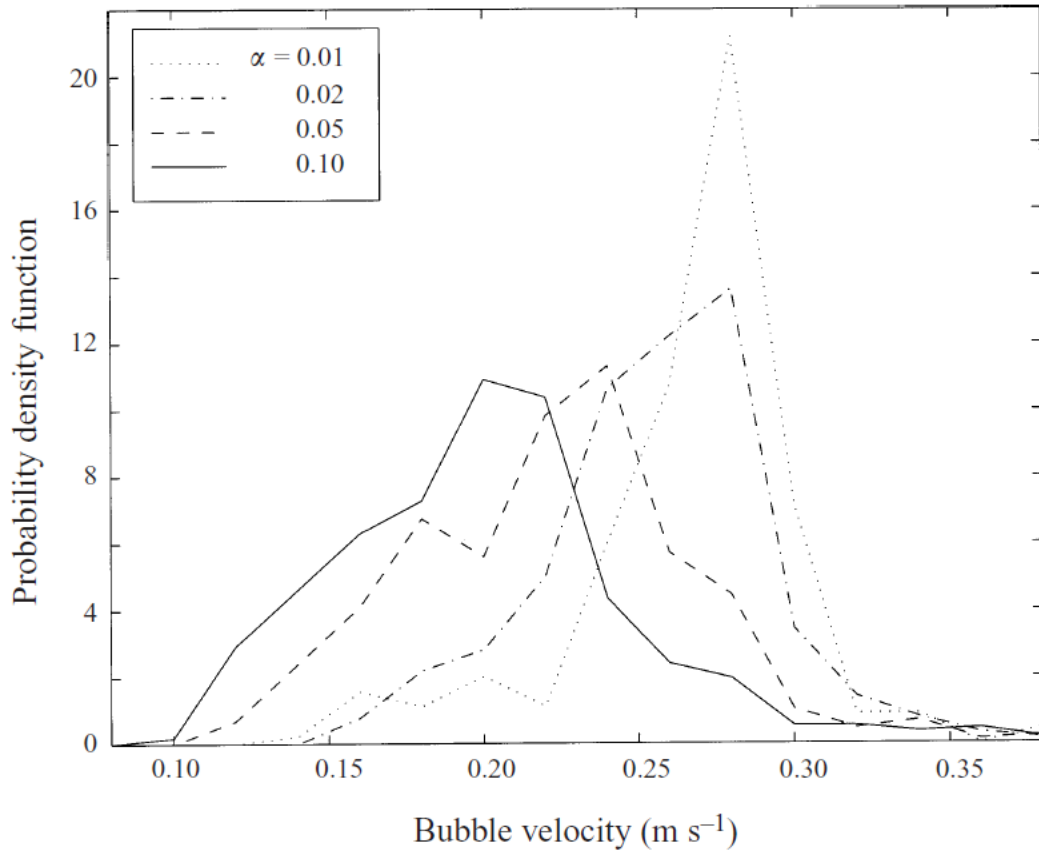


Figure 2.9: Probability density function of bubbles travelling at different speeds for a variety of gas volume fractions. For higher gas volume fractions, the modal value decreases and the width of the distribution increases. From Zenit et al. (2001).

The coefficient of drag, C_d , on a bubble in a homogeneous suspension of spherical bubbles can be characterised in terms of the gas volume fraction (α) and a parameter $A = \frac{u_b^2}{T_b}$ (where u_b is bubble speed and T_b is variance in bubble speed; Spelt & Sangani, 1998).

$$C_d = \frac{1 + \frac{3}{20} \alpha A}{(1 - \alpha)^2} \quad (2.23)$$

Equation 2.23 indicates that as gas volume fraction increases, the drag experienced by each bubble increases, leading to a reduction in speed as observed in experiments (Figure 2.10).

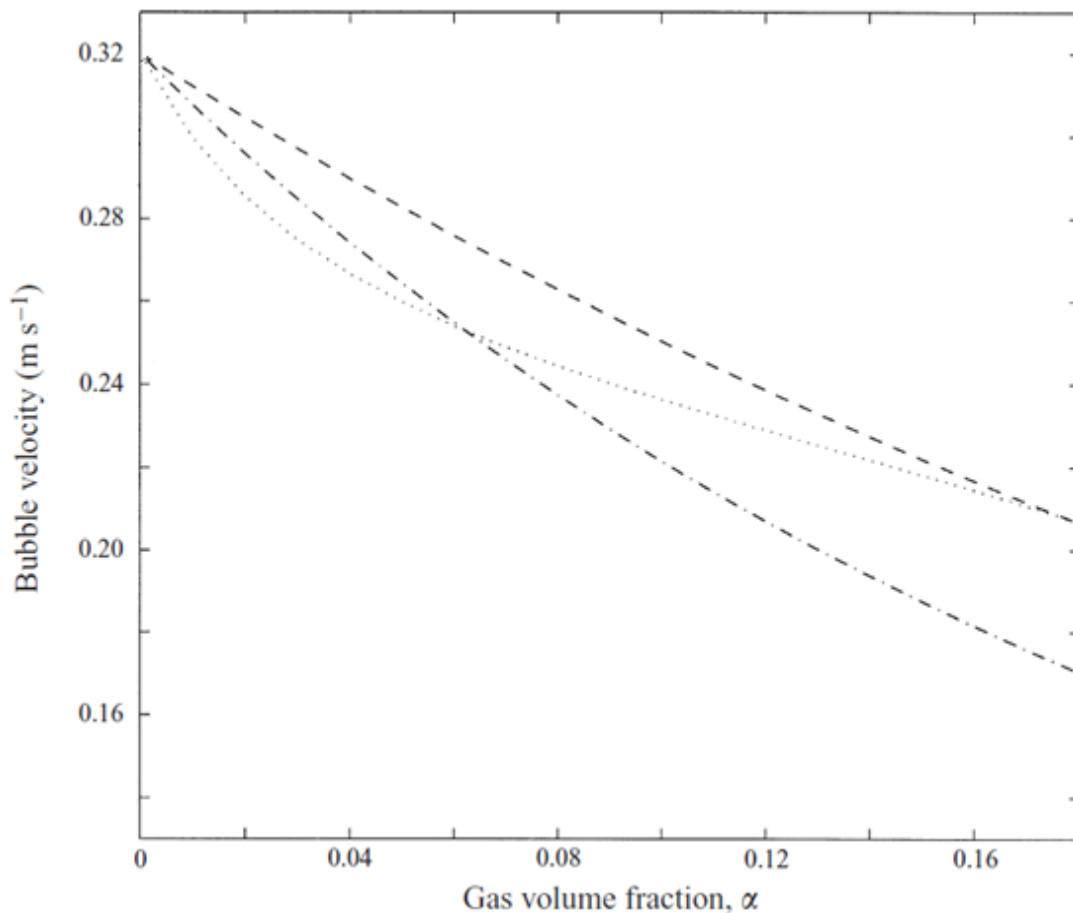


Figure 2.10: Measured bubble velocity of homogeneous (~ 1 mm) nitrogen bubbles in H_2O as a function of gas volume fraction. The open circle is for a single bubble in isolation, while the open diamond is for bubbles in highly dilute suspensions (both indicating an increase in $du_b/d\alpha$ between $\alpha = 0$ and $\alpha \approx 0.005$ compared to all other values of α shown). The dashed, dash-dotted and dotted lines represent model estimates using Equation 2.23 for $A = 20$, $A = 10$ and $A = A(\alpha)$ respectively. $A(\alpha)$ is obtained from a fit of velocity variance measurements. Adapted from Zenit et al. (2001).

In dilute bubbly flows ($\alpha < 0.01$), pairs of bubbles have a tendency to cluster when within a few (2.5-4) bubble radii and the overall bubble concentration does not affect the clustering distances (Martinez et al., 2010). The mechanisms controlling the clustering is unclear, particularly as pairs of bubbles may be expected to repel each other in certain dimensionless regimes (Section 2.5.2). However, a possible explanation is that smaller bubbles have a small wake, causing mutual attraction in the horizontal plane (Batchelor, 1967), while larger bubbles entrain nearby bubbles into the wake due to the reduced pressure behind the bubble (Martinez et al., 2010). It has also been proposed that for larger bubbles, the shear flow induced by the wake causes bubble deformation, generating a lift force towards the larger bubble rather than away from it (Martinez et al., 2010).

The impact of groups of bubbles at a variety of gas volume fractions in the high Reynolds number and low Weber number scenario was such that the velocity of bubbles is reduced from their value for single bubbles in isolation, and the magnitude of $du_b/d\alpha$ was greatest for very low (less than $\alpha \approx 0.005$) gas volume fractions. The reduction in speed was interpreted to be caused by a hindering effect (resulting in an increase in drag) from the volume displacement of fluid as bubbles moved, and the impact of bubble deformation (Zenit et al., 2001; van Wijngaarden, 1993).

2.6. Analogues with Sedimentation

A system of solid spheres falling through a viscous liquid is a similar problem to that of bubbles rising through a liquid. However, there are a number of key differences, firstly the relative density is usually such that the solid spheres are denser than the liquid, causing the solid spheres to move in the opposite direction to bubbles. Secondly, solid spheres do not exhibit the internal fluid flow of gas bubbles, and so their fall speeds in viscous liquid is described better by Stokes' Law than by the Hadamard-Rybczynski model, unless the bubbles are very small (Bond & Newton, 1928). Thirdly, except for very small bubbles, bubbles are deformable under an external non-uniform force (and return to their original shape once the external force is no longer applied), whereas solids are not typically deformable. Deformation of spherical particles would not be expected, although deformation of flocculated particles is possible (Spearman & Manning, 2017).

2.6.1. Hindered Settling

As a solid sphere falls through a static incompressible fluid, conservation of volume and momentum requires that a flow of liquid occurs in the opposite direction. A mathematically equivalent scenario is a sphere of radius a surrounded by a cylinder (radius R) of fluid with terminal fall speed of the sphere (V_0). In this scenario, the frame of reference is that of the sphere, so the sphere is modelled as being stationary with the fluid moving around it. Without the sphere present, the streamlines of the fluid are straight and oriented vertically upwards with an axial flowrate $Q = \pi R^2 V_0$; however, with the presence of the sphere, the streamlines at a distance r and angle θ from the vertical central axis of the cylinder, are curved outward according to the stream function, ψ , for Stokes flow past a sphere (Equations 2.24 & 2.25) (Figure 2.11).

$$\psi(r, \theta) = \frac{1}{2} V_0 r^2 \left(1 - \frac{3a}{2r} + \frac{1}{1} \frac{a^3}{r^3} \right) \sin^2(\theta) \quad (2.24)$$

and

$$\psi(r, 90^\circ) = \frac{1}{2} V_0 r^2 \left(1 - \frac{3a}{2r} + \frac{1}{1} \frac{a^3}{r^3} \right) \quad (2.25)$$

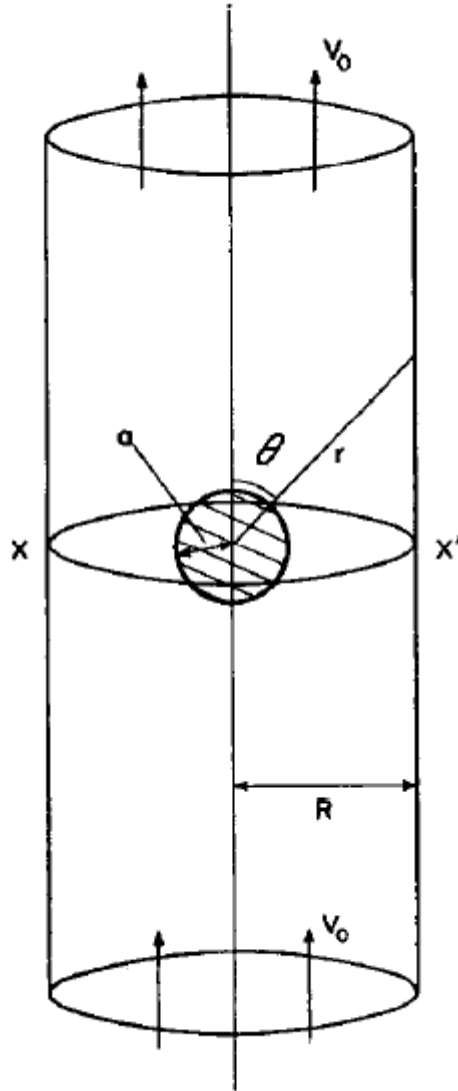


Figure 2.11: Diagram showing a cylindrical column of fluid with radius R flowing past a stationary sphere with radius a at a flow rate of V_0 . The plane XX' is the horizontal plane going through the centre of the sphere. From Oliver (1960).

In the plane XX' (Figure 2.13), the axial volumetric flow rate, Q' is

$$Q' = 2\pi\psi(R, 90^\circ) \quad (2.26)$$

$$Q' = \pi V_0 R^2 \left(1 - \frac{3a}{2R} + \frac{1}{1} \frac{a^3}{R^3} \right) \quad (2.27)$$

$Q - Q'$ is the flow rate of liquid which extends outside of the cylinder of radius R . In the condition that the streamlines around the sphere cannot be bent outside of a given distance from the sphere (for example, due to a constraining wall or another sphere) then the liquid in the horizontal plane of the fluid flow rate around the sphere ($Q - Q'$) must be distributed in the plane XX' , causing an increase in speed of the liquid and sphere

(Oliver, 1960) which has the effect of impeding the speed of the sphere as it falls (when considering the frame of reference of a static observer rather than the sphere). The magnitude of the upward speed, V_A , is given by Equation 2.28 and can be approximated by Equation 2.29 for when $a^3/R^3 \ll a/R$.

$$V_A = \frac{Q - Q'}{\pi R^2} = V_0 \left(\frac{3a}{2R} - \frac{1a^3}{1R^3} \right) \quad (2.28)$$

$$V_A = V_0 \frac{3a}{2R} \quad (2.29)$$

The settling velocity, V_S , of a collection of spherical particles impeded by this process is given as the difference between the terminal velocity given by Stokes' Law, V_0 and the upward flow speed V_A , which is also related to the cube root of the solids concentration, c , and a constant, K_1 , for a uniform particle distribution (Equation 2.30) (Oliver, 1960).

$$V_S = V_0 - V_A = V_0(1 - K_1 \sqrt[3]{c}) \quad (2.30)$$

The impact of other spheres is considered as an effective increase in liquid viscosity giving an effective relative viscosity $\mu_r = (1 - K_2 c)^{-1}$ where K_2 is a constant. This increase results in a relative settling velocity $V_r = V_S/V_0 = (1 - K_1 \sqrt[3]{c})(1 - K_2 c)$ which accurately describes the reduction in speed due to hindered settling of solid particles across a range of volume concentration (Figure 2.12) (Oliver, 1960).

A simpler formulation, applicable for concentrations greater than 0.05, is given as

$$V_S/V_0 = (1 - c)^a \quad (2.31)$$

where the value of a is dependent on the Reynolds number, and whether the particles are solids, droplets, or gas bubbles (Zenit et al., 2001; Richardson & Zaki, 1954).

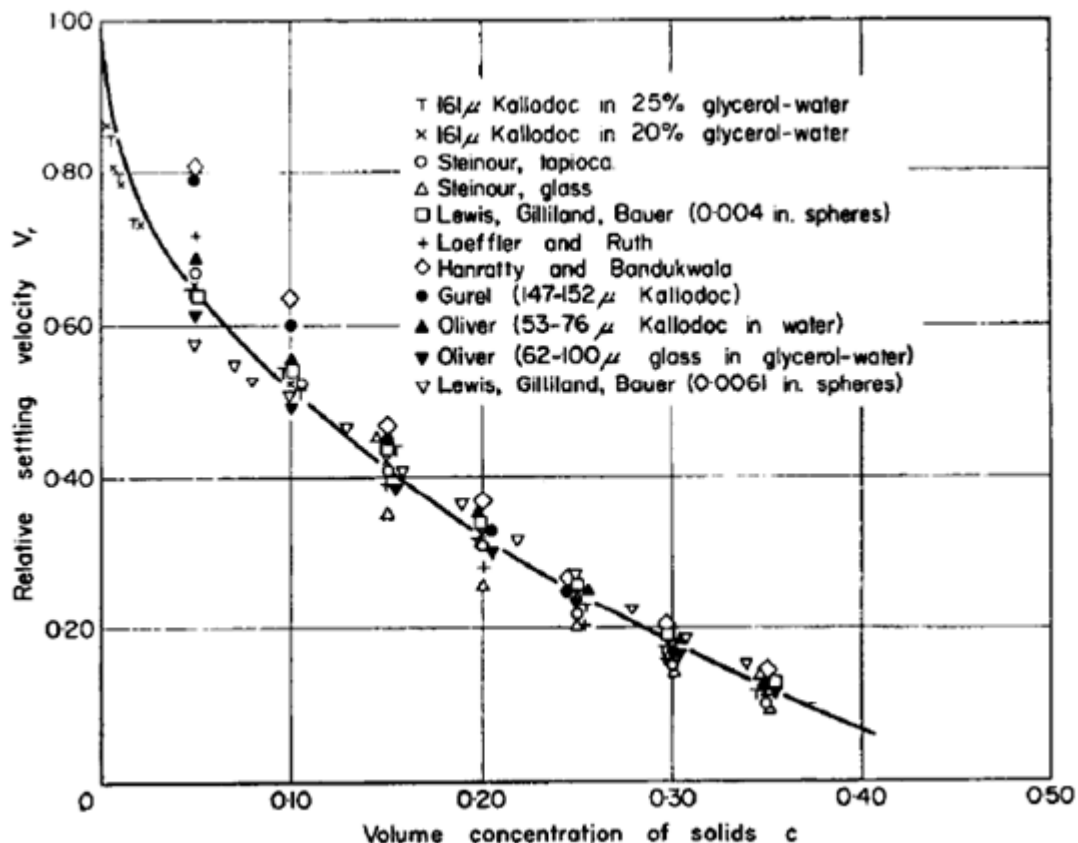


Figure 2.12: Relative settling velocity against the solid volume fraction. Data from multiple experiments are shown and demonstrate that the equation for relative settling velocity describes the experimental results well. Adapted from Oliver (1960).

The data indicate that the settling velocity of solid particles is greatly reduced as the solid volume fraction increases, with a 60 % reduction in settling velocity at just 15 % solid volume fraction (Baldock et al., 2003). However, on local scales, the solid volume fraction is not constant, and the local conditions that each individual sphere experiences is not uniform, leading to spatial and temporal variations in particle velocities distributed around the mean sedimentation velocity (Ladd, 1992).

A consequence of hindered settling is that, because all particles in the distribution, are subjected to an upward fluid flow, particles with a small size or low density may have a sinking velocity (in the absence of other particles) smaller than that of the upward flow, causing a separation of large, or high density, particles from small, or low density, particles (Young & Klima, 2000).

Hindered movement has also observed in bubbles moving upwards (Section 2.5.3), and the physics governing the effect on bubbles is similar to that on

particles. However, the internal gas flow within the bubbles, may act against the hindering effect.

2.6.2. Particle Clustering

Pairs of particles in near-contact with each other have been inferred to induce a local increase of 5-10 % in the average sedimentation velocity from numerical modelling of a monodisperse suspension of rigid spheres (Ladd, 1992). Furthermore, in numerical simulations of dense particles, the preferential particle concentrations could be induced locally from isotropic turbulence of dense particles (Squires & Eaton, 1991). In turbulent conditions, the settling velocity of clusters of droplets has been observed experimentally to increase with concentration (Aliseda et al., 2002). Aliseda et al. (2002) also found that the increase in settling velocity was a function of the Stokes number $Stk = t_0 u_0 / l_0$, where t_0 is the relaxation time of the particle, u_0 , a characteristic speed of the system and l_0 , a characteristic length of the system. The increase in settling velocity due to the clustering had a maximum at a Stokes number of approximately 1.

3. Methods

An analogue experimentation approach was taken in order to gain the greatest understanding of the physics of the system while being able to control many of the parameters. Analogue experiments are also more suitable on a laboratory length scale than using natural volcanic materials, and mitigate the hazards associated with using high temperature samples.

3.1. Requirements

The basis of the experiments involved observing the rise of small (of the order 1 mm) bubbles in a column of viscous liquid. In order to study the effects of bubble interactions in this system, there were several requirements:

- 1) The bubbles produced should match the dimensionless numbers (Re , Mo , Eo) of small bubbles in natural volcanic systems. Specifically, bubbles should have a Reynolds number much less than 1 and be spherical (Section 2.3.5).
- 2) The whole system should be optically transparent so that visual observations can be made by using consumer grade camera equipment.
- 3) Groups of bubbles produced should be observable for a sufficiently long time in order to study their behaviour. If the apparatus was too small, then it would not be possible to make observations over a sufficiently long time to make measurements.
- 4) Control over bubble production. It was not necessary to control precisely the number of bubbles produced within a given time frame because variations were not only acceptable, but beneficial to the experiment as variations allowed for a wider range of bubble number densities.
- 5) The size of bubbles should be effectively a constant over the time and length scale of observations.
- 6) The impact of edge effects must be controllable. This could range from zero edge effects (an infinite, or pseudo-infinite fluid) to strong edge effects (where the size of a bubble or bubble group and the constraining walls are of comparable sizes).
- 7) To investigate the role of non-vertical tubes on bubble behaviour, the experiment needed to have the facility to be inclined in order to restrict the bubbles to a non-vertical path constrained by the surrounding walls.
- 8) Chemical equilibrium. Studying chemical processes was beyond the scope of this work; only physical processes were to be considered.

Additionally, the effects of crystals suspended within magma were neglected and the magma was assumed to have a Newtonian rheology. The assumption of Newtonian

rheology ensured that any effects observed are bubble-driven effects and wall effects rather than non-Newtonian effects. Consequently, the role of crystals was not considered in this work, and a Newtonian fluid was selected as a useful analogue for isolating bubble-driven behaviour.

3.2. Methods Development

A series of preliminary experiments were conducted in order to determine the most effective configuration of equipment and observation practices which would facilitate a wide range of behaviours and allow for accurate measurements of those behaviours.

3.2.1. Equipment Characteristics

A number of unsuccessful prototypes were explored before the final apparatus design was realised; this section identifies key aspects of the final design and discusses some of the unsuccessful attempts. A glass tube filled with silicone oil provides a viscous liquid which is optically transparent and into which bubbles can be produced and observed. This type of approach has been adopted before as an analogue of basaltic magma systems and has demonstrated useful results (James et al., 2004; Lane et al., 2013; Capponi et al., 2016). By attaching this tube to a vacuum pump with an appropriate measurement of pressure, it was possible to control the pressure at the surface of the fluid (Figure 3.1). A baseplate at the bottom of the tube provided an opportunity to introduce bubbles into the system. Injecting gas (or liquid containing at least one dissolved volatile, hereafter referred to as volatile-rich liquid) through the baseplate to produce bubbles and observing those bubbles rise formed the basis of the main experiments. The interior of the tube could be brought to a low pressure using a vacuum pump, and so an injection into the bottom of the tube was done using the force provided by the atmosphere, which was at a greater pressure than inside the tube.

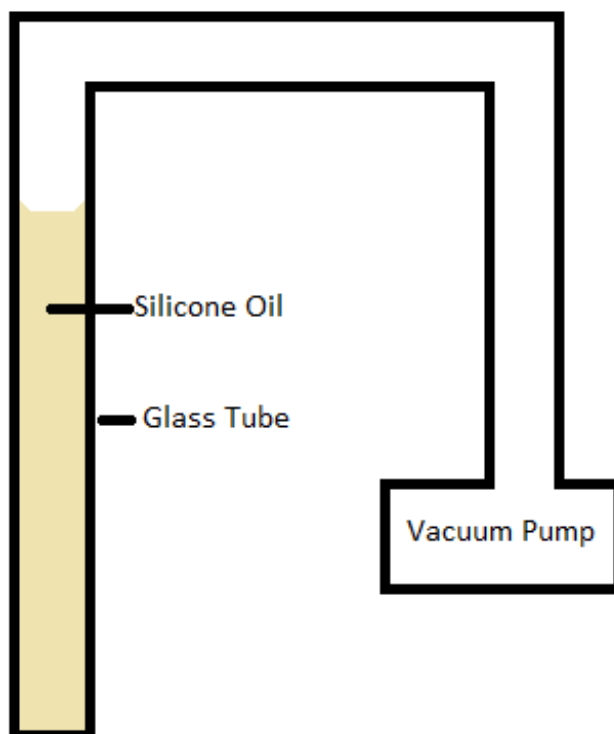


Figure 3.1: A cross section diagram of simplest form of the experimental apparatus, excluding the modifications to introduce bubbles into the base of the tube. A column of silicone oil within a glass tube can be subjected to partial vacuum conditions using the vacuum pump.

Glass tubes with inner diameters of 25 mm and 50 mm were tested, however in order to provide a pseudo-infinite environment for bubbles, the ratio between bubble diameter and wall diameter must be no larger than 0.1 (Brizard et al., 2005). For 25 mm tubing, bubbles or groups of bubbles greater than 2.5 mm across experienced edge effects from the constraining walls. For 50 mm tubing the limit was 5 mm diameter for individual bubbles or collections of bubbles before the onset of edge effects. The largest tubing available had an inner diameter of 80 mm and this provided a pseudo-infinite environment for bubbles or collections of bubbles up to 8 mm across.

3.2.2. Bubble Characteristics

The shape regimes of the bubbles as outlined in Section 2.3.5 indicate that bubbles rising buoyantly in a magma conduit may be taken as spherical based on the Morton, Reynolds and Eötvös numbers in the absence of significant deviations from Newtonian rheology (such as in a viscous cap) or external shear forces.

Morton number is independent of the bubble size and so can be calculated for the bubble-silicone oil system. The kinematic viscosity of the silicone oil was listed in the technical data sheet as $100 \text{ mm}^2 \text{ s}^{-1}$, yielding a dynamic viscosity of 0.1 Pa s

(Wacker, 2020). The technical data sheet for Wacker AS 100 silicone oil did not specify the surface tension of the oil, however, the chemically similar AK 100 silicone oil had a listed surface tension of 0.021 N m^{-1} (Wacker, 2002). It was assumed that AS 100 has a similar surface tension to AK 100, which was a reasonable assumption as other properties (density, viscosity, flash point) were almost identical (Wacker, 2002; Wacker, 2020). The density of AS 100 was measured to be $0.9876 \pm 0.0051 \text{ g cm}^{-3}$ (Section 4.1). The difference in density between the bubble and the oil was taken as the density of the oil, as the bubbles have negligible density relative to the oil. At standard temperature and pressure, the density of air is approximately 1 kg m^{-3} , which could be considered negligible in this system; however, the bubbles in the experiments experienced a pressure of approximately 10 % that of atmospheric pressure, so their expected density was 0.1 kg m^{-3} (approximately 0.1 % of the oil's density). Acceleration due to gravity was taken as 10 m s^{-2} . These values indicated a Morton number of 0.1 and so, $\log(\text{Mo}) = -1$.

For, $\log(\text{Mo}) = -1$, spherical bubbles were expected under conditions of $\text{Re} < 2$ and $\text{Eo} < 5$ (Figure 2.7). An Eötvös number of less than 5 for the experiments indicated that spherical bubbles must have a maximum diameter of 3.3 mm. The transition between a spherical regime and an ellipsoidal regime occurs at approximately these values of Re , Eo . The transition was anticipated to be gradual, so bubbles where $\text{Re} \approx 2$ and $\text{Eo} \approx 5$ could be used, but it was noted that they are at the boundary between spherical and non-spherical. Using $\text{Eo} = 5$ to calculate a theoretical rise speed using the Hadamard-Rybczynski equation, a maximum allowable rise speed (relative to the surrounding liquid) of $U = 0.061 \text{ m s}^{-1}$ was predicted. Using this value in the calculation for Reynolds number provides $\text{Re} = 1.4$, which was consistent with the previous estimate on the upper boundary for the Reynolds number predicted by Figure 2.7. Therefore, any bubble in the silicone oil with a diameter less than 3.3 mm was considered sufficiently small to be assumed to be spherical.

3.2.3. Injections

Injections were characterised by the insertion of gas, or volatile-rich silicone oil into the bottom of the experiment through the baseplate at the bottom of the glass tube (Figure 3.2). Due to the low pressure in the experimental column, atmospheric pressure pushes the gas, or volatile-rich silicone oil, through the injection tube and into the experiment. The injected materials tested were air, 1-propanol dissolved in silicone oil, methanol mixed with silicone oil, diethyl ether mixed with silicone oil, and air dissolved in silicone oil. Each of these materials provided different configurations of bubbles with varying properties.

3.2.3.1. Injection Control

Initial trial injections using a screw clamp on the injection tube (made of flexible plastic vacuum tubing with an inner diameter of approximately 5 mm) were determined to not provide sufficiently fine temporal control, due to the clamp taking a few seconds to open and close by hand. Subsequently, a needle valve was trialled for air injections, which provided very fine control over the rate of air injected, but it lacked consistency in the speed and aperture of opening the valve and was not suitable for oil based injections. Additionally, manual handling the valve often resulted in motion of the experimental tube, which negatively affected observations of the experiments. To eliminate both of these problems, the needle valve was replaced with a solenoid valve because this can be opened and closed remotely (Figure 3.2). This was attached below the base plate using vacuum tubing with an inner diameter of approximately 5 mm and was controlled with a 24 V power supply. When the power supply was on, the valve opened, and the injection occurred as atmospheric pressure provided a force on the open end of the injection tube. When the power supply was off, the valve automatically shut. Using this method, the minimum time for an injection was reduced from around five seconds (when opening and shutting a clamp by hand) to around half a second. For oil-based injections, a syringe was used to hold the oil and, when the solenoid valve opened, atmospheric pressure pushed the syringe plunger, and drove the injection into the experimental tube. The use of a syringe facilitated the control of the volume of oil injected as there were graduations of 1 ml on the syringe, so the level of the plunger could be used to deduce how much oil had been injected, and estimate the rate of injection.

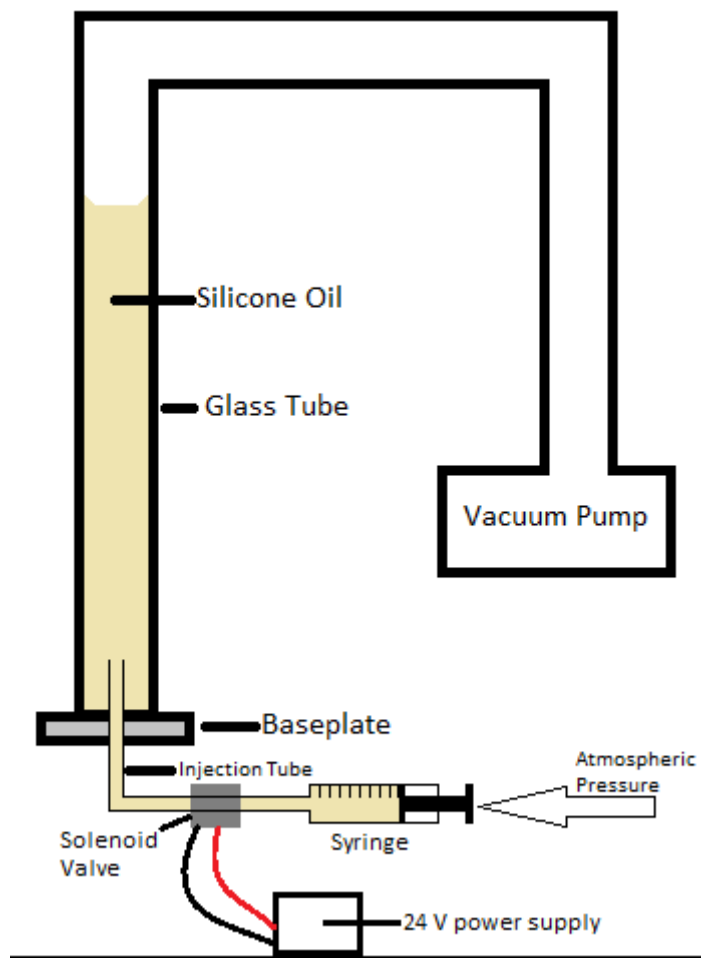


Figure 3.2: This configuration of equipment facilitates the injection of oil mixtures using a solenoid valve to control the timing of the injection. This setup forms the basis of all the main experiments.

3.2.3.2. Air

The introduction of bubbles into the system was provided through two methods, injection of air, or injection of volatile-rich silicone oil. By directly injecting air through the baseplate, streams of bubbles approximately 10 mm in diameter were produced which rose along the central axis of the tube. The rate of gas injection through the baseplate could be controlled using a needle valve, which altered the vertical separation of the bubbles and their size, however it was not possible to control the lateral separation of the bubbles. The bubbles almost exclusively rose along the central axis and so it was not possible to observe the potential interactions between bubbles rising next to each other. Additionally, the bubbles were not spherical due to their size, and exhibited edge effects even in the largest tube diameter available. Consequently, this method was not appropriate for this study.

The alternative method was to inject volatile-rich silicone oil through the baseplate, which caused bubbles to form upon entering the low pressure environment of

the experimental apparatus. To facilitate this, attempts were made to dissolve gases into the silicone oil and inject these into the low-pressure environment of the experimental apparatus.

3.2.3.3. 1-Propanol

1-Propanol was tested as a substance to dissolve into the silicone oil as it was expected to be miscible with the oil as well as a liquid that is known to easily change into a gaseous state. Therefore, it was anticipated that the 1-propanol would exsolve from the oil in the experiment when used in sufficiently high concentrations.

Experiments using < 5% by weight of 1-Propanol in silicone oil resulted in negligible bubble nucleation at the bottom of the experiment. When the 1-propanol-rich oil rose to the top of the column (as it was less dense than the silicone oil without 1-propanol dissolved in it), bubbles formed at the top of tube. The pressure due to the weight of the overlying silicone oil was much lower at the top of the tube (approximately 0.97 kPa at 10 cm depth versus 12.6 kPa at 1.3 m depth), which accounted for why bubble nucleation was more likely to occur here. The observation of bubble nucleation at lower pressures demonstrated that a different chemical with a higher vapour pressure might form bubbles further down the tube.

3.2.3.4. Methanol

The vapour pressure of 1-Propanol is approximately 1.99 kPa at 19.8 °C (Kempe & Kreps, 1969) to 2.80 kPa at 25 °C (Munday et al., 1980) while methanol has a vapour pressure of 12.9 kPa at 19.8 °C (Dever et al., 1955). Due to its higher vapour pressure, methanol was expected to produce more bubbles than 1-Propanol at a greater pressure (depth) in the experiment. When a sample of approximately 5 % methanol, 95 % silicone oil was prepared, the mixture turned a milky white colour. When left for several days, clear liquid separated from the milky liquid at the top of the mixture indicating that the milky colour may have been caused by a very fine suspension of droplets, and that methanol was not soluble in silicone oil.

The milky solution was injected into the experiment as tiny droplets of highly concentrated methanol may act as preferential nucleation sites and, despite not being soluble, it was thought that this configuration could promote nucleation at the base of the experiment. While some bubbles did form in these experiments, they were not significant in numbers, and may not have been comprised entirely of methanol, which implied a lack of control over the nucleation of bubbles.

Furthermore, when bubbles passed through the methanol-silicone oil mixture (which was easily visible as a translucent area in the tube), they rapidly (<1 second) grew

in size. When the bubbles left the areas of methanol and silicone oil, they rapidly decreased in size. This observation indicated that methanol can diffuse into bubbles very rapidly, and provided evidence to suggest that bubbles achieved chemical equilibrium in a time span much shorter than the video observations of the experiments, which typically lasted for 1 minute.

As the behaviour of the bubbles was more complicated than previous experiments when bubbles interacted with areas of increased methanol concentration, this method was rejected. However, it did provide a useful insight into how rapidly chemical equilibrium may be achieved in the experiment.

Additionally, as an insufficient number of bubbles were being produced, a chemical with an even higher vapour pressure was used. For this, diethyl ether was tested as it had a vapour pressure of 58.9 kPa at 20 °C (Chunhua & Wang, 2015).

3.2.3.5. Diethyl Ether

A solution of 2 % diethyl ether and 98% silicone oil was prepared and injected into the experiment. While some bubbles were produced, the number of bubbles generated was still insufficient to observe a variety of group behaviours. While it may have been possible to find another chemical which has an even higher vapour pressure that was also soluble in silicone oil, increased vapour pressure implied increased volatility which gives a heightened safety risk due to accidental ignition of the vapours (which was of particular concern, given the electric equipment in the laboratory). As such, instead of attempting to utilise a more volatile chemical, a less soluble chemical may produce a greater number and number density of bubbles as it more readily exsolved from the oil. Experiments detailed in Chapter 4 show that the oil can dissolve air (or some components of air) to at least 0.4 % by weight. The solubility of the oil varies with pressure so instead of dissolving a volatile substance in degassed oil, it was determined that using oil with air dissolved in it was a viable option.

3.2.3.6. Air and Silicone Oil

Air dissolved in silicone oil presented a number of advantages over mixing silicone oil with other chemicals. Firstly, the sample preparation was simple, as all that was required was to leave a beaker of silicone oil open to the air for three to five days (the dissolution of volatiles was expected to increase logarithmically with time, and so additional days did increase the volatile content, but not linearly). Secondly, as there were no additional chemicals added, there was very little risk of contaminating the oil with leftover chemicals. Thirdly, air is non-toxic and inert, in contrast to diethyl ether which was highly flammable and could cause loss of consciousness if inhaled, or methanol which is toxic in small

quantities, as well as flammable. A disadvantage of using air dissolved in silicone oil was that it was not practical to control the volatile content, nor to easily determine it prior to experiments. As the focus of the experiments was to study bubble behaviour, and not nucleation processes, this was not a significant disadvantage and may be seen as advantageous as it facilitated a range of bubble behaviours.

Using air and oil was observed to produce a wide range of bubble behaviours from single bubbles in isolation through to dense groups of bubbles which nearly formed foams. The bubbles produced were almost all less than 3 mm in diameter, which was within the spherical regime. Thus, the air-silicone oil injections were selected for all experiments.

3.3. Experimental Configuration

Following the preliminary tests and design considerations discussed in Section 3.2, a design was constructed which facilitated the experiments required to tackle the question proposed in the thesis title (Figure 3.3).

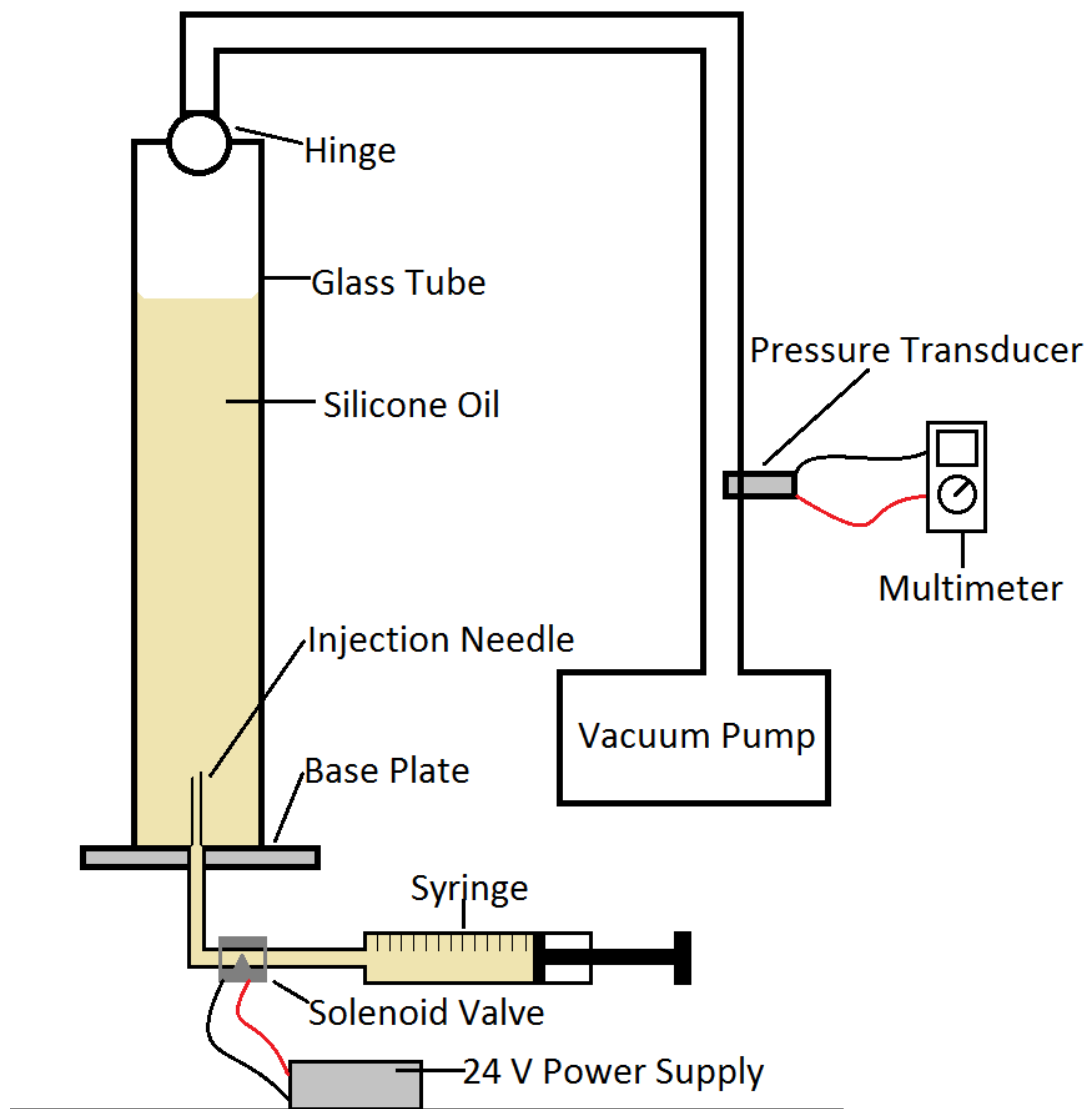


Figure 3.3: Diagram of the final experimental design.

3.3.1. Experimental Tube

This configuration featured a ~3 m long glass tube hanging from the ceiling via a hinge at the top, which allowed the entire experimental tube to be tilted for non-vertical experiments. Glass tubes with different internal diameters of 25 mm, 40 mm, 50 mm and 80 mm were used, and had hand-drawn markings around the circumferences every 10 cm to use as reference points. The tube was connected to a vacuum pump which controlled the ambient pressure inside the experiment. The lowest measurable pressure with a pressure transducer was 10 Pa.

3.3.2. Base Plate

At the bottom end of the tube was the aluminium base plate. The plate was highly polished and secured against the glass tube with three bolt fittings and a Polytetrafluoroethylene (PTFE) ring seal to mitigate air leaks. PTFE is non-reactive so was not expected to contaminate the oil.

The base plate was approximately 1 cm thick and 15 cm in diameter. In the centre of the base plate a hole was drilled, and a push-fit tube connection attached with epoxy, which facilitated the attachment of injection needles of varying sizes. However, only one injection needle was used for all experiments and this was a 17-gauge needle (inner diameter 1.067 mm). The use of the needle confined the injected substances to a smaller volume, which promoted the nucleation of bubbles. The presence of the needle also appeared to inhibit the nucleation of bubbles in the injection tube, which further promoted the nucleation of bubbles inside the experiment. Tests with larger and smaller needles both yielded fewer bubbles, suggesting that the 1.067 mm needle was the optimal of the three needle diameters tested.

3.3.3. Solenoid Valve

The solenoid valve was powered using a 24 V power supply, controlled by a button that enabled the valve to open for < 1 s time periods. A timing device was not required because injection duration did not need to be controlled to a great deal of precision as even the shortest injections produced prolonged emission of bubbles which provided ample opportunity to study a wide array of behaviours.

3.3.4. Pressure

The pressure transducer was used to indicate the pressure at the surface of the experimental oil by reading the voltage from the multimeter. A reading of 10.00 V (or close to this value) indicated atmospheric pressure (~100,000 Pa). 1.000 V indicated approximately 10,000 Pa and the lowest measurable value of 0.001 V indicated 10 Pa. The transducer could only indicate the pressure at the surface of the oil and the pressure inside the oil was calculable from the equation for hydrostatic pressure, P (Equation 3.1).

$$P = d\rho g + P_T \quad (3.1)$$

where d was depth below the surface, g was acceleration due to gravity, ρ was the oil density and P_T was the pressure reading taken from the transducer.

The pressure for a given experiment was set by engaging the vacuum pump to reduce the pressure and allowing air into the experiment to increase the pressure. It was sometimes necessary to engage the vacuum pump in order to maintain a constant pressure

over the course of a data collection session due to small air leaks, and because injecting air-oil mixture into the tube increased the pressure. Such pressure corrections were only necessary at the lowest measurable pressures, as these were proportionally more sensitive to additional gas entering the system, either through injections or air leaks, which were greatest at low experimental pressures.

3.4. Experimental Procedure for Data Acquisition

Each experiment performed had a near identical procedure: while the experimental tube was held at a low pressure, a short (1-5 seconds) injection of oil-air mixture was injected into the base of the experiment and the resulting bubbles were recorded by filming with at least one DSLR camera. The specifics of the tube diameter, tube inclination, the pressure, the injection length and the camera configurations varied in order to capture footage with the most useful information; however, the same core method existed in all the main experiments.

Prior to each new experimental session, the oil in the experimental tube was exposed to the atmosphere for several days, which meant that some air would dissolve into the main body of oil, which resulted in undesirable bubble nucleation. To remove dissolved air from the experimental oil, the tube was inclined by approximately 5° and air injected into the bottom of the tube. The injection of air created a turbulent environment which promoted bubble nucleation, and tilting the experimental tube forced a circulation of oil around the entire tube from top to bottom so that all the oil was effectively degassed prior to experiments. During this process, the initial air bubbles which passed through the tube disturbed the oil. When they reach the surface of the oil the disturbance facilitated nucleation of many bubbles, which formed a foam. The oil was judged to be effectively degassed when very large bubbles (diameter comparable to that of the tube) did not induce nucleation of sub-millimetre bubbles upon reaching the surface of the oil. The degassing process would typically be completed after approximately 5-30 minutes and had to be repeated prior to each daily run of experiments as it was considered impractical to hold the experiment at a vacuum indefinitely due to small air leaks, and because it was equilibrated to atmospheric pressure to avoid implosion when left unattended.

When the degassing process was complete, the experimental tube was returned to the vertical position and the pressure set to the desired value for the experiment. Prior to data acquisition, the solenoid valve was opened for less than five seconds in order to purge any air bubbles that had formed since the previous time the experiment had been used.

3.4.1. Camera Specifications

Three cameras were used to film the experiments: two Canon 600Ds and one Canon 550D, all of which are capable of filming 1920×1080 pixels at 25 Hz resolution or at 1280×720 pixels resolution at 50 Hz. As measurement of bubble size introduced the greatest uncertainty into calculations for rise speed, it was preferable to film in the highest spatial resolution available.

The lenses used were two 50 mm f/1.8 lenses and one 40 mm f/2.8 lens. While using these lenses at their maximum aperture would produce brighter images (and require a lower light sensitivity in the camera's settings to achieve an acceptably bright image), the images were not as sharp at the extreme apertures and the depth of field was very narrow, meaning that only a small number of bubbles were in focus. For the 50 mm lenses at f/1.8, the depth of field at a distance of 80 cm between the central axis of the tube and the camera was 1.6 cm (Fleming, 2005), meaning that bubbles greater than 0.8 cm away from the central axis of the tube were out of focus. Reducing the aperture to f/5.6 increased the depth of field to 5.2 cm (2.6 cm on either side of the central axis) (Fleming, 2005) which applied to the majority of bubbles seen in the experiments.

The amplification of the signal from the camera's light sensor varied depending on the lighting conditions in the laboratory at the time (which were affected by weather and the time of day) to ensure that sufficient light was captured in order to image the bubbles clearly without degrading the video quality with image noise.

Both of the cameras used had APS-C sensors with a crop factor of 1.6 (Canon, 2019), meaning that the effective focal length for the lenses were 80 mm for the 50 mm lenses and 64 mm for the 40 mm lens.

3.4.2. Camera Placement

In order to maximise the amount of data collected in each injection, the cameras were placed on tripods around the experiment such that they covered different parts of the experimental tube. The exact placement varied between experiments in order to capture different features, however the section of tube between 30 cm and 100 cm above the baseplate was the primary area that was used, as preliminary tests showed that this is the region where different types of bubble behaviour developed.

The distance between the cameras and the experimental tube was a compromise between four factors. The principal two factors were spatial resolution and the amount of the tube visible in each frame. Additionally, the parallax effect and the effect of the apparent size of the bubbles according to their position within the tube had to be considered.

Placing the cameras close to the tube resulted in a higher spatial resolution (which allowed for accurate measurements of bubble rise speed and diameter) but reduced the amount of the tube visible in each frame. Additionally, close camera placement increased the parallax effect (which may affect speed measurements) and the variations in apparent bubble size caused by bubbles that are not on the central axis of the experiment (closer bubbles appear larger, further away bubbles appear smaller).

The observation of bubbles required them to be within the field of view of a camera for several seconds in order to detect any variations in rise speed. The typical rise speed of bubbles in preliminary experiments meant that a field of view covering approximately 20-30 cm of the experimental tube was required. Given the focal lengths of the lenses available, this required the cameras to be approximately 70-100 cm away from the central axis of the experimental tube.

Additional cameras at different heights increased the amount of the tube which was filmed, while maintaining a high spatial resolution. However, more cameras produced more data to review and process. Utilising more than one camera also allowed for additional viewing angles, which provided information to determine if a given bubble was near to the side of the tube, or if it was near the central axis, as well as aiding in determining bubble separation distances. A compromise was struck between producing a manageable quantity of data while maintaining a high quality of data (spatial resolution). This compromise was to use either two or three cameras. The decision over whether to use two or three was determined by running the experiment without recording videos and observing by eye where the bubble column was able to exhibit the greatest variety of bubble behaviours ranging from single bubbles to dense groups. It was qualitatively observed that the 50 cm nearest the surface of the oil featured decompressive expansion of bubbles, which made measurements of bubbles' speed over a long duration inaccurate as their speed changed across the measurement period, so this part of the tube was not filmed. Meanwhile inertial effects of the injected oil and the nucleation of the bubbles (which was beyond the scope of this work) were observed in the 10 cm of oil above the base plate. Therefore, in a 140-150 cm tall column of oil, the majority of bubble behaviour that was fruitful to observe occurred between 30 cm and 100 cm above the baseplate. Between 10 cm and 30 cm above the base plate, the bubbles generally had not developed group behaviour that could be studied, and in the inclined tube experiments, the bubbles had not risen to meet the tube wall. This justified the use of up to three cameras with a field of view of between 20 cm and 30 cm each between 30 cm and 100 cm above the base plate.

Depending on the relative height position of the camera, it (and the videos produced by it) was given a three-letter designation. “LOW” was for the lowest camera, “TOP” for the highest camera and “MID” was used when a third camera was positioned between LOW and TOP. The exact height of these cameras varied in order to capture as many different examples of bubble behaviour as possible, and at times was adjusted between experimental runs if desirable bubble behaviour was observed to occur at the edge of frames.

3.4.3. Camera Operation

When the cameras were in place, it was necessary to set their focus manually as automatic focus consistently did not focus on the bubbles. To do this, a small amount of air-oil mixture was injected into the tube, and using the camera’s display in 10× digital magnification mode, the focus was manually set on the rising bubbles. Focussing in this manner was also an opportunity to check that the camera settings were appropriate for the lighting, that the spatial resolution was sufficient to see the bubbles, and that the cameras were aligned with the experimental tube.

At the start of an experiment, recording was initiated using an infrared shutter control which removed any requirement to touch the cameras, which could potentially have moved them or disrupted their focus setting (despite this mitigation effort, some videos still produced out of focus images and could not be used).

3.4.4. Lighting

The cameras used in the experiment (Section 3.4.1) needed to produce sharp images with the least amount of noise achievable. In order to meet this requirement, a bright environment was preferable as it reduced the need for high light sensitivity in the images, which in turn reduced the noise in the images. Additionally, a bright environment allowed for narrower apertures, which generally produce sharper images. In addition to the room lighting, a vertical fluorescent tube light was used to maximise the amount of light shining on the experiment. The fluorescent tube was 2 m long and was placed approximately 40 cm from the experimental tube.

In order to increase the visibility of the bubbles, black cardboard was placed behind the experimental tube as observed by the cameras (Figure 3.4).

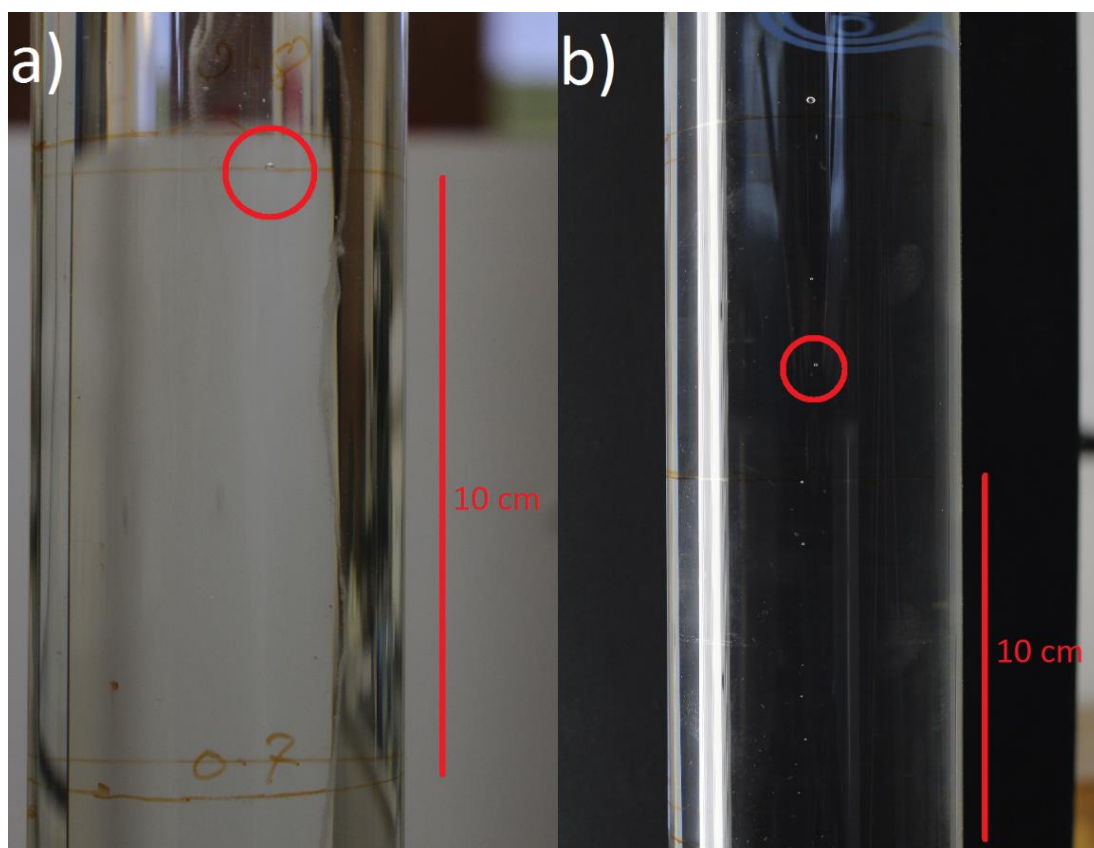


Figure 3.4: Demonstration of the effect that the fluorescent lighting and black cardboard screen have on the visibility of bubbles (examples circled in red). With the lighting and screen in (b), even very small bubbles are clearly distinguished, whereas without it, as in (a), even large bubbles are difficult to observe.

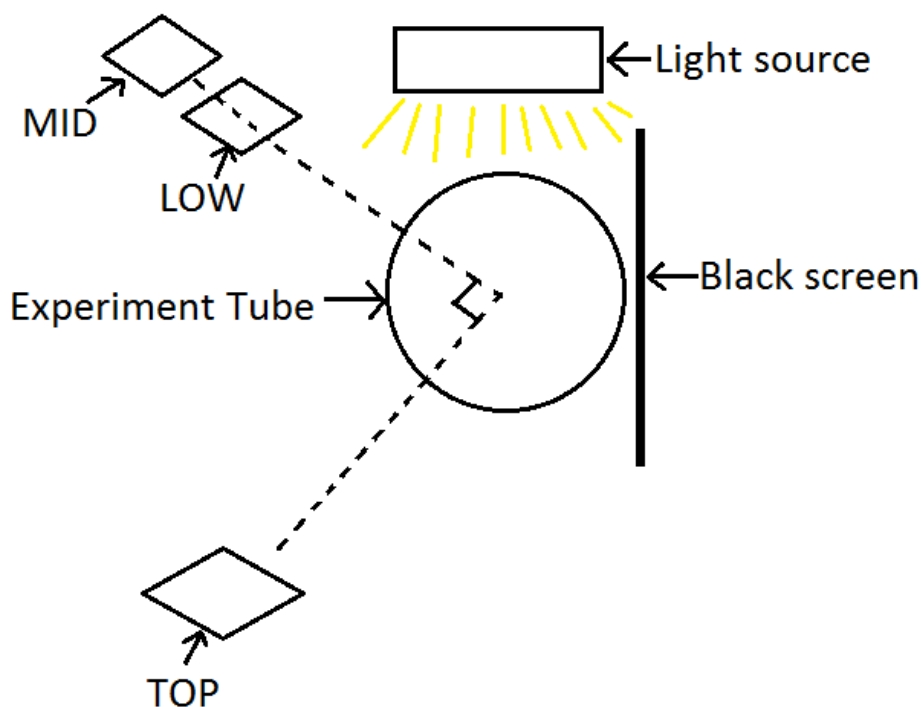


Figure 3.5: A top-down view of how three cameras might be set up for an experiment. The direction of view of the TOP camera is perpendicular to the LOW and MID cameras' direction of view.

Placing the camera perpendicular to the light source inhibited the observation of bubbles due to the reflection of the fluorescent light tubes on the glass of the experimental tube. Placing a camera on the opposite side of the experimental tube from the light source resulted in low contrast images in which the bubbles were not visible. The configuration of cameras shown in Figure 3.5 provided the best compromise between resolving bubbles clearly and observing them across an appropriate length of the experimental tube.

3.4.5. Sample Preparation

The oil-air mixture that was injected into the experiment was prepared by filling a 200 ml plastic beaker with oil and leaving it exposed to air (covered by a loose paper towel covering to reduce dust contamination) for three to five days. To fill the syringe, two methods were adopted. Initially, the plunger was completely pushed and the tip dipped into the oil before drawing the plunger to pull oil into the tube. This had the advantage of resulting in very little air inside of the syringe when performed correctly, but the external parts of the syringe needed cleaning of oil afterwards and required careful monitoring of the level of the oil in the beaker so that the tip of the syringe was always submerged. Later, an alternate method was developed to avoid drawbacks by completely removing the plunger and slowly pour oil into the top of the syringe before replacing the plunger. The

second method only required the air between the oil and the plunger to be purged by upturning the syringe so that the air was at the top of it and then pushing the plunger until oil just started to be ejected.

When the syringe was full of oil-air mixture, it was connected to the end of the experimental tube by pushing the end of the syringe into the end of the injection tube to provide an air tight seal with no additional modifications necessary.

3.5. Data Analysis

The principal form of data analysis for all experiments followed one method. Firstly, to measure the rise speed of a particular bubble and then compare that rise speed with a theoretical rise speed based on the size of that bubble.

3.5.1. Bubble Selection

Whilst each video captured contained, typically, over 100 individual bubbles, it was not practical, or even possible (due to obscuration by other bubbles) to measure every bubble in every video. It was also not necessarily desirable to do so, as once a sufficient number of bubbles were measured such that a clear pattern was observable in the result, additional bubbles did not provide additional insight.

As such, a selection of bubbles which provided the best data in the quickest time was chosen. For a bubble to be a suitable candidate it had to conform to the following criteria in the videos:

- 1) The bubble must be clearly in focus. Suitable focus was determined by the observation of a clear air-oil boundary in the videos. Out of focus bubbles had poorly defined boundaries and so measurement of their diameter was inaccurate.
- 2) The bubble did not exceed 3.3 mm in diameter, as those bubbles were non-spherical. Non-spherical bubbles were not adequately described by Stokes' law.
- 3) The bubble was clearly distinguishable during the period of observation, or clearly observed for sufficiently long period that it would not be mistaken for a different bubble.
- 4) The bubble's path over the observation period spanned the majority of the field of view of the video. The longer the bubble was observed for, the lower the uncertainty in the speed of the bubble.
- 5) The bubble had constant or near constant speed over the observation period. This ensured that the effect of any group behaviour on the bubble was valid over the observation period.

- 6) For bubbles in dilute groups, candidate bubbles had at least three other bubbles within five bubble diameters for the majority of the observation period so that those bubbles were distinguishable from single bubbles.

3.5.2. Image Processing

When a candidate bubble was selected over an appropriate time frame, the video clip within which the bubble was observed was processed to aid measurements. Using VirtualDub (version 1.10.4) software, the video was cropped to only include the experimental tube and set to greyscale to minimise the file size. The contrast was set to maximum (200 %) and the brightness was set to allow for the easiest observation of the bubbles, as judged by eye. The video was then exported from VirtualDub into a collection of still images (image stack) where each still image was a frame from the original video in the Portable Network Graphic (PNG) format.

3.5.3. Bubble Speed Measurement

For a given bubble in an image stack, the measured rise speed was determined by measuring the pixel coordinates (as determined by measuring the centre of the bubble as presented in the still image from the image stack when opened with ImageJ version 1.51k) in the first frame and the pixel coordinates in the end frame. The average speed of the bubble was calculated using the straight line distance between the start and end point.

The distance between the start and end points was converted from a measurement in pixels to a 'real world' distance within the experiment using the outer diameter of the experimental tube as a reference length to determine the image scale (the number of pixels per millimetre). This assumed that the bubble track was along the centre axis of the tube and perpendicular to the direction of view of the camera. However, variations were to be expected and it was anticipated that measurements of many bubbles would cancel out deviations from the central axis, as an equal number would be expected on either side of it in vertical tubes. In the inclined tube, there was a heterogeneity across the width of the tube, but the camera was placed such that it viewed the tube approximately perpendicular to the heterogeneity across the width.

The measured rise speed was then compared to a theoretical model of the rise speed based on the Hadamard-Rybczynski model by plotting them directly on a graph of measured versus theoretical rise speed. Where no group behaviour existed (due to the lack of other bubbles nearby), the values for theoretical and measured rise speed should match each other within uncertainty. Many bubbles with an observed deviation from the line of

measured speed = theoretical speed was indicative that the bubbles are being subjected to an additional effect not described by the Hadamard-Rybczynski model.

3.5.4. Stokes' Law and Hadamard-Rybczynski Model

Stokes' law is valid for solid spheres with a Reynolds number less than 1; however, Stokes' Law neglects the internal rotation of gas within the bubbles. Instead, the Hadamard-Rybczynski model was used to model the rise speed of bubbles. For a maximum Reynolds number of 1, the bubbles selected needed to have a diameter less than 3.3 mm. The Hadamard-Rybczynski model is given by

$$v = \frac{d^2 g (\rho_{oil} - \rho_{bubble})}{12\eta} \quad (3.2)$$

where v is the bubble speed, d is the diameter of the bubble, g is acceleration due to gravity, ρ_{oil} is the density of the oil, ρ_{bubble} is the density of the bubble and η is the oil viscosity. The speed value generated by the Hadamard-Rybczynski is greater than the value generated by Stokes' Law by a factor of 1.5. The density of air at standard temperature and pressure is approximately 1 kg m^{-3} and the experiments were conducted at a much lower pressure than atmospheric pressure. Therefore ρ_{bubble} was lower than 1 kg m^{-3} , and taken to be zero in all calculations as the bubble density was much lower than that of the surrounding oil.

The value for oil viscosity was taken to be $0.143 \pm 0.020 \text{ Pa s}$ at $25 \text{ }^\circ\text{C}$ (Section 4.2); however, not all experiments were conducted at $25 \text{ }^\circ\text{C}$, so the viscosity was modified by interpolating the model from a data sheet for Wacker AK 100 in the regime between $0 \text{ }^\circ\text{C}$ and $25 \text{ }^\circ\text{C}$ (Figure 3.6) (Wacker, nd.). While the oil used in the experiments was AS 100 rather than AK 100, the two fluids had similar properties, so it was taken that, in lieu of data for AS 100, the temperature-viscosity relation would be comparable.

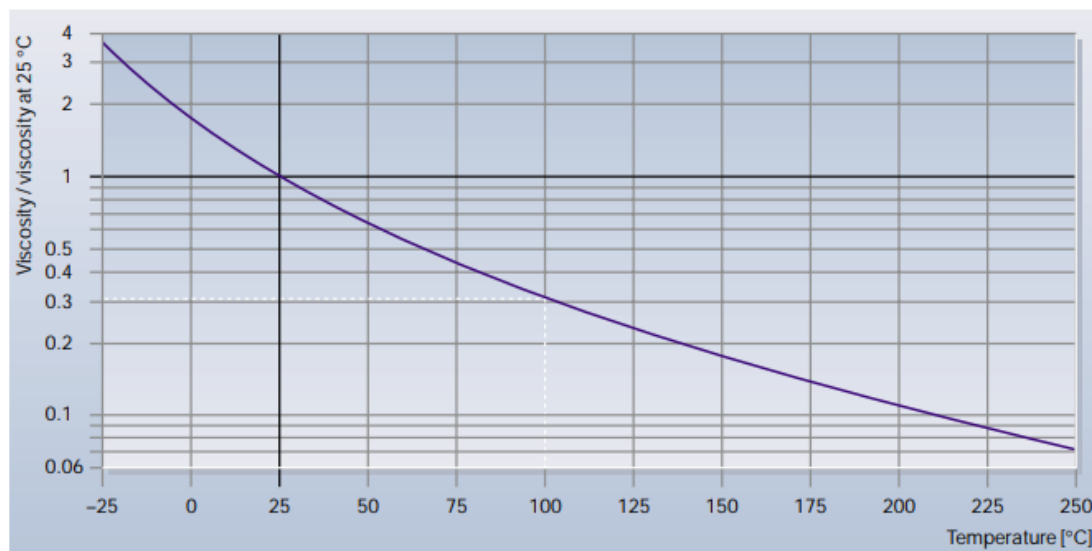


Figure 3.6: Viscosity as a function of temperature for Wacker AK silicone fluids of viscosity greater than or equal to 0.1 Pa s relative to the viscosity at 25 °C. Although this was a different compound than AS 100, in the absence of data for AS 100, the data for AK 100 is taken to be a suitable proxy. Image from the Wacker Silicone Fluid AK data sheet (Wacker, nd.)

The viscosity-temperature graph yielded an empirical equation given by

$$\eta_t = \eta_{25} - 0.025 \eta_{25}(t - 25) \quad (3.3)$$

where η_t was the viscosity at temperature t , η_{25} was the viscosity at 25 °C and t was the temperature in °C.

The density value used in calculating the Hadamard-Rybczynski rise speed was modified as a function of temperature using the coefficient of volumetric thermal expansion ($91 \times 10^{-5} \text{ mL mL}^{-1} \text{ K}^{-1}$) as given in the technical data sheet for AS 100 silicone oil.

The temperature at which each experiment was carried out was determined by a thermometer with a precision of 0.1 °C. The thermometer was placed next to the experimental tube and it was assumed that temperature variations in the laboratory were sufficiently small and slow that the tube could be taken to be at thermal equilibrium with the air. The temperature was monitored periodically over the course of a number of injections, as the fluorescent tube placed near to the experiment produced heat. However, there was negligible variation over a single day as the principal variation in temperature appeared to be from variations in ambient conditions due to the weather and heating system within the building, which were more pronounced between days rather than within a given day. Based on the variation in the temperature measurements, the temperature for all experiments was taken to be 20 ± 3 °C during analysis.

3.5.5. Uncertainty

The uncertainty in distance measurements was estimated by measuring a bubble's diameter 250 times in 250 consecutive video frames. The standard deviation of the diameter values measured was 0.6 pixels, so the standard uncertainty for all pixel distance measurements was taken to be 0.6 pixels. When observing the displacement of a bubble over multiple seconds, the bubble traversed several hundred to approximately 1,000 pixels, so the uncertainty of 0.6 pixels was sufficiently small to be taken as zero.

While there was a source of uncertainty deriving from the parallax effect, this was not of concern, as the cameras were judged to be sufficiently far from the experimental tube that this effect was effectively negligible. The variations from the central axis varied by up to 4 cm (although typically no more than 1-2 cm), whereas the cameras were approximately 70-100 cm away from the central axis, so the deviations from the central axis which may cause a parallax error were taken to be small in comparison to the distance to the cameras.

Additionally, the comparison between measurement and uncertainty was not anticipated to be affected, as although bubbles may have appeared to travel faster (or slower, if they were further away than the central axis) than they actually were travelling, they also appeared larger (or smaller), leading to an overestimate (or underestimate) of their theoretical rise speed. It was expected that, given a sufficiently large number of sampled bubbles, that the over- and under-estimate of theoretical rise speeds would not change the conclusions drawn as an approximately equal number of bubbles would be over-estimated in size as under-estimated in size, with no variation across a range of sizes. An expected result was that the spread of values away from the model may have been wider, but not to the extent that the model could not be verified.

The temporal uncertainty in the time taken for a bubble to traverse that distance was taken as zero, as the DSLR cameras were expected to provide a consistent frame rate during each video of an experimental run, which typically lasted for one minute.

The main source of uncertainty in the experiments derived from uncertainty in the diameter of the bubbles. The uncertainty on the measurement of each distance measurement was taken to be 0.6 pixels based on repeated measurements of diameter, with a negligible uncertainty when converting to metres where the reference distance (tube outer width) was several hundred pixels and clearly resolved. The uncertainty in viscosity was taken as 0.011 Pa s based on the variability of the viscosity between 17 °C and 23 °C, using Equation 3.3. The uncertainty in density at 19.5 °C was calculated as 0.0051 g cm⁻³ (Table 4.1) and the effect of the variability of temperature was negligible on the calculated

rise speed and uncertainty. The variations in viscosity and density were considered to be second and third order effects, with the bubble diameter as the first order effect. Propagation of uncertainties via quadrature was not used as there was insufficient data to determine whether uncertainty was normally distributed around every value. Instead, uncertainties were propagated by consideration of the minimum and maximum values in order to demonstrate the full range of possible values from the uncertainties in the model parameters and experimental values. The use of a minimum-maximum uncertainty does result in larger uncertainties than the quadrature method, however the overall fractional uncertainty in theoretical rise speed was under 20 % for the majority of bubbles.

4. Silicone Oil Characterisation

In order to model the ascent of bubbles in silicone oil (Wacker AS 100), it was necessary to know the viscosity and density of the oil. These parameters were measured experimentally in order to verify the manufacturer's values, as well as to check for variations due to contamination or degradation over time as the oil used in the experiments was purchased approximately three years prior to the experiments, and had been used for previous experiments.

4.1. Density

The manufacturer's specification for oil density at 25 °C was approximately 0.99 g cm⁻³. This was tested by weighing a known volume of oil at a known temperature, in this instance the ambient temperature was 19.5 °C, as determined by a digital temperature probe with a precision of 0.1 °C. A 100 ml graduated cylinder (calibrated at 20 °C and precision of 0.5 ml) was used in order to establish a known volume, and a weighing scale with a precision of 0.001 g was used to weigh the oil. The experiment was also repeated with H₂O to validate the methodology, as the density of H₂O as a function of temperatures is well documented (Aylward & Findlay, 2002). Three measurements were taken where the cylinder was filled with H₂O at ambient temperature in order to check the calibration of the graduated cylinder. The density of the oil was measured as 0.9876 ± 0.0051 g cm⁻³ (Table 4.1), while the H₂O's measured density was 0.9880 ± 0.0051 g cm⁻³, which was approximately 0.5 % lower than the literature value of 0.9982 g cm⁻³, but was in agreement within uncertainty.

Table 4.1: Breakdown of the measurements for determination of H₂O and oil density. Uncertainties in mass are calculated using standard deviation of repeated measurements. Uncertainty in oil density was from propagation of the relative uncertainty in oil mass (shown to be normally distributed from a Kolmogorov-Smirnov test for normality), and the precision value of the graduated cylinder.

Measurement Number	Mass of 100 ml H ₂ O plus graduated cylinder / g	Mass of graduated cylinder / g	H ₂ O density / g cm ⁻³	Mass of 100 ml oil plus graduated cylinder / g	Oil density / g cm ⁻³
1	139.242	40.605	-	139.384	-
2	139.464	40.609	-	139.467	-
3	139.381	40.603	-	139.245	-
Average	139.362 ± 0.112	40.606 ± 0.003	0.9880 ± 0.0051	139.365 ± 0.112	0.9876 ± 0.0051

Given a linear coefficient of thermal expansion of $9.1 \times 10^{-4} \text{ }^\circ\text{C}^{-1}$ (according to the manufacturer's specification), at an ambient temperature of $19.5 \text{ }^\circ\text{C}$, an oil density of 1.005 g cm^{-3} was expected. The measured value of $0.9876 \pm 0.0051 \text{ g cm}^{-3}$ was 1.7 % lower than the expected value. The measurements for both oil and H_2O were slightly lower than their expected values, which suggested a small systematic error in the experiment, which could be due to inaccurate graduations on the cylinder, or incorrectly filling it. The measured density of the oil did not agree with the manufacturer's value within uncertainty, which was indicative of possible degradation or contamination of the oil. For the purposes of modelling the rise speed of bubbles, the measured value was used as this better reflected the properties of the oil used in the experiments.

4.2. Viscosity

The manufacturer's specification for kinematic viscosity was $100 \text{ mm}^2 \text{ s}^{-1}$ at $25 \text{ }^\circ\text{C}$ and using the specified (rather than measured) density of 0.99 g cm^{-3} , a dynamic viscosity of 0.101 Pa s was inferred. The specified, rather than measured, density was used, as this was a representation of the implied dynamic viscosity from the manufacturer. The data sheet did not indicate whether there was a difference in viscosity between oil containing a high volatile content and oil which did not. However, as the main experiments used degassed oil, this was also used in a series of falling ball viscometry experiments, from which the oil's viscosity was determined.

4.2.1. Equipment

The falling ball viscometer used was a glass tube with a round, sealed, bottom and narrow, open, top and an inner diameter of approximately 40 mm and solid white graduations at 25 mm, 100 mm, 175 mm, 200 mm and 220 mm above the lowest part of the cylindrical portion of the viscometer (Figure 4.1). These graduations were marked around the entire circumference of the tube, which helped to mitigate the parallax effect when taking measurements. The tube had a funnel attachment at the top which helped ensure that spheres dropped into the tube fell along its central axis. A clamp stand held the viscometer tube in a vertical position. Spheres falling through the viscometer were videoed using a Canon 600D with a Canon 75-300 mm f/4-5.6 lens. The camera was placed on a tripod approximately 2.5 m from the viscometer and the height was adjusted such that the 175 mm graduation ring on the viscometer appeared as a single line to minimise parallax effects (Figure 4.2).

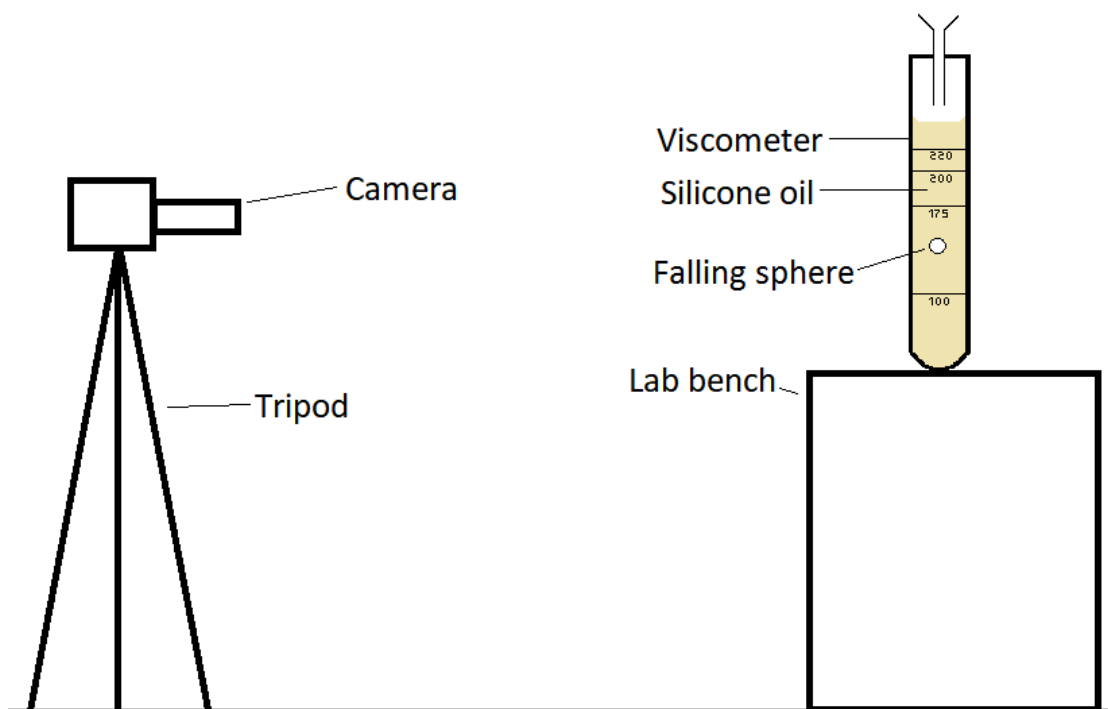


Figure 4.1: Summary of the experimental setup for falling ball viscometry, not drawn to scale. Note that the oil was almost colourless but is represented by a pale tan colour here for visual clarity.

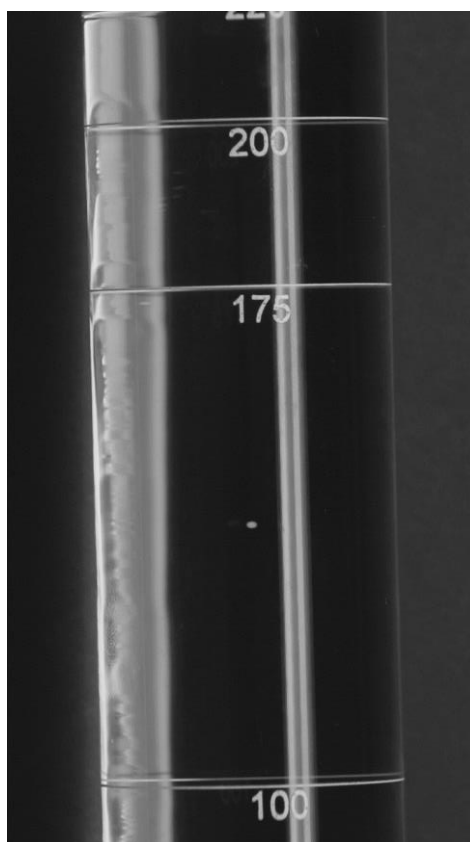


Figure 4.2: Sample image from a falling ball viscometry experiment. A 1 mm Delrin sphere was falling through the viscometer. The two vertical white lines near the centre of the tube were reflections of the fluorescent strip lighting used to illuminate the experiment.

4.2.2. Spheres

In order to verify Newtonian behaviour, spheres of varying size and density made from the polymer Delrin, and steel were used (Table 4.2).

The diameter of the Delrin spheres were measured using two sets of electronic callipers and by taking high resolution (3456×5184 pixels) images of the spheres with a Canon 600D camera and a Canon MP-E 65mm f/2.8 1-5 \times macro lens with a Macro Twin Lite MT-24EX flash to aid in producing sharp images. The spheres were placed on a reference scale with divisions of 0.1 mm (Figure 4.3). The optical method also allowed for detailed inspection of the surface textures of the spheres. The diameter values derived from the optical method were closer to the listed diameter than the electronic callipers as well as having the smallest uncertainty and, when used to calculate density, the results were closer to the manufacturer's specifications.

Density was calculated by weighing ten spheres on a weighing scale (with a precision of 0.001 g) and dividing by the total volume, determined using the measured diameters. The uncertainty in the weight measurements was estimated as 10 % because the total weight of ten spheres was comparable to ten times the precision of the weighing scale.

Optical inspection of the spheres showed that the 2.5 mm, 3 mm Delrin spheres and the steel spheres were uniformly smooth and spherical; however, five out of the ten 1 mm Delrin spheres had significantly rougher surface textures and were therefore not spherical (Figure 4.3). It was not known why half of the spheres had this variation, but it may have been a manufacturing defect or due to a chemical reaction caused by previous experiments using the spheres. It was expected that these spheres would fall through the oil at a slower speed, which would increase the uncertainty in measured viscosity due to greater variation in measured fall speed.

Table 4.2: Summary of the size and density data for the four types of spheres used in the falling ball viscometry experiments. The uncertainty in diameter was based on the standard deviation of ten measurements. Uncertainty in density was calculated from the uncertainty in diameter and the precision of the weighing scale. The optical values shown here are after an adjustment to account for the parallax effect.

Material	\emptyset /mm	Measured Diameter /mm			Listed Density /g cm ⁻³	Measured Density /g cm ⁻³
		Callipers 1	Callipers 2	Optical		
Delrin	1	0.919 ± 0.025	0.964 ± 0.011	1.009 ± 0.018	1.41	1.30 ± 0.14
	2.5	2.450 ± 0.009	2.460 ± 0.008	2.469 ± 0.006		1.41 ± 0.14
	3	2.956 ± 0.001	2.977 ± 0.015	2.985 ± 0.013		1.46 ± 0.15
Steel	1.5875	1.535 ± 0.007	1.573 ± 0.007	1.585 ± 0.012	7.785	7.72 ± 0.10

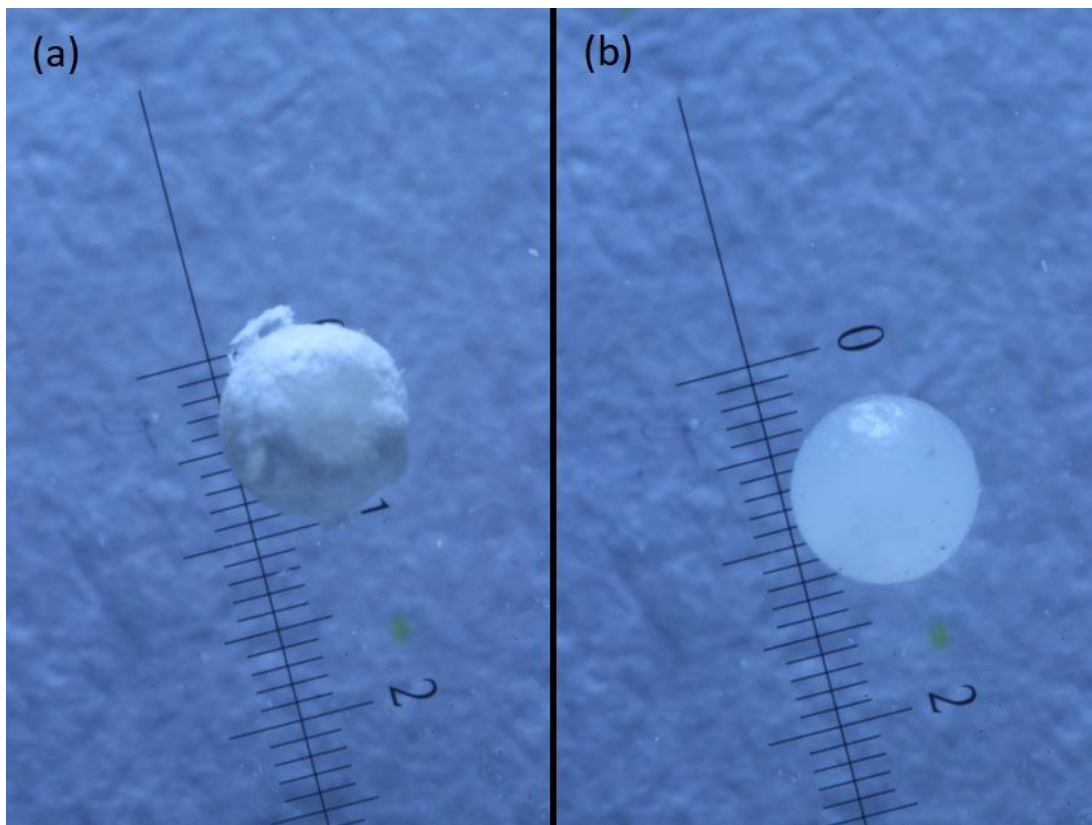


Figure 4.3: Example images from the optical characterisation of 1 mm Delrin spheres showing the different surface textures. In (a), the ball had a rough surface texture which may have affected the fall speed through the oil. In (b), the ball appeared to have a smooth surface texture and appeared to have a uniform shape. Scale labels were in millimetres, with the smallest subdivisions being 0.1 mm.

4.2.3. Method

The velocity measurements were performed by dropping up to 10 spheres of each type into degassed silicone oil and filming their descent in Full HD (1920 × 1080 pixels) at 25 Hz. Each sphere was dropped approximately one minute after the previous sphere had passed the 100 mm graduation. The lag time between each drop was to allow for movement in the oil to dissipate and minimise the likelihood of oil motion affecting the paths of the spheres. When the required number of spheres were dropped, the oil was removed from the viscometer, the spheres were collected and washed to remove oil from them. The experiment was repeated with the degassed oil. When using degassed oil, it was slowly poured into the viscometer to avoid agitation which may have facilitated gas dissolving back into the oil due to increased surface area.

The time taken for each sphere to travel between the 175 mm to 100 mm graduations was determined to the nearest 0.04 s. Then, using Stokes' law (Equation 4.1), the ball diameter, ball density and oil density, the oil viscosity, η , was calculated,

$$\eta = \frac{d^2 g (\rho_{sphere} - \rho_{oil})}{18 v_{average}} \quad (4.1)$$

where d was the diameter of the sphere, g was acceleration due to gravity, ρ_{sphere} was the density of the sphere, ρ_{oil} was the density of the oil and $v_{average}$ was the average speed of the sphere between the two graduations. Stokes' Law was assumed to be valid when the Reynolds number of the system was less than one and when edge and end effects did not apply. The average Reynolds numbers for the 1 mm Delrin, 2.5 mm Delrin, 3 mm Delrin, and 1/16" steel spheres across the experimental runs were 0.011, 0.182, 0.253, and 0.919 respectively, indicating a suitable flow regime for Stokes' law ($Re < 1$). The viscometer had an inner diameter of 40 mm meaning that spheres with diameter less than 4 mm had negligible edge effects (Brizard et al., 2005). End effects were neglected as the lowest point of measurement was 100 mm above the end cap of the viscometer, which for 1-3 mm spheres resulted in a maximum reduction in fall speed of 1 % at that depth (Brizard et al., 2005).

The time and position measurements had very low fractional uncertainties. The uncertainty in position was based on judging when the sphere had passed the graduations on the viscometer. This was judged as approximately a half of a sphere diameter in a change in position of 75-25 sphere diameters between the two graduations used, resulting in a fractional uncertainty of 0.7 % to 2 %. The uncertainty in time was taken as half of one frame interval (0.02 s). The majority of the spheres travelled at a sufficiently slow speed such that the measured time greatly exceeded the uncertainty in the time, typically taking 5 seconds for the 3 mm Delrin spheres, 7 seconds for the 2.5 mm Delrin spheres and 45-60 seconds for the 1 mm Delrin spheres. These measurements resulted in fractional uncertainty in timing of 0.03 % to 0.4 %, so this was considered negligible.

The ambient temperature of the experiment was 25 °C, which was the same as for the manufacturer's specification of viscosity.

4.2.4. Falling Ball Viscometry Results

The measured viscosity values were greater than the manufacturer's specification of 0.1 Pa s, with the calculated values ranging from 0.102 Pa s to 0.169 Pa s (Figure 4.4). The highest Reynolds number of all the spheres was less than one, which validated the use of Stokes' law.

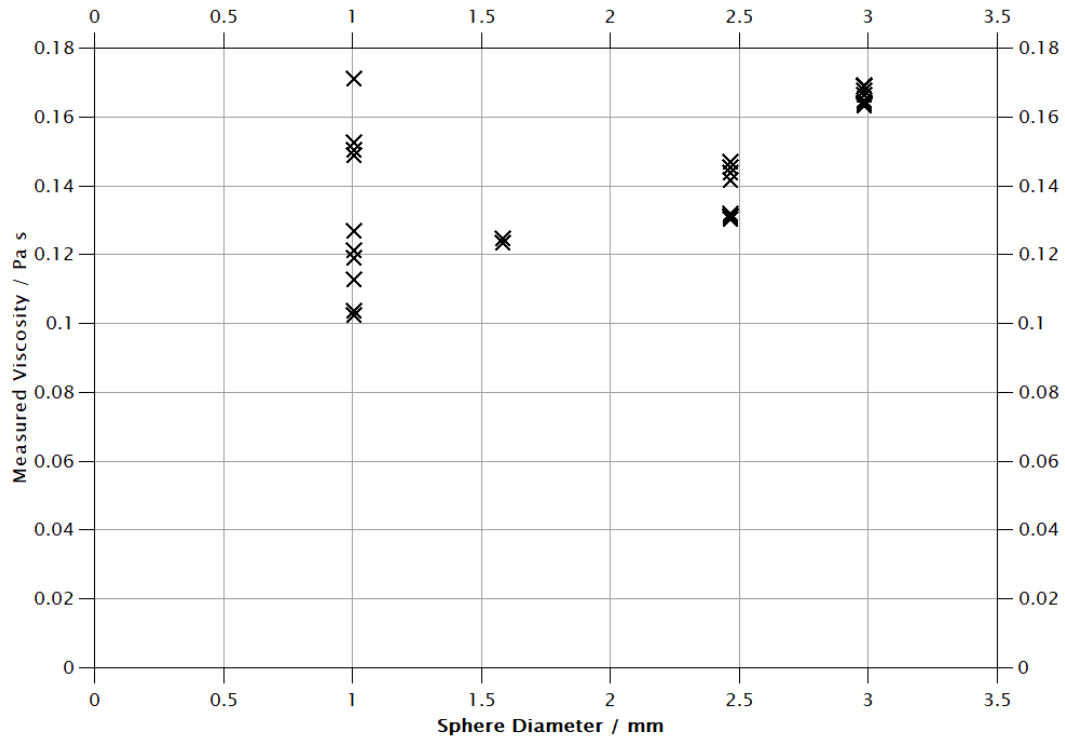


Figure 4.4: Measured viscosity for different sphere diameters.

These results range from a minimum value of 0.102 Pa s to a maximum of 0.169 Pa s and an average of 0.143 ± 0.020 Pa s. The stated uncertainty value is the error on the mean of the individually calculated viscosities for each run of the falling ball viscometer, which were normally distributed around 0.143 Pa s. The calculated viscosity value was not in agreement with the manufacturer's value of 0.101 Pa s. Regardless of the disagreement with the manufacturer's value, the measured value of 0.143 ± 0.020 Pa s was taken as the viscosity of the oil at 25 °C, as the higher than expected (compared to the manufacturer's specification) viscosity may be unique to the batch of oil used in the experiments. Due to this, as noted in Section 3.5.5, the experimental uncertainty used for viscosity was based on the variation in viscosity expected due to observed temperature fluctuations, described by Equation 3.3. Temperature-based uncertainty was used because the inconsistent surface textures of the 1 mm spheres (shown in Figure 4.3) resulted in a high experimental uncertainty of 0.020 Pa s, and the high sensitivity of viscosity to temperature.

4.3. Compressibility

The compressibility of the silicone oil was assessed by observing the volume changes of a 140 cm tall column of oil in 80 mm tubing. Decompression from atmospheric pressure (~100,000 Pa) to the lowest measurable pressure (10 Pa) yielded no visible change in

volume, as measured by eye (< 1 mm change in the length of the column of oil). This indicated a maximum compressibility of $7 \times 10^{-9} \text{ m}^2 \text{ N}^{-1}$, which was consistent with the manufacturer's specification of $1 \times 10^{-9} \text{ m}^2 \text{ N}^{-1}$ at $25 \text{ }^\circ\text{C}$. Given the range of pressures utilised in the main experiments, the compressibility of the silicone oil was effectively zero and so did not need to be taken into consideration when referring to oil density.

4.4. Thermal Expansion

The temperature of the oil was assumed to be the same as that of the laboratory. Typically, the room was around $20 \text{ }^\circ\text{C}$, but there were temporal variations affected by the weather and heating system within the building. The total height of the column of oil in the experiments was observed to change between days of different ambient temperatures. For a column height of around 150 cm in 50 mm tubing, a change of 10 ± 2 mm was observed between a day where the ambient temperature (determined using a temperature probe next to the experiment) was $20 \pm 1 \text{ }^\circ\text{C}$ and another day where the ambient temperature was $25 \pm 1 \text{ }^\circ\text{C}$, giving a temperature range of $5 \pm 1.4 \text{ }^\circ\text{C}$. A mark was drawn on the side of the tube at both ambient temperatures. The height difference between those marks was used to calculate the change in volume. A 10 ± 2 mm difference in the column height over a $5 \text{ }^\circ\text{C}$ temperature change in a 150 cm column, indicated a fractional volume change of $(6.7 \pm 1.3) \times 10^{-3}$ per $5 \pm 1.4 \text{ }^\circ\text{C}$, or $(1.3 \pm 0.44) \times 10^{-3} \text{ }^\circ\text{C}^{-1}$. This was a straightforward method to estimate thermal expansion, and it agreed with the quoted value of $0.94 \times 10^{-3} \text{ }^\circ\text{C}^{-1}$ within calculated uncertainties.

4.5. Volatile Content

In order to establish the volatile content of the samples injected into the main experiment, a 200 g sample of oil was left exposed to air for approximately one week (which was comparable to the sample preparation in the main experiment). An empty 2 L soft drinks bottle (made from polyethylene terephthalate) was weighed on a weighing scale with a precision of 0.001 g. The sample was then poured into the bottle and a permeable cap, constructed from absorbent paper towels, was placed into the neck of the bottle to prevent any foamy oil escaping the bottle during the degassing process, whilst allowing gas to escape. The assembled bottle, oil and cap was weighed. Next, the bottle was decompressed to $< 10 \text{ Pa}$, causing the sample of oil to degas rapidly through bubble nucleation. The vacuum conditions were maintained until the rate of bubble nucleation was approximately one per second for a ~ 200 g sample of oil. At this point, it was assumed that the amount of volatile remaining in solution was negligible compared to the amount present before decompression. The sample was then re-equilibrated to atmospheric pressure and quickly

removed from the vacuum chamber and weighed again. This experiment was performed at room temperature (20 ± 2 °C).

The change in measured weight indicated a volatile content of $(5 \times 10^{-4} \pm 0.04)$ wt. % (Table 4.3). Approximately one minute after the first measurement of the degassed oil was taken, the bottle was weighed again and a value of 383.862 ± 0.002 g was obtained, and after a further five minutes, a value of 383.873 ± 0.002 g was obtained. The rapid increase in weight suggested a rapid initial diffusion of gas into the oil, although there may also have been diffusion into the bottle and paper towel.

Table 4.3: Summary of the volatile extraction experiment. The uncertainty in the weight measurements was based on the variation observed in repeat measurements. Given the sensitivity of the weighing scale, the variation could be explained by local air currents.

Item	Bottle	Bottle, Volatile-rich Oil & Cap	Bottle, Degassed Oil, & Cap	Volatile-rich Oil	Volatile Extracted	Weight % of Volatile-rich Oil
Weight /g	34.317	383.987	383.838	349.235	0.149	0.04 %
Uncertainty /g	0.002	0.002	0.002	0.002	0.002	5×10^{-4} %

The manufacturer suggested a maximum volatility of 1.5 % for thermal degassing (based on a 5 g sample held for two hours at 250 °C) rather than degassing through decompression. Thermal degassing of a small sample of AS 100 oil in a thermogravimetric analysis machine indicated a 1 % weight loss after 4.5 hours at 240 °C, which was consistent with the manufacturer's specifications. However, the result from decompressive degassing was favoured over thermal degassing, as it more closely reconstructed the pressure and temperature conditions in the main experiments presented in Chapters 5, 6 and 7.

4.6. Optical Distortions

Observations of spheres within the falling ball viscometry experiment were distorted by refraction at the oil-glass and glass-air interfaces, caused by differences in the refractive indices as well as tube geometry. The sizes of spheres (or bubbles) could still be determined by observing the length of the object in the direction parallel to the tube walls, as no optical distortion occurred in that direction. However, in order to appropriately gauge the distance between bubbles in experiments, and aid in determining bubble sphericity, distortions in the horizontal direction were characterised. A short section of glass tubing,

of the type and diameter to be used in the main experiments, was filled with oil, and a trimmed ruler inserted (Figure 4.5).

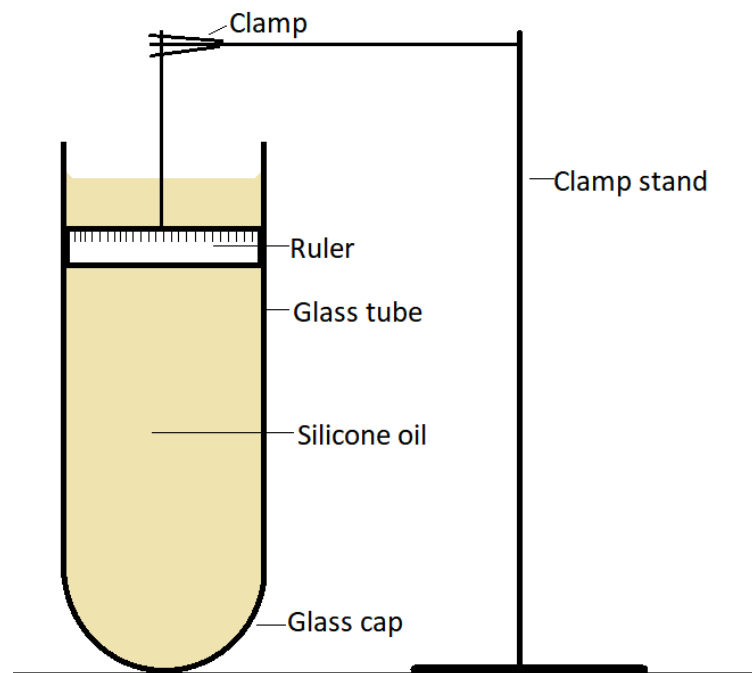


Figure 4.5: Experimental setup for determining optical distortions. The silicone oil has been shaded a pale tan colour here for visual clarity.

A photograph was taken of this setup from a distance of approximately one metre (which was comparable to the distance between the tube and cameras in the main experiment). Additionally, another photo was taken with the ruler in the same place but without the tube and oil in order to compare with the first photograph (Figure 4.6). The separation between each millimetre marking on the two photographs of the ruler was measured in pixels. From this, a profile of the optical distortion (as represented by changes in image scale) could be determined (Figures 4.7 and 4.8).

The experiment was conducted for both 80 mm tubing and 40 mm tubing, because these were the most common types used in the main experiment. For the 40 mm tubing, the process was performed with the camera close to the tube and again with the camera further away to test if the camera placement affected the perceived optical distortion. The “near” measurements were conducted approximately one metre away from the tube while the “far” experiments were conducted approximately two metres away. For the 80 mm tube, the experiment was performed at a distance of approximately 1 m.

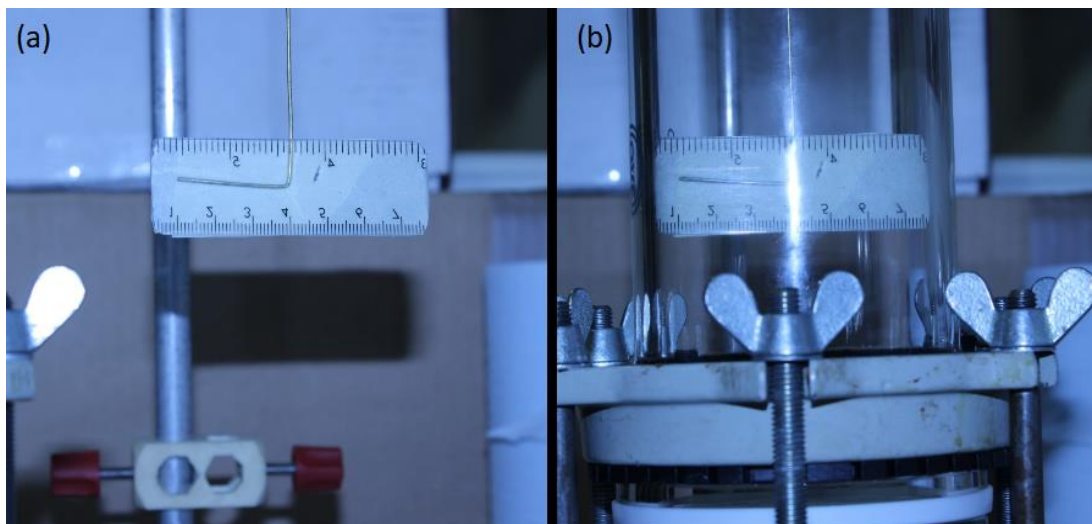


Figure 4.6: Images showing the ruler (a) and the same ruler in the same place, but submerged in oil inside of a glass tube (b).

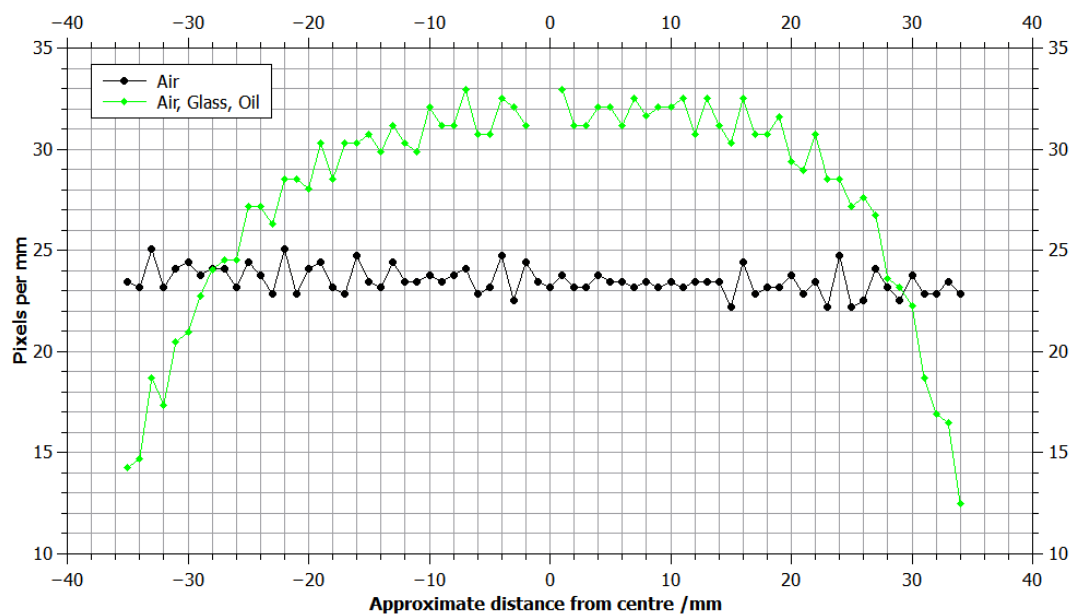


Figure 4.7: Characterisation of horizontal optical distortions in an 80 mm tube. The missing data for "Air, Glass, Oil" between -2 mm and +1 mm was due to reflections on the glass rendering the scale unreadable (Figure 4.6(b)).

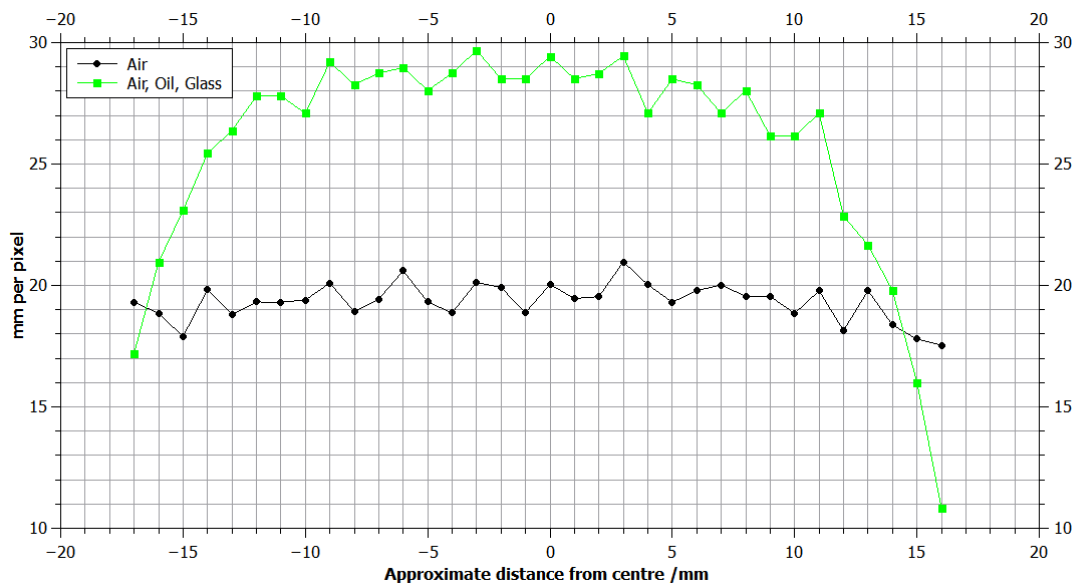


Figure 4.8: Characterisations of optical distortions in a 40 mm tube.

Across most of the width of the tubes, the presence of air, glass and oil increased the number of image pixels per millimetre (which had the appearance of stretching what was seen inside the tube) but, at the edges of the tubes the number of pixels per millimetre was lower (compressing what was seen). A notable difference, however, was the extent to which this took place. When the extreme points were neglected (the 5 points nearest the edges for the 40 mm tube and the 10 points nearest the edges for the 80 mm tube), the ratio between the baseline scale and the distorted scale can be compared (Table 4.4).

Table 4.4: Summary of the average number of pixels per millimetre for the non-extreme values for different tubes.

Tube	Average Scale in Air /pixels per mm	Average Scale with Glass and Oil /pixels per mm	Ratio Between Baseline and Distortion
80 mm	23.5 ± 0.7	30.5 ± 1.7	1.30 ± 0.08
40 mm (Near)	19.3 ± 0.8	28.2 ± 1.0	1.46 ± 0.08
40 mm (Far)	14.9 ± 0.4	21.3 ± 0.9	1.43 ± 0.07

The 40 mm tubing induced slightly greater distortions than the 80 mm tubing. A negligible difference in the ratio between the baseline and 40 mm (Near), and the baseline and 40 mm (Far) tubes suggested that the distance between the camera and the tube did not change the observed optical distortion. Ultimately, these experiments indicated that narrower tubes produce more prominent distortions of the images of bubbles in the main experiments. The average distortion ratio for bubbles which were not close (5-10 mm) to the edge of the tube are characterised by the last column in Table 4.4.

4.7. Bubble Sphericity

Bubbles were required to be spherical in order to model their vertical ascent correctly, and the properties of the oil contributed to the shape of the bubbles in the main experiments. The sphericity of the bubbles was tested using two methods. Firstly, the height and width of a sample of bubbles was imaged, with lateral optical distortions observed in Section 4.6 taken into consideration. If the bubbles were spherical, then the ratio between the height and width of bubbles would match the measured optical distortions in that part of the tube. The second method was to calculate the Reynolds and Eötvös numbers of every bubble in the main three experiments and compare the values to those found for spherical bubbles of the same Morton number (Figure 2.7).

4.7.1. Height to Width Ratios

For every bubble observed in the main experiments, the optical effects demonstrated in Section 4.6 meant that no bubbles appeared spherical within the imagery, even if they were in fact spherical. The Hadamard-Rybczynski model required that the bubbles are spherical, and so non-spherical bubbles would invalidate the use of the model. All bubble images appeared to be slightly wider than they were high. For the 80 mm tube, the ratio between the size of the millimetre markings in the air photograph and the air-oil-glass photograph (Figure 4.7) was calculated in order to quantify the magnitude of the optical distortion at different points across the width of the tube. The ratio indicated, relative to when there were no distortions (when there was just air between the ruler and the camera), how much wider the millimetre markings on the ruler appeared to be as a result of the optical distortions from the oil and cylindrical glass tube. A quadratic fit was calculated across the central part of the tube in order to characterise the variation in distortion as a function of the position across the central part of the tube (Figure 4.9).

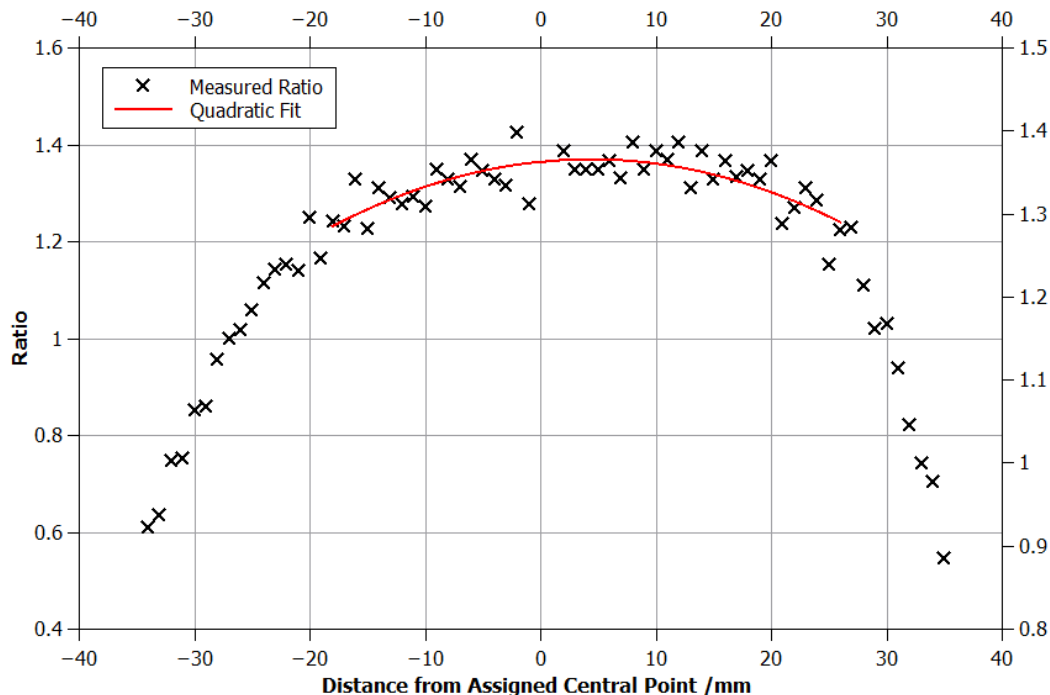


Figure 4.9: Quadratic fit of the central part of the measured distortion ratios of the 80 mm tube.

The central part of the tube (between -18 mm and +26 mm relative to the assigned zero mark on the ruler configuration shown in Figures 4.5 and 4.6) was used as this was where the bubbles in the main experiment were located. The actual distortion across the tube may not have been truly quadratic, however given the variability of the data, a polynomial fit provided an adequate description of how the distortions changed across the width of the tube. It was an empirical description relevant only to the specific tube and silicone oil used in these experiments, not an explanatory model, and so it should not be applied in any other circumstance than the distortion of objects in the experimental tube filled with silicone oil. Higher-order polynomial fits across the full width of the tube either were not characteristic of the data in the central region of the tube, or required polynomials of many terms which were asymmetric around the central axis of the tube, for which there was no physical justification. Given the geometrical symmetry of the tube and lack of indication of heterogeneities (as judged by eye) in the refractive index of the glass in different parts of the tube, higher-order polynomial fits were rejected in favour of a quadratic fit. The quadratic fit had the equation

$$y = 1.36 + 0.00241x - 0.000277x^2 \quad (4.2)$$

where y was the ratio between the size of a 1 mm marking in the air photograph and the air-oil-glass photograph while x was the position in mm along the ruler, relative to the assigned central point. The assigned central point was at approximately the 4 cm marking

on the ruler (Figure 4.5), however the position of the zero point was not at the central point of the tube. To take this into consideration, the location of the maximum was calculated (4.35 mm) and the fit modified such that variable x referred to the distance in mm from the central point of the tube (Equation 4.3).

$$y = 1.36 + 0.00241(x + 4.35) - 0.000277(x + 4.35)^2 \quad (4.3)$$

The expected height to width ratio of a given bubble in the tube was calculable from the position of the bubble in the tube using Equation 4.2. The modelled value was then compared with the observed height to width ratio for each bubble. The modelled ratio and the observed ratio would agree for spherical bubbles. For the seventeen bubbles from the pseudo-infinite experiment which were sampled for this, all observed and predicted ratios between height and width agreed within uncertainty (Table 4.5, Table 4.6 and Figure 4.10). The uncertainty of the observed ratio was calculated from the minimum and maximum possible ratios given an uncertainty of 0.6 pixels in the measurement of both the height and width.

Table 4.5: Observed ratio of bubble height to bubble width. Intermediate calculations and position data are in the supplemental data (Section 10.2).

Bubble Number	Bubble Height / mm	Bubble Width / mm	Observed Ratio between Height and Width	Minimum Ratio	Maximum Ratio
1	20	26	1.300	1.233	1.371
2	15	21	1.400	1.308	1.500
3	16	22	1.375	1.289	1.468
4	14	19	1.357	1.260	1.463
5	11	15	1.364	1.241	1.500
6	11	15	1.364	1.241	1.500
7	9	13	1.444	1.292	1.619
8	11	15	1.364	1.241	1.500
9	18	24	1.333	1.258	1.414
10	14	20	1.429	1.329	1.537
11	14	20	1.429	1.329	1.537
12	12	16	1.333	1.222	1.456
13	9	13	1.444	1.292	1.619
14	10	14	1.400	1.264	1.553
15	9	12	1.333	1.188	1.500
16	10	14	1.400	1.264	1.553
17	9	12	1.333	1.188	1.500

Table 4.6: Observed and measured ratios between the height and width of bubbles.

Bubble Number	Observed Ratio	Distance from Central Axis / mm	Modelled Ratio	Residual
1	1.300	-3.5	1.362	0.062
2	1.400	-2.8	1.363	-0.037
3	1.375	-3.8	1.361	-0.014
4	1.357	-1.4	1.365	0.008
5	1.364	-3.6	1.362	-0.002
6	1.364	-1.2	1.365	0.001
7	1.444	0.5	1.365	-0.079
8	1.364	-4.1	1.360	-0.003
9	1.333	-2.4	1.364	0.030
10	1.429	1.8	1.364	-0.064
11	1.429	-1.8	1.364	-0.064
12	1.333	-1.1	1.365	0.032
13	1.444	-4.9	1.359	-0.086
14	1.400	-8.8	1.344	-0.056
15	1.333	-6.9	1.352	0.019
16	1.400	-3.9	1.361	-0.039
17	1.333	-3.1	1.363	0.029

The observed and modelled ratios matched well and the magnitude of the residuals was smaller than the magnitude of the experimental uncertainties (Figure 4.10). Further, there was no statistically significant correlation (Pearson's $R = 0.1522$, $p = 0.5598$) between the modelled ratio and the residual between the modelled and observed ratios, indicating that the quadratic model for generating the modelled ratios appropriately described the optical distortions across a range of distances from the central axis.

Comparisons between observed and modelled optical distortions were not carried out for the 40 mm tube, as it was not expected that the tube diameter would measurably affect bubble shape given the size of bubbles measured in Chapter 5, 6 and 7.

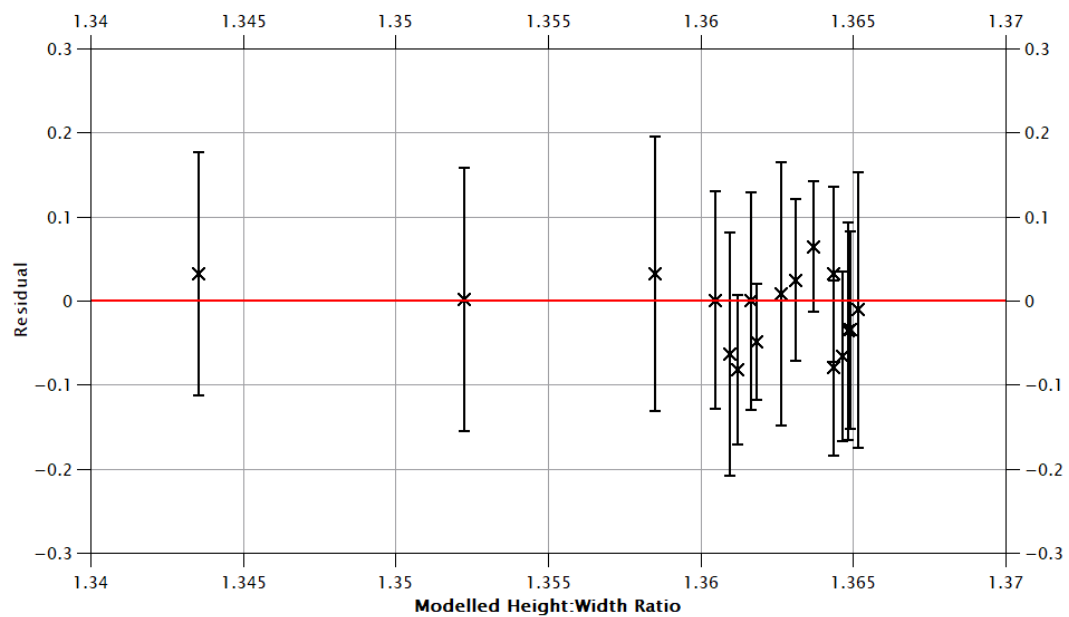


Figure 4.10: Residual between the modelled and observed height:width ratios against the modelled height:width ratio. In all cases, the experimental uncertainty was greater than the magnitude of the residual.

4.7.2. Dimensionless Number Analysis

For every bubble measured in the main experiment, it was possible to calculate the Reynolds and Eötvös numbers which, when plotted against each other, may be used to establish if those bubbles should be spherical based on published regime diagrams (Clift et al., 1978). The theoretical rise speed was used for the characteristic speed in the Reynolds number calculation as the observed speed of many bubbles was influenced by bubble-bubble interactions which were not anticipated to affect the shape of bubbles. The Reynolds and Eötvös numbers of all bubbles measured in the main bubble grouping configurations (i.e. single bubbles and bubbles in dilute and dense groups) indicated that those bubbles were in the spherical regime (Figures 4.11).

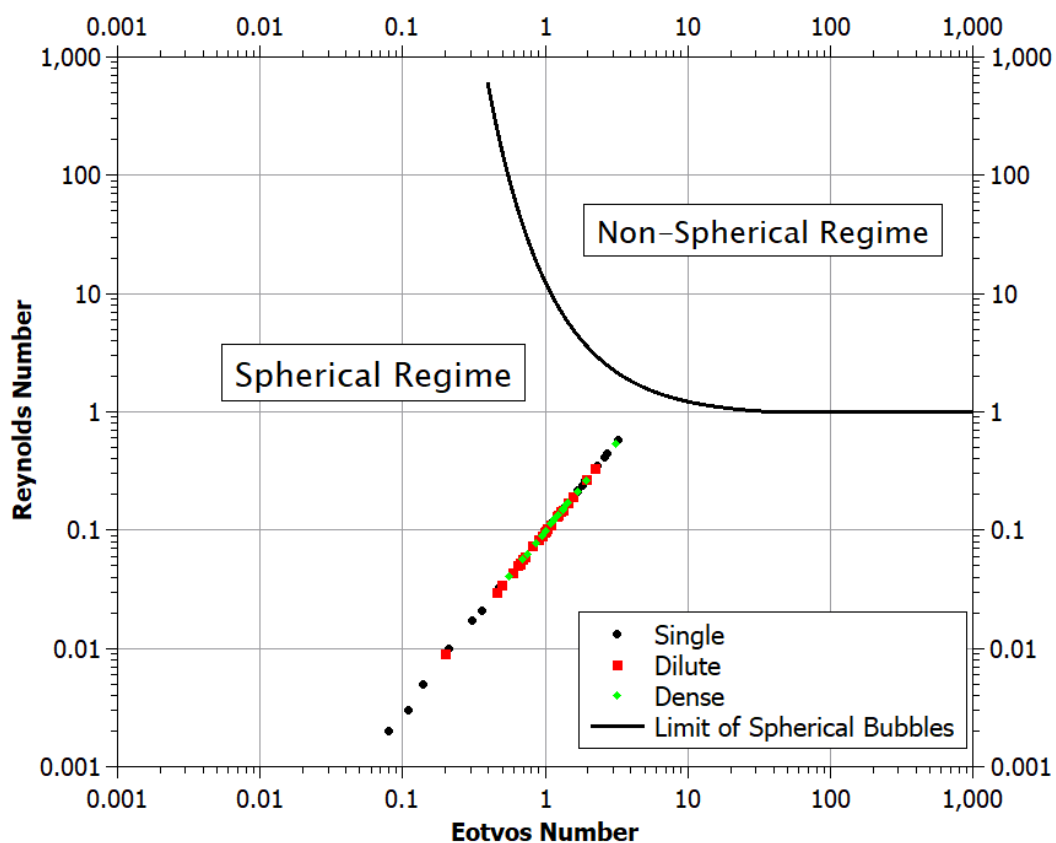


Figure 4.11: Shape regime plot for bubbles in the pseudo-infinite tube. The black line indicates the limit of spherical bubbles such that bubbles below the line were in the spherical regime. The curve was determined empirically from the boundary between spherical and non-spherical bubbles shown in Figure 2.2. Note that both the horizontal and vertical scales are logarithmic.

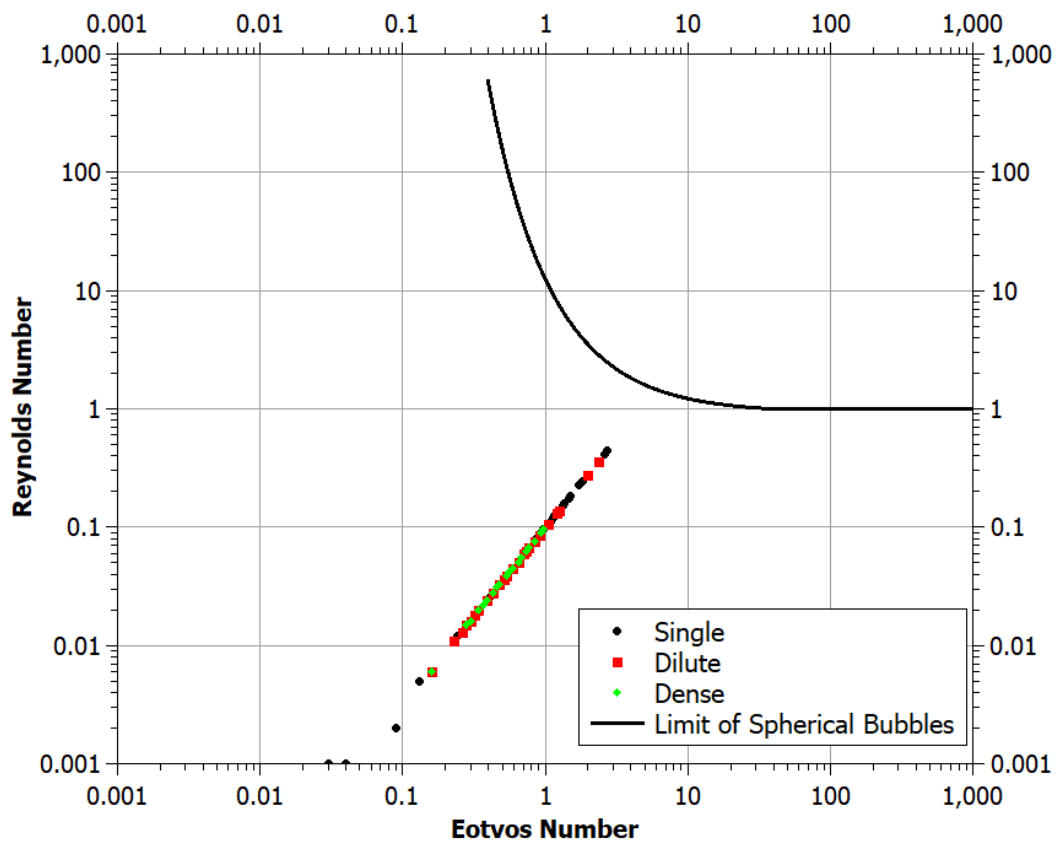


Figure 4.12: Shape regime plot for the bubbles in the constrained tube experiments.

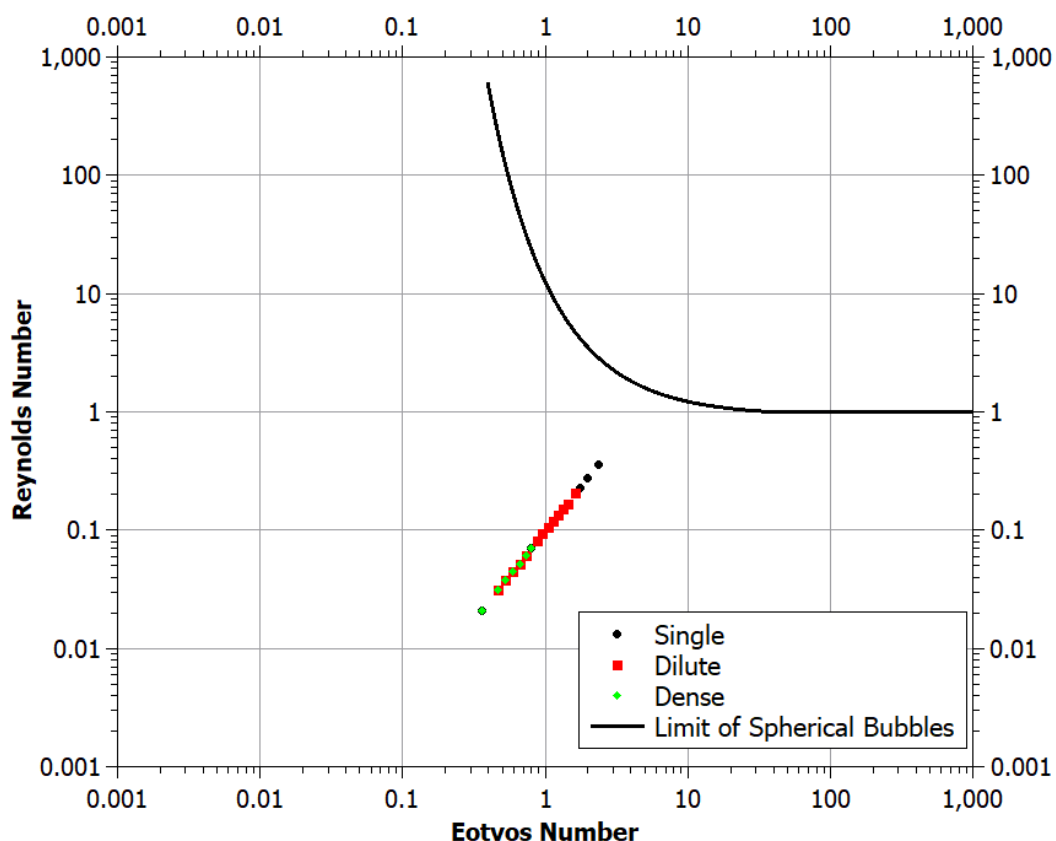


Figure 4.13: Shape regime plot for the bubbles in the inclined tube experiments.

4.8. Summary

The oil characterisation experiments demonstrated some variation between the manufacturer's specifications and measured values. In most cases, the discrepancy was small (Table 4.5). In instances where the measured values disagreed with the manufacturer's values, the measured values were preferentially used as the discrepancies may be due to contamination or degradation of the oil, as well as imprecision in the manufacturer's values. Analysis of the dimensionless numbers of the bubbles in single, dilute group and dense group configurations that were modelled using the Hadamard-Rybczynski equation in Chapter 5, 6 and 7 indicated that those bubbles were in a spherical shape regime. Further, the height to width ratio of a sample of imaged bubbles in the pseudo-infinite tube was measured and compared with a model for the height to width ratio. The model was generated from the observed optical distortions. In the sample of bubbles observed, the expected distortion matched the observed distortion within experimental uncertainty, further supporting the assertion that the bubbles used were spherical. As the bubbles were determined to be spherical within the measurement limits

and, any measured deviation from the Hadamard-Rybczynski model cannot be explained by non-sphericity of bubbles.

Table 4.7: Summary of the findings of this chapter, the measured results were the results to be used for the analysis of data in the main experiments.

Oil property	Manufacturer's Specification	Measured Result	Note
Density	Approximately 0.99 g cm^{-3} at $25 \text{ }^\circ\text{C}$, calculated to be 1.005 g cm^{-3} at $19.5 \text{ }^\circ\text{C}$.	$0.9876 \pm 0.0051 \text{ g cm}^{-3}$	Measurement at $19.5 \text{ }^\circ\text{C}$.
Viscosity	Approximately $100 \text{ mm}^2 \text{ s}^{-1}$, implying 0.101 Pa s .	$0.143 \pm 0.020 \text{ Pa s}$	Measurement at $25 \text{ }^\circ\text{C}$.
Compressibility	$1 \times 10^{-9} \text{ m}^2 \text{ N}^{-1}$	$< 7 \times 10^{-9} \text{ m}^2 \text{ N}^{-1}$	No observed change in height of the oil in the tube with pressure.
Thermal Expansion	$0.94 \times 10^{-3} \text{ K}^{-1}$	$(1.3 \pm 0.44) \times 10^{-3} \text{ K}^{-1}$	
Volatile Content	" $< 1.5 \%$ "	$(4 \pm 0.05) \times 10^{-2} \%$	Manufacturer used thermal degassing, whereas measurements used decompression.
Optical Distortions	No data, as specific to experiments.	Figures 4.7 and 4.8, Equation 4.3 for the 80 mm tube.	

5. Bubbles in Pseudo-infinite Fluids

Bubble behaviour can be described both qualitatively and quantitatively. Qualitative description comprised observation and categorisation of features seen within the experiments while the quantitative data were based on measurements of the bubbles' physical properties, specifically, their size and rise behaviour.

5.1. Injection

Upon opening the solenoid valve, a pulse of approximately 0.5-2 ml of un-degassed silicone oil was introduced into the experiment via the injection needle. At this point, only a small number (typically between 10 and 100) of very small ($\ll 1$ mm diameter) bubbles could be observed by eye in the experiment. There was a pressure difference of approximately 0.9 atmospheres on either side of the solenoid valve, so the oil was forced through the injection needle at a speed much greater than the natural rise speed of the bubbles within it. Upon injection into static oil, the inertia of this fast-moving fluid was largely dissipated within 10 cm of the needle tip, as indicated by the movement of the very small bubbles, which had negligible rise speed. The movement of oil due to injection therefore had a negligible effect on measurements made higher up in the experimental apparatus. Additionally, upon injection into the lower pressure environment, some of the volatiles dissolved in the oil nucleated into bubbles. The size and quantity of these bubbles was observed to be affected by the pressure at the top of the experiment. At lower pressures, more bubbles nucleated and those bubbles tended to be larger. A greater number of bubbles was expected at lower pressures as the Gibbs free energy for nucleation was inversely proportional to the volatile supersaturation pressure squared (Section 2.3.1).

The duration of the injection dictated how many bubbles were produced in total, but there was no apparent increase in bubble number density for longer duration injections. Instead, a sustained column of bubbles between the needle tip and the top of the oil was produced for a longer period of time. Short injections of less than one second resulted in the emission of bubbles from the injection needle for several seconds to a minute after the solenoid valve has closed. The rate of bubble emission after valve closure was much lower than when the valve was open. The closed-valve bubble emissions were interpreted as the escape of bubbles that nucleated in the tube between the valve and needle tip. After injection, the bubbles rose through the tube and after approximately 2-3 minutes, most of the bubbles had completely passed through the tube.

5.2. General Bubble Behaviour

As bubbles rose buoyantly relative to the surrounding oil, their rise speed corresponded to their size. The rise speed of smaller bubbles, where the Reynolds number was less than 1, was modelled using the Hadamard-Rybczynski model. This was referred to as the buoyant rise speed, where the dominant control on the bubble's speed relative to the tube walls was buoyancy. Quantitative analysis of bubbles with Reynolds numbers greater than 1 was beyond the scope of this work as their motion cannot be adequately described by the Hadamard-Rybczynski equation. Observations showed that the vast majority of bubbles rose vertically within the conduit with larger bubbles rising faster due to a larger buoyancy force, however this was not always the case and there were instances where this behaviour was not observed. Initially, small bubbles in isolation were studied as a baseline measurement.

5.3. Single Bubbles

The simplest type of bubble interaction was no interaction at all. Observations of single bubbles – bubbles that were not near the walls of the tube or other bubbles – also allowed validation of the use of the Hadamard-Rybczynski model in this experiment, as the theoretical rise speed indicated by this model should be consistent with the measured rise speed in the tube, assuming static liquid conditions.

A sample of 25 bubbles was selected from the videos of the experiments and their positions were recorded over time (varying from a minimum of 38 frames, maximum of 225 frames and average of 120 frames) in order to measure their rise speed (referred to as 'measured speed'). This was taken as the average speed between the initial and final positions of the bubbles. Bubble size was measured in order to model their rise speed according to the Hadamard-Rybczynski equation (referred to as 'theoretical rise speed'). All distances were initially measured in pixels but then converted to an absolute length via a scaling factor where a known length (the tube diameter) was measured in pixels.

Comparison of the measured and theoretical rise speed showed that, for single bubbles in a pseudo-infinite fluid, the Hadamard-Rybczynski equation, which accounted for internal gas circulation arising from fluid movement at the liquid-gas interface, accurately predicted the measured bubble rise speed from the measured bubble diameter across a range of bubble sizes (Figure 5.1). There was strong agreement between the theoretical and measured rise speeds with a high, and statistically significant, correlation between these values (Pearson's $R = 0.9867$, $p < 0.0001$).

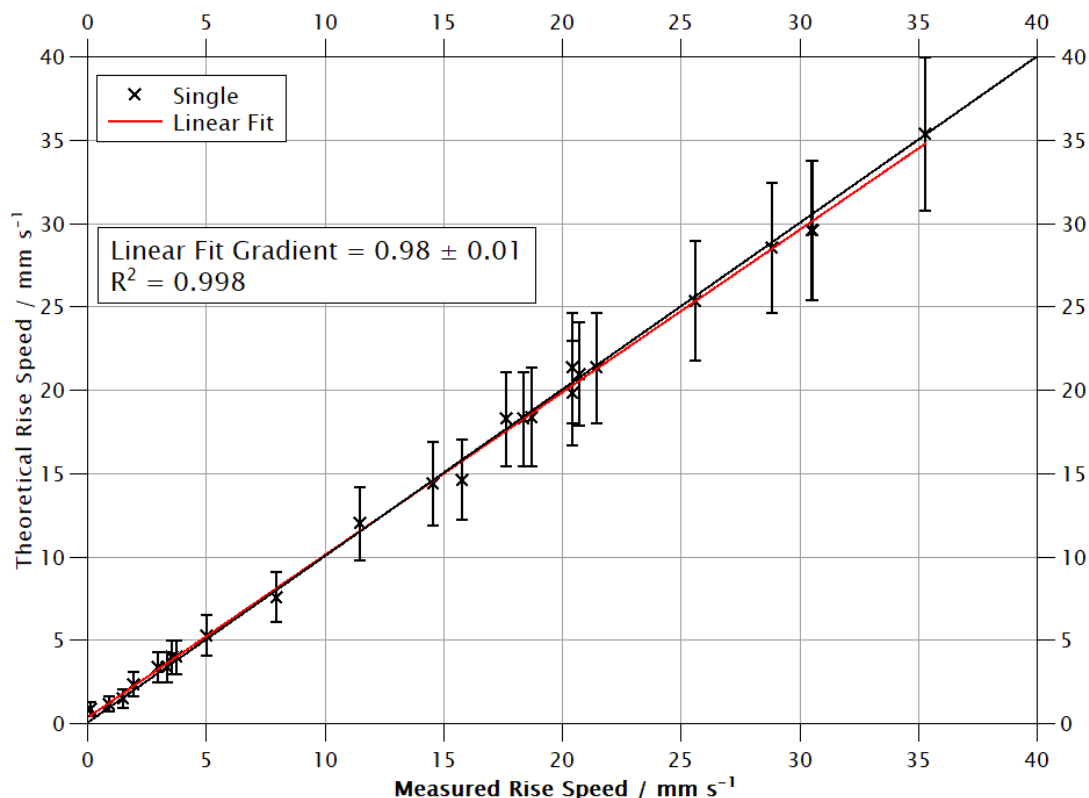


Figure 5.1: Measured versus theoretical rise speed for single bubbles. The black line marks where theoretical and measured values are equal, so results falling on this line represent values where the Hadamard-Rybczynski model accurately describes those bubbles' motion.

The average residual between the measured and theoretical rise speed was $-0.02 \pm 0.11 \text{ mm s}^{-1}$ (the uncertainty here was taken as the standard deviation, as the residuals were normally distributed; Table 10.1) indicating very close alignment between theory and measurements. There was a moderate negative (Pearson's $R = -0.47$), but not statistically significant ($p = 0.0180$, note that the boundary of significance and non-significance is taken to be $p = 0.01$ here and in all other tests of statistical significance presented henceforth) correlation between the theoretical rise speed and residual, indicating no systematic variation of residual with bubble size. In all but one bubble, the magnitude of the residual was less than the magnitude of the experimental uncertainty (Figure 10.1), indicating agreement between measurement and theory. The linear fit between the measured and theoretical values had a gradient of 0.98 ± 0.01 with $R^2 = 0.998$ further indicating a very strong agreement between the measured value and the theoretical value.

In addition to the average speed across the measurement period, variations in speed were assessed by tracking the positions of bubbles in multiple frames and using the

average bubble speed between each frame of the video. Calculating the inter-frame speed facilitated further examination of the bubbles movement by showing variations in the speed over the measurement time (Figure 5.2). Measured variations were likely caused by variations in the identification of the bubble centres, although it was possible that some fluctuations in speed could occur due to the disturbance of the oil caused by the motion of other bubbles. As these bubbles were categorised as single bubbles, the influence of oil motion was anticipated to be minimal. The tracking of bubbles was done manually and the software used recorded the selected position coordinate to the nearest 0.01 pixel width (which were not truncated to the nearest integer value), there was also variability in the recorded position due to human variability in judging the centre of the bubble. The values were not truncated to the nearest integer as, in some cases, the centre of the bubbles was judged to be approximately halfway across a particular pixel and for very small bubbles, a half-pixel difference in the recorded position would result in the measured bubble speed being much greater, or less, than the actual speed of that bubble in the tube. The measured speed values for smaller bubbles, which move more slowly, appear to be more distorted as the magnitude of variations in the value of the measurements was larger, although the average speed across the measurement period was still in agreement with the Hadamard-Rybczynski model. The measured bubble speeds maintained a consistent average over the measurement period (Figures 5.2, 5.3, 5.4), which showed that these bubbles travelled at a constant speed. The bubbles shown in Figure 5.2, 5.3 and 5.4 are for bubbles with diameters of 1.02 mm, 1.55 mm and 2.43 mm respectively. That range of bubble diameters spans the majority of bubble sizes measured in the experiments presented in this chapter, as well as Chapters 6 and 7.

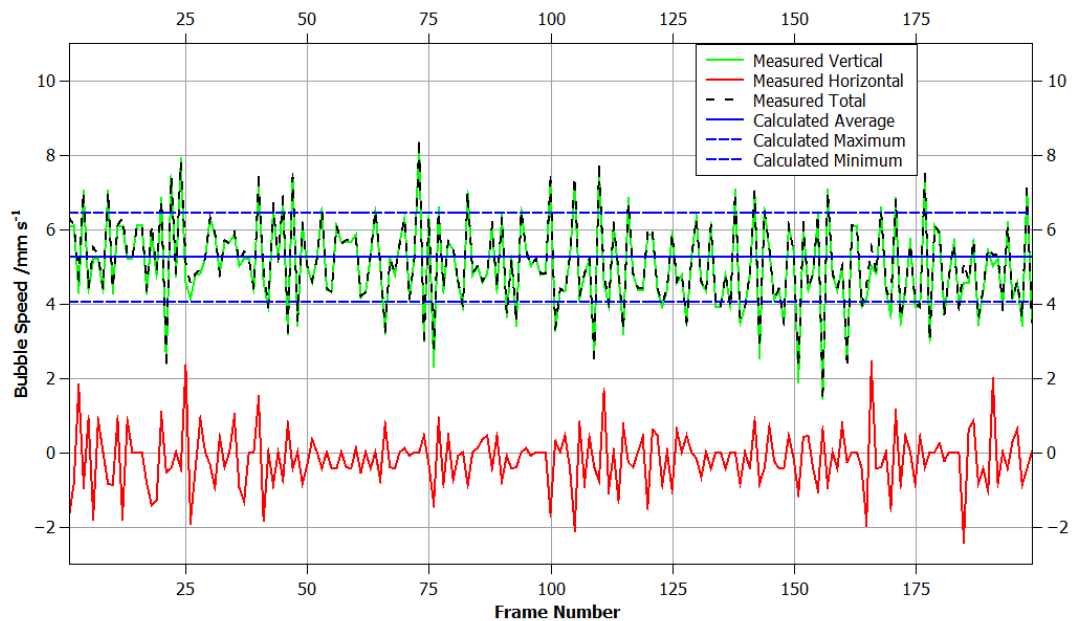


Figure 5.2: An example of the motion of a bubble in a pseudo-infinite experiment from RUN15_LOW3 PS1. The green line represents vertical speed, the black dashed line shows the total speed, the red line shows measured horizontal speed, the blue line represents the theoretical speed as described by the Hadamard-Rybczynski model, with the blue dashed line indicating the uncertainty values.

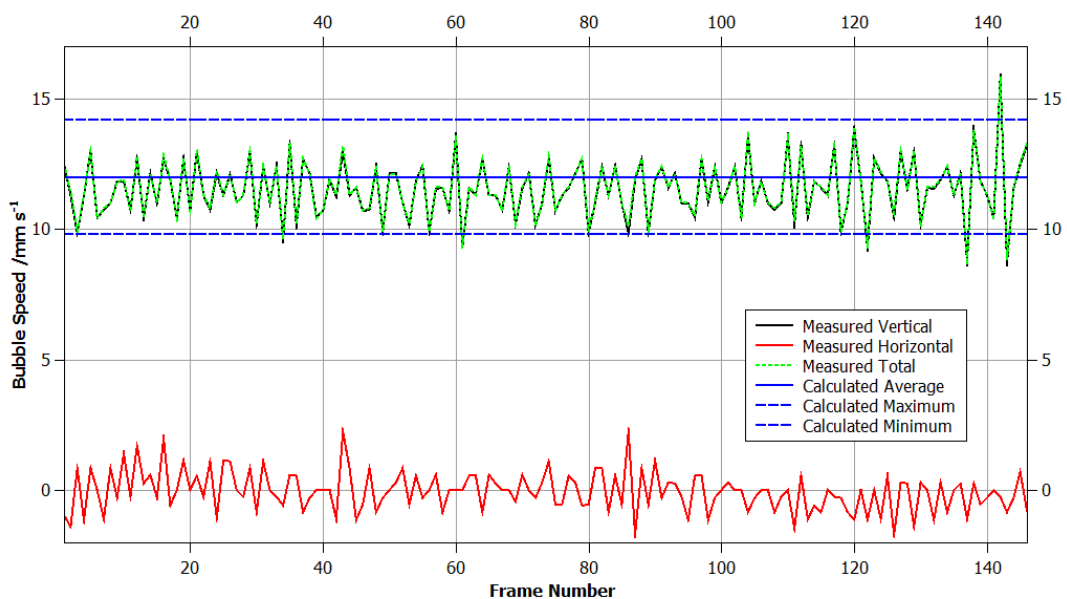


Figure 5.3: A bubble (RUN06_MID PS13) travelling through pseudo-infinite fluid. As with Figure 5.2, there was very close agreement with the Hadamard-Rybczynski model and no evidence of notable lateral motion.

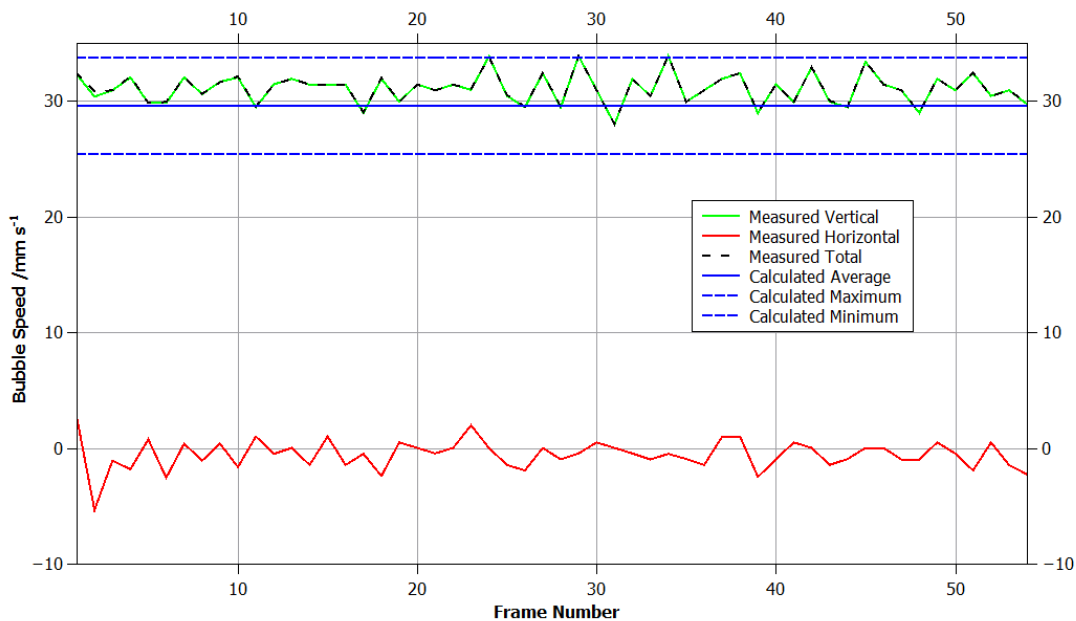


Figure 5.4: A single bubble (RUN06_MID PS12) travelling through a pseudo-infinite fluid. As with Figures 5.2 and 5.3, there was very close agreement with the Hadamard-Rybczynski model and no evidence of notable lateral motion.

There was consistent agreement with the model as the measured vertical data (green line) fell within the theoretical prediction based on the bubble's size (solid blue line bounded by the dashed blue lines). In Figure 5.2, the lateral speed had a mean value of $-0.18 \pm 0.05 \text{ mm s}^{-1}$ indicating a measurable lateral movement across the observation time. This apparent lateral movement indicated that, relative to the camera, the bubble was travelling 0.036 radians from vertical. However, comparison of the apparent lateral motion of the bubble with the apparent tilt of the tube (-0.034) radians showed that this apparent lateral motion was almost entirely accounted for by the camera not being aligned vertically. The measurement of the bubbles' displacement used both the horizontal and vertical change in position, so a correction for tilt was not necessary for single bubbles.

5.3.1. Summary of Single Bubbles

Repeated measurements of bubbles of varying sizes travelling in isolation through a static, pseudo-infinite fluid have shown that, for sufficiently small bubbles, the model could appropriately predict the measured rise speed. There was agreement with the model within uncertainty values, except for the smallest point, indicating that uncertainty estimates were of an appropriate magnitude. The smallest point may not have been in focus, causing it to appear larger than it actually was.

The Hadamard–Rybczynski model therefore provided robust values of expected rise speed for small (less than approximately 3 mm diameter) bubbles travelling in isolation in a static, pseudo-infinite fluid. The Hadamard–Rybczynski model forms the theoretical basis against which all forthcoming discussion of bubble-bubble and bubble-wall interactions will be referenced.

5.4. Bubbles of Significantly Differing Size

The next simplest type of bubble interaction, after single bubbles, was between two bubbles. It was uncommon to observe two bubbles of a similar size within less than five bubble diameters of each other while otherwise in isolation from all other bubbles. Paired interactions of similar-sized bubbles were therefore insufficiently frequent to significantly affect overall bubble behaviour in the pseudo-infinite case. However, nearly every experimental run saw at least one very large (> 10 mm diameter) bubble produced before or during the emission of the smaller (~ 1 mm diameter) bubbles. These larger bubbles visibly affected the motion of smaller bubbles (Figure 5.5) and appeared, in some cases, to temporarily increase the rise speed of smaller bubbles.

The passage of a large bubble (> 5 mm diameter) through the tube altered the paths of smaller neighbouring bubbles. The exact style and extent of the path alteration depended on the relative position of the bubbles; however, a narrower lateral separation resulted in more prominent effects. Bubbles which were approximately the same height in the tube as the larger bubble at a given time were observed to move laterally away from the larger bubble before returning to approximately their original position (Figure 5.5).

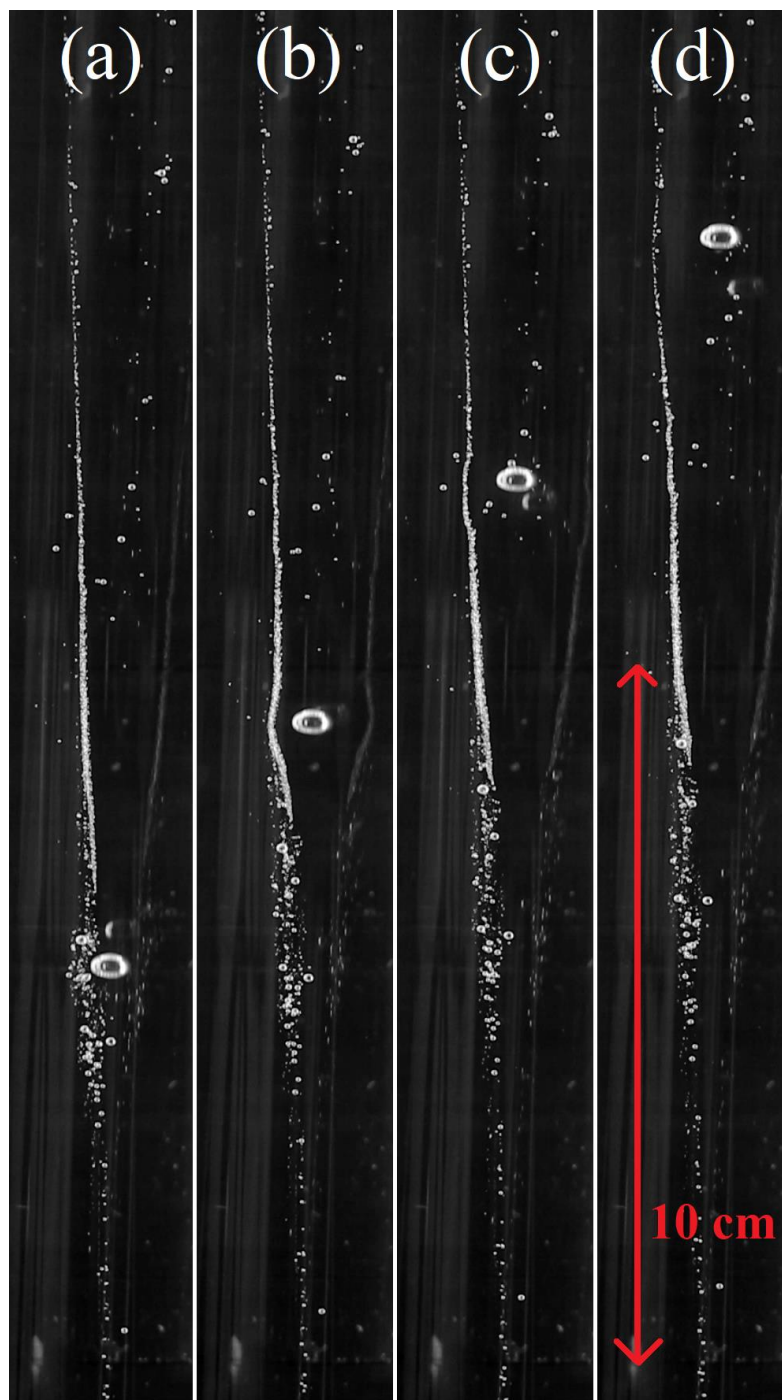


Figure 5.5: A large bubble (approximately 5 mm tall) interacting with many smaller bubbles at varying separation distances. (a) An extended line of very small ($\ll 1$ mm diameter) bubbles was left in the wake of a very large bubble (~ 50 mm diameter) at the start of experiment (not shown). These bubbles were still rising in the wake of that bubble, but were moving much slower than the larger bubble below. In (b), the larger bubble was at the same height as the lower portion of the stream of bubbles. A significant bend in what was originally a near straight line of bubbles was observed. This was due to the passage of the larger bubble. In (c) a similar effect was seen, however the bubble stream was further away from the larger bubble and so the effect was much reduced. Similarly, in (d) the effect was barely visible. The time interval between each frame shown was 0.4 seconds.

Small bubbles overlying the larger bubble were initially accelerated vertically as the larger bubble approached from underneath at a greater speed, pushing the overlying oil upwards. When the larger and smaller bubbles were very close (approximately 1-2 mm separation), the smaller bubble rapidly moved laterally while the larger one overtook it (Figure 5.6). When the smaller bubble was no longer above the larger one, it rapidly decelerated over a duration of approximately two seconds towards its buoyant rise speed. The process of a larger bubble overtaking a smaller one in this manner had the effect of temporarily raising the smaller bubble through the tube at a speed much greater than its buoyant rise speed for a short period of time (Figures 5.7 and 5.8).

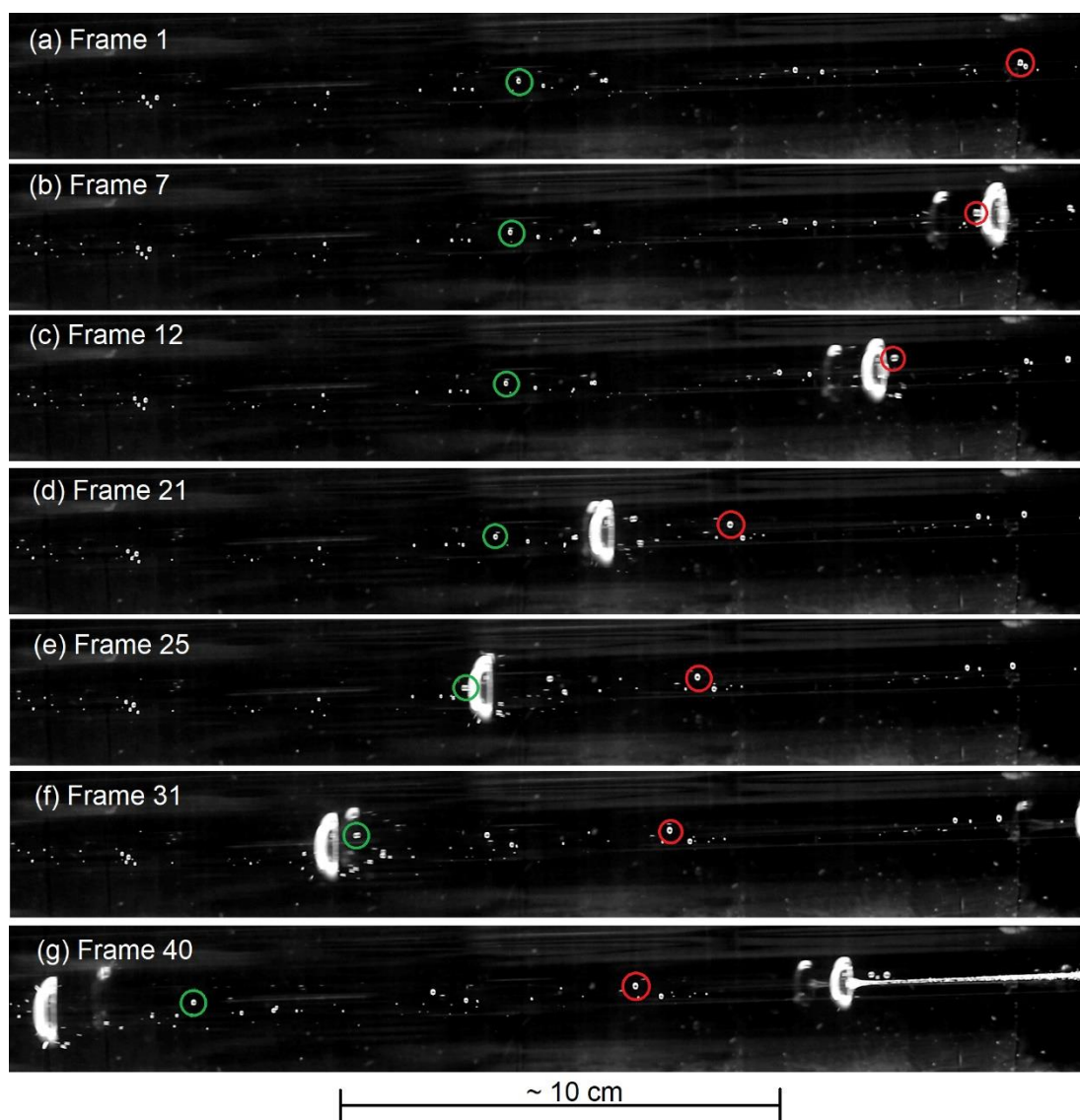


Figure 5.6: Example images of two interactions between a small bubble and a much larger bubble from RUN03_LOW3. The bubble circled in red is RUN03_LOW3 PS1 (Figure 5.7) and the bubble circled in green is RUN03_LOW3 PS3 (Figure 5.8).

As with single bubbles, several examples of this kind of behaviour were selected based on their clarity of observations and the smaller bubble's position tracked over a short time period (in this case 40 frames, equal to 1.6 s). Figures 5.7 and 5.8 demonstrate two instances of small bubbles interacting with much larger bubbles.

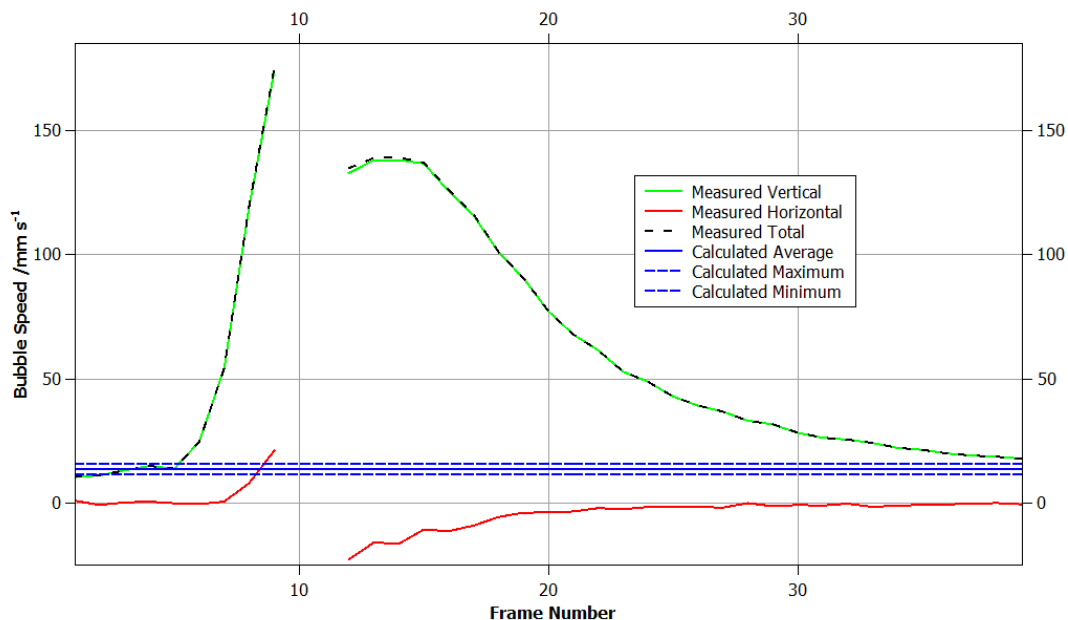


Figure 5.7: The measured versus theoretical rise speed of a small bubble (RUN03_LOW3 PS1) interacted with a much larger bubble which subtended and then overtook the smaller bubble. The gaps in the data were from frames where the smaller bubble were not clearly visible on the image, so data were not collected.

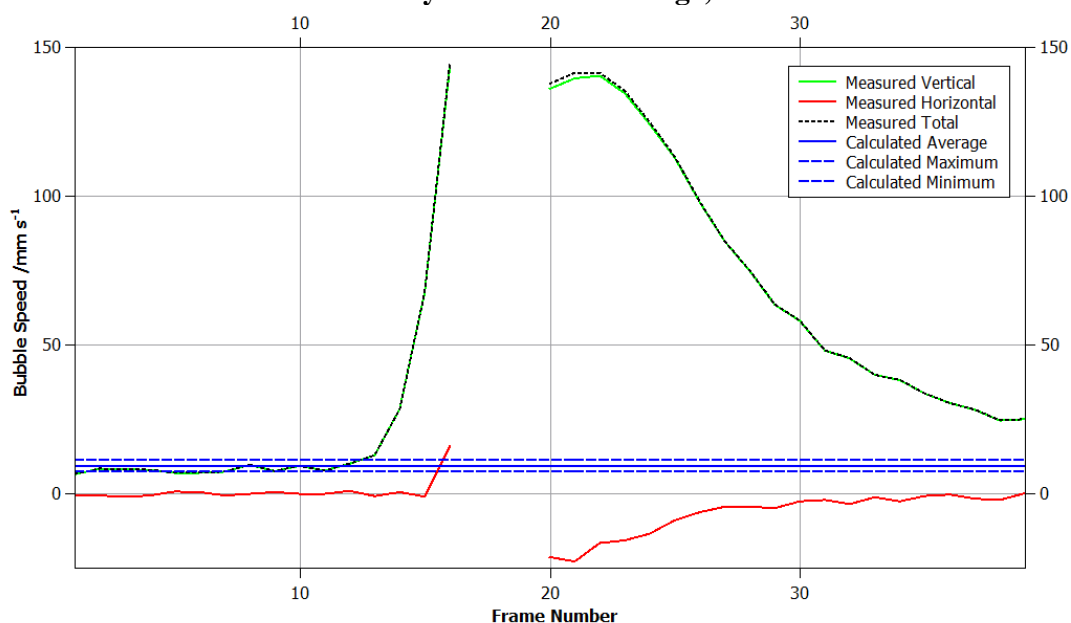


Figure 5.8: A further example of a small bubble (RUN03_LOW3 PS3) interacting with a larger one. The deceleration of this bubble is not shown as it moved out of the field of view of the camera.

These instances exhibited the same pattern of behaviour. Firstly, the speed of the smaller bubble, when travelling in isolation, agreed well with the Hadamard–Rybczynski model. As the larger bubble approached from underneath the bubble rapidly accelerated vertically to at least an order of magnitude greater than its normal rise speed. After the vertical acceleration began, there was a small lateral acceleration, but the magnitude of the acceleration is much less than in the vertical direction. At this point, the smaller bubble ceased to be visible for approximately 3 to 5 frames (0.12 to 0.20 seconds). The vertical speed of the bubble was lower than the speed immediately before it stopped being visible, but it still accelerated for a further 3 to 5 frames, at which point it vertically decelerated towards the rise speed of a single bubble (although this was not observed in the above examples due to the bubbles leaving the field of view of the camera). The lateral speed of the bubble after it became visible again was in the opposite direction from its prior lateral acceleration, but of a comparable magnitude. The lateral speed also returned towards zero once the larger bubble overtook the smaller one.

The features of the smaller bubble's motion can be interpreted through the motion of the oil around the larger bubble. As the larger bubble moved vertically, it pushed oil upwards and outwards. The effect on the surrounding oil was greater nearer to the bubble (Figure 5.5). As it approached the smaller bubble, the smaller bubble's speed relative to the tube wall was increasingly dominated by the speed of the oil from the larger bubble rather than its speed relative to the oil. The speed increased non-linearly as the bubble separation reduced (Figures 5.7 and 5.8). When the two bubbles were almost touching (separation distance approximately equal to the diameter of the smaller bubble), the smaller bubble was moved laterally by the lateral moving oil. The camera could not record motion in the direction away from the camera, so all lateral motion appeared to be perpendicular to that. When the lateral motion began, the larger bubble began to overtake the smaller one. At this point the smaller bubble's motion was at its greatest. This was indicated in Figures 5.6 and 5.7, as well as the images of those bubbles in the videos (e.g. Figure 5.5), where the bubble appeared to be blurred as it moved too quickly for the camera to properly image it. The disappearance of the bubbles in the videos was mainly due to the speed of the bubble making accurate imaging unfeasible and partially due to the larger bubble obscuring the smaller bubble or introducing large optical distortions. When the larger bubble had fully overtaken the smaller one, the smaller one had a lateral motion towards the original lateral position. When the larger bubble had completely passed, the smaller bubble decelerated slowly as its speed was still largely controlled by the wake of the larger bubble. The consequence of this motion was that the smaller bubble's final

position in the video was higher in the tube than it would have otherwise had no interaction taken place (excess height; Figure 5.9). When the excess height of nine small bubbles was plotted against time, it was evidenced that they were subjected to no downward motion by the downward-moving oil around the larger bubble (Figure 5.9). This indicated that the return flow around the larger bubbles was either highly localised, or slower than the buoyant rise speed of the smaller bubbles. These findings suggest that the passage of large bubbles was an effective method for increasing the outgassing efficiency of a bubbly fluid.

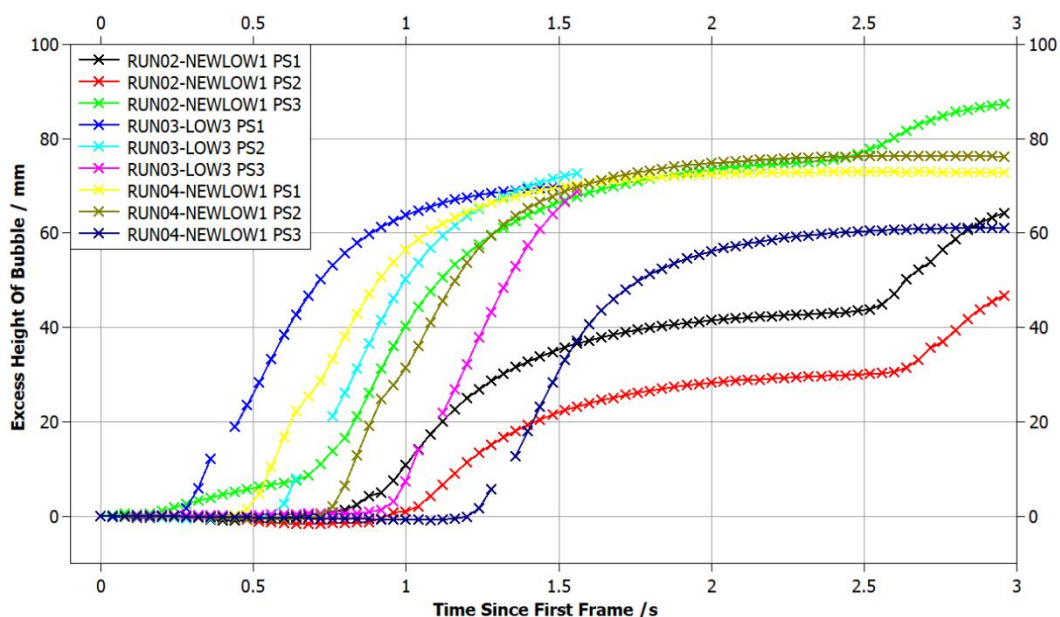


Figure 5.9: The excess height gained by nine smaller bubbles interacting with a much larger bubble. The data gaps are where the bubbles were not visible. The increase in speed for RUN02_NEWLOW1 bubbles was due to another large bubble passing through the tube and interacting with those bubbles.

5.5. Group Behaviour

Group behaviour in this study was taken to mean the effect on the rise speed of more than two bubbles of comparable sizes due to fluid dynamic effects while in close (<5 diameter separation) proximity to each other. For the purposes of studying a range of styles of behaviour, group behaviour was divided into two main forms: dilute columns and dense groups. These classifications did not encompass all styles of groups possible, however the classifications applied to the majority of bubbles within the experiments where group behaviour was sufficiently pronounced to be measurable in the equipment.

Dilute columns are collections of bubbles with a relatively low number density (gas volume fraction of approximately 0.1 % to 5 %) that move vertically as an approximately cylindrically symmetric group (Figure 5.10). The dilute columns tended to have a non-unimodal bubble size distribution and non-uniform number density, meaning that the gas content by volume of a given region within the experiment constantly varied and covered a large range of values. As such, estimates of the gas volume fraction were broad approximations and the classification of a group of bubbles as a dilute column was judged by eye.



Figure 5.10: A sample image from RUN10_MID showing two examples of a dilute column. The cluster of between the two boxes had a bubble number density too great to be considered a dilute grouping, however it also would not have been considered a dense group as this cluster was transient and did not maintain a high bubble number density for a sufficient length of time in order to take measurements.

Dense groups represented the most extreme form of bubble grouping seen in these experiments and feature a sufficiently large number of bubbles within a volume that they mostly obscured the tube wall behind them (Figure 5.11). The gas volume fraction of dense groups was difficult to determine, as many bubbles were not visible; however, they were estimated as being at least 10% gas volume fraction based on visual comparison with other studies with known gas volume fractions from Zenit et al. (2001).

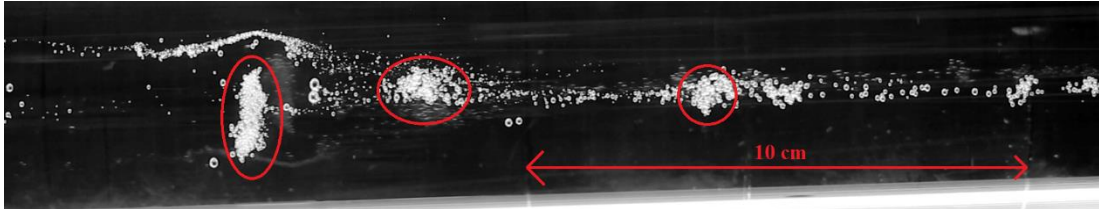


Figure 5.11: Three examples of dense groups from RUN2_LOW2. The direction of motion in this image was right to left. The majority of the bubbles not circled would be considered as being part of dilute groups.

As they moved through the oil, the relative position of individual bubbles in dense groups was often changing such that the group as a whole appeared to have an internal toroidal motion. The topmost bubbles tended to move from the centre of the group, towards its side. The bubbles on the side of the group travelled slightly more slowly than the bulk speed of the group, such that they ended up at the bottom and then migrated towards the centre. This rotational motion was most clearly displayed in groups with very high bubble number density and with very small bubbles, which were usually too small to resolve with the camera, preventing quantitative analysis of the internal toroidal motion within dense groups.

In order to simplify the categorisation of dense groups, only groups where the total number of bubbles stayed approximately constant were measured. This meant that groups that incorporated another group would only be measured after their combination.

5.5.1. Group Formation

One of the most significant observations made in preliminary experiments was that, after injection of volatile-rich oil that nucleated into bubbles, multiple discrete groups of bubbles formed, despite the injection of oil into the base of the experiment being short in duration and had a relatively consistent flow rate, as judged from the motion of the plunger of the syringe. An injection at a constant rate was expected to produce evenly distributed bubbles, however, multiple discrete groups would form after each injection. These groups mainly formed within the first 5-10 seconds after injection, however, smaller groups

appeared to form later than this. In Figure 5.12, for example, a dense group of bubbles broke apart, but a new smaller group emerged from the remnants of the previous one. The second-generation of groups did not have the same toroidal motion observed in the first generation of groups. The experimental apparatus which connected the base plate to the experimental tube prevented direct observation of the formation and early development of the first-generation dense groups (Figure 5.13a). From a different viewing angle (Figure 5.13b), it was possible to view the tip of the injection needle, however the curvature of the glass caused very large optical distortions. Such a viewing angle was sufficient to observe that, although some small bubbles did form prior to emission into the experimental tube, dense groups did not form until after the volatile-rich oil was injected into the experiment.

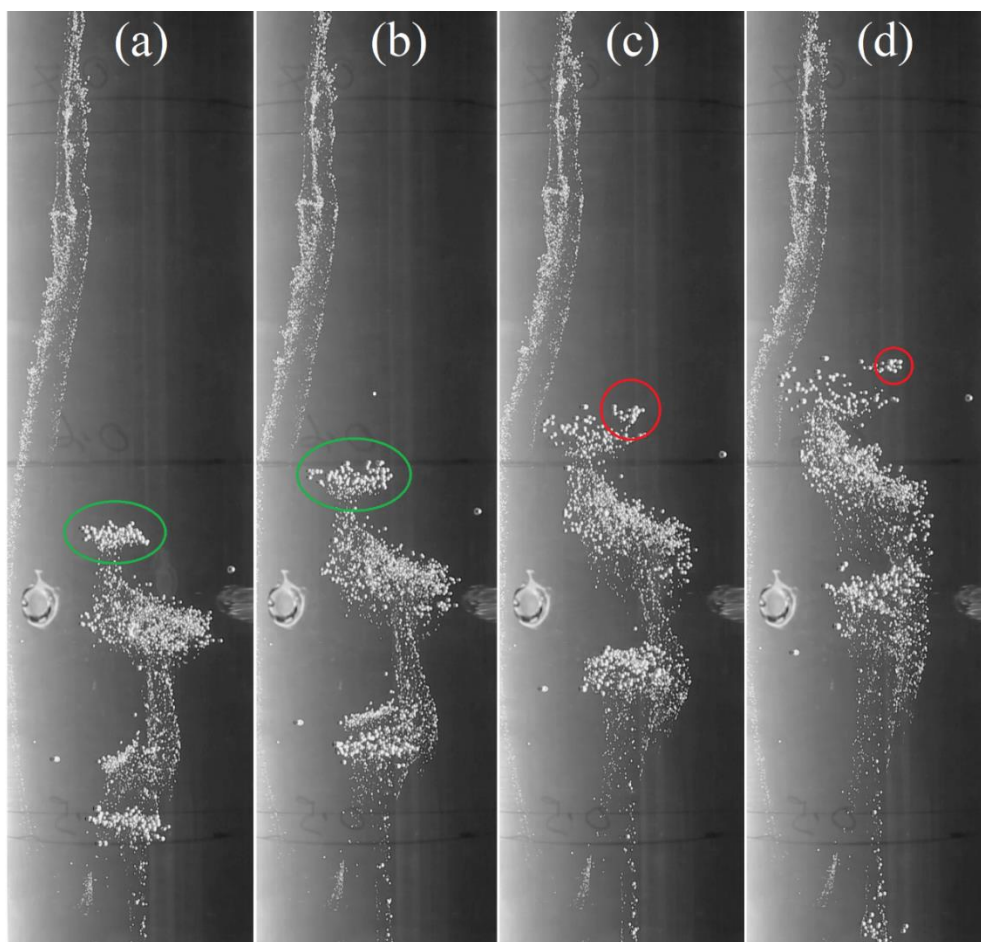


Figure 5.12: Demonstration of preferential formation of groupings of bubbles. In (a) and (b) the larger dense grouping of bubbles can be seen (highlighted in green) breaking apart and becoming less dense. In (c) and (d) a small but dense group of around ten bubbles forms (highlighted in red). The time interval between each frame shown here was 1.2 s. The static round feature in the centre-left of the images was a hole in the tube wall that was repaired with epoxy. Three height markers can be seen which were 10 cm apart and indicated the heights of 0.5 m, 0.6 m, and 0.7 m above the base plate.

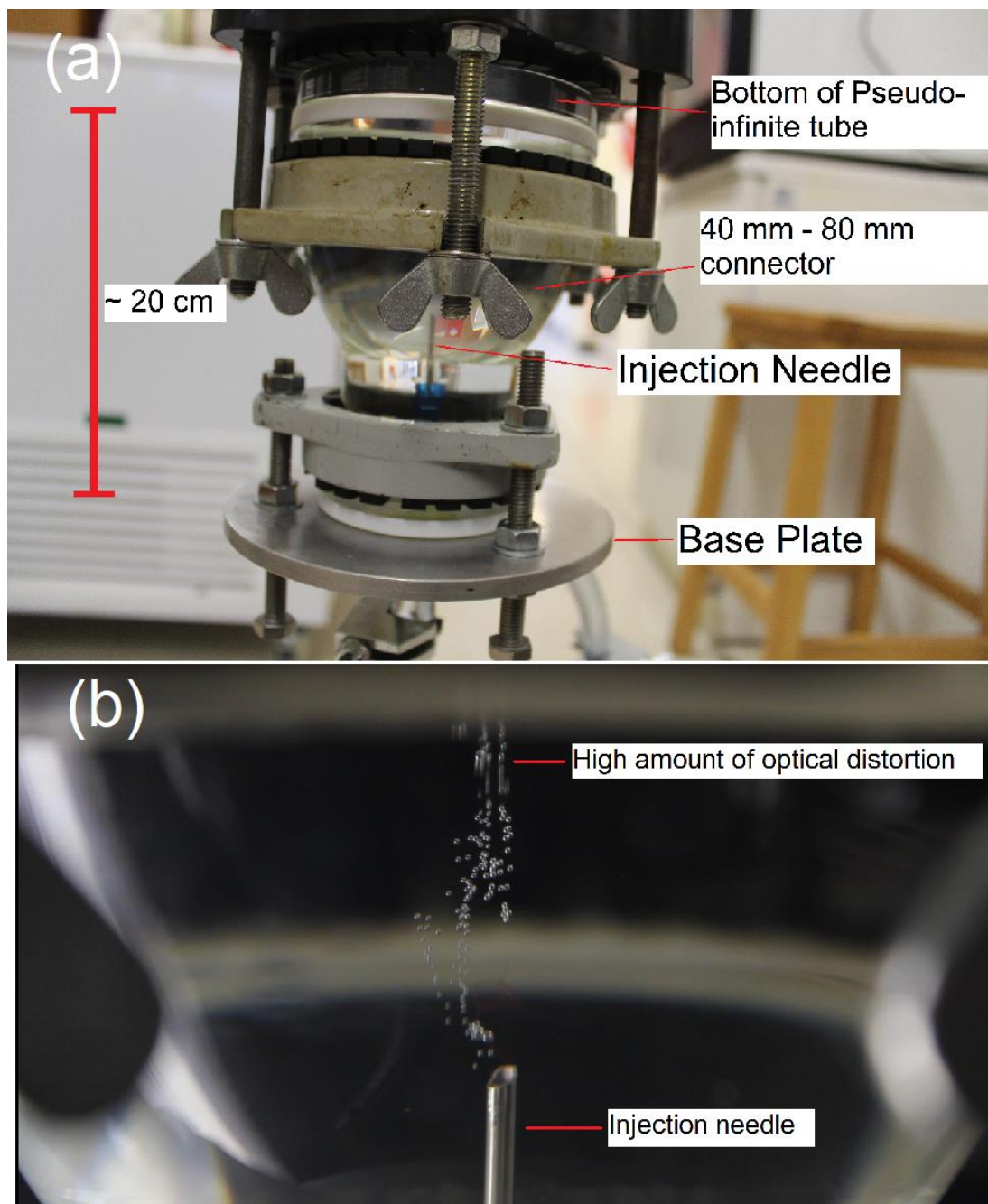


Figure 5.13: Photograph of the lower portion of the experimental tube, showing that the apparatus obscured the observation of the early behaviour of the bubbles (a) and a highly distorted image of the injection needle (b).

5.5.2. Pairs of Similar Sized Bubbles

Touching pairs of bubbles were uncommon, with only ~ 10 instances observed across all videos of the pseudo-infinite experiments. Each injection produced on the order of 10^3 to 10^5 bubbles, indicating a frequency of approximately 1 touching pair forming per 1.5×10^3 to 1.5×10^5 bubbles produced in this experimental apparatus. When touching pairs of bubbles were found (Figure 5.14), the pairs did not often split unless other bubbles were

nearby and interacted with the pair. In some circumstances they coalesced, however this was rarely seen in the areas of the tube that were filmed. It was more common higher up in the tube where expansion dominated and the duration that the bubbles were in contact was longer, but these parts of the tube were not measured.

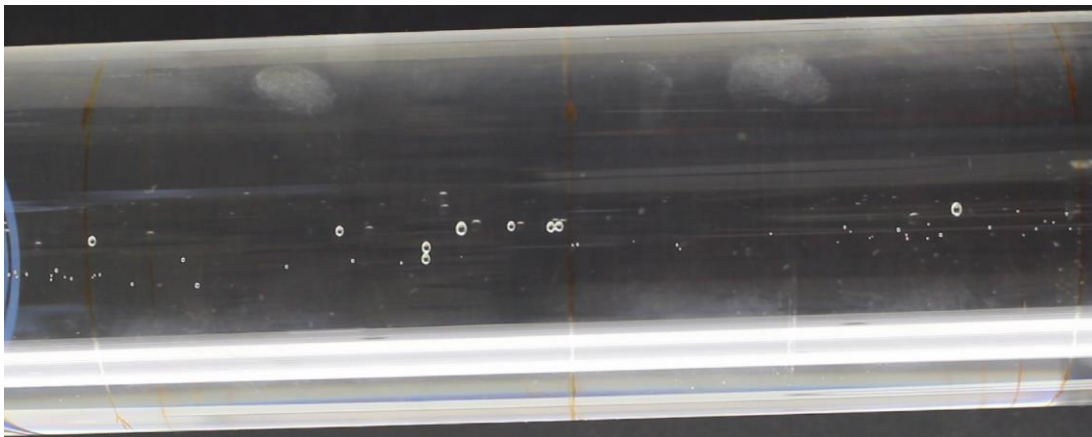


Figure 5.14: Example of two pairs of bubbles in a pseudo-infinite tube in RUN07_LOW. Touching pairs of bubbles was an uncommon type of interaction and observing two instances of it at the same time occurred only once, shown here.

5.5.3. Coalescence

A feature which was expected in these experiments, but not seen frequently, was the coalescence of two or more bubbles. Indeed, no instance of bubble coalescence between bubbles smaller than 1 mm in diameter were recorded in the pseudo-infinite case. Some examples of coalescence occurred near the surface of the oil where decompressive expansion causes the bubbles' volume to increase significantly over a vertical displacement of a few bubble diameters (e.g. when the base pressure is at 10 Pa, the bubble volume increased by a factor of approximately 50 in the final 0.5 m of ascent). Even when two or more bubbles were in prolonged contact, they did not normally coalesce in the timescale of these experiments. Film drainage of a single bare bubble of 1 mm diameter in a 0.17 Pa s fluid was on the order of approximately 20 s (Kočárková et al., 2013). 20 s was a greater duration than most touching pairs of bubbles were visible for in the field of view of each camera, so this provided an explanation as to why coalescence between the few observed touching pairs was not often observed on the cameras. As the timescale was inversely proportional to the bubble diameter, greater coalescence rates were expected in the higher sections of the tube, but as expansion began to increase the rise speed of bubbles in that part of the experimental tube, it was not recorded on the cameras.

5.5.4. Dilute Columns

30 bubbles inside a dilute column were selected and their average speed measured. Their vertical dimension was used to calculate their theoretical speed. The direct comparison of the measured and theoretical rise speeds showed that bubbles travelling in dilute columns rose slightly faster than expected (Figure 5.15). There was a moderate correlation between the measured and theoretical rise speed (Pearson's $R = 0.3902$, $p = 0.0330$). The gradient of a linear fit between the measured and theoretical rise speeds was 0.36 ± 0.03 ($R^2 = 0.152$) (the uncertainty in gradient was weighted from the experimental uncertainties) indicating that the bubbles' diameter had some influence over the actual rise speed, but only weakly and as the bubbles grew larger, the deviation away from the model increased. The average residual (the residuals between theoretical and measured rise speeds are plotted in Figure 10.2) between theoretical and measured rise speeds was $11.1 \pm 1.1 \text{ mm s}^{-1}$, indicating that bubble diameter alone was insufficient to predict the measured rise speed.

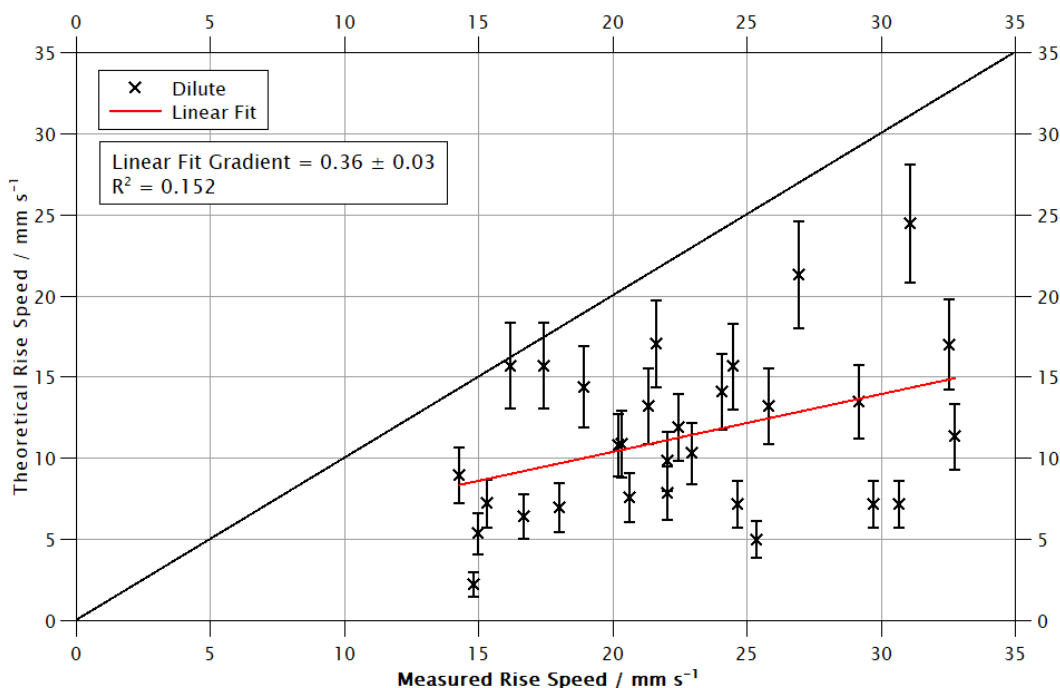


Figure 5.15: Theoretical versus measured rise speed for bubbles in the dilute column. The black line indicates where the theoretical and measured values are equal.

Of the 30 points measured, only two (approximately 7 %) were consistent with the theoretical rise speed within uncertainty, while the rest did not agree within uncertainty.

This was strong evidence to suggest that these bubbles were consistently rising faster than would be expected and therefore that the surrounding bubbles acted as a group to increase the vertical speed of the surrounding oil, relative to the tube wall.

A selection of three bubbles that appeared to be characteristic of bubbles travelling in a dilute column were measured in greater detail by measuring their position in every video frame, and their instantaneous speed measured (Figures 5.15 and 5.16). These results showed that while the bubbles were within the dilute group, they were traveling faster than their theoretical speed. There was, however, considerable temporal variability, which was not unexpected as the number of nearby (within 5 diameters) bubbles and their relative separation was observed to be constantly changing. The increases in speed appeared to match areas of heightened bubble number density (for example, Figures 5.16 and 5.17) suggesting that the controls on group behaviour were local bubble number density and gas volume fraction. It was not possible to determine if one bubble at a given distance would have the same effect as many small bubbles with the same total volume as the production of bubbles could not be controlled to facilitate this. It was proposed that the surrounding bubbles entrained some oil with them, meaning that the measured bubble was rising through vertically ascending oil. Therefore, the measured bubble speed was a proxy measurement of the local oil speed plus the rise speed of the bubble in a static fluid.

As a measured bubble's speed varied due to other bubbles around it, it was asserted that the effect that the measured bubble had on the surrounding bubbles was also variable over time. Specifically, that the surrounding bubbles caused the measured bubble rise faster, but the faster rise speed of the measured bubble also facilitated a faster rise speed for the bubbles around it due to increased oil speed. As bubbles rise faster, they may approach areas of greater bubble number density, thus increasing the magnitude of the effect they experienced. Alternatively, they may rise into an area of lower bubble number density and so decelerate to match the local conditions.

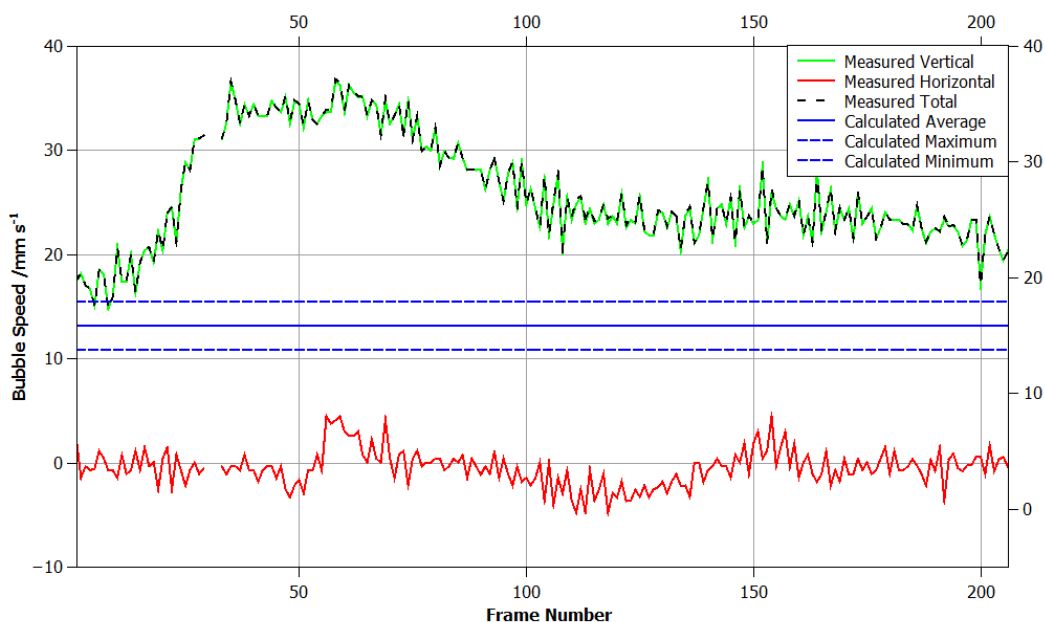


Figure 5.16: An example of the movement of a small bubble through a dilute column of other bubbles of similar volume, from RUN06_MID PS4. The gap in the data at approximately frame 30 was due to another bubble briefly obscuring the one being measured. The Hadamard-Rybczynski model was used to obtain the calculated value for the bubble's speed, with the minimum and maximum values (dashed blue lines) calculated using the upper and lower bounds from the experimental uncertainty in the bubble's size.

While the measured bubble was in more bubble-rich areas, the measured rise speeds were, in some cases, in excess of the theoretical rise speed by five uncertainty values for brief periods of time. In the case of RUN06_MID PS4, five uncertainty values above the theoretical value would be 24.85 mm s^{-1} , (theoretical speed was 13.15 mm s^{-1} with an uncertainty of 2.34 mm s^{-1}) which was sustained for approximately three seconds between Frames 25 and 100 (Figure 5.16). Additionally, bubbles were observed to briefly achieve even higher speeds exceeding ten uncertainty values away from the theoretical speed. Again, in RUN06_MID PS5, a speed greater than 24.35 mm s^{-1} (theoretical speed of 7.85 mm s^{-1} plus 10 times the uncertainty of 1.65 mm s^{-1}) was sustained for approximately two seconds (Frames 66 to 111) (Figure 5.17). These data show that, even for moderate bubble densities, bubble rise speed may be multiple times faster than the theoretical prediction which led to significantly increased movement of gas towards the surface. However, the peak speeds were not sustained for extended time periods as the bubbles surrounding the measured bubble were also constantly moving relative to the measured bubble and so the local bubble number density was constantly changing.

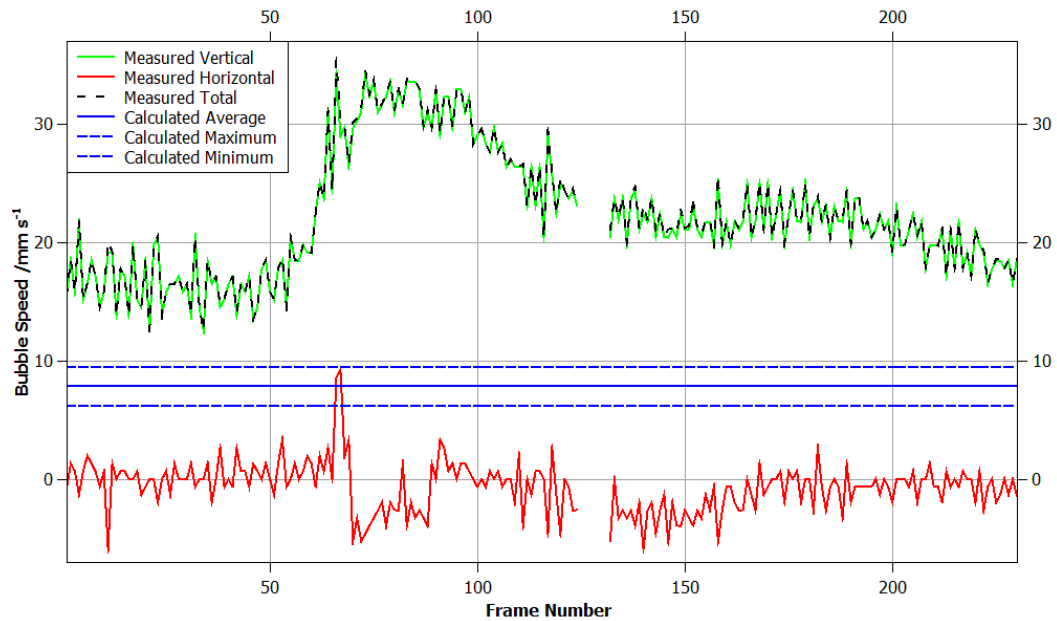


Figure 5.17: Measured and theoretical rise speeds of RUN06_MID PS5. The gap in the data were frames where the bubble was not clearly visible.

The abrupt changes in local number density and gas volume fraction for each bubble could induce changes in the measured rise speed by as much as a factor of 2 within one second (Figure 5.17, Frame 50 to Frame 75). If the rise speed of a bubble diverged from that of its neighbours, it may move into a region of higher or lower local bubble number density. However, when a bubble did not have a different rise speed compared to the surrounding bubbles, the local conditions tended to remain constant. This phenomenon could only occur when the size of a bubble had some contribution to its measured rise speed. As such, bubbles of similar sizes tended to group together, with larger bubbles rising faster than smaller ones. A possible consequence of this behaviour was size stratification; however, the experiments could not have been run for a sufficient duration to observe a fully stratified tube of bubbles as the tube was of insufficient height to allow for long term behaviour to develop.

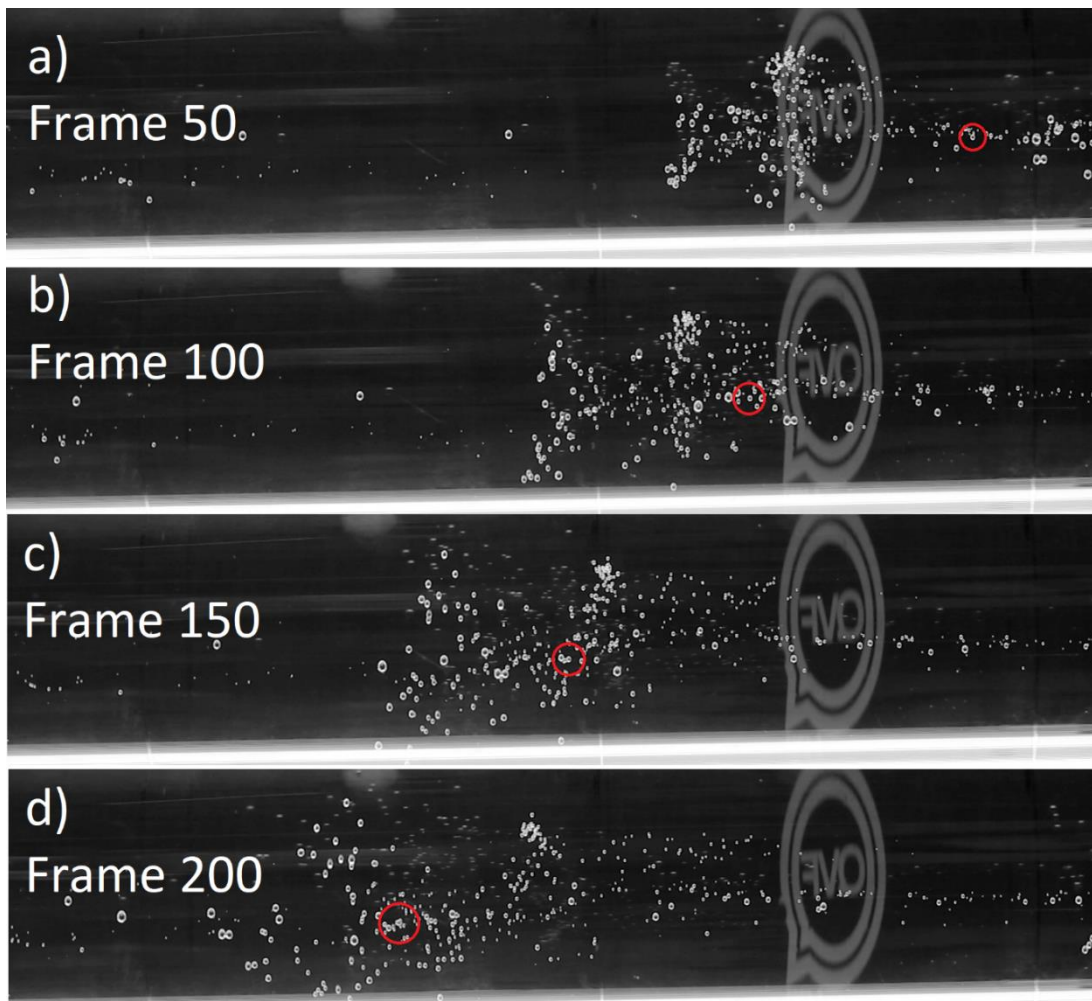


Figure 5.18: Images from the video RUN06_MID with bubble PS5 highlighted at the centre of the red circles. The frame numbers correspond to the frame from the first measurement (and therefore Figure 5.17), as measurements did not start on the first frame of the video, but rather the 19th frame as the bubble was not in the field of view of the camera for the first 18 frames.

The dilute columns studied here were commonly seen within the experiments to the extent that every experimental run exhibited this kind of group behaviour at some point. It was shown that even relatively low bubble number densities greatly increased the rise speed of bubbles (e.g. Figure 5.18a); however, this effect had a high degree of variability (e.g. Figure 5.16) in these experiments. The physical and temporal limitations of the apparatus did not allow for long term behaviour to develop as there was only a limited time available between the nucleation of the bubbles and when decompressive expansion of the bubbles significantly changed their shape and size across the duration of measurement. In the experiments presented here, the time available for measurements was to the order of one minute. As such, only transient interactions were studied, but they

illustrated that dilute bubble distributions could measurably increase the rise speed of bubbles within the group.

5.5.5. Dense Groups

Measurements of 30 bubbles within dense groups demonstrated a significant deviation from theoretical predictions (Figure 5.19) as every bubble measured was multiple uncertainty values away from matching the theoretical and measured speeds.

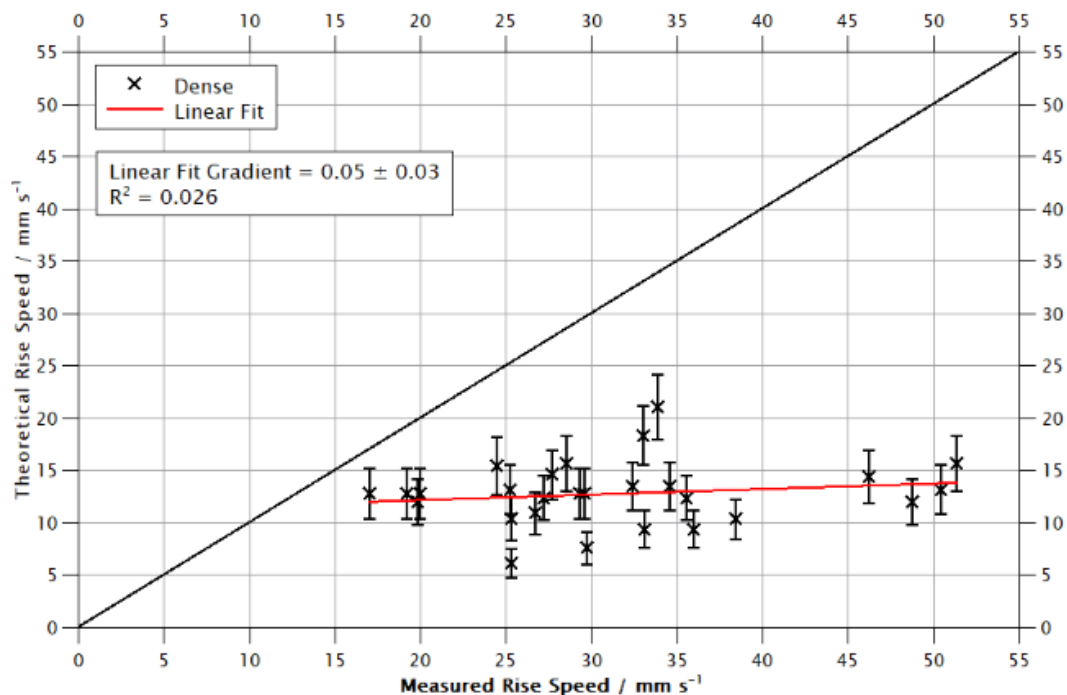


Figure 5.19: Theoretical versus Measured speeds of 30 bubbles in dense groups in the pseudo-infinite tube.

The measured speeds range from a minimum of 17.1 mm s^{-1} to a maximum of 50.5 mm s^{-1} whereas the theoretical speeds range from a minimum of 6.1 mm s^{-1} to a maximum of 21.0 mm s^{-1} . The larger range of measured values demonstrated that, despite a relatively consistent bubble size, there was great variability in their speed, indicating that the main control on rise speed for bubbles in dense columns was not bubble size. This was further shown by the low correlation between the measured and theoretical rise speeds (Pearson's $R = 0.224$, $p = 0.234$) with no trend across different bubble sizes as there was also no correlation between the theoretical rise speed and the residual between theoretical and measured speeds (Pearson's $R = 0.108$, $p = 0.570$). Furthermore, the gradient of the

linear fit between theoretical and measured rise speed was close to zero (0.05 ± 0.03), again suggesting measured bubble rise speeds were independent of their size.

The two fastest bubbles (Figure 5.20c and 5.20d) were in groups of approximately similar density to the slowest bubbles (Figure 5.20a and 5.20b). While the two slowest bubbles here appeared to be part of larger groups with more bubbles, the fastest bubbles were in a dense group that was underneath another dense group. It was therefore likely that this dense group was itself not moving through static fluid, but rather travelling through the wake left by the group higher up in the tube. Additionally, the slower bubbles were situated on the extremities of the groups, where it was expected that bubbles would move at a lower speed due to friction from the surrounding, slower moving, oil. The selection criteria of the bubbles required that the bubbles were visible for a sufficiently long duration in order to take measurements and the bubbles on the edges of groups were more often visible for several seconds, which resulted in bubbles on the edge of dense groups being more appropriate candidates to measure. For example, the bubbles highlighted in Figures 5.20a and 5.20b were both visible for 200 frames whereas the bubbles in 5.20c and 5.20d were only easily visible for 30 and 18 frames respectively.

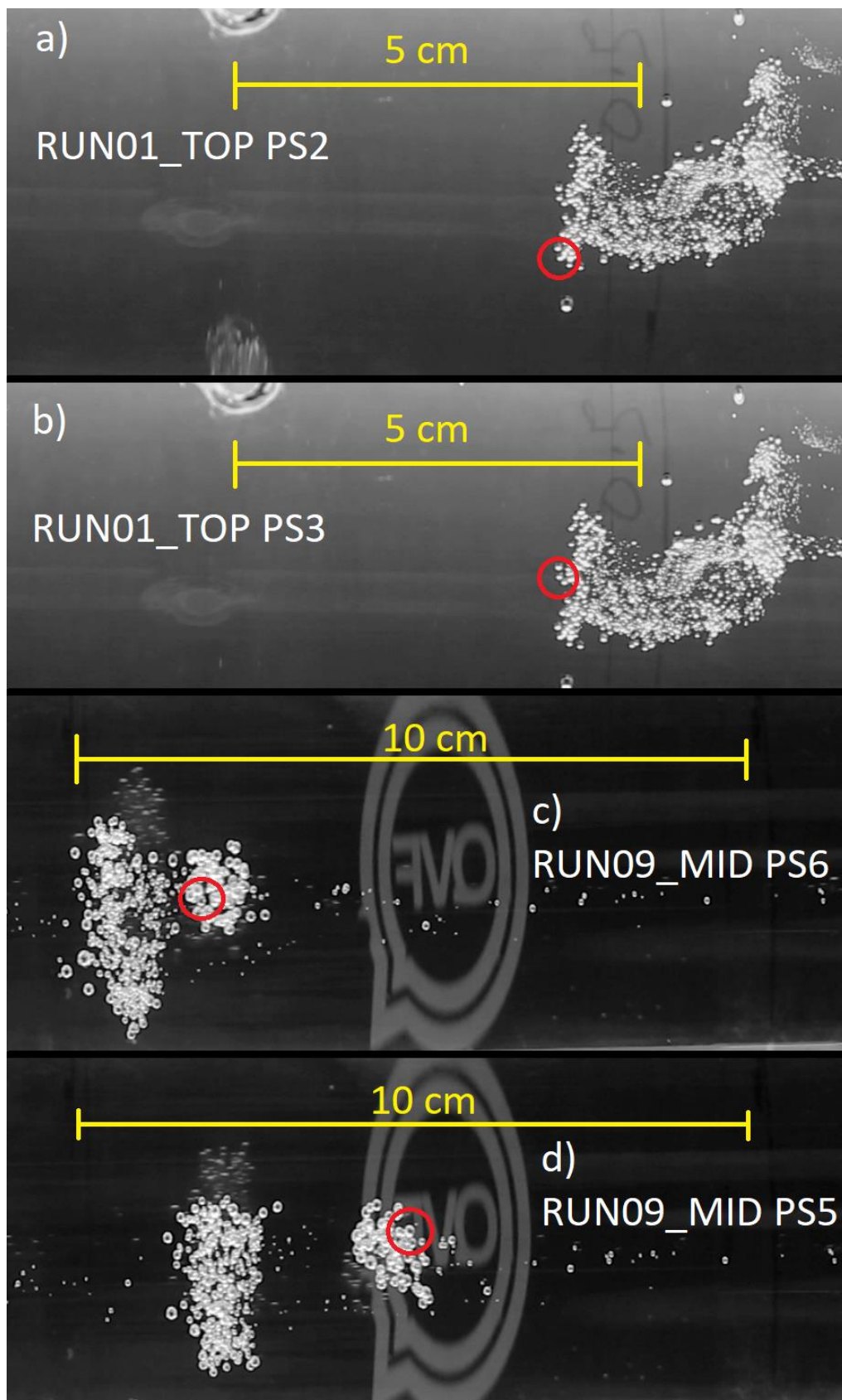


Figure 5.20: Sample images from the two slowest moving bubbles measured in dense groups (a and b) and the two fastest moving bubbles in dense groups (c and d), the measured bubbles were at the centre of the red circles. In these images, the direction of motion was from right to left.

The pressure at the top of the experiment appeared to affect the number density and size of these groups. In RUN01, RUN02 and RUN03, when the pressure was at the lowest detectable value (~ 10 Pa), multiple very dense groups formed (as demonstrated in Figure 5.10). By contrast, later runs at higher pressures up to ~ 10 kPa (for example, Figure 5.10) saw a greater prevalence of lower density groupings, although dense groups did form (Figure 5.20d) they did not appear to be as dense as the groups found in other runs (for example, Figure 5.11). This was likely because the pressure drop from the injected oil was greatest at the lowest experimental pressures and therefore more of the dissolved gas formed into bubbles, and these bubbles nucleated at a greater rate.

The rate of ascent of dense groups did not immediately appear to be linked to the estimated volume of those groups (Figure 5.21) (Pearson's $R = 0.173$, $p = 0.492$). The volume of these groups was estimated by measuring the top, bottom and sides of the group and modelling the group as an ellipsoid. Further inspection of some of these groups revealed that, like with bubbles in dilute groups, the surrounding context of these groups appeared to be important.

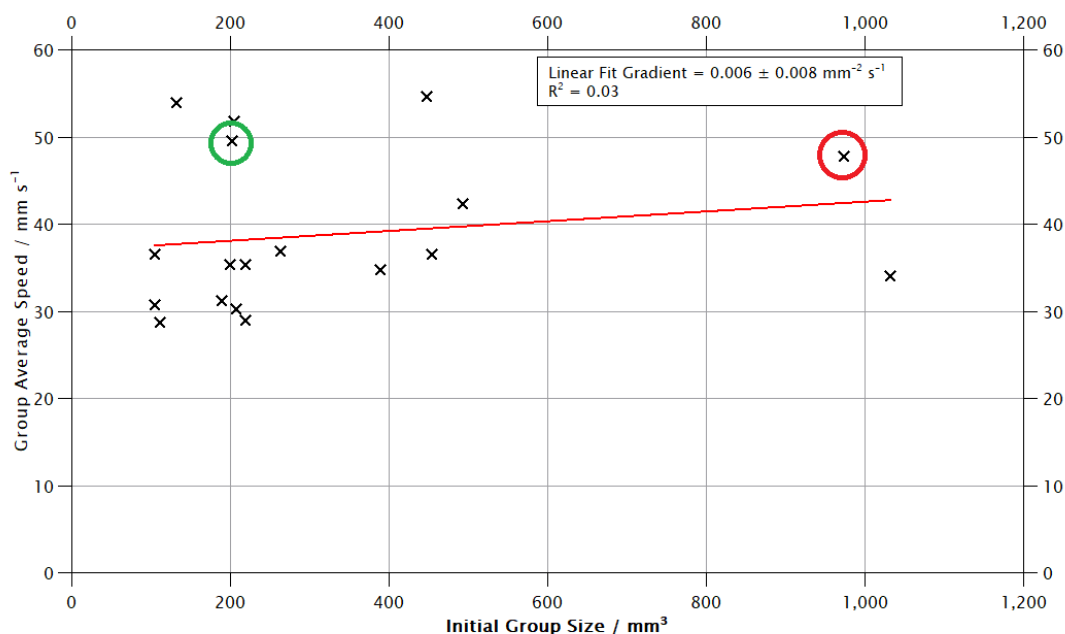


Figure 5.21: Measured rise speed against initial group size for 18 dense groups. The two groups examined in further detail are circles in red and green. These colours correspond to the same groups in Figure 5.22.

Two of the groups in Figure 5.22 (which were found in RUN09_LOW) can be directly compared, as they were observed at the same time in the same images, but in different parts of the tube (Figure 5.22). The larger group, circled in red, had an initial

volume of approximately 974 mm^3 and ascended at an average speed of 47.7 mm s^{-1} , whereas the other group, circled in green, had an initial volume of 202 mm^3 and ascended at a slightly greater speed of 49.5 mm s^{-1} . The discrepancy between the ascent rates of these two groups may be affected by surrounding bubbles and bubble groups.

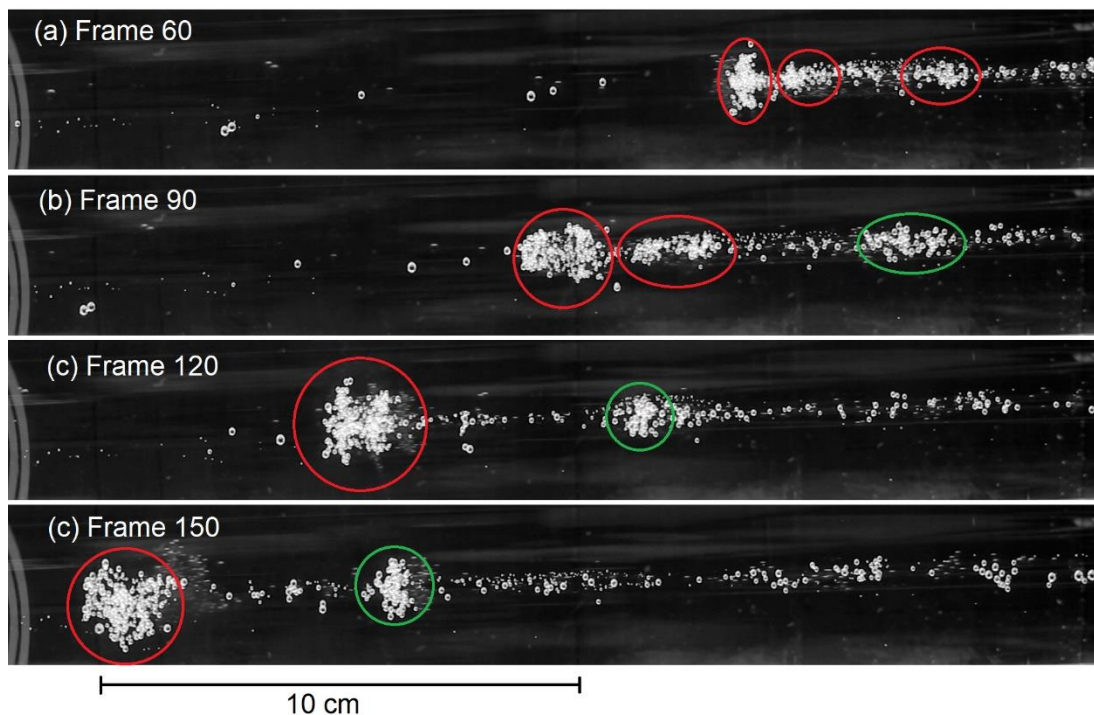


Figure 5.22: The progression of the two dense groups from RUN09_LOW. Both groups were only measured between Frames 120 and 150, with the earlier frames provided for additional context. The larger group, circled in red, was formed of three smaller groups, which consolidated into one larger group at around Frame 120, whereas the smaller group, circled in green, travelled through the column of bubbles trailing behind the larger group. As the time interval between each frame was 0.04 s , there was an interval duration of 1.2 s between each of the frames shown here.

The data show that the larger group, despite containing many more bubbles, travelled slightly slower than the smaller group and had approximately similar bubble number densities (while the group was mainly opaque, there were still observable gaps between the bubbles, to an estimated gas volume fraction of $0.1-0.3$). The larger group was not preceded by another group of large bubbles, whereas the smaller group was sufficiently close to the larger one that it may have been travelling in its wake giving a greater rise speed than expected, given the size and bubble number density of the group.

Another pair of groups, from RUN08_LOW initially indicated that the larger group of the pair ascended faster with an initial volume of 494 mm^3 and a measured rise speed of 42.2 mm s^{-1} , whereas the smaller group had an initial volume of 220 mm^3 and a

rise speed of 28.9 mm s^{-1} . Upon further inspection, the smaller group was travelling upward through a part of the tube with a relatively low number of bubbles ahead of it, and no groups of any notable size that could have affected its rise speed (Figure 5.23), whereas the larger group was travelling behind the smaller one, and rapidly approaching it from underneath. The smaller group changed shape from approximately spherical to a flat and broad shape across the period of observation, as well as decelerating (Figure 5.24)



Figure 5.23: Ascent of two dense groups through the experimental tube from RUN08_LOW. The smaller group is circled in red and the larger group circles in green. The smaller group observation duration was from Frame 50 to Frame 175 whereas the larger group only formed as one single group in Frame 150, so the observations began on that frame. The blue circles show the constituent groups that later combined to form the larger group circled in green. The time interval between each frame was 0.04 s, and an interval duration of 1.0 s separating the frames shown here.

The ascent of the smaller group was modelled as a single large spherical bubble with a diameter of $7.5 \pm 0.5 \text{ mm}$ (the equivalent diameter for an ellipsoid of volume

220 mm³, with an estimated uncertainty). The group was estimated to have a gas volume fraction of 0.10, leading to a density difference between the group and the surrounding oil of 0.099 g cm³. Using this model, and taking into consideration the observed internal rotation of bubbles within the group as an analogue for the internal rotation of gas in a single bubble, the Hadamard-Rybczynski equation predicted a rise speed of 28 ± 6 mm s⁻¹, which agreed with the measured average rise speed across the observation time of five seconds (29 mm s⁻¹), however the instantaneous speed of the group across that time period varied (Figure 5.24). The high degree of variability in the measured instantaneous speed was likely due to difficulty in ascertaining the centre of the group, particularly as it was changing shape, however the reduction in speed was still clearly shown. Further, the Hadamard-Rybczynski model assumes a spherical bubble rather than a highly deformable group of bubbles, so could not be expected to produce an accurate prediction of group rise speed. The model of Park et al. (2017) (Section 2.5.1), which allows for a variety of bubble shapes as bubbles grow larger, yielded a predicted rise speed of 24 ± 3 mm s⁻¹.

The simple model was highly sensitive to the estimate of the gas volume fraction. At 0.15, the theoretical speed was 42 ± 8 mm s⁻¹ and at a gas volume fraction of 0.05 the result was 14 ± 3 mm s⁻¹. The gas volume fraction of the dense groups was challenging to constrain accurately, so the modelling presented here is highly approximate. Further, the change of shape of the group was not taken into consideration, nor the increase in volume (and therefore reduction of the gas volume fraction) across the observation period, however the model still provided a result which was comparable to the observed speed.

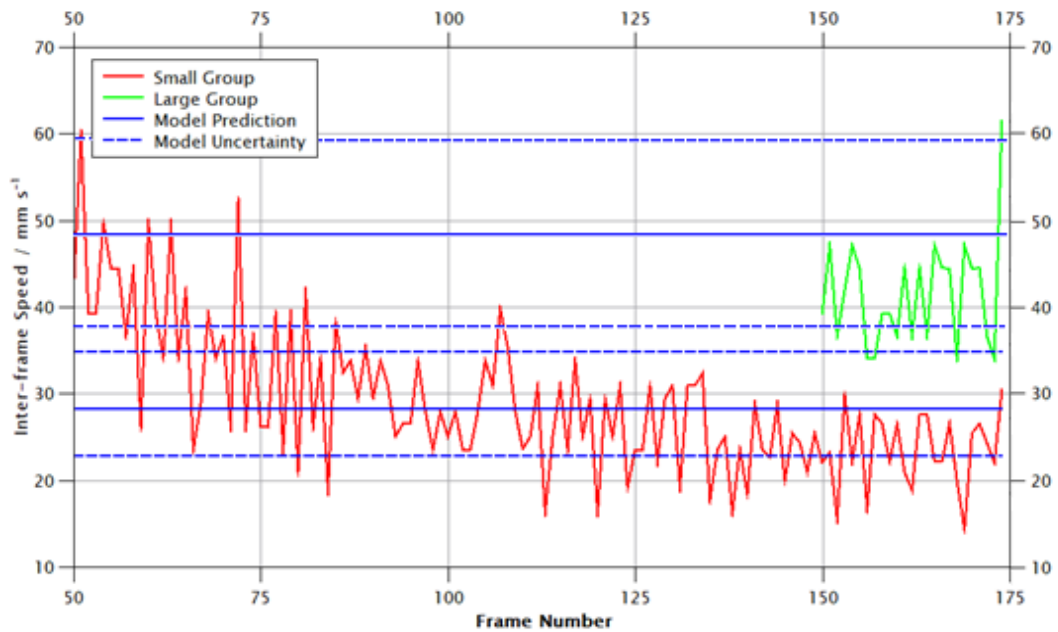


Figure 5.24: Instantaneous speeds of two dense groups from RUN08_LOW. The smaller group (circled in red in Figure 5.23) was observed to change shape across the observation period which coincides with a reduction in speed. The “Large Group” data correspond to the large group circled in green in Figure 5.23.

The initial gas volume fraction may have been over-estimated, while the assumption of a constant volume was also not correct, as well as the assumption of the group remaining spherical. Using the ellipsoidal model, the volume of the smaller group was found to increase from 220 mm^3 to 693 mm^3 . The very large increase in volume arose due to the observed width of the group increasing by more than 200 % (this was assumed to have symmetry in the direction away from the camera), while the height decreased by approximately 30 %. Despite these simplifications, the model was able to provide realistic estimates for the ascent speed of the smaller group, which was likely travelling through static, or nearly static, oil. When the Hadamard-Rybczynski model was applied to the larger of the two groups using the same gas volume fraction of 0.1, an initial volume of 494.0 mm^3 (providing an equivalent diameter of 9.81 mm), a theoretical rise speed of $48.3 \pm 10.7 \text{ mms}^{-1}$ was computed. The measured rise speed of the group was 42.2 mms^{-1} across the 25 frames observed and so the theoretical and observed rises speeds agreed. It was noted that the percentage uncertainty value on the theoretical rise speed was 22%, that there was a high level of sensitivity in the theoretical value for small variations in the gas volume fraction, that the measurement of speed was made across a short (25-frame) time interval, and that the size and shape of the bubble group changed across that time interval.

Consequently, the agreement between the theoretical and observed rise speeds for this larger group may have been coincidental, as the Hadamard-Rybczynski model was not anticipated to be accurate for the scenario.

5.5.6. Group Breakups

As groups ascended through the tube, they all eventually broke apart and the bubble number density reduced. Typically, as the groups broke apart, the individual bubbles moved laterally. Group breakup typically occurred after the group's speed reduced (Figure 5.25) and the shape of the groups became flatter and wider (Figure 5.26), while the volume increased (Figure 5.27). The volume of the groups was calculated by taking measurements of the position of the top, bottom and sides of the group and modelling the groups as ellipsoids. As the total number of bubbles in these dense groups did not appreciably change prior to breaking up, the reduction in speed could not be attributed to shedding bubbles, reducing the total gas volume of the group. The volume of bubbles slightly increased across the measurement period due to decompressive expansion, which would increase the gas volume fraction of a group, increasing the difference in density relative to the surrounding oil and thus increasing the speed of the groups. The role of decompressive expansion did not appear to be a significant control on the rise speed of the groups studied, as the groups' speed decreased as they ascended through the tube (Figure 5.25). The change in speed may be connected to the increase in volume and change in shape of the groups prior to breakup. The increase in volume reduced the bubble number density of the groups, which in turn reduced the density difference between the dense group and the surrounding oil. The change in shape from approximately spherical, or prolate spheroid shape, to an oblate spheroid shape (e.g. the smaller group in Figure 5.22) may affect the coefficient of drag experienced by the group.

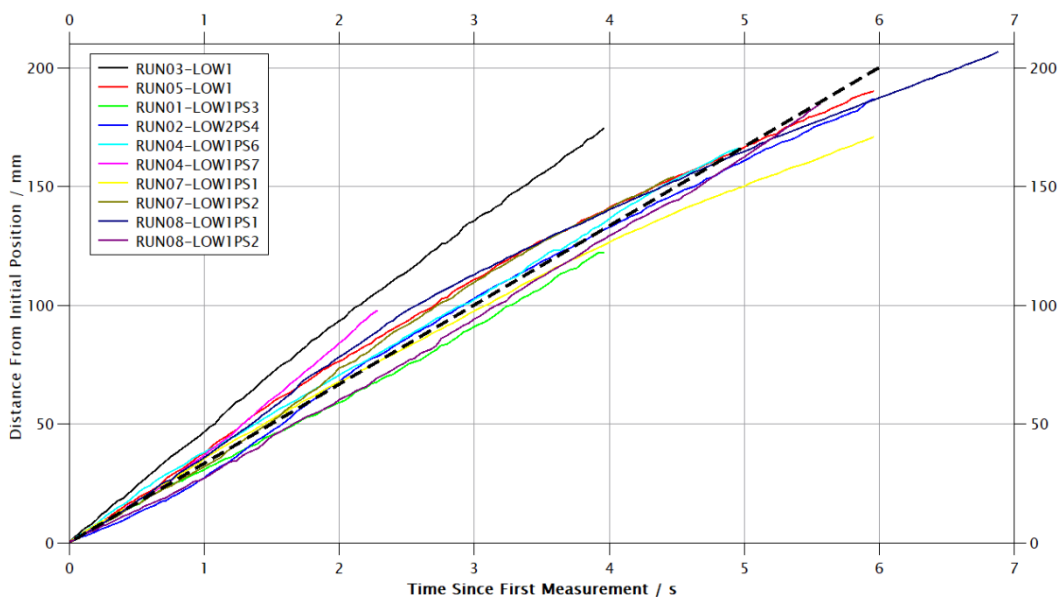


Figure 5.25: The distance from the initial position of the centre of ten dense groups. The black dashed line is a straight reference line to illustrate that most of these groups decelerated over time. The observations ended when the groups were judged to be breaking up, or if they left the field of view of the camera.

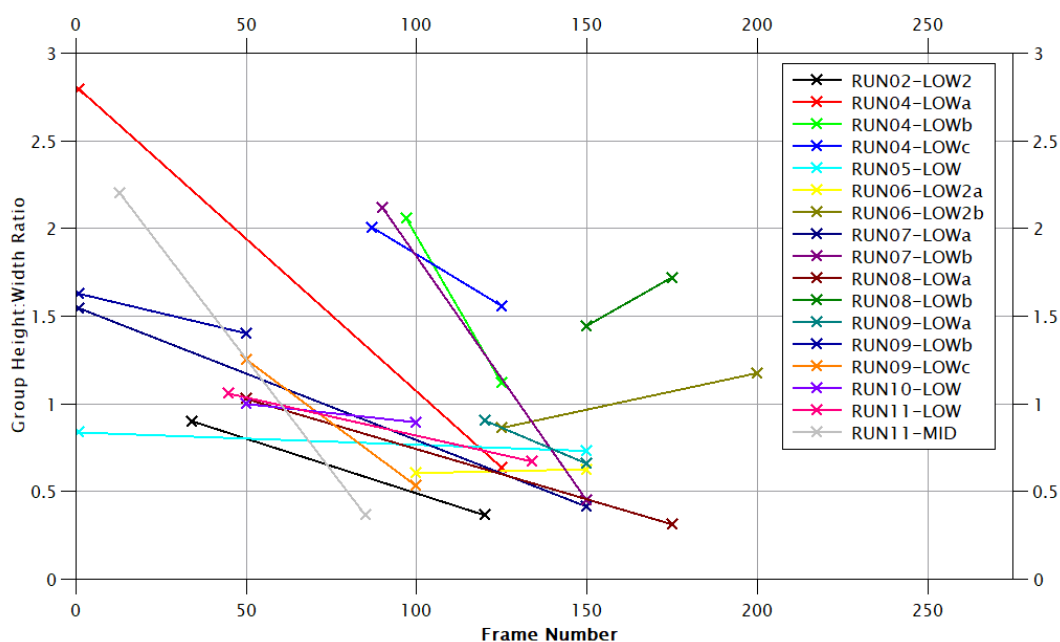


Figure 5.26: Height to width ratio of 17 dense groups as they began to break apart. All but one (RUN08_LOWb, shown as the group circled in green in Figure 5.23) became flatter and wider, as shown by the reduction in this ratio over time. The frame numbers refer to each specific video, so cannot be compared between experimental runs.

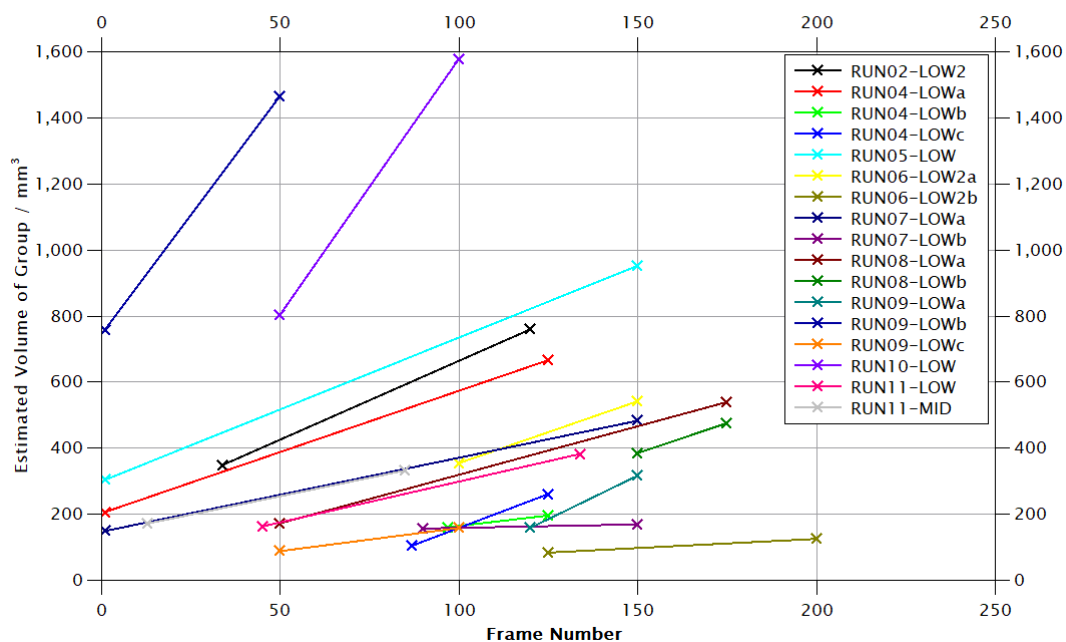


Figure 5.27: Change in volume of 17 groups as they began to break apart. In all cases shown here, the volume of the groups increased, even if the increase was small in some cases, most of these groups increased in volume by a factor of 1.5-3. The frame number refers to each specific video, so were not comparable between groups, but demonstrate the duration of time that elapsed between the measurement.

Groups often broke up when they passed through or overtook other groups above them in the tube. This suggested that the resistance to the upward movement from overlying static oil was, at the point of breakup, stronger than the mechanism holding the bubbles together. Groups generated in this experiment appeared to be unstable over timescales of >10-20 s. It was impossible to determine if large groups with a high bubble number density would later reform given sufficient time, because the experimental tube had a high pressure gradient in its top half (the pressure at the top of the oil was 100 to 10,000 Pa, increasing by approximately 10,000 Pa at a depth of one metre). This meant that bubbles expanded rapidly towards the top and so steady state behaviour could not develop. A much taller experimental tube would facilitate observations over a longer time scale and may reveal if groups reform over time and whether repeated formation and breakup of groups can be expected.

5.6. Summary

The results presented here demonstrate that the Hadamard-Rybczynski equation provides an accurate description of the rise speed of isolated small bubbles in the experimental tube.

For the pseudo-infinite case, isolated spherical bubbles ascended through the tube as expected, justifying the use of this model to estimate theoretical bubble rise speeds and thus compare with measured values to when group behaviour occurred. Following the injection of volatile-rich oil into the bottom of the tube, groups of bubbles were observed to form with a variety of estimated gas volume fractions ranging from under 1 % to greater than 10 % (Figure 5.11).

The number density of produced bubble groups could be loosely controlled by adjusting the pressure at the top of the experiment, the number density of bubble groupings produced could be loosely controlled. Groups of bubbles were shown to have a greater rise speed, relative to the walls of the tube, than any of their constituent bubbles would be expected to have in isolation (Figures 5.14 and 5.18). For lower number density groupings, the increase in speed appeared to be influenced by the number and proximity of bubbles within five diameters of measured bubbles. As the rise speed was still partially affected by the size of the bubbles (Figure 5.15), there were temporal variations in the measured bubble rise speed (Figures 5.16 and 5.17) as the number and proximity of bubbles around the measured bubble varied.

In dense groupings, the speed of individual bubbles appeared to be matched to the speed of the dense group as a whole, which was in turn controlled by multiple factors. While groups did appear to slow down as volumetric expansion reduced their gas volume fraction, this coincided with a change in their shape to be wider and flatter, and there was no significant correlation between the size and measured speed of the groups measured. Instead, the broader context of the groups themselves appeared to strongly influence their rise speed, as a large group travelling through approximately static fluid ascended at a slower rate than a smaller group travelling behind that larger group (Figures 5.22 and 5.23). When a small dense group was travelling through static fluid, the Hadamard–Rybczynski equation and Park et al. (2017) models for individual bubbles could potentially provide adequate predictions of the bubble group speeds, despite substantial assumptions being made, such as the group retaining constant volume and shape. Although it was impossible to determine exactly how volume, gas volume fraction, group shape and the surrounding conditions affected the bulk rise speed of groups, alteration of at least one of these factors occurred concurrently with a change in speed. However, it cannot be definitively shown that all four proposed independent factors affected the rise speed of groups because the factors are likely to be coupled, so an increase in rise speed caused by a change to one parameter potentially affected other parameters.

While there were a variety of bubble groups and types of interactions between bubbles, all the data indicated that bubble interactions served to increase the rise speed of the measured bubbles beyond variations that could be reasonably expected from experimental errors alone. It can therefore be summarised that bubbles in proximity to each other within a pseudo-infinite fluid ascend more rapidly than equivalent individual, isolated bubbles, and that bubble-bubble interactions thus serve to increase the rate and efficiency of gas mass transport towards the surface.

These experiments have discussed only the behaviour of bubbles in an approximately wall-free environment. The following chapter examines behaviour in vertical constrained tubes as a means of understanding the effect that walls may have on the behaviour of bubbles.

6. Bubbles in Vertical Constrained Tubes

In order to examine the influence of constraining walls on the rise speed of bubbles, the experimental and analytical approach adopted for Chapter 5 was repeated with a tube with an internal diameter of 25 mm.

6.1. Single Bubbles

Single bubbles were examined within the 25 mm tube to determine whether the use of the Hadamard-Rybczynski equation as a baseline to compare bubble interactions remained valid. For the tube of internal diameter 25 mm, Brizard et al. (2005) predict that edge effects should not affect the rise speed of bubbles with a diameter less than 2.5 mm; additionally, measuring single bubbles provided an opportunity to determine if physical effects were introduced by the constraining wall. As in Chapter 5, the speed and size of 36 candidate bubbles was measured and the theoretical rise speed compared directly against the measured rise speed (Figure 6.1)

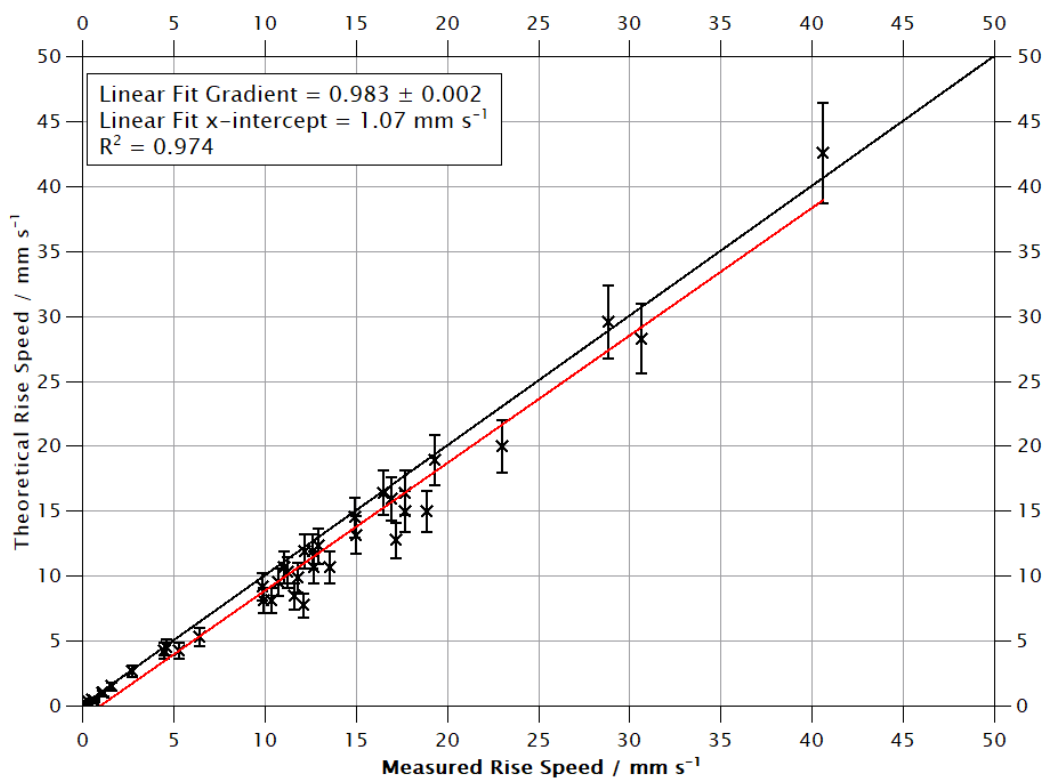


Figure 6.1: Theoretical and measured rise speeds for single bubbles in a constrained tube. As in Chapter 5, the black line represents the points where measured speed and theoretical speed are equal.

There was good agreement between the theoretical and measured rise speeds with a high correlation between these values (Pearson's $R = 0.9871$, $p < 0.0001$) and no significant correlation between the theoretical values and the theoretical-measured residual (Pearson's $R = 0.0562$, $p = 0.738$) (Figure 10.4). However, many of the bubbles were rising slightly faster than expected to the extent that the x-intercept of the linear fit between theoretical and measured rise speeds was 1.07 mm s^{-1} , while in the pseudo-infinite case, the x-intercept was -0.37 mm s^{-1} , indicating slightly better agreement between theory and measured results. The x-intercept indicated that the bubbles were typically travelling around 1 mm s^{-1} faster than expected using the Hadamard-Rybczynski model, although not all of the bubbles deviated from theory, with the model accounting for the rise speed of 19 of the 36 bubbles within experimental uncertainty. Further, the average residual of single bubbles in the constrained case was 1.25 mm s^{-1} , again indicating that the bubbles were rising around 1 mm s^{-1} faster than predicted by the model. Of the bubbles where the residual was greater than the experimental uncertainty, the average residual between theoretical and measured rise speeds was 2.2 mm s^{-1} .

To assess potential reasons for the increased measured rise speed two bubbles were tracked before, during and after the injection of oil. From these measurements, it was possible to determine that, while the injection was ongoing, there was an increase in the speed of bubbles (Figure 6.2, Frames 90-150; Figure 6.3, Frames 150-190); however, bubbles before the injection still had measured rise speeds greater than the theoretical values.

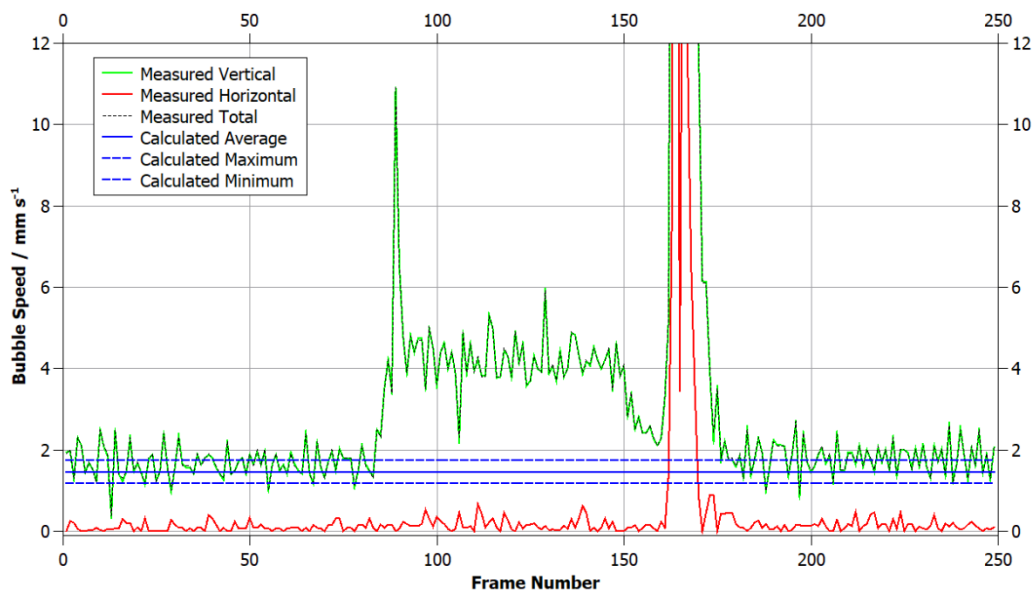


Figure 6.2: Inter-frame measured speed and theoretical speed of bubble RUN18_LOW PS1. The plot was cropped to more clearly show the detail in the lower speed values as a large bubble passed through the experimental tube which increased the speed of the RUN18_LOW PS1 bubble between frames 160 and 180 to a maximum of 62.2 mm s^{-1} .

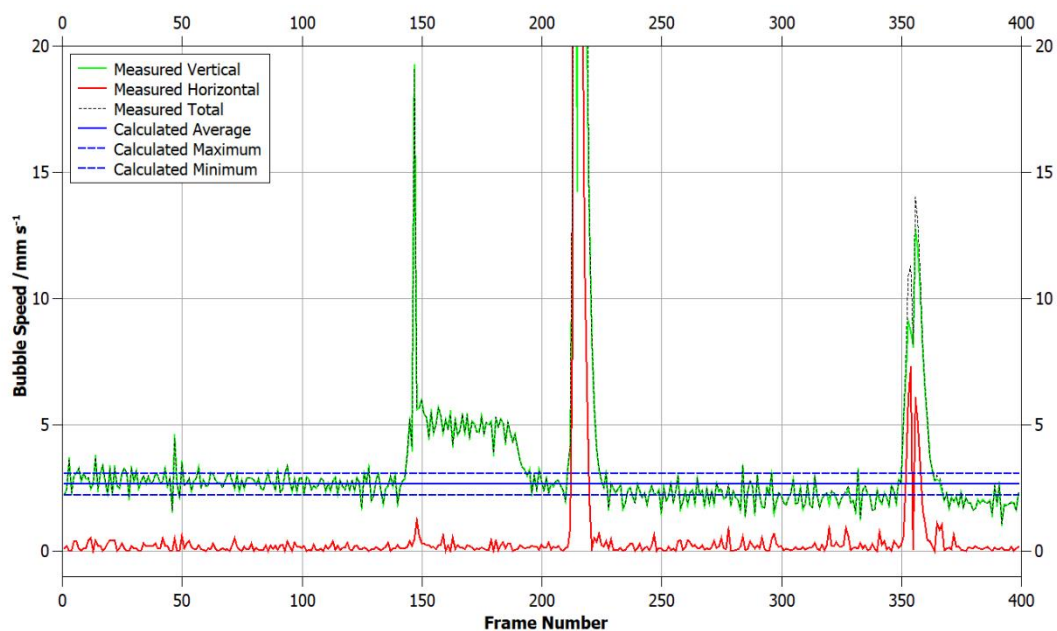


Figure 6.3: Inter-frame measured speed and theoretical speeds of bubble RUN19_LOW1 PS1. Extreme values have been cropped to show detail in the smaller values. The maximum measured speed was 65.6 mm s^{-1} , achieved in Frame 216.

In the previous two figures, the injection period was marked by a sustained, constant increase in the bubbles' speed (between Frames 90 and 150 in Figure 6.2 and Frames 150 and 190 in Figure 6.3). At the start of the injection the speed increased for approximately the duration of a single frame interval (0.04 s) which was interpreted as due to the sudden emission of a very large bubble (diameter greater than half of the tube diameter) from the needle. The very large bubble was likely the coalesced product of many smaller bubbles trapped in the tube between the injection needle and the solenoid valve from the previous experimental run. The increased speed corresponding to the duration of the injection was likely caused by the volume of the oil injected (typically between 1 and 2 ml per injection occurring at approximately 1 ml s^{-1} based on observations of the position of the plunger in the syringe during injections) and the volume of the bubbles nucleating from that oil. The nucleation of bubbles displaced oil vertically. The gas mass fraction of the injected oil was measured as being at least 0.04 % (Table 4.3), so for a 2 ml oil injection weighing 1.97 g, it would be expected that up to 788 μg may nucleate into bubbles (approximately 2.72×10^{-5} mol of air). Under the assumption of an ideal gas, an absolute temperature of 293 K and an ambient pressure of 20 kPa, the initial volume of bubbles after nucleation would be 3315 mm^3 . Given that the internal diameter of the tube was 25 mm, the cross sectional area of the tube was 491 mm^2 , and so an increase in volume at the base of the tube of 3315 mm^3 , would be expected to result in the oil rising by 6.8 mm. This would represent the upper estimate given that not all of the volatiles dissolved in the oil would nucleate at 20 kPa. For a 1 ml injection in the 25 mm tube, the expected increase in height was 3.4 mm, assuming that the injection of oil from the syringe was at a constant rate. In contrast, in a tube of 80 mm internal diameter (i.e. the pseudo-infinite tube), a similar increase in volume would be expected to increase the height of overlying oil (and therefore bubbles) by 0.15 mm. The excess height achieved by the bubble RUN19_LOW1 PS1 between the start of the oil injection and the bubble's interaction with a much larger bubble was approximately 5.5 mm (Figure 6.4), indicating that the previously calculated upper estimate of 6.8 mm was reasonable, and provides a plausible explanation for why several of the measured bubbles travelled at a greater speed than predicted by the Hadamard-Rybczynski model.

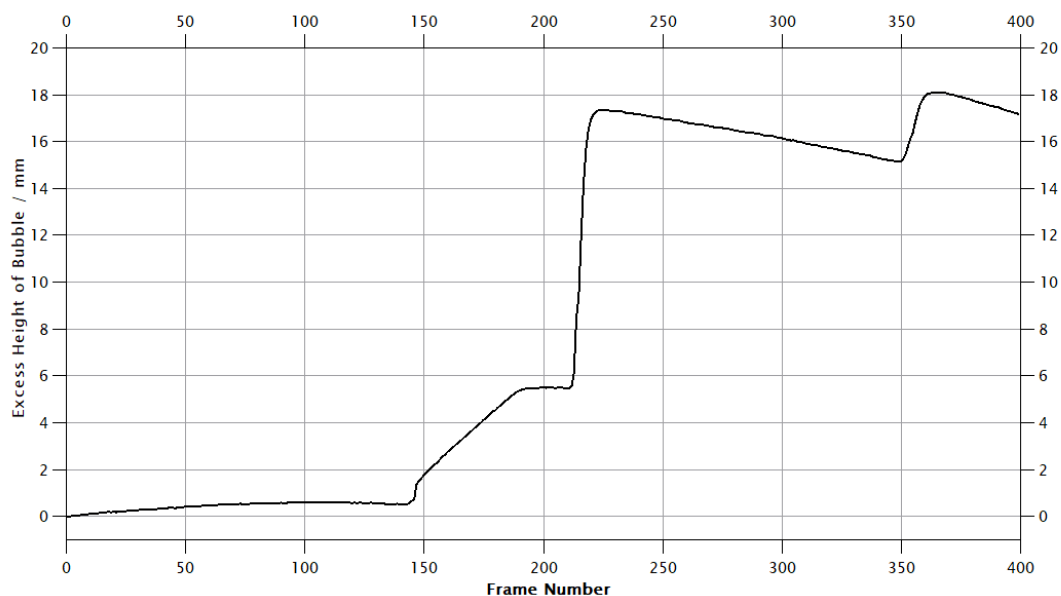


Figure 6.4: Excess height of the bubble RUN19_LOW1 PS1 (this was the same bubble as Figure 6.3). The injection of oil into the base of the apparatus began on frame 148 and ended at approximately frame 190. The increases in height around frames 210 and 355 were due to interactions with large bubbles.

The injection duration was approximately 2 s, suggesting that, if 1-2 ml was injected in this period, the bubble's rise speed in this period would be expected to increase by 3.4 mm s^{-1} due to the volume of the nucleating bubbles below the measured bubble. In some cases (e.g. RUN18_LOW1 PS1 and RUN19_LOW1 PS1), the period over which the measurement of rise speed was taken occurred before the injection (ending on Frames 85 and 146 respectively), so the Hadamard-Rybczynski equation described those bubbles well. However, for other bubbles, the measurement of the speed prior to injection was not always possible. The effect of the oil injection was not anticipated to have a measurable effect at the time of data collection, such as in RUN17_LOW1 PS1, where the first observed frame for that bubble in the image sequence was after the injection had begun. The measured rise speed for RUN17_LOW1 PS1 exceeded the theoretical rise speed by 3.9 mm s^{-1} across 43 frames of measurement. The injection had a duration of approximately 1.16 s, so a 3.4-6.8 mm increase in height due to that injection would result in an anticipated increase in the rise speed of bubbles of approximately $3.9\text{-}7.9 \text{ mm s}^{-1}$. The lower end of this estimate (which in of itself was an upper limit from the assumption that all the dissolved volatile in the oil exsolved into gas bubbles) was consistent with the observed excess speed when compared the measured and residual rise speeds.

6.2. Dilute Groups

Candidate bubbles for dilute groups needed to be in within five bubble diameters of at least three other bubbles over the duration of measurement. All bubbles were required be part of a vertically moving column of dilute (approximately 0.1-5 % gas volume fraction) bubbles. Additionally, the bubbles needed to be clearly visible for a sufficiently long time (typically greater than one-second) in order to make measurements and less than 3.3 mm in diameter so that the bubbles maintained a spherical shape, otherwise the Hadamard-Rybczynski equation would not be a valid description of their theoretical behaviour. In the constrained tube, 44 candidate bubbles (with diameters ranging from 0.59 mm to 2.27 mm) in dilute groups were selected in order to demonstrate a clear pattern of behaviour (Figure 6.5). Dilute bubble grouping was the most common type of group in the experiments, reflecting that the definition of a dilute group constitutes a wide range of gas volume fractions. More bubbles from dilute groups were selected for analysis than any other category of grouping (i.e. dense or no grouping/single bubbles) and there was much greater variation in the measured speeds. By measuring a greater number of bubbles it was possible to identify a pattern of behaviours as an average across all of the gas volume fractions studied.

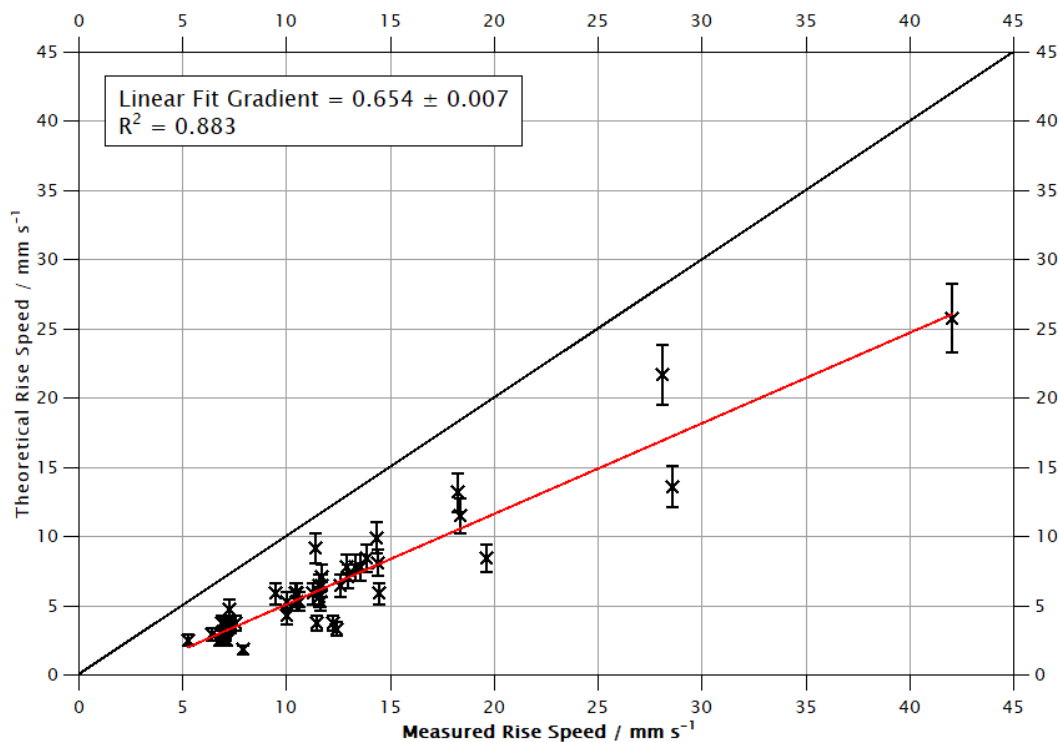


Figure 6.5: Theoretical versus measured speeds for bubbles in dilute columns. In all cases, the bubbles travelled approximately twice as fast as the Hadamard-Rybczynski equation predicted for their volume, indicating strong group behaviour. The linear fit shows a constant speed increase of approximately 2.5 mm s^{-1} in the measured values, as well as a gradient of 0.654 ± 0.007 indicating that larger bubbles rose disproportionately faster than expected under the Hadamard-Rybczynski model.

The bubbles in dilute groups rose much faster than the model predicted (which assumed individual, spherical, bubbles in static fluid). However, unlike in the pseudo-infinite case, a strong correlation was found between the measured and theoretical rise speeds (Pearson's $R = 0.9398$, $p < 0.0001$), indicating that the size of a given bubble had an influence on the rise speed of that bubble, despite being part of a group which considerably increased the rise speed of that bubble. A possible reason for this was that in the pseudo-infinite case, the non-constricting walls allowed for greater lateral movement of bubbles in response to the other bubbles (and bubble groups) which surrounded it, causing greater variations in the local bubble number density across time. Whereas in the constrained case, the constraining walls resulted in the local bubble number density to remain relatively constant. The correlation between the theoretical rise speed and measured-theoretical residual was -0.5805 ($p < 0.0001$) indicating that smaller bubbles had lower ascent velocities than larger bubbles within the same group, even when their lower buoyant rise speed was taken into consideration. This may be due to a hindering

effect where a downward motion of oil was generated by the larger bubbles, which then impeded the ascent of the smaller bubbles.

Further, the lower position of the camera at a single place along the tube and a narrower field of view (due to the lens used) meant that in the constrained case, the observed groups tended more often to be in well-defined vertically moving columns rather than the head of a dilute rising plume of bubbles which were observed in Chapter 5, although not all dilute groups in the Pseudo-infinite case were of this nature. The impact of a relatively constant surrounding of a measured bubble would be a relatively constant rise speed, which would facilitate the size of the bubble to have an appreciable impact on the measured rise speed, whereas in the pseudo-infinite experiments, the rise speed of the bubbles in dilute columns was observed to vary considerably (Figure 5.16, 5.17).

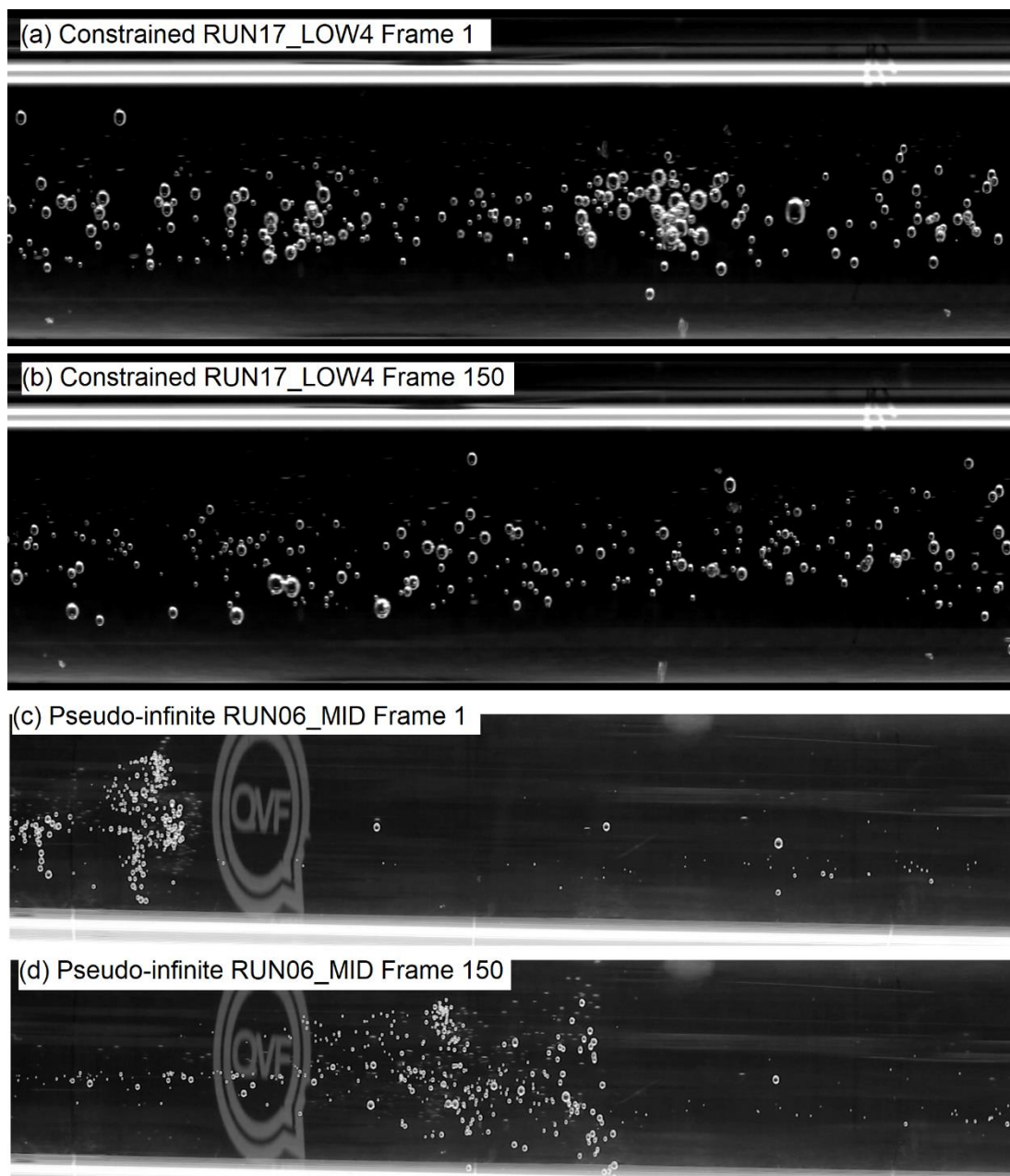


Figure 6.6: Comparison between dilute groups in the constrained tube and the pseudo-infinite tube. Aside from two areas of increased number density in Frame 1, there was a relatively (compared to (c) and (d)) uniform bubble number density within the column of bubbles and a similar bubble number density in (b), and the shape of the column of bubbles did not vary greatly across the time period. Whereas in (c), the bubble number density was not consistent across the group and as the group developed into what is seen in (d), the group spread laterally, further changing the bubble number density. Note that for the Pseudo-infinite images, the images were flipped horizontally so that the direction of motion in all four images was from left to right. The field of view for (a) and (b) was approximately 10 cm, whereas the field of view for (c) and (d) was approximately 20 cm.

The consistency of the local bubble number density over time for the constrained groups may have resulted in a consistent increase in bubble speed from the column of oil travelling upwards. This was evidenced by the relatively consistent rise speed of a bubble in such a dilute group (Figure 6.7) compared to a bubble in a dilute group in the Pseudo-infinite case (Figures 5.15 and 5.16). In contrast, the Pseudo-infinite experiment showed the continual development and lateral expansion of the of the group, which would have resulted in the local bubble number density of the measured bubbles changing constantly, masking the dependence of bubble size on the rise speed of a given bubble at a given time due to extensive variations in local bubble number density causing the bubble to rise through oil which itself was rising at many different speeds across the observation period.

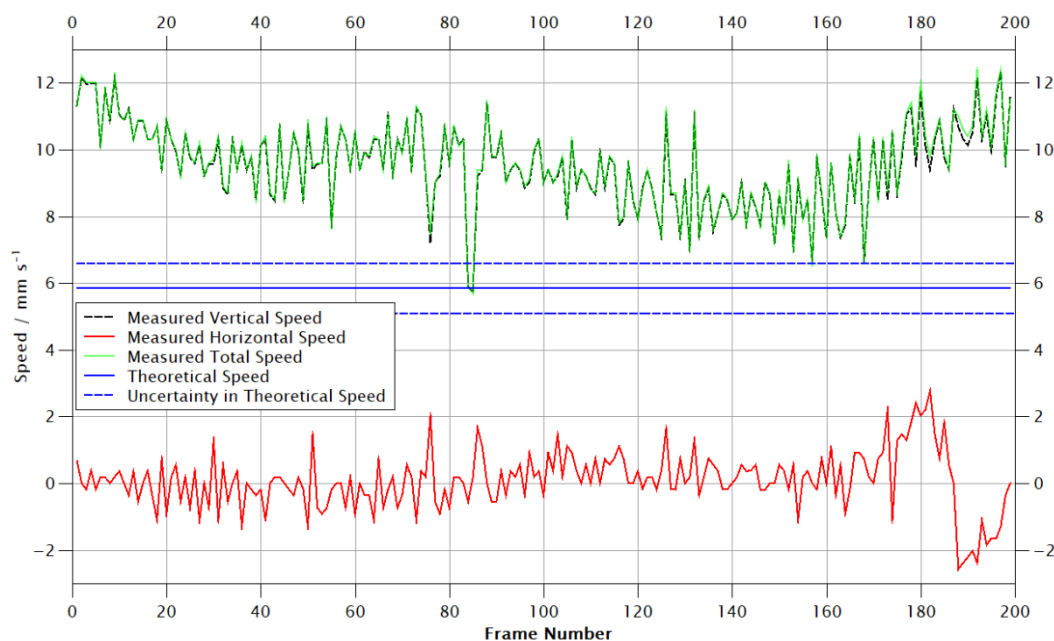


Figure 6.7: The variation in speed over time of RUN17_LOW4 PS6 across an 8-second observation period. While there was some variation across this time, it typically travelled at $10 \pm 2 \text{ mm s}^{-1}$, representing a more consistent speed than in Figures 5.15 and 5.16 (which were for Pseudo-infinite RUN06_MID) in the pseudo-infinite case.

The average ratio between the measured and theoretical values for dilute groups in the 25 mm tube was 2.1 ($\sigma = 0.6$, normally distributed), indicating an overall increase to the gas mass transport of approximately a factor of two. The ratio was comparable to the ratio found for dilute groups in the Pseudo-infinite tube (2.4, $\sigma = 1.3$, normally distributed), but slightly lower, which may be due to wall effects. However, the two average ratios between measured and theoretical rise speeds agreed within their standard deviations, so there was not a significant difference between these values.

The bubbles in dilute groups in the Constrained case had a greater range of measured values for the dilute groups ranging $5.3\text{-}42.1\text{ mm s}^{-1}$, compared to $14.3\text{-}32.8\text{ mm s}^{-1}$ in the Pseudo-infinite case. However, the majority of bubbles in the Constrained case had a measured rise speed between 5 mm s^{-1} and 15 mm s^{-1} , suggesting that, overall, the Constrained bubbles travelled slower than in the Pseudo-infinite case. This could be due to viscous effects with the constraining wall, and/or a consequence of selecting smaller bubbles due to the spatial resolution in the Constrained experiments being much greater, so smaller bubbles were resolved more clearly. As the data showed that bubbles travelled faster than the theory predicts, the dominant effect modifying the bubble's speed was the group behaviour of the bubbles, rather than the edge effects, which would slow down the bubbles through viscous opposition to movement.

6.3. Dense Groups

Bubbles in dense groups travelled much faster than their theoretical speed indicating a strong group effect (Figure 6.8). The gradient of the linear fit was much closer to zero than for single and dilute columns, suggesting that bubble size was not the main control on an individual bubble's speed. Further, there was no statistically significant correlation between the measured and theoretical rise speeds (Pearson's $R = 0.247$, $p = 0.147$), suggesting that the size of a bubble was not a significant control on the measured rise speed of that bubble. There was also no significant correlation between the theoretical rise speed and the theoretical-measured residual (Figure 10.6) (Pearson's $R = 0.3731$, $p = 0.0250$) indicating that within the group there was no significant change in rise speed with respect to bubble size.

While there were some variations in the size of bubble measured, reflected in the range of theoretical speeds ($1.8\text{-}10.6\text{ mm s}^{-1}$), dense groups tended to be mainly composed of bubbles of similar sizes (the bubbles measured ranged from 0.59 mm to 1.46 mm in diameter). This was in contrast to the dilute groups which had a greater range of bubble diameters: from 0.59 mm to 2.27 mm . The comparatively homogeneous bubble size in the dense groups suggested that these groups formed when many similar sized bubbles nucleated in a sufficiently small volume over a short time period and any larger bubbles that nucleated could break free from the groups before they rose into the field of view of the camera. The nucleation process was not easily observable due to optical distortions and the construction of the experimental apparatus (Figure 5.13) in the experiments so it was not possible to test this hypothesis.

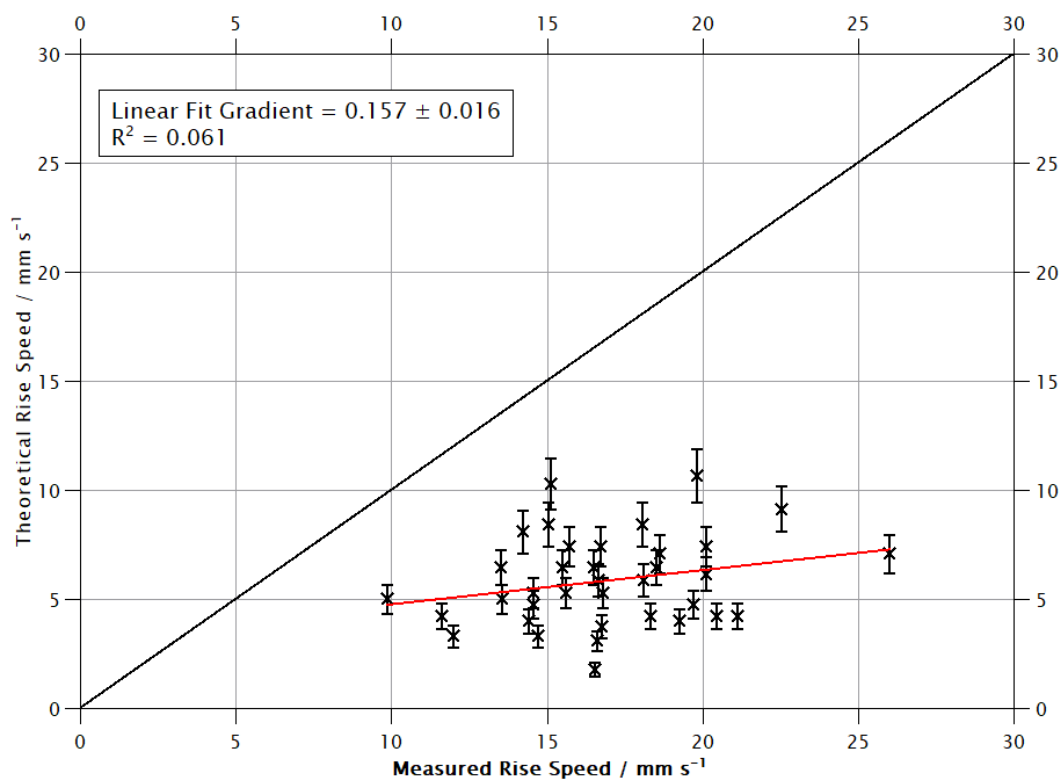


Figure 6.8: Theoretical and measured rise speeds for selected bubbles in dense groups. A very weak positive correlation was shown between the measured and theoretical rise speeds.

The average ratio between the measured and theoretical rise speeds was 3.3 ($\sigma = 1.5$, normally distributed) in the 25 mm tube which was slightly higher than the average ratio of 2.6 ($\sigma = 0.9$, normally distributed) for the Pseudo-infinite case, suggesting that the walls of the tube constrained the bubbles in the groups closer together, reducing the group's overall density relative to the surrounding oil. The ratio of 3.3 also showed that the high gas volume fraction groups were an even more effective means of increasing the rise speed of bubbles than dilute groups by approximately 50 % across the two samples of bubbles selected in the experiments.

In the Constrained case, bubbles in dense groups (9.9-26.0 mm s⁻¹; mean = 16.9 mm s⁻¹, $\sigma = 3.2$ mm s⁻¹, normally distributed) ascended more slowly than in the Pseudo-infinite case (17.1-51.4 mm s⁻¹; mean = 31.0 mm s⁻¹, $\sigma = 9.2$ mm s⁻¹, normally distributed). Due to the constraining walls, there may have been non-negligible wall effects. To test this, a group travelling through static fluid in the 25 mm tube was compared with a group travelling through static fluid in the Pseudo-infinite tube (Figure 6.9). The group in the constrained tube had an estimated initial volume of 195 mm s⁻¹ (effective diameter of 7.2 mm if the group was a sphere of the same volume) and an estimated gas

volume fraction of approximately 0.25. This yielded an estimated density difference between the oil of 0.296 g cm^{-3} , whereas the group in the pseudo-infinite tube had an estimated initial volume of 264 mm s^{-1} (effective diameter 8.0 mm) and an estimated gas volume fraction of 0.15. Thus, the estimated density difference between the group and the oil was 0.099 g cm^{-3} . The group in the constrained tube travelled at an average speed of 23.3 mm s^{-1} for 3.8 s while the group in the pseudo-infinite tube travelled at 36.8 mm s^{-1} for 5.0 s .

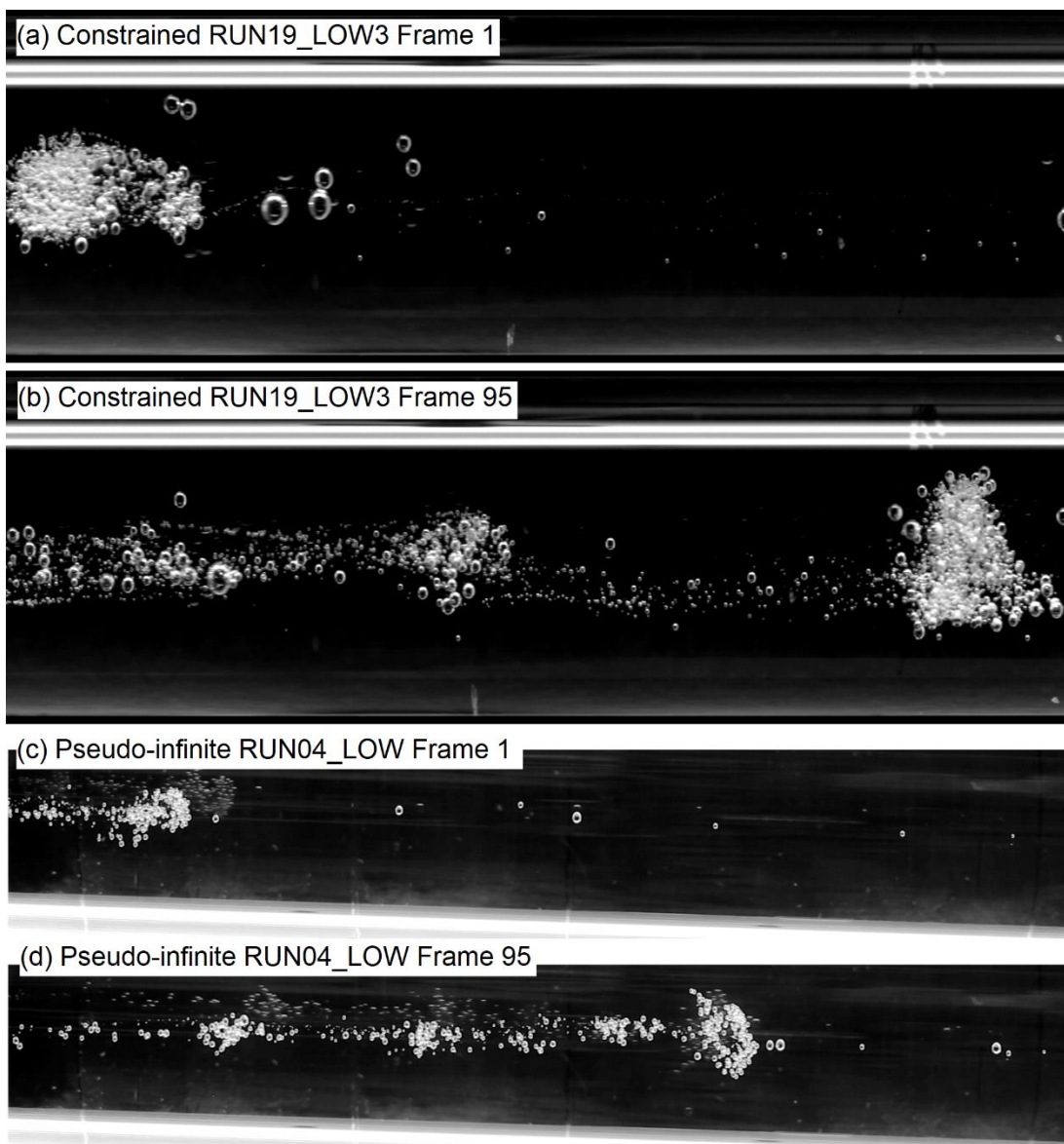


Figure 6.9: Two dense groups. (a) and (b) show a dense group in the constrained experiment while (c) and (d) show a constrained group in the pseudo-infinite experiment. The field of view in (a) and (b) was approximately 10 cm whereas the field of view in (c) and (d) was approximately 20 cm. The dense group in (c) has a larger estimated volume than the group in (a), despite appearing to be smaller in the image.

Using the Park et al. (2017) model for large bubbles it was possible to provide a first-order estimate of the speed by modelling them with the same volume and density difference between the oil. For the constrained group, the Park et al. (2017) model projected a rise speed of 50.2 mm s^{-1} and a rise speed of 39.4 mm s^{-1} for the pseudo-infinite group. The model predicted the rise speed of the pseudo-infinite group reasonably well given that the volume and gas volume fraction values were estimates. However, the value it returned for the constrained group was much higher than the observed value. The constrained dense group, however, had an estimated width of 6.4 mm, meaning that its diameter was approximately 25% of the width of the tube itself. For a solid sphere of the same size, anticipated edge effects can be accounted for (Brizard et al., 2005), it would be expected that the edge effects would serve to increase the drag force by a factor of 1.9, given the relative diameters of the bubble group and tube, and in this instance, it was assumed that the edge effects on a solid sphere are comparable to those experienced by a group of bubbles, which has an internal rotation of bubbles and is highly deformable. In order to balance buoyancy, the speed of the sphere would reduce by the same factor, indicating an expected rise speed of 26.4 mm s^{-1} for the constrained dense group. While the adjusted model prediction was still larger than the observed value of 23.3 mm s^{-1} , it indicated that even with a number of assumptions, the edge effects induced by the reduction of the tube diameter may adequately explain why the dense group in the constrained tube travelled much slower than expected. The group in the pseudo-infinite case had an equivalent diameter of 8.0 mm, which was $1/10^{\text{th}}$ of the tube's internal diameter (80 mm) and so edge effects were negligible (Brizard et al., 2005).

6.4. Other Features

The relative incidence of touching pairs of bubbles in constrained tubes was much lower than non-touching bubbles; however, a greater number of touching pairs were observed in the 25 mm tube experiments than the pseudo-infinite tube experiments. 75 instances of touching pairs were observed across 10 videos, as opposed to 10 instances across 15 videos in the pseudo-infinite experiment. Each video was approximately 45 to 60 seconds in duration and with an estimated total number of bubbles to be on the order of 10^5 to 10^6 . As such, only approximately 150 ($1.5 \times 10^{-2} \%$ to $1.5 \times 10^{-1} \%$) of the bubbles that nucleated formed into touching pairs so they constituted a very minor fraction of the modes of bubble behaviour, and the majority of bubbles did not generate touching pairs. As such, the role of touching pairs in altering the outgassing efficiency of the bubbly flow in the tube was taken to be negligible and not studied in further detail. Fewer than five instances of the coalescence of touching pairs was observed, indicating that either the timescale of

coalescence was longer than the typical timescale that touching pairs are visible for (10-20 seconds), or that an additional force or deformation would have been required to promote significant coalescence. The rarity of coalescence events in these experiments showed that coalescence was not a significant mechanism for increasing the rise speed of gas towards the surface in these experiments, in the portion of the tube where the camera was recording.

More than two bubbles touching, or foams, were not observed. As such, it was determined that simply reducing the inner diameter of the tube from 80 mm to 25 mm, while not changing any other parameter was insufficient to cause foams to form. A further reduction of the diameter of the tube, or alterations to the shape or inclination of the tube walls may promote foam production.

6.5. Summary

As with the pseudo-infinite experiments, the single bubbles were appropriately modelled, within uncertainty, by the Hadamard-Rybczynski model. However, a detectable increase in measured speed was noticed in some bubbles. The bubbles which rose at speeds greater than expected were observed, at least partly, during or shortly after the injection of oil at the base of the experiment. By tracking the position of these bubbles before, during and after the injections it was possible to show that before the injection, the model agreed with observed rise speeds well, but during the injection period, the bubbles temporarily accelerated vertically. Simple modelling suggested that the nucleation of bubbles was a plausible explanation for both the increase in height achieved by the bubbles and the increase in speed during the injection period.

The dilute groups demonstrated different behaviour to the pseudo-infinite case as there was a strong and statistically significant correlation between the theoretical and measured rise speeds (as opposed to a weak and non-statistically significant rise speeds in the pseudo-infinite experiments). It was proposed that the reason that the size of bubbles had a measurable effect on the measured rise speed in the constrained case was because the bubbles experienced a relatively constant local bubble number density in the dilute case due to the lack of lateral expansion of groups, whereas in the pseudo-infinite experiments, the bubble groups were able to expand laterally over time, changing their local gas volume fractions and bubble number densities. It was interpreted that the temporal variations observed in the pseudo-infinite cases masked the dependence of bubble size on rise speed. Therefore, in the constrained case, where the conditions remained relatively consistent, a pattern of dependence on bubble size was detectable but had previously been masked in the pseudo-infinite case by the possible lateral expansion

of the groups themselves. Additionally, as smaller bubbles appeared to travel slower than the larger bubbles even after their lower buoyant rise speed was taken into consideration, as shown by the statistically significant correlation between the theoretical-measured residual and theoretical rise speed. This may have been caused by a hindering effect whereby the motion of the large bubbles through the tube impeded the rise of smaller bubbles.

For dense groups there was, as with the pseudo-infinite experiments, no statistically significant correlation between the theoretical and measured rise speeds, indicating that the size of the bubbles was not a significant control on the speed at which the bubbles rose. There was a small increase in the ratio between measured and theoretical speeds compared to the pseudo-infinite case, potentially suggesting that dense groups may be more strongly affected by constraining walls causing the dense groups to have a greater gas volume fraction and so a faster rise speed. However, the majority of the bubbles travelled at a slower rate (16.9 mm s^{-1} ; $\sigma = 3.2 \text{ mm s}^{-1}$) than in the pseudo-infinite experiments (31.0 mm s^{-1} ; $\sigma = 9.2 \text{ mm s}^{-1}$). As there was no statistically significant correlation between the bubble size and the measured rise speed, the preference to select more smaller bubbles in the constrained tube (due to higher spatial resolution) cannot explain this. Instead, it was proposed that the narrower tube generated non-negligible edge effects, and modelling showed that a typical dense bubble group in the constrained case would be expected to have edge effects which may explain the observed reduction in speed. Although the model assumed a single spherical bubble/sphere rather than a highly deformable group of bubbles, the model outputs were not expected to be accurate beyond a first-order approximation.

Touching pairs of bubbles were observed to be slightly more common in the constrained tube than in the pseudo-infinite tube. However, they still constituted a very small fraction of the total number of bubbles produced and there was no evidence to suggest that these had an important role in affecting the overall rise speed of gas bubbles in the tube. Additionally, no evidence of foams was observed, indicating that nucleation and vertical wall constraints were insufficient in order to produce foams within the experiments. Coalescence was, as in Chapter 5, rarely seen, although given that the estimated time scale for coalescence was comparable to, or greater than, the time that bubbles were typically visible for, this was not unexpected.

In each of the three main bubble types observed (single bubble/in a dilute group/in a dense group), differences noted between the constrained and pseudo-infinite cases. In the single bubbles, the injection of oil into the tube at the same time as the observations of rise

speed causes the bubbles to increase in speed such that the Hadamard-Rybczynski model did not accurately describe the bubble's motion relative to the tube walls. However, bubbles which were observed prior to injection were described well, and the dilute and dense groups were observed approximately 5-20 s after the injection ended, so the increased speed during oil injection would not have affected those groups.

In the dilute groups, the impact of bubble size on measured rise speed was no longer masked by variations in the local conditions (bubble number density and gas volume fraction) experienced by that bubble. It was proposed that the constraining walls impeded lateral motion of groups, meaning that the column of bubbles had fewer vertical heterogeneities in bubble number density than in the pseudo-infinite tube.

In the dense groups, the diameter of the groups was sufficiently large as to be a significant fraction of the tube's diameter, and so measurable edge effects were expected in the constrained tube that were negligible for comparable groups in the pseudo-infinite case. Simple modelling of the groups as spheres suggested that, to first order, edge effects from the tube walls may be responsible for the observed reduction in the ratio between the theoretical and measured rise speeds for the constrained tube compared to the pseudo-infinite tube.

7. Bubbles in Inclined Tubes

Having investigated bubble rise behaviour in pseudo-infinite fluids and laterally constrained fluids in the experiments described in the previous two chapters, the experiments reported in this chapter considered the behaviour of bubbles in an inclined conduit. The inclination of the tube was 4.3° and yielded visibly different bubble behaviours compared to the vertical tube in Chapter 6. Steeper inclinations would have required significant modifications to the apparatus due to the position within the laboratory. The results presented in Chapter 7 were from the 40 mm internal diameter tube. A 40 mm tube was used as strong optical distortion in the 25 mm tube meant many of the bubbles were no longer visible. The 80 mm tube was deemed too heavy to incline safely.

7.1. General Features of Behaviour

As expected, bubbles typically rose to the upper side of the tube creating a visually noticeable difference in the bubble number density across the width of the tube (Figure 7.1). The vast majority of bubbles rose in a narrow column parallel to the tube walls, referred to as the main stream.



Figure 7.1: Example of typical bubble behaviour in an inclined tube (internal diameter of 40 mm). This image was from 11.56 s in video RUN07_LOW. Note that the camera was not aligned perfectly vertically, and was approximately 2° from vertical, making the tube inclination in the image appear greater than 4.3° .

However, larger bubbles showed a notable exception to the wall-hugging behaviour and tended to travel further away from the tube walls than smaller bubbles. This was interpreted as the effect of the laterally moving, and incompressible, oil around the bubble pushing the bubble away from the wall.

Despite larger bubbles separating from the tube wall, almost every bubble observed in these experiments was found within one third of the tube's diameter away from the upper side tube wall, except for during dense group breakups (Section 7.4.1), where bubbles temporarily moved laterally much further than large bubbles acting independently before rising buoyantly. In the breakup of dense groups, some bubbles could traverse

approximately 80 % of the tube's width (for example, Figure 7.6, Frame 300), however these bubbles later rose buoyantly towards the main stream of bubbles.

7.2. Single Bubbles

As with the previous instances of single bubbles, the Hadamard-Rybczynski equation successfully modelled the measured rise speed of the bubbles (Figure 7.2). The Hadamard-Rybczynski model assumed that the bubbles were travelling vertically and not near the tube wall, however no adjustment was made to account for the inclination of the tube, as it was not known exactly what effect the tube wall would have on measured rise speed. The strong agreement between theoretical and measured values for single bubbles in the rise speed justify not accounting for this, as the magnitude of the effect must have been small relative to the magnitude of the uncertainties. For the inclined tube, twenty bubbles were measured as single bubbles and of these, all agreed with the model within uncertainty, indicating that, for single bubbles, the inclination of the wall did not yield a measurable deviation from the Hadamard-Rybczynski model, justifying the lack of correction to the model for an inclined tube. There was a strong correlation between the measured and theoretical rise speeds (Pearson's $R = 0.9939$, $p < 0.00001$), indicating close agreement of the model across all measured bubble sizes. Additionally, there was a low-to-moderate, but not statistically significant, correlation between the theoretical rise speed and the residual between the theoretical rise speed and measured rise speed (Pearson's $R = 0.3324$, $p = 0.1522$) indicating that any variations away from the model were random and not systematic.

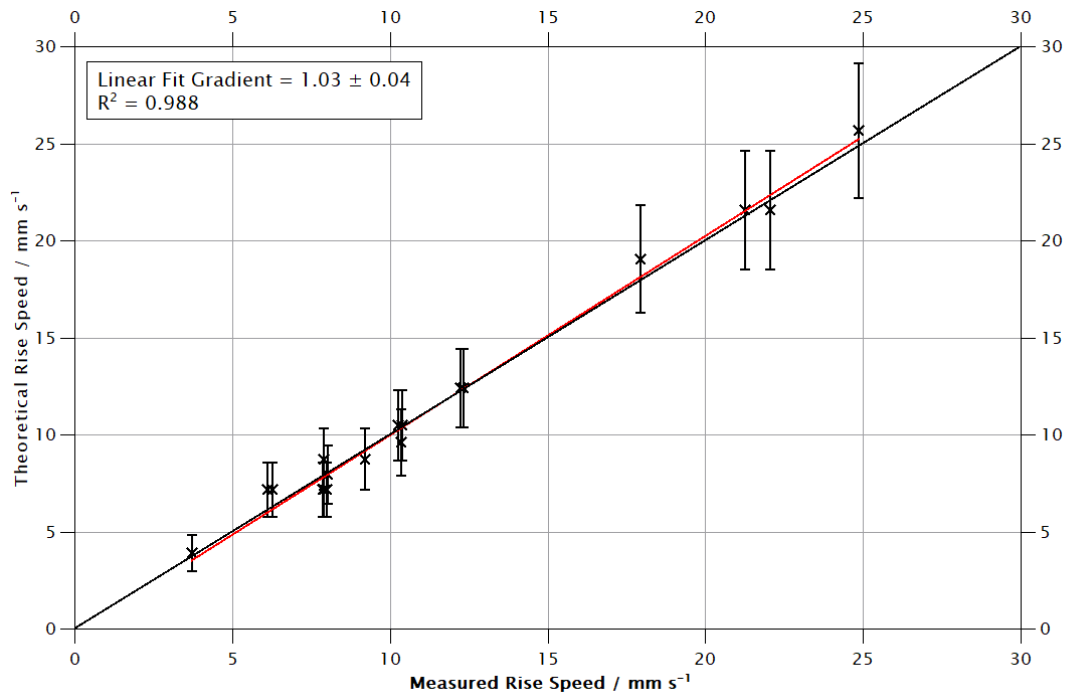


Figure 7.2: Theoretical and measured rise speeds for single bubbles in an inclined tube.

7.3. Dilute Groups

The bubbles in dilute groups behaved in a similar manner to the dilute groups in Chapter 6, where the bubbles consistently rose faster than expected by the single-bubble model and there was a strong correlation (Pearson's $R = 0.8557$, $p < 0.0001$) between the theoretical rise speed and measured rise speed (Figure 7.3). There was a weak positive gradient (0.462 ± 0.027 , $R^2 = 0.732$) between the theoretical and measured values, indicating further that the size of a bubble has some control on the measured rise speed of that bubble. The correlation between the theoretical rise speed and measured-theoretical residual was $R = -0.5206$ ($p = 0.0023$) indicating that smaller bubbles have lower ascent velocities than larger bubbles within the same group, even when the lower buoyancy of those bubbles was taken into consideration. This may be due to a hindering effect reducing the rise speed of the smaller bubbles, as suggested may have been the case in Chapter 6. This effect was not observed clearly in Chapter 5, which may be because the size-dependent rise speed of the bubbles was not clearly observed rather than the effect not occurring.

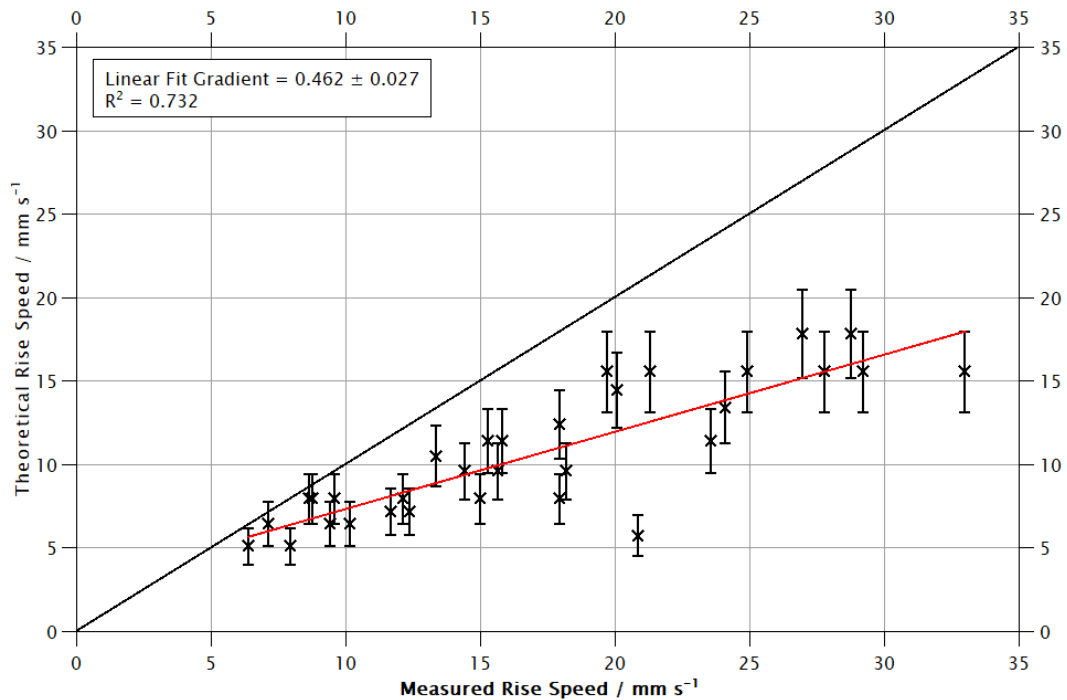


Figure 7.3: Theoretical and measured rise speeds for bubbles in dilute groups in an inclined tube.

The average ratio between measured and theoretical values was 1.6 ($\sigma = 0.5$, distributed normally), which was lower than the ratio for vertical tubes (2.1, $\sigma = 0.6$). Visual inspections of typical dilute groups (Figure 7.1 versus Figures 6.6a and 6.6b) showed that a similar number of bubbles were confined to a smaller relative width of the tube, so bubble number density and gas volume fraction were higher. Because local bubble number density appeared to be a significant control on a bubble's speed within a group, it was expected that these bubbles in the inclined tube would have faster average rise speeds than in the vertical tube. However, as the bubbles in the inclined tube were much closer to the tube wall, it was possible that viscous effects reduced the rise speed of the groups. Additionally, some of the bubbles classified as dilute bubbles were part of very dilute groups and so their rise speeds would only have been expected to have only very marginally increased thus reducing the average ratio between measured and theoretical rise speed. Furthermore, as the inclination of the tube caused groups to have a higher bubble number density, visually differentiating between a dilute group and a dense group was less clear than in Chapters 5 and 6. It was not possible to clearly observe bubbles for a sufficiently long duration to make measurements in the densest groups, so there was an unplanned selection bias in favour of bubbles in more dilute groups due to the increased bubble number density. The selection bias and viscous effects due to the proximity to the

tube form plausible explanations for why the average ratio between measured and theoretical values was lower in these experiments than in the vertical tube.

One notable difference between the vertically constrained and inclined dilute bubbles was that the linear fit between theoretical and measured rise speeds had an x-intercept of -5.80 mm s^{-1} in the inclined case (Figure 7.3), as opposed to $+2.5 \text{ mm s}^{-1}$ in the vertically constrained experiments (Figure 6.5). In the pseudo-infinite dilute group there was no statistically significant correlation (but the x-intercept was approximately $+9 \text{ mm s}^{-1}$). The negative x-intercept for the inclined case indicated that the measured speed values of all bubbles were being reduced by a mechanism separate from the size-dependent interactions observed previously. The reduction in speed appeared to be consistent across a variety of bubble sizes as the trend line observed in Figure 7.3 was shifted laterally towards the left (i.e. lower speed values) separately from the changes in the line's gradient found in single bubble and bubble-bubble environments (Figures 5.1, 5.15, 6.1, 6.15). As a result, the increased rise speed of an individual bubble cannot be explained exclusively by the increase in rise speed from bubble-bubble interactions. This suggested that the stream of dilute bubbles (and any entrained oil), as a whole group, travelled slower than in the non-inclined experiments as this effect would manifest as a systematic reduction in the increase in rise speed for all bubbles, regardless of their size. However, the bubbles were shown to rise faster than predicted by the Hadamard-Rybczynski model, indicating that the effect of group behaviour to increase the ascent of bubbles through the tube was greater than the reduction in speed of the whole column of bubbles caused by viscous effects with the wall.

7.3.1. Bubble Driven Convection

While the majority of bubbles rose within a relatively small section of the tube's width, the main stream of bubbles entrained oil and moved it vertically upwards with the bubbles. As the net momentum of the oil must be zero (as the oil within the tube did not move as a whole), there must also have been a portion of the tube where oil moved downwards. This was not directly observable as the movement of the oil could only be inferred from the movement of bubbles within it. It was proposed that, as there were no observations of bubbles moving downwards in the videos (particularly during breakups of dense groups, for example in Figure 7.6), that the downwards flow of oil was likely to be slower than the vertically rising oil, but a greater mass of oil moved downwards.

It was probable that such an effect also existed in the columns of bubbles in the pseudo-infinite and constrained tubes, however there were no observations of bubbles moving down in any of these experiments.

7.4. Dense Groups

Bubbles in dense groups, as in Chapters 5 and 6, travelled many times faster than bubbles in dilute groups. In the inclined tube, the average ratio between the measured and theoretical speeds of bubbles in dense groups was 3.7 ($\sigma = 1.2$, normally distributed) compared to 3.3 ($\sigma = 1.5$) and 2.6 ($\sigma = 0.9$) in the constrained and pseudo-infinite experiments. This indicated that the bubbles moved multiple times faster than expected under the Hadamard-Rybczynski model, but there was considerable variation in that ratio with a minimum of 2.2 and a maximum of 6.0. The average ratio between theoretical and measured rise speeds was higher than for dense groups in the previous two experiments; however, there was still agreement within a standard deviation, so this increase was not considered notable. The viscous effects with the wall, suggested to slow dilute groups in the inclined tube, may be mitigated as larger bubbles (and groups of bubbles) tended to travel further away from the tube wall and so may have reduced viscous effects.

As in the pseudo-infinite and constrained vertical tubes, the gradient of the linear fit between measured and theoretical speeds was close to zero and for inclined tubes it was $(2.5 \pm 96.1) \times 10^{-3}$, indicating virtually no relation between bubble size and measured rise speed. Further, there was no correlation between the measured and theoretical rise speeds (Pearsons's $R = 0.0042$, $\sigma = 0.9886$, normally distributed) indicating that, in dense groups in the inclined tube, the size of the individual bubbles could not be used to determine the rise speed of that bubble. Only 14 bubbles were measured, as few suitable candidate bubbles were visible for a sufficiently long duration as to make useful measurements. The groups appeared to have higher bubble number density than in previous experiments, and this may partially explain why the bubbles in these dense groups travelled slightly faster than in the dilute or pseudo-infinite experiments.

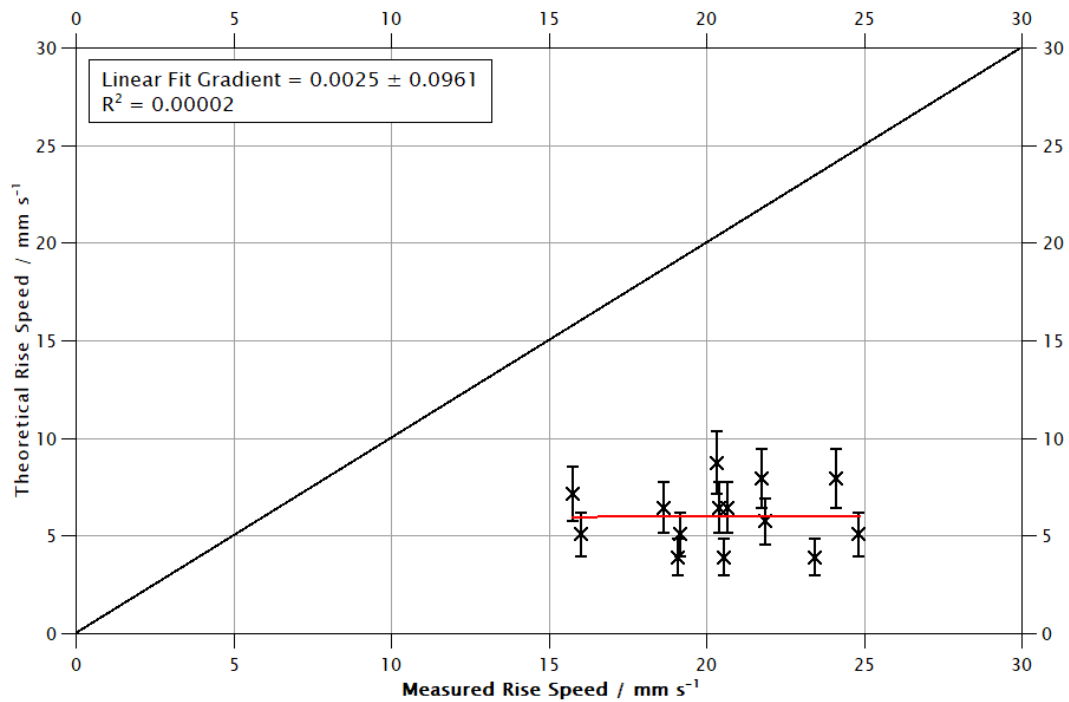


Figure 7.4: Theoretical versus measured rise speed for dense groups in an inclined tube.

The data also showed that there was little differentiation between the dense and dilute groups as, in the inclined tube, the classification of dilute and dense groups when making measurements was less distinct than in the previous chapters. This was likely a consequence of the inclination causing the dilute groups to have higher bubble number densities, approaching those of the dense groups.

7.4.1. Dense Group Breakups

As with dense groups in Chapters 5 and 6, dense groups maintained their form for a limited duration (approximately 5-10 seconds) before they broke apart and the bubbles which previously formed the group travelled at a lower rise speed. It was observed in the pseudo-infinite and constrained cases that dense groups tended to disintegrate laterally, which was a pattern also seen in the inclined experiments (Figures 7.5 and 7.6). In the inclined case, however, just before the dense groups broke apart, they moved away from the main stream of bubbles and into the region of the tube where the oil may have been moving downwards due to balancing the momentum of the upward moving oil entrained in the main stream. The combined effect of moving into downwards moving oil and the reduction of the group's bubble number density (and increase in volume) as it disintegrated caused the individual bubbles to decelerate relative to the tube walls. This was demonstrated in Figure 7.6 where there was very little movement of individual bubbles between

Frames 250 and 300 compared to the faster group movements between Frames 50 and 100. In Figure 7.5, however, the group had not fully disintegrated by Frame 251 and shortly after this frame the group left the field of view of the camera so its complete breakup process was not recorded.

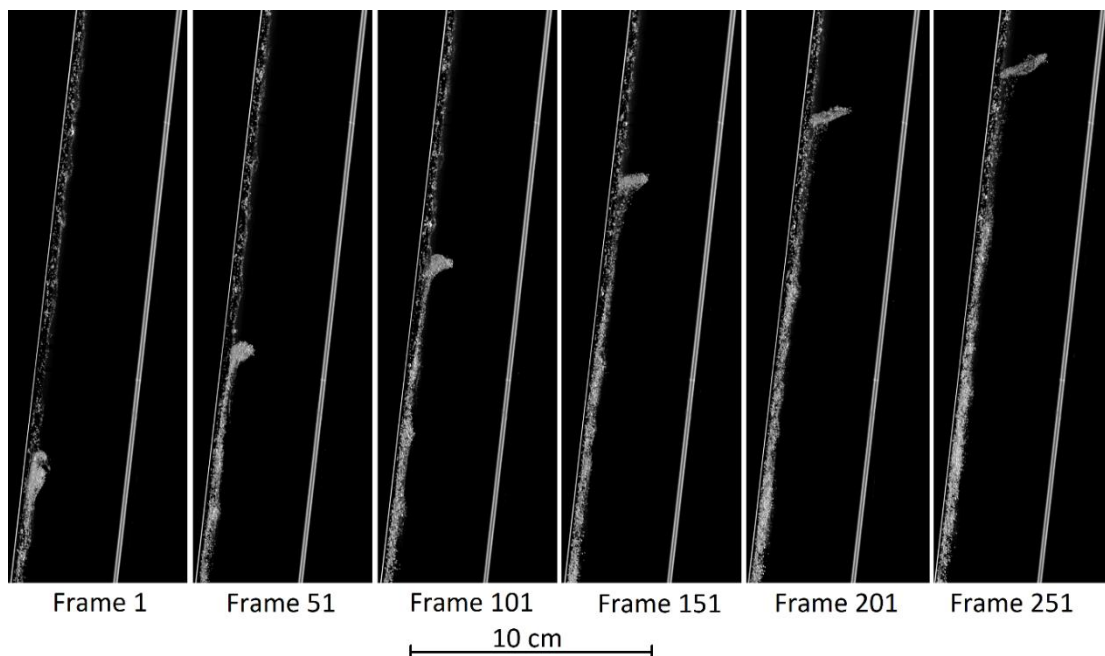


Figure 7.5: Images from RUN06_LOW1 demonstrating the breakup of a dense group.

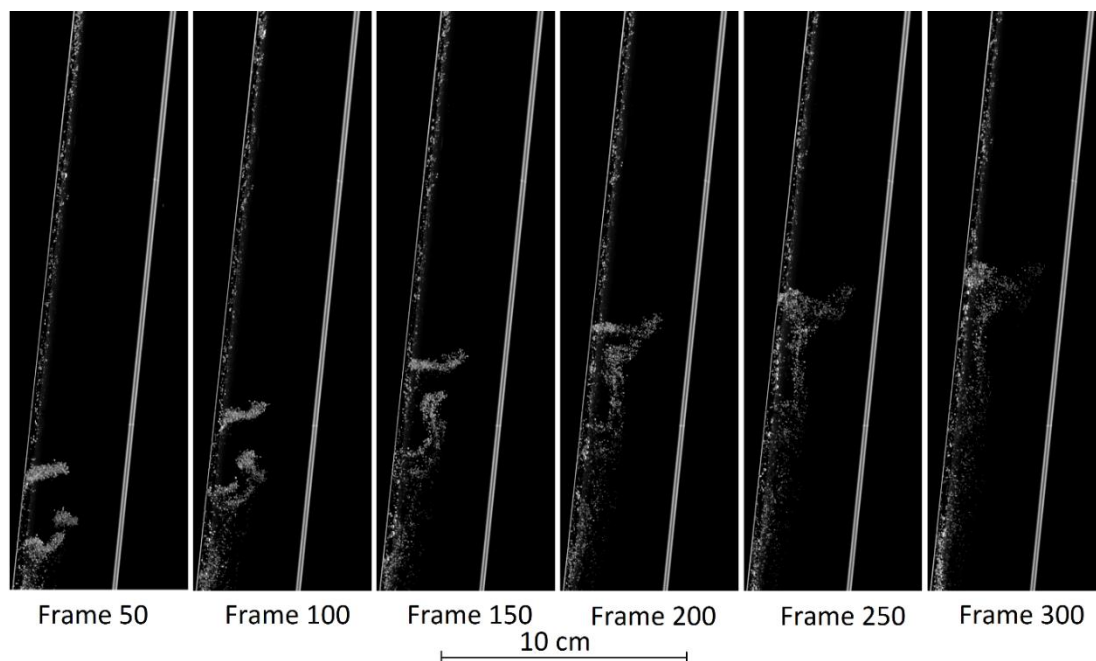


Figure 7.6: An example of the breakup of two dense groups from RUN07_LOW1.

7.5. Other Features

As in all previous experiments, touching pairs of bubbles and subsequent coalescence events were not observed in sufficient numbers to be considered a significant factor in affecting the overall movement of bubbles towards the surface. This may be due to the asymmetric shear force caused by viscous effects with the upper tube wall preventing bubbles from remaining in contact with each other. In a touching pair of bubbles, the bubble that was nearer to the wall would experience a greater viscous effect than the one further away, and this would result in those two bubbles rising at different speeds, causing them to no longer travel as a pair. Additionally, as no touching bubbles were observed, no foams were observed either, indicating that tube inclinations below 5° were insufficient to produce foams nor did they promote the coalescence of small bubbles into large bubbles, within the other parameters of this experimental equipment and the sections of the tube that were videoed.

7.6. Summary

These experiments, utilising a tube with an inclination of 4.3° from vertical, showed that even a shallow inclination produced visibly distinctive bubble formations, specifically that the main stream of bubbles occupied a relatively small portion of the tube's width near to the upper wall with a greater bubble number density than in the vertical experiments. Despite the visually observable increase in bubble number density in the main stream, the data suggested that this had a small impact on the rise speed of the bubbles compared to similar bubble number densities in vertical tubes as the average ratio between theoretical and measured speeds was similar, and comparable within a single standard deviation. The dilute groups did appear to travel slower than in the vertical constrained case, but dense groups travelled faster in the inclined case than in the vertical constrained case. This suggested that the viscous effects of the wall were comparatively stronger for the dilute groups, or that the dense groups were not as strongly affected by wall effects. Broadly, there was not a significant difference in the measured rise speeds between inclined and vertical constrained tubes, indicating that an inclination of 4.3° was insufficient to notably alter the overall rise speed of bubbles in the tube, except in dilute groups.

8. Discussion

8.1. Evaluation of Experimental Results

8.1.1. Bubbles Interactions Increase Rise Speed

In all measured instances where more than one bubble was present within approximately 5 diameters of other bubbles, the speed of ascent of those bubbles was increased (Figures 5.15, 5.19, 6.5, 6.8, 7.3 and 7.4). The main implication of this finding is that, while the Hadamard-Rybczynski model adequately described the buoyant ascent of a bubble in a static fluid, the bubbles themselves were generating a localised upward movement of oil. This was true, even for small bubbles (sub-millimetre scale) at relatively low gas volume concentrations (approximately 0.1 % and greater), and measurably increased the rise speed of all the measured bubbles in that system. The ratios between theoretical and measured rise speeds for even dilute groupings of bubbles were frequently in excess of 2, indicating that bubbles were often travelling at more than double the speed predicted by the Hadamard-Rybczynski model. As such, there was sufficient evidence to suggest that in order to accurately describe bubbly flow, interactions that increase bubble rise speed should be taken into consideration, as well as the hindering effects observed in other experiments (Section 2.5.3) which may have been responsible for the systematic variation in the theoretical-measured residual for the bubbles in dilute groups in constrained and inclined tubes. It was suggested that the reason for the increased speed was an increase in the speed of the oil, relative to the tube wall, that the bubbles moved through (due to overlying bubbles). Although not clearly demonstrated, bubbles with closer proximity appeared to have their rise speed increased more than bubbles further apart from each other as the effect on the oil by a moving bubble was greater nearer to that bubble, but the rise speed of a particular group of dense bubbles was also affected by the wider context of the group (Section 5.5.5). A greater effect at closer proximity was not unexpected, given that previous work had shown that the effects of bubble-bubble interactions were greater at shorter distances and the magnitude of the Stokes flow function around bubbles reduces with distance from the bubble (Equation 3-2 of Clift et al., 1978). The interaction with the fluid flowing around a bubble would therefore be reasonably expected to be greater at closer proximity.

8.1.2. Formation of Groups

In addition to rising faster when in groups, it was observed that collections of bubbles self-organised into groups soon after nucleation. It was interpreted that the clustering of

bubbles could be the partially the result of the Venturi effect. The Venturi effect would predominantly apply to pairs of bubbles which were separated only laterally, and sufficiently close that the flow field around each bubble overlapped with the flow field of the other, causing the speed of the downward moving oil between them to be greater than the speed of the downward moving oil on the outward side of a pair of bubbles. The increase in speed may result in a small reduction in pressure between them, which pushed the bubbles closer together. Previous work has also suggested that the Venturi effect may be responsible for the observed attractive relative motion between laterally separated bubbles (Legendre et al., 2003), although it has also been attributed to small deformations inducing lateral lift (van Wijngaarden, 1993). Although, conversely, for the Reynolds numbers of the bubbles in the Chapter 5, 6 and 7 experiments and the separation of the bubbles, previous work has suggested that the bubbles should be acting repulsively, rather than attractively (Yu et al., 2019). The high viscosity of the oil relative to the size of the bubbles may have meant that any attractive or repulsive behaviour was not detectable during the period that bubbles were visible on the videos, or that interactions with other bubbles and bubble groups elsewhere in the experimental tube disrupted the attractive/repulsive behaviour between a given pair of bubbles. Due to the lack of observation of the formation of groups, and the conflicting theoretical assessment that the bubbles should have been repelling each other, it was not clear exactly how or why the bubble groups formed, and due to the configuration of the experimental apparatus, it was not possible to observe the very early behaviour of the groups (Figure 5.13). However, some form of attractive mechanism caused multiple dense groups to form after the injection of volatile-rich oil into the tube, as evidenced by the existence of those groups (which did not form prior to the oil's emission from the injection needle), even if the mechanism for their formation could not be established.

For vertically aligned pairs of bubbles, the trailing bubble can deform while in the wake of the leading bubble causing it to accelerate upwards, although in volcanic cases, this would not be expected to occur for bubbles greater than 5 mm diameter (Manga & Stone, 1994). Deformations causing lateral motion may have been present in the experiments presented in Chapters 5, 6 and 7, but small deformations (e.g. $<O(10\%)$ increase in one axis as per Manga & Stone (1993) and Manga & Stone (1994)) may not have been detectable due to the spatial resolution of the videos, and observed lateral motion may have been exclusively caused by the motion of the oil that a given bubble was in. Many of the bubbles had small Eötvös numbers (mean of 0.85, $\sigma = 0.5$, maximum of 3.1) and dimensionless analysis showed that single bubbles ascending in static oil were in

the spherical regime. Closer bubble groupings appeared to accentuate the overall group effect and thus further increase their speed, as the bubbles in dense groups were found to ascend faster than bubbles in dilute groups.

In dilute groups, bubbles were able to move at a speed that was partially accounted for by their size (as opposed to dense groups where the size of the bubble had no statistically significant correlation to the observed rise speed). In those dilute groups, similar sized bubbles could be expected to rise at a similar speed (although this was a speed greater than their predicted buoyant rise speed). If those bubbles were located within approximately five bubble diameters of each other, the flow fields around those bubbles would have overlapped for longer periods of time than two bubbles of different size, and so self-organising groups generally contained bubbles of similar sizes. It was not clear how similar the bubble sizes needed to be in order to remain part of that group, as groups constantly changed their arrangements in terms of where bubbles were located within the group relative to each other, and long term behaviours were not possible to observe in the experiments. The transitory behaviour of groups made it impractical to provide general numerical descriptions of the groups and criteria for their formation. Substantial increases in temporal and spatial resolution in images may facilitate empirical descriptions, however the dataset collected for the preceding chapters was insufficient to make these descriptions.

The formation of dense groups occurred predominantly below the field of view of the camera and so the formation of those groups was not recorded. Further, the apparatus connecting the experimental tube to the base plate, and optical distortions caused by adaptors to modify the tube width meant that observation of processes shortly after bubble nucleation was not possible. Consequently, it was not possible to observe how dense groups formed, and the formative mechanism of dense groups could not be identified.

8.1.3. Bubbles Travel Faster in Most Configurations

Every bubble measured as part of a group travelled faster than predicted by the Hadamard-Rybczynski model. This included bubbles near to the constraining wall in Chapter 7 where the group-driven increase in rise speed was apparently greater than the viscous wall effect reducing bubble speeds. The average ratio between measured and theoretical rise speed in the inclined tube was 1.6 ± 0.5 , as opposed to 2.1 ± 0.6 and 2.4 ± 1.3 in the constrained and pseudo-infinite tubes respectively, indicated that bubbles were ascending at a slightly slower speed in the inclined tube where they were nearer the tube wall. However, the ratios were still mostly in agreement within their standard deviations, not all bubbles that nucleated were measured and not all bubbles within the tubes were valid candidate bubbles. In the inclined tube in particular, some bubbles were impossible to measure as

optical distortions completely obscured some bubbles from the camera. As discussed in section 7.3.1, there must have been portions of the experimental tube with downward moving oil. Bubbles in those regions must travel slower (relative to the tube wall) than if they were in static oil. The selection criteria for measurement and group types studied did not account for bubbles that may be in downward moving oil. Qualitative observations suggested that very few bubbles moved downwards relative to the tube walls, indicating that the speed of the downward moving oil was normally less than the buoyant rise speed of the bubbles. In the constrained and inclined experiments, the smaller bubbles in dilute groups appeared to travel at a slower speed relative to the larger bubbles, even after the lower buoyancy was accounted for. This may have been due to a hindering effect caused by the larger bubbles acting on the smaller ones.

8.1.4. Bubble Induced Convection

Bubble induced convection was a complicated interaction between the bubbles and the momentum of the oil. It facilitated bubbles rising vertically much faster, relative to the tube wall, than they otherwise would have travelled. Without an external force causing bubble deformation leading to lateral lift, there was no reason for any bubbles to spontaneously travel laterally away from the convecting column of oil. There were fewer than twenty observations of touching pairs of bubbles without vertical symmetry travelling laterally, however these were not investigated further due to their rarity in the experiments.

Within the experiments, bubbles nucleated from oil injected into the centre of the base plate. Thus, for all vertical experiments, there was an expectation for convection to occur around the central axis of the tube, driven by the lower bulk density of the mixture in the centre compared with the oil nearer to the edge of the tube.

There was no particular reason why convections could not also form away from the central axis, depending on the (unpredictable) distribution of bubble nucleation near to the tip of the injection needle. By contrast, in the inclined tube, the component of the bubble speed towards the tube wall was non-zero and so the upward component of bubble-driven convection was consistently observed in the same portion of the tube near the wall.

8.1.5. Shallow Inclinations Altered Flow Configuration

The experiments demonstrated that a tube inclination of $<5^\circ$ caused near-immediate changes to the distribution of bubbles throughout the tube such that virtually all the bubbles were observed to travel near to the upper side of the tube. The only exceptions to this were during the breakup of dense groups and the largest of individual bubbles, which appeared to have the speed necessary to move measurably away from the tube wall.

Greater deviations from vertical may yield different results, as the viscous effect with the nearest wall may eventually overcome the increased local bubble number density/gas volume fraction above a particular critical angle. The experiments demonstrated that an inclined system may present a very different spatial bubble distribution to the vertical system at even shallow inclinations. Although the experimental results did show a slight decrease in the average speed of the groups in the inclined tube (Section 7.3), it was within the standard deviation of the average ratio between the measured and theoretical rise speeds in each of the three experiments. Additionally, bubbles within very dense groupings of bubbles were not easily measured as they were not visible for a sufficient duration in order to make measurements. Generally, only bubbles on the edge of those dense groups were measured, and the time between the starting and end positions was usually shorter than for bubbles in dilute groups, as a given bubble was rarely clearly visible in a dense group for an extended duration. As such, there was a selection bias against what were likely to have been the fastest moving bubbles in the inclined tube. There was a greater bubble number density in the main stream of bubbles in the inclined tube compared to the other two tubes due to the inclination itself confining bubbles to the upper portion of the tube. The increase in number density resulted in increased difficulty when selecting bubbles to be measured, as they were more often obscured by other bubbles. The obscuration of bubbles due to increased local bubble number density may be even more pronounced at greater angles of inclination, so future experiments may require adjustments in order to facilitate measurements at greater angles of inclination.

8.1.6. Returns Flows were Slow and/or Wide

A consequence of bubble driven convection is that some oil must be moving downward. There were no quantitative measurements of bubbles travelling downwards, which was partially a consequence of the selection criteria for groups not including outlying bubbles, but it may also have been due to the speed of the downward moving oil being less than the buoyant rise speed of bubbles in these areas. As bubbles in dilute groups often travelled faster than twice their buoyant rise speed, it was inferred that the upward convection speeds could be greater than the buoyant rise speed of those bubbles. Further, if a bubble were to drift towards the downward moving portion of the oil, for whatever reason, it would experience a non-uniform flow across the upper surface of the bubble, which could impede the bubble's lateral motion, possibly due to deformation-induced lateral lift, and inhibiting its entrainment further into the downward moving oil.

In order to balance momentum, the downward component must either include the same mass travelling at the same speed, or a greater mass travelling at a slower speed, or

a smaller mass moving at a greater speed. Given that only minimal qualitative observations of downward moving bubbles were made, the second scenario was judged to be more likely. A greater mass of oil moving slower than the upward component would require that the downward portion of the tube occupied a greater portion of the tube's width than the upward component to ensure a balance of momentum. The expected downward velocity profile likely varied across the width of the tube as the speed at the tube walls and at the boundary between the upward and downward portions would both have been zero, with continuously increasing speed across the tube width until the point of maximum downward speed (Figure 8.1).

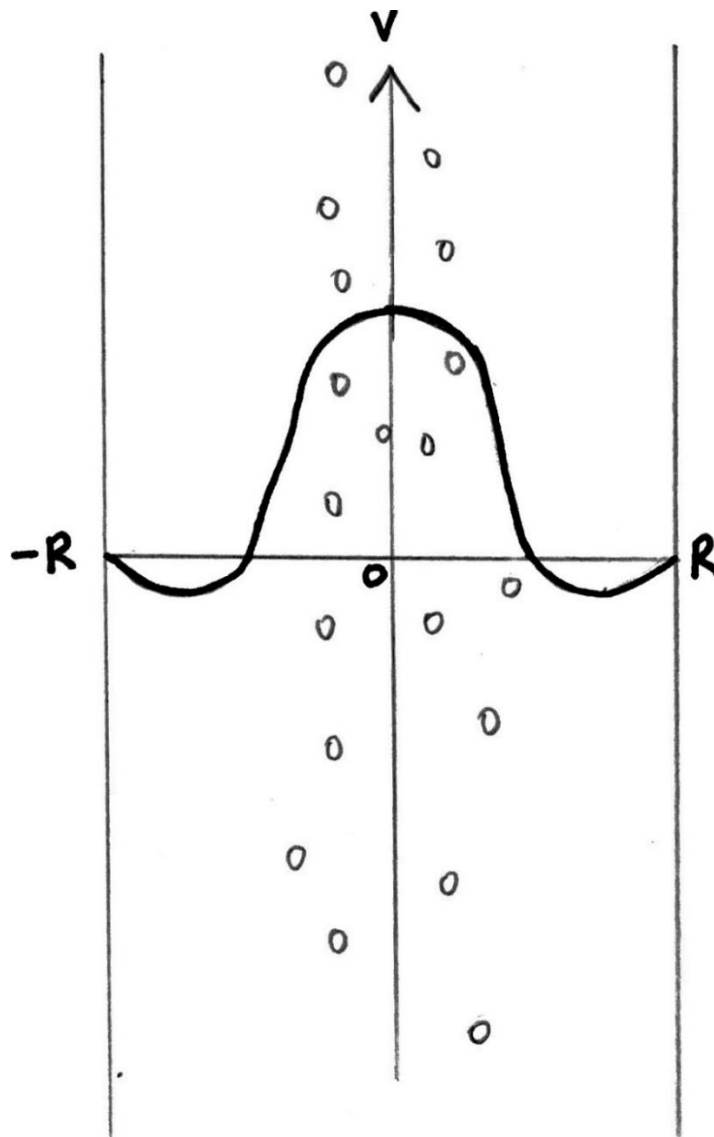


Figure 8.1: Sketch plot of how the vertical velocity of the oil, v , may vary with distance from the centre of the tube (marked as 0) across a tube with radius R when a column of bubbles (small grey circles) rises through the centre of the tube. Due to the conservation of momentum, the integral of v with respect to the distance from the central axis evaluated between $-R$ and R must equal zero, unless the surface of the oil is rising. Not drawn to scale.

In the inclined tube, as the upward portion of the bubble driven convection was confined to a small part of the tube's width near to a wall, the downward moving oil likely occupied the remaining parts of the tube's width resulting in slower, but wider, downward moving oil than in the vertical tubes (Figure 8.2).

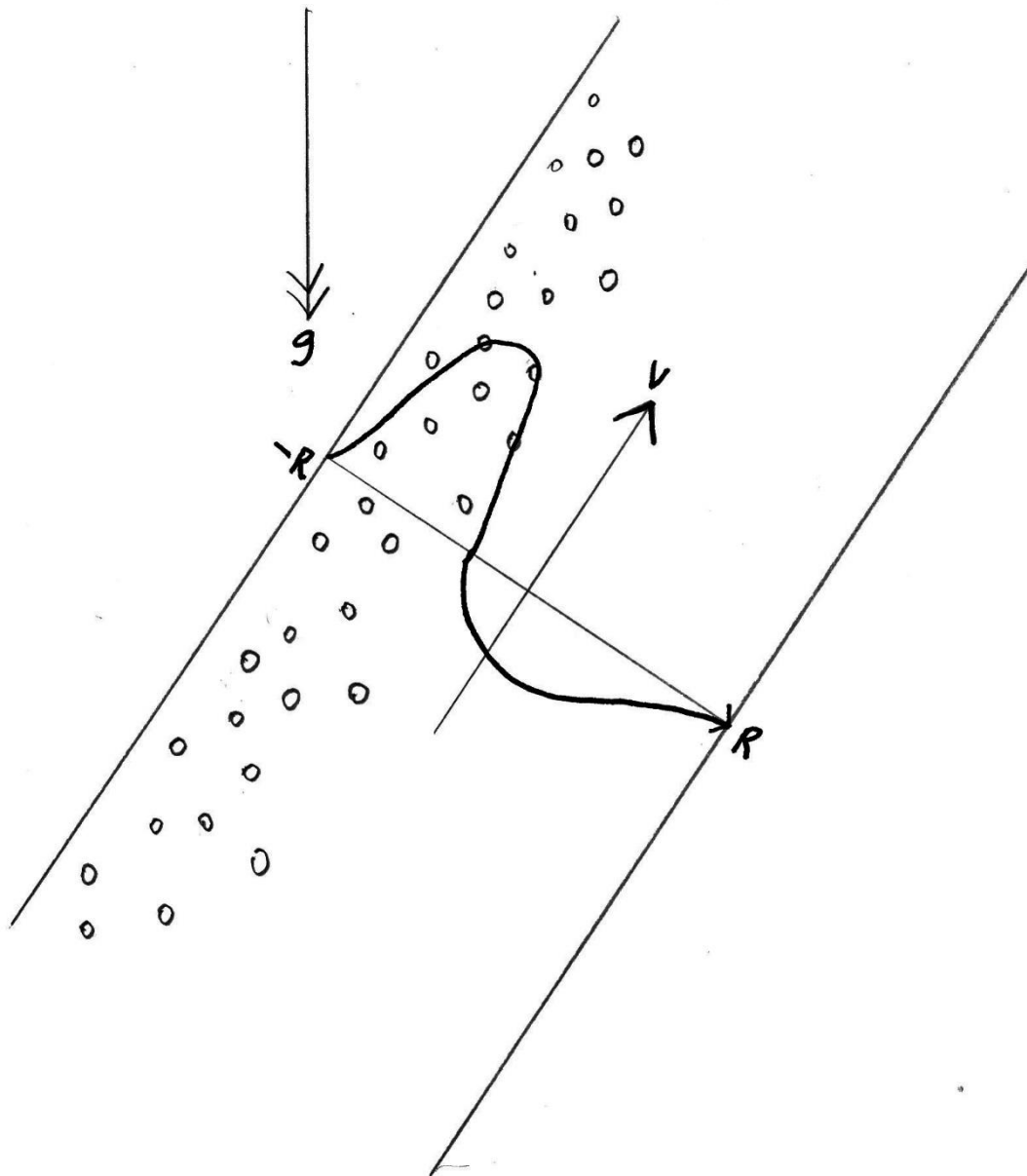


Figure 8.2: Sketch plot of the expected velocity of oil of an inclined tube in the direction of the tube walls. The direction of acceleration due to gravity, g , is shown. Not drawn to scale.

8.1.7. Coalescence was Rare

It was initially thought that the experimental conditions may be appropriate for observing coalescence and examining the effect that fewer, larger, bubbles had on the movement of gas through the tube. However, the experiments showed very few instances of coalescence

indicating that, at least in the parameter space explored, coalescence was not a primary mechanism for increasing the efficiency of gas bubble separation from oil. The timescale of coalescence was anticipated to be of the order of 20 s (Section 5.5.3) which was comparable to, or less than, the amount of time that bubbles were typically observed on the videos. However, this timescale was for touching pairs of bubbles, which were not observed in significant numbers, nor were non-touching pairs seen to become touching pairs. As touching pairs were not seen to form on the videos, the few that were observed must have formed at a point in the tube below the LOW camera. As such, it was inferred that they formed at the point of, or shortly after, the nucleation of bubbles, so the control on the touching pairs may have been linked to the rate and quantity of nucleation events just after the oil was injected into the experimental tube. The formation of touching pairs may have been related to contaminant particles in the oil providing a preferential nucleation site for bubbles, akin to heterogeneous bubble nucleation in magmas (Shea, 2017). The quantity of nucleation events could have been controlled by injecting different quantities of oil, injecting oil with varying amounts of dissolved air in it, altering the pressure difference between the syringe and the experimental tube, and altering the rate of decompression between the syringe and the base of the experimental tube. Altering the rate of decompression and the amount of dissolved air may have had the greatest impact, but would also have required substantial changes to the apparatus and procedure in order to increase the rate of decompression and increase the amount of dissolved air.

8.1.8. Size Stratification

In dilute groups, larger bubbles were shown to have their speed increased by a greater amount than smaller ones, and this dependence on bubble size was significant in the constrained and inclined cases (Figures 5.13, 6.5, and 7.3). This resulted in bubble columns tending to develop size stratification as the larger bubbles ascended to the surface at a faster speed than the smaller ones, rather than all the bubbles travelling at the same speed regardless of the size of the bubble, as seen in dense groups. As the larger bubbles travelled towards the top of the tube much faster than the smaller ones, and that bubbles of comparable sizes tended to group together. Given a sufficiently long duration and length of tube following an injection of volatile-rich liquid, a likely consequence appears to be size stratification, and for this to develop alongside the expected stratification arising purely from larger bubbles having greater buoyancy.

The size stratification was in addition to the stratification which may occur from the hindered rising of bubbles, a process used in numerous industrial applications (Young & Klima, 2000). The hindering effect may have caused the smaller bubbles in the

dilute groups for the constrained and inclined tubes to have disproportionately lower rise speeds compared to the larger bubbles in those groups, as evidenced by the systematic drift in the theoretical-measured residual as theoretical rise speed increased (Figures 10.5 & 10.8). Numerical modelling has shown that, even when the effect of group behaviour on bubbles' speed was not taken into consideration, size stratification occurred (Figure 4 of Frederix et al., 2019). However, as the standard deviation of bubble sizes became greater, effects not seen in the experimental tube were predicted, specifically that the larger bubbles occupied the edges of the tube while the smallest bubbles occupied the centre of the tube. Note that, unlike in the experiments, the bubbles in the Frederix et al. (2019) simulations were not from a single region in the centre of the tube. Despite the discrepancy between experimental observations and numerical modelling, even in the simulation with the greatest variety of bubble sizes calculated by Frederix et al. (2019), vertical size stratification was still demonstrated. Given the size-dependent nature of bubble's rise speed in dilute groups as shown in Figures 6.5, and 7.3, theoretical models may have under-estimated the extent to which bubbly columns self-organise into size stratified columns on relatively short length scales, which then affected the rise speed of those bubbles.

The effect of inclination of the tube on vertical size stratification was not measured. As there was an observed lateral size stratification when the tube was inclined, the largest bubbles occupied the same parts of the tube's width prior to group effects stratifying the bubbles' size vertically. The lateral size stratification may have aided in forming the vertical size stratification more rapidly, further increasing the efficiency of separating gas from the oil.

As a particular bubble moved through the tube while surrounded by other bubbles, it would have travelled either faster than the bubbles around it (due to being larger than them), slower than them (due to being smaller than them) or the same speed as them (due to being the same size). The relative speed also depends on the angle of separation between the bubbles (Wijngaarden et al., 2003; Hallez & Legendre, 2003), which induces varying vertical and lateral relative motion. As such, all the bubbles are constantly changing their relative positions, even when surrounded by bubbles of equal size, as observed in all experimental videos (See supplementary data: Section 10.2). However, when surrounded by bubbles of comparable size, it would not be likely that a bubble ascends faster once they achieve the same height, but only to ascend faster when they are trailing (Hallez & Legendre, 2011; low Re scenario in Kusuno et al., 2019). This would facilitate bubbles achieving the same vertical height, so groups of similarly sized bubbles would not

separate vertically, given no external forces applied in a non-uniform manner across the group. It was likely, therefore, that vertical size stratification was an inevitable outcome of the bubbles rising through a tube, given a sufficiently long duration, and caused the bubbles to tend to rise in groups of comparable sizes. Given a sufficiently long duration of injection of bubbles into the experiment, multiple distinct groups featuring similar-sized bubbles could form from a constant source of bubbles lower down in the tube, even with time-invariant bubble nucleation. These groups may travel at similar speeds to each other, although not necessarily, as the overall group speed appeared to be linked to the overall group size, as well as the surrounding circumstances of the group. An analogue between the circumstances of bubbles and groups of bubbles may be appropriate, as the dense groups trailing behind other dense groups were observed to travel faster (Section 5.5.5), and a bubble trailing behind another accelerates towards the leading bubble (Hallez & Legendre, 2011; Kusuno et al., 2019). However, distinct groups of different constituent bubble sizes would not necessarily reach the surface at the same time, causing temporal variations in the gas flux at the surface. The gas flux rate at the surface would likely vary temporally and may appear to be cyclical in nature, although there may be variations in the duration between each group arriving at the surface.

8.1.9. Short Scale Heterogeneities were Unavoidable

A significant problem in numerically describing the phenomena observed in the experiments was the presence of heterogeneities in several parameters, and the variation of those parameters on short timescales (of the order of 1 s) and length scales (approximately 1-5 cm). The parameters that exhibited spatial and temporal heterogeneities were primarily the local bubble number density, inter-bubble separation, local gas volume fraction, and bubble size distribution.

The local bubble number density, or gas volume fraction, varied considerably both spatially and temporally. It was not possible to control this parameter effectively as the main controls on the experiment (pressure at the top of the oil and injection duration) mainly affected the quantity of bubbles that nucleated, and the duration of time across which the nucleation events occurred.

Across the width of the tube, the number density of bubbles varied substantially, as the bubbles tended to rise vertically above the injection site rather than drift towards the walls. As such, the edge of the vertical tubes had almost zero bubbles, but the centre was populated by the majority of the bubbles which were found approximately within around 2 cm of the central axis in the pseudo-infinite tube and within 1 cm in the 25 mm tube. Across the width of the main column of observed bubbles, there did not appear to be a

variation in number density, size or speed. The heterogeneity in bubble number density across the width of the tube was a feature caused by the single injection site at the centre of the base plate. This was a notable difference to many other previous experimental and theoretical works where bubbles or falling solid particles were produced (or modelled) across a full width of the experimental container. In these other studies, lateral heterogeneities in the bubble distribution did not develop (for example, Zenit et al., 2001; Martinez et al., 2010; van Wijngaarden, 1993; Oliver, 1960; Ladd, 1992; Ladd, 1996; Squires & Eaton, 1991; Baldock et al., 2004; Caflisch & Luke, 1985). The heterogeneity in bubble number density across the width of the tube may be responsible for the observed increase in bubble ascent speed, given that previous experiments generally found that the ascent speed of bubbles (or sinking speed of particles) decreased according to gas volume (or solid volume) fraction. The hindering process requires that the flow around a sphere may not occur beyond a certain lateral extent (Oliver, 1960), and for a distribution of bubbles extending from one wall to another, the flow must be constrained as the bubbles cannot all be moved laterally away from each other due to the constraining walls. However, in the experiments presented here, the column of bubbles, or a dense group of bubbles, were not necessarily bound by the walls and the bubbles themselves were not restricted in their lateral movement. The ability for bubbles to move laterally rather than have their flow constrained may impede the hindering effect. Within the dense groups, hindering could occur while the volume of the group remains constant, so the rise speed of the bubbles within the group relative to the group may be impeded, but the rise speed of the group as a whole was much greater than the rise speed of the bubbles if they were in isolation. It was not possible to test if hindering occurred within dense groups as bubbles at the centre of dense groups were not possible to observe, and the groups themselves tended to display toroidal motion within the group, which may completely disrupt or mask the hindering process. In the dilute groups in the constrained and inclined tubes, the larger bubbles deviated from the Hadamard-Rybczynski model more than the smaller bubbles, as evidenced by the statistically significant correlation between theoretical rise speed and measured rise speed in those cases (Figure 6.5, 7. 3, 10.5 & 10.8). This may be evidence that the smaller bubbles were experiencing a hindering effect that was not applicable for larger bubbles, furthering the size stratification effect.

On larger length scales, such as the length of the experimental tube itself, large temporal variations in gas volume fraction were not observed. The exception to this was at the start and end of experimental runs, when the tube transitioned from having almost no bubbles present, to having a developed column of bubbles passing through it (in the

first 10-30 seconds of each run) and then slowly returning back to very few bubbles present (approximately two to three minutes after a single, 1 second, injection of volatile-rich oil). Despite the mostly homogeneous nature of the bubbly flow across its length scale once the bubbles had been allowed sufficient time to develop, the heterogeneities on short scales were related to the overall increases in speed of bubbles across the whole tube. The short-scale heterogeneities dictated the long-scale implications and must therefore not be ignored when describing the entire system.

The presence of heterogeneity on short scales was unavoidable and the statistical nature of bubble nucleation made this impossible to control in the experiments presented in Chapter 5, 6 and 7. Accurately analytically modelling the behaviour of even a small number of bubbles travelling near to each other through the oil is likely to be impossible given current mathematical knowledge, as neither the n-body problem nor the Navier-Stokes equation have known exact general analytical solutions. Numerical modelling can solve the equations but would require accurate knowledge of the initial conditions, which may not be possible in practice and solving the n-body problem requires approximation of an infinite power series that only appreciably converges after millions of terms (Diacu, 1996). Generalising the system by describing the heterogeneities with a small number of parameters may facilitate building a numerical description of the system. For example, modelling the dense groups in terms of a rising plume head may be appropriate, or describing them in terms of a continuous medium with very low surface tension.

8.1.10. Dense Groups

The dense groups were observed to have an internal toroidal vortex ring-like motion of the bubbles (Figure 8.3, Section 5.5.5), which suggested that the oil flowed around the dense groups rather than percolating through the group (Figure 8.4)

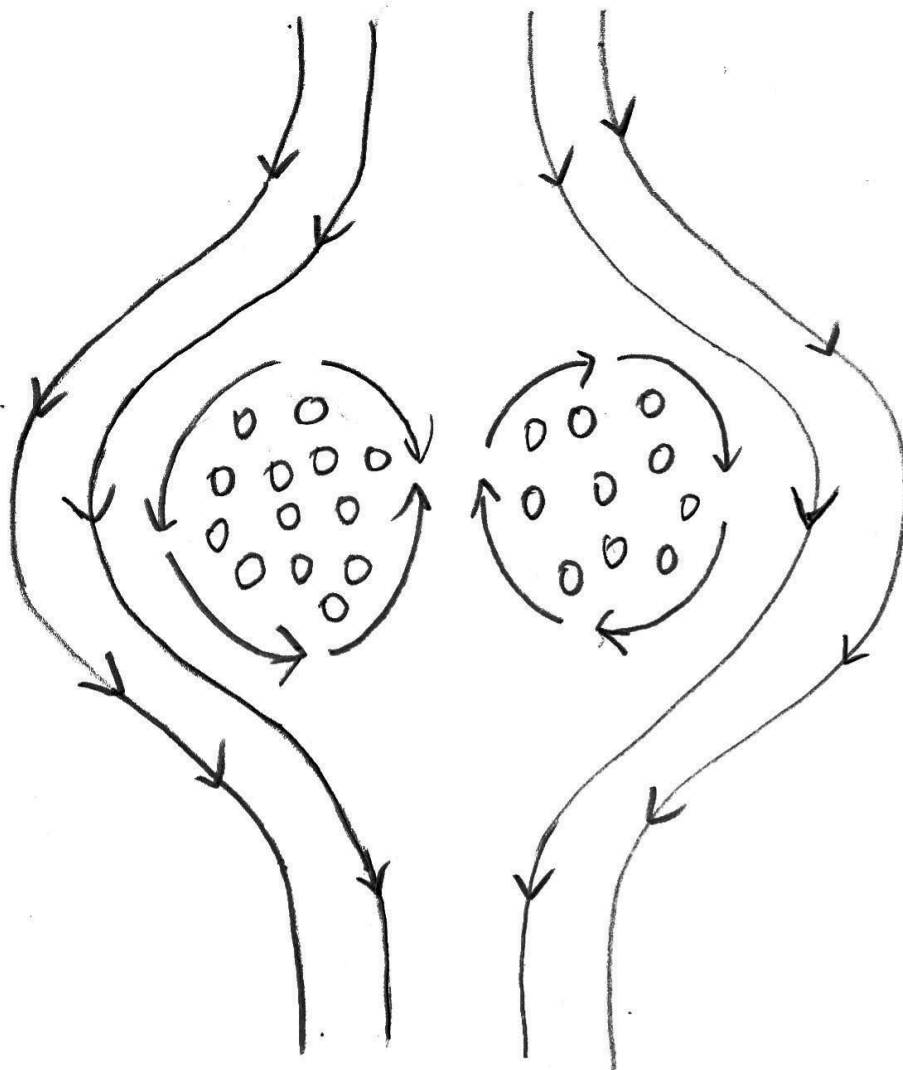


Figure 8.3: Cross section sketch of a dense group showing the internal motion of bubbles within the group which may cause the observed toroidal motion of bubbles within the group, in the frame of reference of that group. The black lines show the motion of the oil around the group, while the grey arrows indicate the observed motion of bubbles within the group. Not drawn to scale.

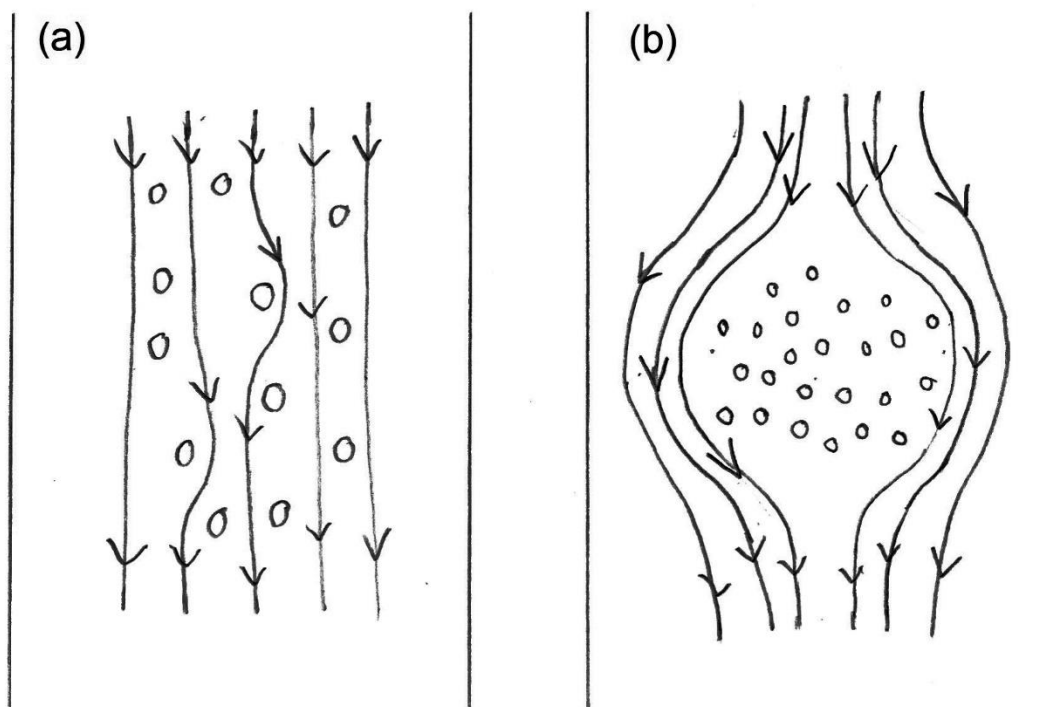


Figure 8.4: Sketch demonstrating how the oil may flow through the group in dilute groups (a) or around a dense group (b). Note that the flow lines of the oil are in the frame of reference of the group itself rather than relative to the tube walls. Not drawn to scale.

The dense groups with very small bubbles (approximately <0.1 mm diameter) and very high bubble number densities (for example in the Pseudo-infinite RUN03_LOW video, MVI_6884, between 17 and 23 seconds) showed this toroidal motion more clearly. Other groups with fewer, larger, bubbles (for example in the Pseudo-infinite RUN06_LOW video, MVI_6887 also between 17 and 23 seconds) did show the same type of behaviour, but the rotation of the bubbles within the group was less obvious. Toroidal behaviour was therefore not exclusive to the dense groups with very high bubble number density and very small bubbles of negligible buoyant rise speed relative to the bulk speed of the group. The presence of the rotational motion within the dense groups may be due to the oil flowing around the bubble group rather than through it, as the laterally moving oil around the group pulls the bubbles, and their surrounding layer of oil, at the edge of the group outwards and down (relative to the centre of the group). By the conservation of momentum within the group, there must be bubbles and/or oil moving upwards within the group and due to rotational symmetry around the vertical axis, the downward motion cannot happen on the outer edge of the group, but rather through the middle, causing internal rotation within the group (Figure 8.3).

Toroidal vortices may maintain relatively constant speeds when other configurations of fluids would have had their speed substantially impeded due to viscous effects, and larger vortex rings are more stable than smaller ones (Batchelor, 1967). However, the dense groups in the experiments were observed to slow down and change shape (becoming wider and flatter) before they broke apart, ending the toroidal motion (Sections 5.5.6 and 7.4.1).

As dense groups ascended, the volume of the groups increased slightly (Figure 5.27), and they grew wider and flatter (Figures 5.23 and 5.26), but it was not clear if the increase in size was comparable to previous observations where vortex rings are observed to increase in radius (Batchelor, 1967). The increase in size may be due to the decompressive expansion of the constituent bubbles and the associated increase in repulsive force as the separation between bubbles decreases (Yu et al., 2011). The disintegration of the dense group may occur when the groups become too wide for the lateral flow around the group to sustain the toroidal motion against the viscous effects of the oil between the bubbles in the group.

8.2. Volcanic Context of Experimental Results

The findings outlined in Section 8.1 discussed processes that happened when air bubbles were present in oil, and may reveal a number of possible phenomena present in volcanic processes. The relevance of these findings extends mainly to lower viscosity magmas with gas volume fractions of approximately 0.1 % to 20 % and where the rate of decompression is negligible. As such, the physical phenomena described in Chapters 5, 6 and 7 may not be relevant to near-surface processes in volcanic systems, where significant bubble growth through decompression (Sparks, 1978) occurs on a shorter timescale than the bubble group effects. Neither are they likely to be relevant at great depth where the gas volume fraction is very low and so there are insufficient bubbles to induce group effects, instead, between these extremes (e.g. at depths of a few hundred metres to a few thousand metres), there is scope for the grouping of bubbles to have sufficient effect to alter the gas mass transport of bubbles appreciably during the timescale available. The timescale upon which bubble effects could take place would be limited by the rate of magma ascent, as faster rising magma would cause the bubbles to more rapidly ascend towards a depth where decompressive expansion is no longer negligible.

The experiments showed that even small inclinations away from a vertical configuration changes the overall configuration of bubbles in the tube. In natural systems, local conduit variability and inclined conduits (Chouet et al., 2008), suggest that the general bubble behaviour seen in inclined tubes, where bubbles rise to the upper wall, can

be expected to occur in natural systems, too. The experiments presented in Chapters 5, 6 and 7 featured a discrete pulse of injected oil in the centre of the tube which nucleated into multiple groups of bubbles. In a volcanic conduit with rising magma, viscous effects with the walls would mean that magma in the centre of the conduit ascends much faster than the magma at the conduit walls, and the shear stress is proportional to the rate of change of magma speed with respect to distance from the centre (Neuberg et al., 2006; Marsden et al., 2019). This is supported even in higher viscosity natural systems, such as in the highest inferred magma strain rates in the rhyolitic Newberry eruption occurring within lithic-bearing pyroclasts derived from conduit walls (Rust & Cashman, 2007). These features of magma ascent mean that bubbles near to the central axis of a conduit would experience lower shear stresses than bubbles near to the conduit walls, causing comparatively low amounts of bubble deformation from a spherical regime. The relatively low stress in the centre means that the experimental tube with an injection of bubbles into the centre may be an appropriate analogue, in terms of the stress regime, for the bubbles in the centre of a magmatic conduit with moving magma.

The main finding of the experiments was that many configurations of bubbles in a tube increased the rise speed of those bubbles by a factor of between (approximately) 2 and 5 when the bubbles distribution is sufficiently heterogeneous that dense groupings, such as those described in Section 5.5.5, are formed. In the event that these dense plume-like groups may form, and given it is an appropriately low-shear environment, the rate of gas ascent to the surface in the centre of a conduit may be multiple times faster than the buoyant ascent of those bubbles would indicate, and the effect of hindered ascent (e.g. Manga, 1996) may be overcome by dense bubble groupings and bubble-driven convection (but there may be evidence of hindering for dilute groups; Figures 10.5 & 10.8). Furthermore, the entrainment of oil with those bubbles created bubble-driven convection currents that the majority of bubbles travelled through. While the magma is not static and rises towards the surface, the momentum balance between the upward moving bubble driven convection and a restoring downward component may exist. It is possible that the magnitude of the downward component is much less than the speed of the bulk of the magma, if the downward portion extends over a greater width of the conduit, although circulation of magma does not necessarily cause net upward movement of magma. The boundary between the upward and downward moving material would necessarily require shear stress as the speed of the magma across the width of the conduit changes from relatively high upward speed, to zero, to relatively high downward speed. This shear localisation could, given an appropriate dissolved volatile content, induce additional

bubble nucleation (Han & Han, 1988) beyond what would otherwise be expected in a natural system where bubble group effects are neglected.

The size stratification of bubbles in the conduit would have a much greater duration in which to develop and so the presence of larger bubbles moving ever faster towards the surface due to their group effects may yet still increase the localised shear within the conduit, adding further to nucleation events (Tatibouët & Gendron, 2004). However, if the groups themselves can facilitate shear-induced nucleation, the bubbles that nucleate would not be the same size as the group that facilitated that nucleation, and they likely would not form within the group. This is because the strain caused by bubbles within a group would be low compared to the strain induced by the bubble group. Given the assumption of some inclination in the conduit, these bubbles would likely travel towards the centre of the bubble induced convection. A continuous process of nucleation (Blower et al., 2001a; Polacci et al., 2009) could be caused by the ascent of bubble groups may provide additional bubbles to the conduit and those bubbles in turn may form into size-stratified groups. As there is only a limited quantity of volatile species dissolved in magma from which bubbles may nucleate, without a constant supply of fresh magma, the process of fast moving groups causing additional nucleation events leading to further fast moving groups cannot recur indefinitely.

The presence of bubble number density heterogeneities in the experiments is likely to be replicated in natural systems over sufficiently short length and time scales (Blower et al., 2001a; Blower et al., 2003). While size stratification facilitates local homogeneity of bubble size, the self-organisation of those groups into more tightly packed groups creates heterogeneity over slightly larger length scales, as well as size stratification over even greater length scales. Additionally, the configuration of bubbles in inclined tubes is likely to be replicated in inclined conduits, as bubbles will still have a component of their buoyancy toward the upper conduit wall. The heterogeneities caused by nucleation are likely to be even more pronounced in a natural system as instead of a single injection of oil into a small section of the experimental tube (relative to the volume of oil in the tube in total), nucleation is an ongoing process across a greater spatial and temporal scale than in the experiment (e.g. Polacci et al. (2009) inferred continuous bubble nucleation at Stromboli). As such, there could be an even greater variety of bubble sizes present in a given region of the magma conduit. While size stratification will ensure that larger bubbles are found closer to the surface, it may still be expected that bubbles of many sizes will be present at most parts of the conduit as nucleation is driven by bubble induced convection and the passage of large bubble groups through the conduit. This is supported by textural

studies of ejected pyroclasts (e.g. Shea et al., 2010), which typically record multiple vesicle nucleation events, and by numerical models of non-equilibrium degassing (Blower et al., 2003).

8.2.1. Experimental Limitations

While the experiments provided an appropriate physical regime within which to examine the behaviour of bubbles, there were a number of simplifications that did not necessarily reflect volcanic behaviours.

8.2.1.1. Role of Crystals

The experiments did not consider the role of crystals as a rheology modifier (Caricchi et al., 2007), or as preferential nucleation sites (Shea, 2017). This would have been impractical to implement experimentally, as finding suitably sized particles (relative to the size of the bubbles) which were also neutrally buoyant, or nearly neutrally buoyant, in the oil and which could also later be removed from the oil for reuse in other experiments was not easily achievable. Furthermore, the presence of crystals may have negatively affected the ability to measure the size and speed of bubbles in the tube by obscuring them. The role of crystals was neglected as the zeroth-order behaviour of bubbles was the experimental priority, however understanding the behaviour of bubbles in a crystal-free environment facilitates further study into how crystals modify individual and group bubble behaviour. The experiments of Chapters 5, 6 and 7 were designed to examine only the simplest versions of the problem at first, and so deliberately avoided crystal analogues.

8.2.1.2. Non-Newtonian Effects

The experiments presented in Chapters 5, 6 and 7 were intended to examine the simplest rheological case, so non-Newtonian effects were intentionally avoided. Shear experiments on silicate melts have described shear-thinning behaviour in crystal-free melts (Webb & Dingwell, 1990) and a reduction in flow index (n in equation 2.4) and an increase in flow consistency (K in Equation 2.4) in Strombolian and Etnean samples (Vona et al., 2011). As such, the use of a Newtonian fluid in the experiments was not necessarily an appropriate analogue for all natural volcanic systems, although performing experiments in a Newtonian fluid and then a shear-thinning fluid would facilitate identifying effects caused by deviation from a Newtonian regime. In a shear thinning fluid, the rise speed of groups of bubbles compared to individual bubbles would likely be increased, as a larger, faster moving group imparts a greater shear stress on the surrounding melt than a single, slower moving, bubble. Experimental observations of vertically aligned

chains of bubbles in shear-thinning solutions indicate substantial changes to bubble shape and interactions between bubbles (Kliakhandler, 2002). This would facilitate an even more rapid gas mass transport towards the surface than suggested by the experiments presented in Chapters 5, 6 and 7.

8.2.1.3. Non-linear Tubes

The experimental tubes were not designed to generate an active bubble trap in order to produce and measure foam formation and travel. Foams were not observed in any experiment, indicating that nucleation and bubble interactions alone were insufficient in the parameter space used to produce foams. Other experiments using non-linear containers that trapped bubbles (Jaupart & Vergnolle, 1988) were able to successfully generate foam rafts, showing that alternative tube geometry was a method by which configurations of bubbles with a greater local bubble number density than in the experiments presented in Chapter 5, 6 and 7 could be generated.

8.2.1.4. Long-Term Behaviours

The length of the tube meant that bubble groups were only allowed to propagate for approximately thirty seconds before decompressive expansion significantly affected the size of bubbles over shorter timescales than the measurements would have been. It was not clear from the experiments whether dense group formation and breakup was an event which happens only once after the bubbles nucleated or if it would occur repeatedly, given a constant supply of bubbles and a sufficiently lengthy tube and duration of observation. The long-term behaviours would be closer to that of natural system behaviours as, rather than the lifetime of a bubble being on the order of one minute, bubbles in volcanic systems may undergo prolonged interaction with surrounding bubbles. The timescale of interaction may span months or years after nucleation but prior to eruption, depending on the rate of magma ascent. A taller tube, higher viscosity oil and smaller bubbles would facilitate longer term behaviours, however smaller bubbles would have a smaller area of effect around them.

8.2.1.5. Persistent Nucleation Caused by Rising Magma

As the oil in the tube had a net momentum of zero, it was not possible to determine how the continuous nucleation expected from decompression, and subsequent growth, as the magma rises towards the surface (as inferred for Stromboli by Polacci et al., 2009) would affect the bubble group behaviours observed in the experiments. The continuous supply of new bubbles may facilitate the repeated formation of additional groups that would not

form if only a single nucleation event were to occur, increasing the overall rise speed of bubbles, however as the bubbles form and grow diffusively, the surrounding melt would increase in viscosity, reducing the buoyant rise speed of the bubbles. It was unclear whether the additional bubbles would increase the overall rise speed of the gas phase or if the increased viscosity and hindering effects would reduce it. As the viscosity of oil used in the experiments did not appear to be strongly related to the quantity of air dissolved in it, this may not be possible to investigate without using a different fluid in the experiments.

8.2.2. Future Work

As alluded to in the previous section, there are several modifications or additions to the experimental setup that may aid in further understanding the role that bubble interactions have in controlling the ascent of gas towards the surface, or to more closely resemble the kinds of conditions anticipated in a natural system.

- Utilising non-cylindrical tube geometries would provide the opportunity to study the formation of foams and their interactions with other bubbles. Varying the angle of inclination at different parts of the tube to include some horizontal sections may allow for foam formation which would then facilitate observations of interactions between foams and other bubbles and bubble groups.
- Significantly longer tubes would facilitate observing the long-term evolution of bubble groups. To reduce bubble expansion during ascent, experiments could be carried out at elevated pressure, however increasing the pressure reduces the quantity of bubbles which nucleate at the bottom of the experiment.
- Increasing the number of injection sites would allow for a more complete bubbly flow that is not biased to mainly rising through the central axis of the tube and so would be closer to a natural system, where bubbles may nucleate from the magma at any point across the width of the conduit.
- The use of a non-Newtonian fluid rather than the (Newtonian) silicone oil would more accurately replicate the expected physical properties of magma. The higher shear stress imposed by bubble groups (compared to individual bubbles) would facilitate even more rapid rise speeds of those groups in a shear-thinning fluid.
- Examining a wider variety of bubble group classifications beyond “dense” and “dilute”. Categorising experiments by gas volume fraction would be

challenging as observed short-scale heterogeneities would infer different categories. The dense and dilute classifications provided a distinction between two of the most common modes of bubble grouping, but measuring the effect of increasing gas volume fraction on those groups would provide a greater understanding of why some bubbles move in the dense group configuration and some in the dilute configuration.

8.3. Application of Results to Volcanic Cases

In order to apply the findings of the experiments to volcanic systems, it would be necessary to modify conduit models to incorporate the experimental findings to accommodate the impact of bubble groupings on the ascent of gas bubbles through a conduit.

A more thorough empirical description of how different configurations of bubble groups and heterogeneities in bubble distribution across the width of a conduit affect the overall gas mass transport would be required to adjust numerical models. This would also have to consider the roles of shear and deformation of larger bubbles (Manga & Stone, 1994) on the behaviour of the bubbles beyond what was observed in Chapter 5, 6 and 7. Additionally, it would be required to determine the conditions necessary for the formation of different modes of bubble grouping. For example, understanding the factors determining the formation of dense groups, where the liquid flows around the bubble group, versus the formation of dilute groups, where the liquid flows between bubbles. It was not clear from the experiments why some bubbles that nucleate assemble into dense groups while others develop into the dilute groups, as the onset of group behaviour was not captured by the cameras.

It would not be practical to model each bubble in a natural system (mainly due to the required precision in the initial conditions of the model and computing power required to run it) so a more general description of the bubble configurations would be required to describe the formation and impact of the heterogeneities in bubble distribution through a conduit. The heterogeneities in gas volume fraction and local mean inter-bubble separation could be used to describe the increase in the ascent speed of gas bubbles in the system.

8.3.1. Convection within a Magma Conduit

Previous work has introduced conceptual models for the convection of magma due to the change in density when bubbles form. Specifically, dense, bubble-free magma sinks, pushing less dense, bubble-rich, magma upwards (Kazahaya et al., 1994; Fowler & Robinson, 2018). Previous work has referred primarily to magma between the exsolution depths of CO₂ and H₂O (Stevenson & Blake, 1998); however, it is proposed

that such effects may exist at different depths and induced by other means. In addition to the magma rising from convection produced from sinking dense magma, there may also be bubble-driven convection effects within the rising portion of magma. Furthermore, at more shallow depths, where the majority of volatiles have exsolved from the melt. Therefore, the process of degassing-driven convection creating an increase in magma density and subsequent magma sinking would no longer occur. Therefore, when the magma has been mostly depleted of its volatile content, convection within the conduit could be driven almost exclusively by bubbles. The bubbles in convecting magma within the top 100-300 m of a conduit has previously been recorded from textures of pyroclasts (Carey et al., 2013) and the possibility of bubble separation from the magma by buoyancy was considered, requiring a bubble diameter in excess of 10 cm to decouple from magma in the downward moving portion of the conduit. In the work of Carey et al. (2013), the millimetre-scale bubbles which did not decouple from the magma formed a halo of micron-scale bubbles around them, which nucleated due to decompression as the magma approached the surface. The bubbles which did not escape to the atmosphere were brought downwards by the convecting magma and the bubbles in the ‘halo’ began to re-dissolve into the melt. The impact of bubble grouping may facilitate the escape of bubbles smaller than 10 cm diameter if the increased ascent speed of the bubble group exceeded the downward speed of the magma ($0.1\text{-}0.3\text{ m s}^{-1}$). Alternatively, if the group effect did not result in a net-upward movement of the bubbles, it may cause a reduction in the downward speed of the bubbles, relative to the conduit walls, while in the downward moving magma. The impact of the reduction in speed would increase the time scale of the re-dissolution of the halo of bubbles (which was found to be on the order of $10^3\text{-}10^4$ seconds). An increase in the time for re-dissolution may imply that the actual rate of convection was slightly higher than the $0.1\text{-}0.3\text{ m s}^{-1}$ proposed by Carey et al. (2013).

A similar experimental setup to the one described in Chapter 3 has been used previously to examine different types of flow behaviour (Pioli et al, 2017) and has also shown that gas bubbles in aqueous solutions of glucose syrup have a preference to group into an ascending column. However, instead of the vertically rising column causing downward surrounding flow, localised bubble-driven convection cells developed parallel to the upward moving liquid (Figure 8.5). The dimensionless numbers used to characterise different flow regimes (Kapitsa and Froude numbers) were consistent with those estimated for the experiments performed in this study ($\log(Ka) \approx 1$, $\log(Fr) \approx 0$) in the regime termed “laminar bubble street”, which most closely resembles the behaviour observed in experiments, but not dense groups. The study by Pioli et al. (2017) appears to have non-

zero net momentum as the liquid (aqueous solutions of glucose syrup) entrained between the bubbles has an upward momentum that is seemingly not balanced by a downward motion of syrup solution elsewhere in the experimental container, as such the form of the bubble-driven convection cells observed may not be exactly as represented in their results (Figure 8.5). The experimental results presented in Chapters 5, 6 and 7 do not indicate the presence of convection cells of the nature observed by Pioli et al. (2017); however, in their experiments bubbles were generated at equal separations across the full cross section of the container, rather than in the centre as in the experiments shown in Chapter 5, 6 and 7. The differences in bubble generation may account for the differences in observed behaviour, despite the two experiments covering comparable dimensionless regimes.

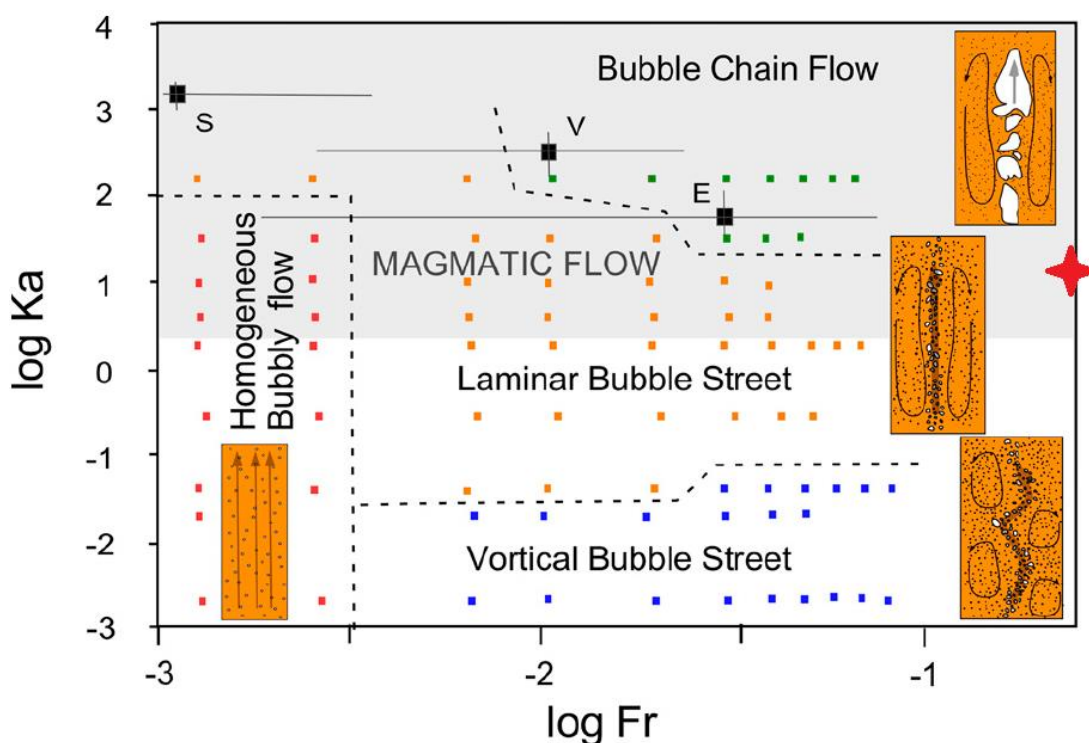


Figure 8.5: Map of different flow patterns characterised by Froude and Kapitza numbers. In the inset images, orange denotes the liquid while white denotes gas bubbles, the red, orange, green and blue squares show the regimes of experiments performed by Pioli et al. (2017) while the large red cross shows the approximate regime of the experiments presented in Chapters 5, 6 and 7. From Figure 1 of Pioli et al. (2017).

The previous models assume vertical conduits, however experiments showed that even slight inclinations radically altered the configuration of gas bubbles within the experimental tube (Figure 7.1). The model of gas-rich magma rising along a central axis with the degassed, denser, magma sinking nearer to the conduit walls is therefore not necessarily an accurate representation of flow regimes in all natural systems. Additionally,

the H₂O mass flux as a function of H₂O mass fraction degassed (Figure 4(b) of Stevenson & Blake, 1994) will likely be an underestimation. This is because the passage of gas bubbles through the conduit does not take into consideration the bubble group effects and increased rise speed (and therefore mass flux). So, for a given measured H₂O mass flux, the actual mass fraction of H₂O degassed is likely to be lower than the model suggests.

8.3.2. Gas Puffing Rate

A description has been previously developed to account for cyclical variations in gas puffing rates at Stromboli (Manga, 1996) however the empirically determined bubble rise speed, $U(\varphi)$, where the bubble rise speed was a function of gas volume fraction and bubble concentration (Equation 8.1) was not in agreement with the findings of the oil-air bubble experiments presented in Chapters 5, 6 and 7.

$$U(\varphi) = U_0 \left[\frac{1}{1 + \varphi} \right]^n \quad (8.1)$$

where U_0 is the rise velocity of bubbles as described by the Hadamard-Rybczynski model for gas bubble concentration of φ and a constant n taken to be $n=3$ in Manga (1996).

The Manga model posits that a bubble layer, with relatively homogeneous bubble number density across the width of the container, hinders the ascent of that layer. The experiments shown in Chapters 5 and 6 show that heterogeneities in bubble number density (dense groups) can ascend at much greater speeds than the buoyant rise speed of an individual bubble. The thesis experiments use an injection in the centre of the tube, causing inhomogeneities in bubble number density across the width of the tube which may not necessarily be present in a system where bubbles nucleate across the full width of a container. However, the experiments in Chapter 7 also showed that small inclinations of the tube created inhomogeneities across the width of the tube, such that axial symmetry was lost (Section 7.1, Figure 7.1). It would be expected that, had bubbles been nucleated across the full width of the tube, they would still rise towards the upper side of the tube and create an inhomogeneity across the width of the tube. The inhomogeneity across the width of the tube causes the part of the tube with a greater gas volume fraction to have a lower density and ascend buoyantly, ultimately creating bubble-induced convection (Sections 7.3.1, 8.1.4 and 8.1.5). In a volcanic conduit, inclinations from vertical might be expected (e.g. Chouet et al., 2008) and so it would be inevitable that an initially homogeneous layer of bubbles would develop heterogeneities across the conduit width, reducing the impact of the hindered effect on the bubbles and facilitating an increased bubble rise speed.

Manga's (1996) findings have also been used to generate a model to account for the temporal variations in gas puffing (Ripepe et al., 2002). Considering the effects of the heterogeneities, which serve to increase the bubble rise speed, may affect the numerical model outcomes considerably as instead of dense concentrations of bubbles reducing bubble rise speed, they would be modelled to increase rise speed, in line with experimental observations. The explanation that temporal variations in gas puffing rate was a consequence of variations in magma supply rate (Ripepe et al., 2002; Kondo et al., 2019) may not be the full explanation. Experiments showed that a short injection of volatile-rich oil at the base of the experimental tube resulted in groupings of bubbles of similar sizes, and multiple distinct groups may form from that short injection of volatile-rich oil (for example, the Pseudo-infinite RUN03_LOW video, MVI_6884, where several dense groups formed from a ~2 second injection and the gas flux passing through the centre of the frame varies constantly plus Figures 5.21, 5.22, and 6.9). The experiments showed that a single short injection of oil may result in variations in gas flux from the development of dense groups, which then ascended at varying speeds, ultimately reaching the surface of the oil at different times. Abstracting this observation to the volcanic case, a temporary increase in the magma supply rate could be expected to lead to the formation of multiple groups of bubbles within the magma, which would ascend at varying speeds, arriving at the surface of the conduit at different times, suggesting that the variations in gas flux at the surface may not be exclusively caused by variations in gas flux, but by the development of bubble groups from a single nucleation event. While variations in magma supply rate have been suggested from ground deformation measurements (Kondo et al., 2019), the sensitivity of Stromboli's activity to variations in magma supply rate may be connected to the organisation of bubbles into groups.

8.3.3. Gas Pistoning

The cyclical emission of gas along with changes in the height of an active lava lake and mild explosive activity was a notable feature at Mauna Ulu, Hawai'i in the 1971-74 events and August 2011 events (Tilling, 1987). Gas pistoning features a slow inflation of the lava lake (for example approximately 10-15 minutes between intervals in August 2011) and a very rapid (1-2 minutes) release of gas (Chouet & Dawson, 2015). The explanatory model adopted comprises of a foam forming at the top of a vertical conduit from an even distribution of bubbles across the width of the conduit (Chouet & Dawson, 2015), while the conduit system below Mauna Ulu appears not to be vertical. The bubbles that feed that foam would approach it from underneath at a different rate than their buoyant rise speed due to their group behaviour, and so either the volume of gas ejected per deflation event

would be greater, or the frequency of the emissions would be lesser, depending on whether the control on the timing of the emissions is based on the volume of gas present, or another factor.

The 1971-74 inflation events and subsequent eruptions at Kilauea indicated that the magma conduit of Kilauea was, in parts, highly inclined (Duffield et al., 1982). The inflation was centred approximately 8.5 km West North West of the vent at Mauna Ulu, and the centre of the magma causing the inflation was measured to be at a depth of approximately 2-4 km (Dvorak et al., 1983) indicating that the average inclination of the conduit between where the magma was stored prior to eruption and where it eventually reached the surface was approximately 65° to 77° away from vertical. At this inclination, the processes observed in the experimental tube, with an inclination less than 5° , would likely be far more extreme and a different regime of bubble behaviour may be present than what was observed in the experiments. The component of the bubble's buoyancy directed towards the conduit walls would exceed that of the component parallel to the conduit walls, so the rise speed of the bubbles may be reduced, rather than increased, by the inclination.

While previous work has linked ash morphology to bubble sizes and shapes (Liu et al., 2015), it is not expected that evidence of group behaviour would be recorded in cooled erupted material. Rapid decompressive expansion of bubbles and significant changes in rheological properties near the surface (Del Bello et al., 2015; Oppenheimer et al., 2020) plus vesiculation during and after eruption may overprint any characteristic patterns caused by group behaviour, such as regions of bubbles with similar diameters.

9. Conclusion

Analogue experiments have shown that freshly-nucleated bubbles within a liquid may form into groups and those groups ascend at much greater (2-5 times) speeds than expected from the buoyant rise speed of those bubbles. The bubbles formed into two broad classifications, distinguished by whether the surrounding oil flows around the bubble group (dense groups) or between the bubbles (dilute groups). The interactions observed experimentally therefore increased the rate at which gas travelled through the tube, changing the outgassing rate at the surface of the experimental tube and, when applied to volcanic cases, it was reasonable to assert that bubble groupings may act to alter the way in which basaltic systems separate the gas phase from the melt phase. This would be facilitated by heterogeneities in the distribution of bubbles across the width of a conduit. Heterogeneities can be self-forming, and/or induced by inclination of the conduit.

Experiments showed that a single injection event resulted in the formation of multiple groups of bubbles which and then rose faster than the buoyant rise speeds of those bubbles if they were in isolation. For groupings of lower gas volume fraction (< 5 %) (dilute groups), it was observed that smaller bubbles ascended through the experimental tubes slower than larger bubbles, even when their lower buoyant rise speed was taken into consideration. This was interpreted as evidence of a hindering effect between the bubbles, although those smaller bubbles were still travelling at a greater speed than their buoyant rise speed in isolation (as described by the Hadamard-Rybczynski equation), so the magnitude of the group effect exceeded any possible hindering effects. Furthermore, it was noted that for the groupings with the highest bubble number density within the experiments (dense groups), there appeared to be a preference for bubbles of the same size to group together, causing distinct waves of bubbles rising at different speeds, and thus reaching the surface at different times. Thus, cyclical eruptive behaviour caused by repeated waves of bubbles reaching the surface, interspersed with periods of very few bubbles, may be possible from a single magma injection.

The experiments showed that conduit inclination could have a large impact on the bubble distributions, such that even shallow inclinations from the vertical would result in highly heterogeneous bubble distributions across the conduit width. These heterogeneities in distribution were observed to increase bubble rise speed towards the surface. Conduit inclination is not a commonly considered parameter in current conduit models, but the qualitative observations suggest it may be significant for promoting bubble-driven convection. At low conduit inclinations (<5° from vertical), the viscous effects with the

tube walls did appear to slightly reduce the rise speed of groups, but not for bubbles in isolation.

The results presented provide the starting point for additional experimentation and analysis from which existing conduit models can be improved, ultimately with the intention of being able to mitigate volcanic hazards from basaltic systems more effectively.

10. Appendices

10.1. Residual and Statistical Information

The Kolmogorov-Smirnov test was used to establish if the theoretical, measured and residual values were normally distributed. Distributions are normally distributed when the K-S test returns a non-significant result. In the case of normal distribution, the Pearson's correlation coefficient was used. In the case that at least one variable was not normally distributed, the Spearman's Rank correlation test was used. The requirement for significance for the K-S test and correlations was taken to be 0.01.

10.1.1. Pseudo-infinite Single

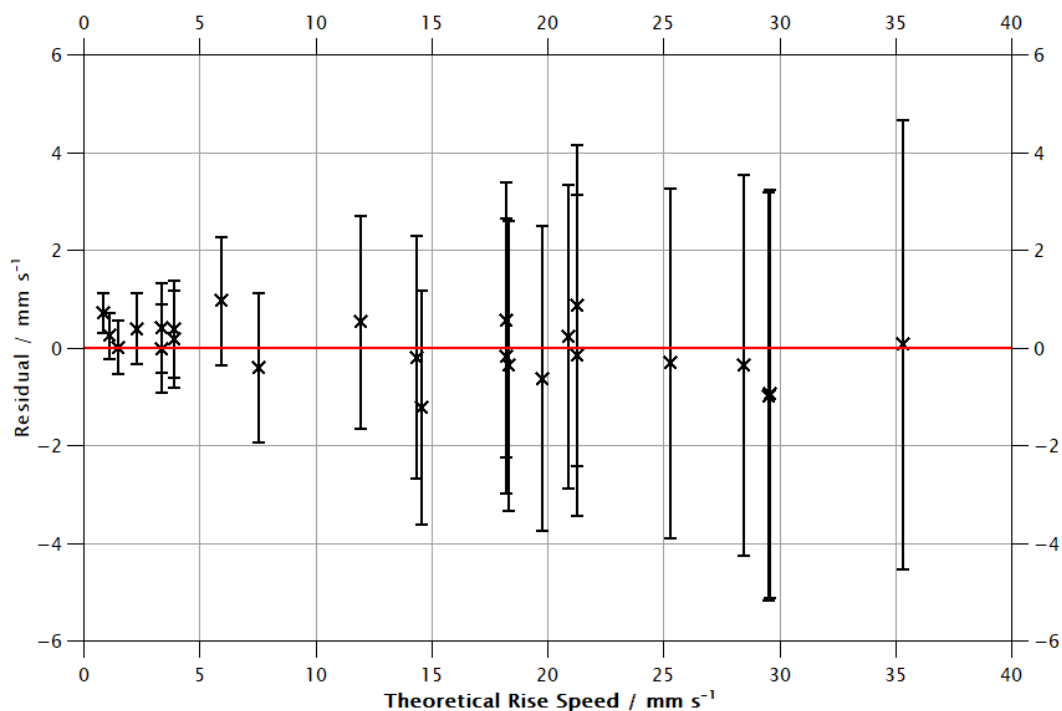


Figure 10.1: Residual between theoretical and measured rise speed against theoretical rise speed for single bubbles in the Pseudo-infinite tube. The red line denotes where the residual is equal to zero.

Table 10.1: Tests for normality for single bubbles in the Pseudo-infinite tube.

	Theoretical	Measured	Residual
Kolmogorov-Smirnov test output (D)	0.1546	0.1729	0.0787
Significance (p)	0.5380	0.3984	0.9943

Table 10.2: Theoretical-Measured correlation and Theoretical-Residual correlation for single bubbles in the Pseudo-infinite tube. The theoretical, measured and residual values were all normally distributed, so Pearson's R is used.

	Theoretical-Measured	Theoretical-Residual
Pearson's R	0.9867	-0.4695
Significance (p)	<0.0001	0.0180

10.1.2. Pseudo-Infinite Dilute

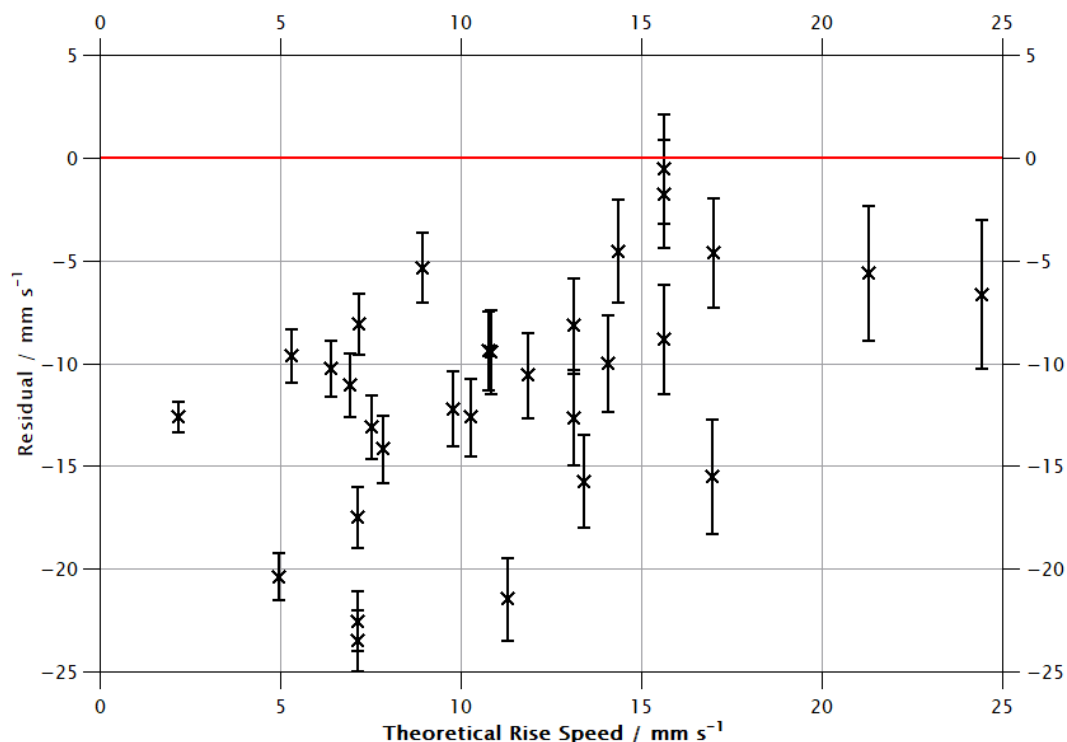


Figure 10.2: Residual between theoretical and measured rise speed against theoretical rise speed for bubbles in dilute groups in the Pseudo-infinite tube.

Table 10.3: Tests for normality for bubbles in dilute groups in the Pseudo-infinite tube.

	Theoretical	Measured	Residual
Kolmogorov-Smirnov test output (D)	0.1237	0.0893	0.1091
Significance (p)	0.7029	0.9529	0.8300

Table 10.4: Theoretical-Measured correlation and Theoretical-Residual correlation for bubbles in dilute groups in the Pseudo-infinite tube. The theoretical, measured and residual values were all normally distributed, so Pearson's R is used.

	Theoretical-Measured	Theoretical-Residual
Pearson's R	0.3902	0.4930
Significance (p)	0.0330	0.0056

10.1.3. Pseudo-infinite Dense

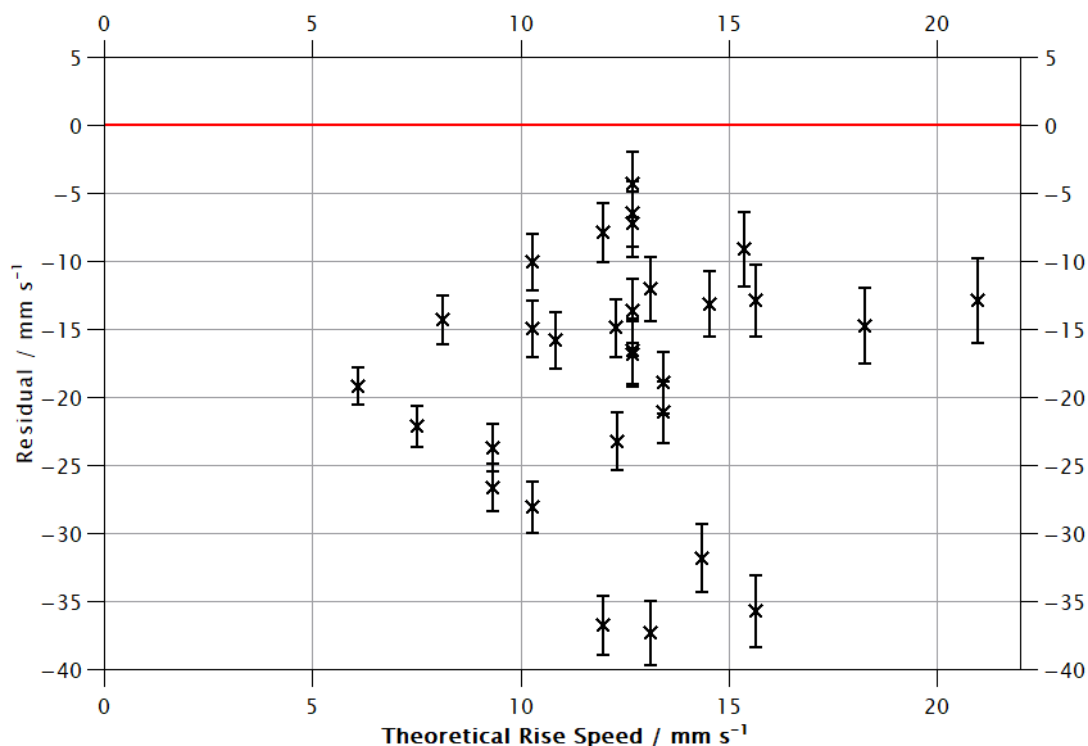


Figure 10.3: Residual between theoretical and measured rise speed against theoretical rise speed for bubbles in dense groups in the Pseudo-infinite tube.

Table 10.5: Tests for normality for bubbles in dense groups in the Pseudo-infinite tube.

	Theoretical	Measured	Residual
Kolmogorov-Smirnov test output (D)	0.1434	0.1370	0.1555
Significance (p)	0.5214	0.5552	0.4203

Table 10.6: Theoretical-Measured correlation and Theoretical-Residual correlation for bubbles in dense groups in the Pseudo-infinite tube. The theoretical, measured and residual values were all normally distributed, so Pearson's R is used.

	Theoretical-Measured	Theoretical-Residual
Pearson's R	0.2239	0.1081
Significance (p)	0.2343	0.5696

10.1.4. Constrained Single

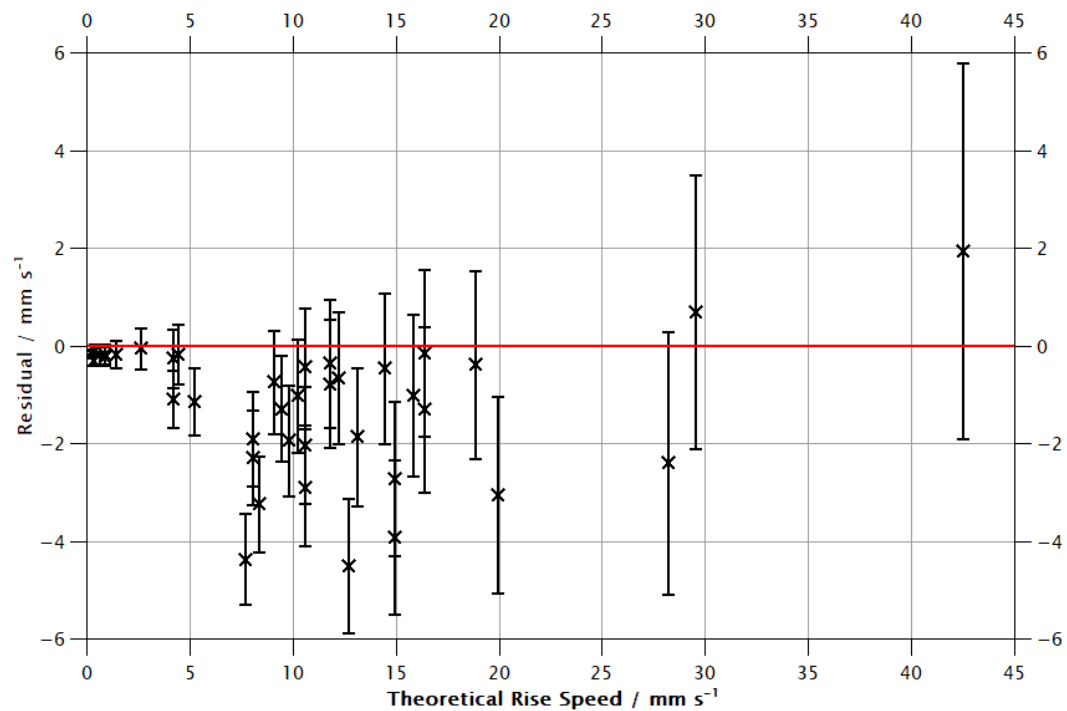


Figure 10.4: Residual between theoretical and measured rise speed against theoretical rise speed for single bubbles in the Constrained tube.

Table 10.7: Tests for normality for single bubbles in the Constrained tube.

	Theoretical	Measured	Residual
Kolmogorov-Smirnov test output (D)	0.1392	0.1110	0.1455
Significance (p)	0.4155	0.6965	0.3620

Table 10.8: Theoretical-Measured correlation and Theoretical-Residual correlation for single bubbles in the Constrained tube. The theoretical, measured and residual values were all normally distributed, so Pearson's R is used.

	Theoretical-Measured	Theoretical-Residual
Pearson's R	0.9871	0.0562
Significance (p)	<0.0001	0.7375

10.1.5. Constrained Dilute

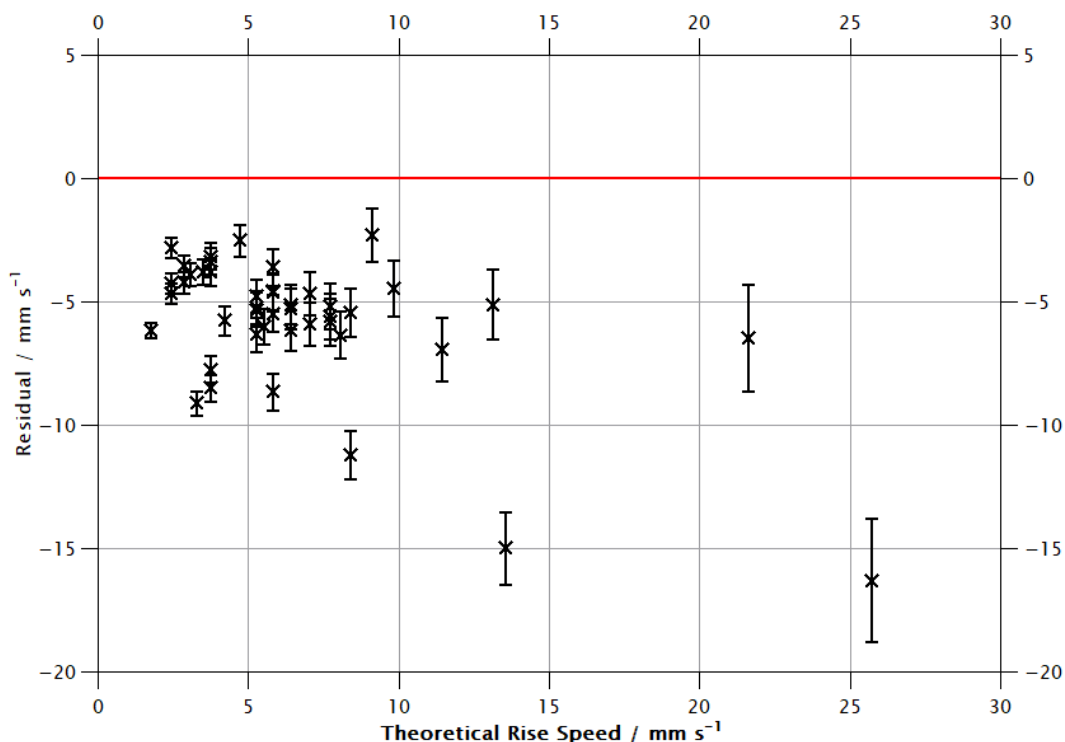


Figure 10.5: Residual between theoretical and measured rise speed against theoretical rise speed for bubbles in dilute groups in the Constrained tube.

Table 10.9: Tests for normality for bubbles in dilute groups in the Constrained tube.

	Theoretical	Measured	Residual
Kolmogorov-Smirnov test output (D)	0.1537	0.1758	0.2227
Significance (p)	0.2363	0.1242	0.0213

Table 10.10: Theoretical-Measured correlation and Theoretical-Residual correlation for bubbles in dilute groups in the Constrained tube. The theoretical, measured and residual values were all normally distributed, so Pearson's R is used.

	Theoretical-Measured	Theoretical-Residual
Pearson's R	0.9398	-0.5805
Significance (p)	<0.0001	<0.0001

10.1.6. Constrained Dense

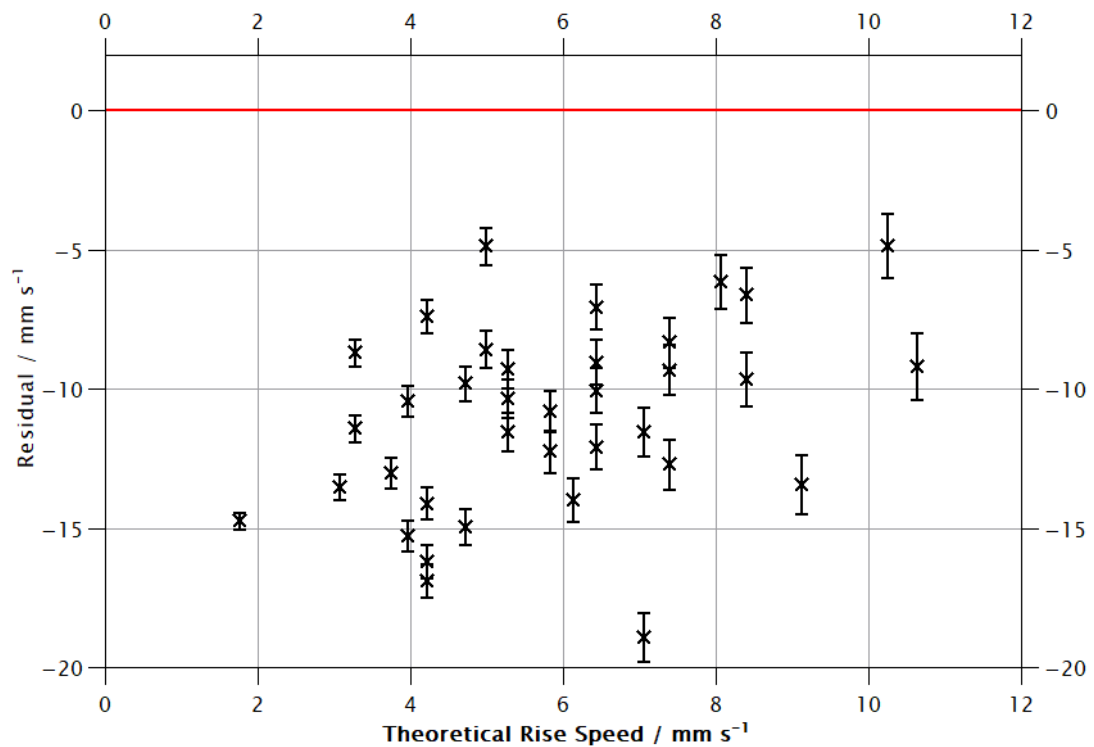


Figure 10.6: Residual between theoretical and measured rise speed against theoretical rise speed for bubbles in dense groups in the Constrained tube.

Table 10.11: Tests for normality for bubbles in dense groups in the Constrained tube.

	Theoretical	Measured	Residual
Kolmogorov-Smirnov test output (D)	0.1097	0.1177	0.0712
Significance (p)	0.7387	0.6576	0.9869

Table 10.12: Theoretical-Measured correlation and Theoretical-Residual correlation for bubbles in dense groups in the Constrained tube. The theoretical, measured and residual values were all normally distributed, so Pearson's R is used.

	Theoretical-Measured	Theoretical-Residual
Pearson's R	0.2465	0.3731
Significance (p)	0.1473	0.0250

10.1.7. Inclined Single

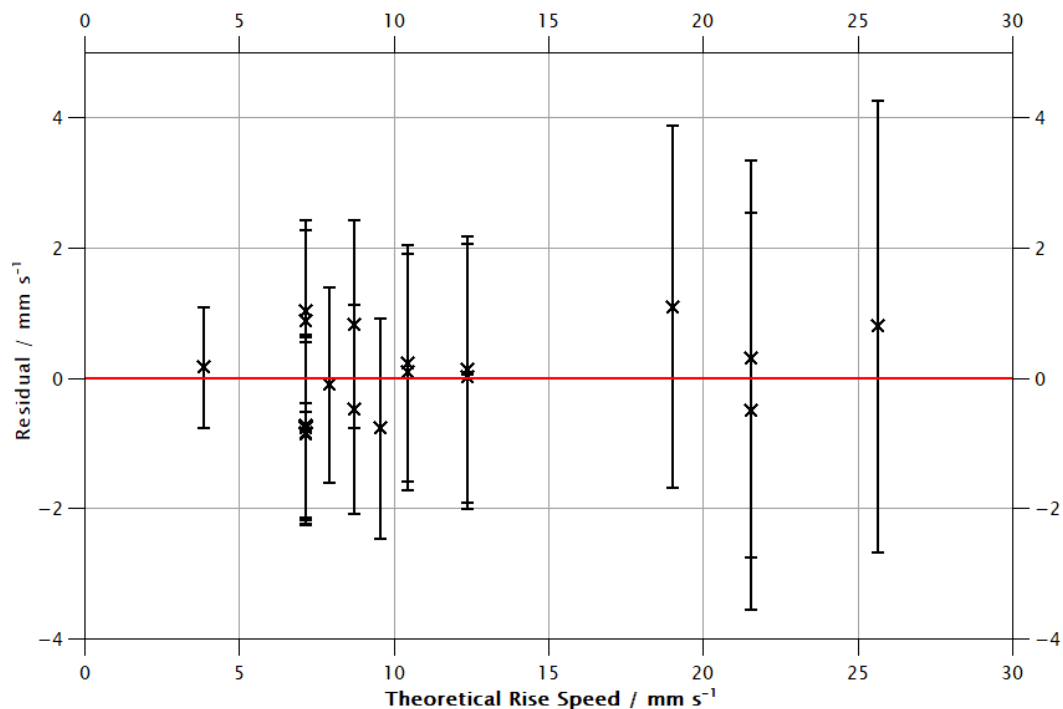


Figure 10.7: Residual between theoretical and measured rise speed against theoretical rise speed for single bubbles in the Inclined tube.

Table 10.13: Tests for normality for single bubbles in the Inclined tube.

	Theoretical	Measured	Residual
Kolmogorov-Smirnov test output (D)	0.2440	0.2525	0.1621
Significance (p)	0.1560	0.1305	0.6125

Table 10.14: Theoretical-Measured correlation and Theoretical-Residual correlation for single bubbles in the Inclined tube. The theoretical, measured and residual values were all normally distributed, so Pearson's R is used.

	Theoretical-Measured	Theoretical-Residual
Pearson's R	0.9939	0.3324
Significance (p)	<0.0001	0.1522

10.1.8. Inclined Dilute

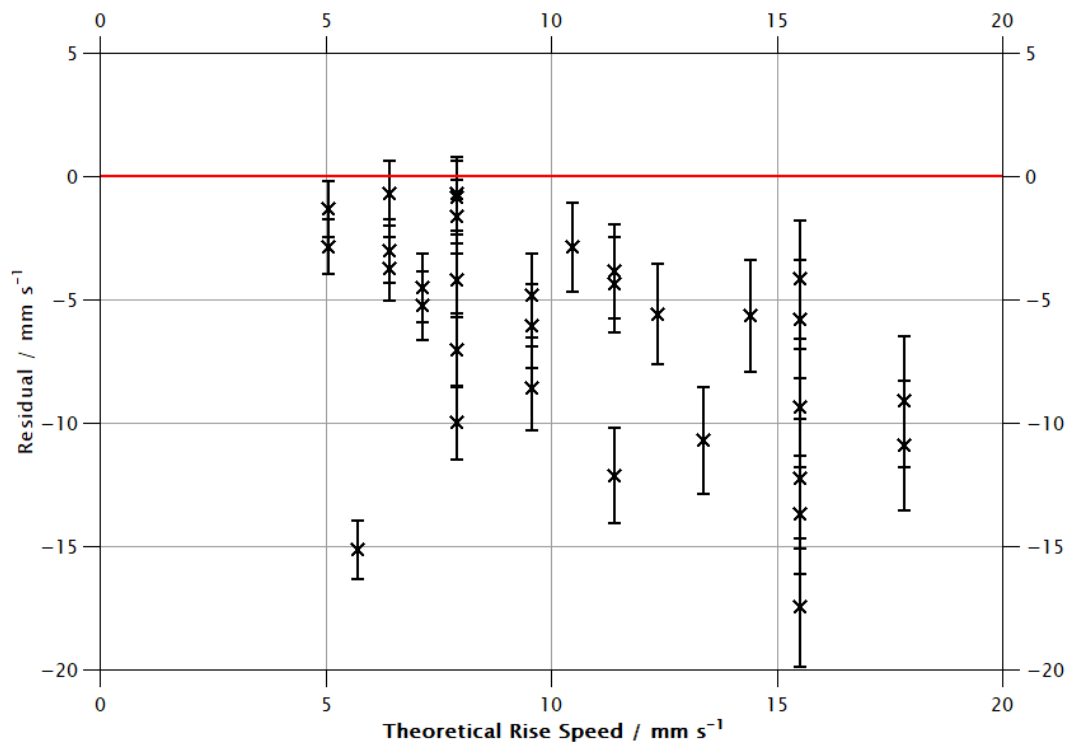


Figure 10.8: Residual between theoretical and measured rise speed against theoretical rise speed for bubbles in dilute groups in the Inclined tube.

Table 10.15: Tests for normality for bubbles in dilute groups in the Inclined tube.

	Theoretical	Measured	Residual
Kolmogorov-Smirnov test output (D)	0.1923	0.1082	0.1669
Significance (p)	0.1645	0.8090	0.3007

Table 10.16: Theoretical-Measured correlation and Theoretical-Residual correlation for bubbles in dilute groups in the Inclined tube. The theoretical, measured and residual values were all normally distributed, so Pearson's R is used.

	Theoretical-Measured	Theoretical-Residual
Pearson's R	0.8557	-0.5206
Significance (p)	<0.0001	0.0023

10.1.9. Inclined Dense

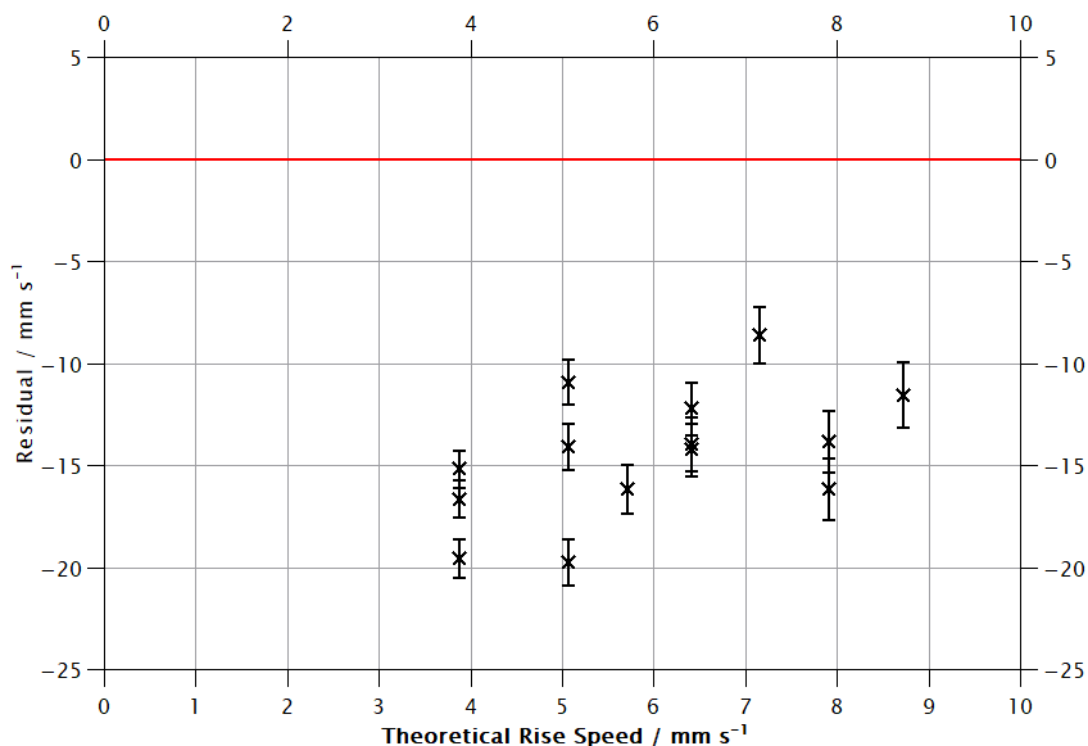


Figure 10.9: Residual between theoretical and measured rise speed against theoretical rise speed for bubbles in dense groups in the Inclined tube.

Table 10.17: Tests for normality for bubbles in dense groups in the Inclined tube.

	Theoretical	Measured	Residual
Kolmogorov-Smirnov test output (D)	0.1499	0.1168	0.1257
Significance (p)	0.8668	0.9791	0.9598

Table 10.18: Theoretical-Measured correlation and Theoretical-Residual correlation for bubbles in dense groups in the Inclined tube. The theoretical, measured and residual values were all normally distributed, so Pearson's R is used.

	Theoretical-Measured	Theoretical-Residual
Pearson's R	0.0042	0.5066
Significance (p)	0.9886	0.0645

10.2. Location of Data

A long-term storage solution for the raw and processed data is anticipated to be provided by Lancaster University Library to accompany this thesis, however readers are invited to contact the Author (m.roscoe2@lancaster.ac.uk or matt.roscoe92+thesis@gmail.com) if this data set cannot be found or if additional data is required.

While it is possible to connect frames used in analysis to the raw videos from where they originated, the frame numbers where the image stacks were cut were not always recorded and may take some effort to recover, if desired. However, typically cuts were made at frame numbers that were multiples of 100, 50 or 25 so that the image stacks covered a duration of an integer number of seconds.

11. References

Allard, P., 1997. Endogenous magma degassing and storage at Mount Etna. *Geophysical Research Letters*, 24(17), pp. 2,219-2,222.

Aliseda, A., Cartellieri, A., Hainaux, F. & Lasheras, J. C., 2002. Effect of preferential concentration on the settling velocity of heavy particles in homogeneous isotropic turbulence. *Journal of Fluid Mechanics*, Volume 468, pp. 77-105.

Amaya-Bower, L. & Lee, T., 2010. Single bubble rising dynamics for moderate Reynolds number using Lattice Boltzmann Method. *Computers & Fluids*, Volume 39, pp. 1191–1207.

Aylward, G. H. & Findlay, T., 2002. *SI Chemical Data (5th Edition)*. Milton, Queensland: Wiley.

Baldock, T. E., Tomkins, M. R., Nielsen, P. & Hughes, M. G., 2004. Settling velocity of sediments at high concentrations. *Coastal Engineering*, Volume 51, pp. 91-100.

Blackburn, E. A., Wilson, L. & Sparks, R. S. J., 1976. Mechanisms and Dynamics of Strombolian Activity. *Journal of the Geological Society*, Volume 132, pp. 429-440.

Blower, J. D., Keating, J. P., Mader, H. M. & Phillips, J. C., 2001. Inferring Volcanic Degassing Processes from Vesicle Size Distributions. *Geophysical Research Letters*, 28(2), pp. 347-350.

Blower, J. D., Keating, J. P., Mader, H. M. & Phillips, J. C., 2003. The Evolution of Bubble Size Distributions in Volcanic Eruptions. *Journal of Volcanology and Geothermal Research*, Volume 120, pp. 1-23.

Blower, J. D., Mader, H. M. & Wilson, S. D. R., 2001. Coupling of Viscous and Diffusive Controls on Bubble Growth During Explosive Volcanic Eruptions. *Earth and Planetary Science Letters*, Volume 193, pp. 47-56.

Bond, W. N. & Newton, D. A., 1928. LXXXII. Bubbles, drops, and Stokes' law. (Paper 2). *The London, Edinburgh, and Dublin Philosophical Magazine and Journal of Science*, Volume 5, pp. 794-800.

Brizard, M., Megharfi, M., Verdier, C. & Mahé, E., 2005. Design of a high precision falling ball viscometer. *Review of Scientific Instruments*, 76(2).

Burton, M., Allard, P., Muré, F. & La Spina, A., 2007. Magmatic Gas Composition Reveals the Source Depth of Slug-Driven Strombolian Explosive Activity. *Science*, Volume 317, pp. 227-230.

Burton, M. R., Mader, H. M. & Polacci, M., 2007. The role of gas percolation in quiescent degassing of persistently active basaltic volcanoes. *Earth and Planetary Science Letters*, Volume 264, pp. 46-60.

Cafilisch, R. E. & Luke, J. H. C., 1985. Variance in the sedimentation speed of a suspension. *Physics of Fluids*, 28(3), pp. 759-760.

Canon, 2019. *Canon EOS 600D Specifications*. [Online] Available at:

https://www.canon.co.uk/for_home/product_finder/cameras/digital_slr/eos_600d/specification.html

[Accessed 20 09 2019].

Capponi, A., James, M. R. & Lane, S. J., 2016. Gas slug ascent in a stratified magma: Implications of flow organisation and instability for Strombolian eruption dynamics. *Earth and Planetary Science Letters*, Volume 435, pp. 159-170.

Carey, R. J., Manga, M., Degruyter, W., Gonnermann, H., Swanson, D., Houghton, B., Orr, T. & Patrick, M., 2013. Convection in a volcanic conduit recorded by bubbles. *Geology*, 41(4), pp. 395-398.

Castruccio, A., Rust, A. C. & Sparks, R. S. J., 2010. Rheology and flow of crystal-bearing lavas: Insights from analogue gravity currents. *Earth and Planetary Science Letters*, Volume 297, pp. 471-480.

Castruccio, A., Rust, A. C. & Sparks, R. S. J., 2014. Assessing lava flow evolution from post-eruption field data using Herschel-Bulkley rheology. *Journal of Volcanology and Geothermal Research*, Volume 275, pp. 71-84.

Chouet, B., Dawson, P. & Martini, M., 2008. Shallow-conduit dynamics at Stromboli Volcano, Italy, imaged from waveform inversions. *Geological Society, London, Special Publications*, Volume 307, pp. 57-84.

Chouet, B. & Dawson, P., 2015. Seismic source of dynamics of gas-piston activity at Kilauea Volcano, Hawai'i. *Journal of Geophysical Research: Solid Earth*, 120(4), pp. 2,525-2,560.

Chouet, B., Hamisevicz, N. & McGetchin, T. R., 1974. Photoballistics of Volcanic Jet Activity at Stromboli, Italy. *Journal of Geophysical Research*, 79(32), pp. 4,961-4,976.

Chunhua, B. & Wang, Y., 2015. Study of the explosion parameters of vapor-liquid diethyl ether/air mixtures. *Journal of Loss Prevention in the Process Industries*, Volume 38, pp. 139-147.

Cimarelli, C., Costa, A., Mueller, S. & Mader, H. M., 2011. Rheology of magmas with bimodal crystal size and shape distributions: Insights from analog experiments. *Geochemistry Gephysics Geosystems*, 12(7), pp. 1-14.

Clift, R., Grace, J. & Weber, M. E., 1978. *Bubbles, Drops and Particles*. s.l.:Dover.

Day, P., Manz, A., Zhang, Y., 2012. *Microdroplet Technology: Principles and Emerging Applications in Biology and Chemistry*. Springer Science & Business Media

Del Bello, E., Lane, S. J., James, M.R., Llewellyn, E. W., Taddeucci, J., Scarlato, P. & Capponi, A., 2015. Viscous plugging can enhance and modulate explosivity of strombolian eruptions. *Earth and Planetary Science Letters*, Volume 423, pp. 210-218.

Dever, D. F., Finch, A. & Grunwald, E., 1955. The Vapor Pressure of Methanol. *The Journal of Physical Chemistry*, 59(7), pp. 668-669.

Diacu, F., 1996. The Solution of the n-body Problem. *The Mathematical Intelligencer*, 18(3), pp. 66-70.

Dixon, J. E., 1997. Degassing of alkalic basalts. *American Mineralogist*, Volume 82, pp. 368-378.

Duffield, W. A., Christiansen, R. L., Koyanagi, R. Y. & Peterson, D. W., 1982. Storage, Migration, and Eruption of Magma at Kilauea Volcano, Hawaii, 1971-1972. *Journal of Volcanology and Geothermal Research*, Volume 13, pp. 273-307.

Dusenbery, D. B., 2011. *Living at Micro Scale: The Unexpected Physics of Being Small*. Cambridge, Massachusetts: Harvard University Press.

Dvorak, J., Okamura, A. & Dieterich, J. H., 1983. Analysis of Surface Deformation Data, Kilauea Volcano, Hawaii October 1966 to September 1970. *Journal of Geophysical Research*, 88(B11), pp. 9,295-9,304.

Ervik, Å. & Bjørklund, E., 2018. The transition in settling velocity of surfactant-covered droplets from the Stokes to the Hadamard-Rybczynski solution. *European Journal of Mechanics - B/Fluids*, Volume 66, pp. 10-19.

Fleming, D., 2005. *Depth of Field Calculator*. [Online]
Available at: <https://www.dofmaster.com/dofjs.html>
[Accessed 20 09 2019].

Fowler, A. C. & Robinson, M., 2018. Counter-current convection in a volcanic conduit. *Journal of Volcanology and Geothermal Research*, Volume 356, pp. 141-162.

Frederix, E. M. A., Cox, T. L. W., Kuerten, J. G. M. & Komen, E. M. J., 2019. Poly-dispersed modeling of bubbly flow using the log-normal size distribution. *Chemical Engineering Science*, Volume 201, pp. 237-246.

Gardner, J. E. & Webster, J. D., 2016. The Impact of Dissolved CO₂ on Bubble Nucleation in Water-Poor Rhyolite Melts. *Chemical Geology*, Volume 420, pp. 180-185.

Gaudin, D. et al., 2017. Integrated puffing and explosions in a general scheme for Strombolian-style activity. *Journal of Geophysical Research: Solid Earth*, Volume 122, pp. 1,860-1,875.

Gonnermann, H. & Manga, M., 2012. Dynamics of magma ascent in the volcanic conduit. In: S. A. Fagents, T. K. Gregg & R. M. Lopes, eds. *Modelling Volcanic Processes: The Physics and Mathematics of Volcanism*. s.l.:Cambridge University Press, pp. 55-84.

Gonnermann, H. M. & Manga, M., 2007. The Fluid Mechanics Inside a Volcano. *The Annual Review of Fluid Mechanics*, Volume 39, pp. 321-356.

Gurioli, L. et al., 2013. Dynamics of Strombolian explosions: Inferences from field and laboratory studies of erupted bombs from Stromboli volcano. *Journal of Geophysical Research: Solid Earth*, Volume 119, pp. 319-345.

Hallez, Y. & Legendre, D., 2011. Interaction between two spherical bubbles rising in a viscous liquid. *Journal of Fluid Mechanics*, Volume 673, pp. 406-431.

Hamilton, D. L. & Oxtoby, S., 1986. Solubility of Water in Albit-Melt Determined by the Weight-Loss Method. *The Journal of Geology*, 94(4), pp. 626-630.

- Han, J.H. & Han, C.D., 1988. A study of bubble nucleation in a mixture of molten polymer and volatile liquid in a shear flow field. *Polymer Engineering & Science*, Volume 28, pp. 1616-1627.
- Holtz, F., Behrens, H., Dingwell, D. B. & Taylor, R. P., 1992. Water solubility in aluminosilicate melts of haplogranite composition at 2 kbar. *Chemical Geology*, Volume 96, pp. 289-302.
- Hornyak, E. J. & Weinberg, M. C., 1984. Velocity of a Freely Rising Gas Bubble in a Soda-Lime Silicate Glass Melt. *Journal of the American Ceramic Society*, Volume 67, pp. 244-246.
- Houghton, B. F. & Gonnermann, H. M., 2008. Basaltic explosive volcanism: Constraints from deposits and models. *Chemie der Erde*, Volume 68, pp. 117-140.
- Huppert, H. E., Shepherd, J. B., Sugurdsson, H. & Sparks, S., 1982. On Lava Dome Growth with Applications to the 1979 Lava Extrusion of the Soufriere of St. Vincent. *Journal of Volcanology and Geothermal Research*, Volume 14, pp. 199-222.
- Hurwitz, S. & Navon, O., 1994. Bubble nucleation in rhyolitic melts: Experiments at high pressure, temperature and water content. *Earth and Planetary Science Letters*, Volume 122, pp. 267-280.
- Istituto Nazionale Geofisica e Vulcanologia, 2019. *Eruzione Stromboli. Comunicato straordinario del 4 luglio 2019*. [Online]
Available at: <https://ingvvulcani.wordpress.com/2019/07/04/eruzione-stromboli-comunicato-straordinario-del-4-luglio-2019/>
[Accessed 16 September 2019].
- Istituto Nazionale Geofisica e Vulcanologia, 2019. *Nuovo parossismo a Stromboli, 28 agosto 2019*. [Online]
Available at: <https://ingvvulcani.wordpress.com/2019/08/30/nuovo-parossismo-a-stromboli-28-agosto-2019/>
[Accessed 16 September 2019].
- James, M. R., Lane, S. J. & Houghton, B. F., 2013. Unsteady Explosive Activity: Strombolian Eruptions. In: S. A. Fagents, T. K. P. Gregg & R. M. C. Lopes, eds. *Modeling Volcanic Processes (1st Edition)*. Cambridge: Cambridge University Press, pp. 107-128.
- James, M. R., Lane, S. J., Wilson, L. & Corder, S. B., 2009. Degassing at low magma-viscosity volcanoes: Quantifying the transition between passive bubble-burst and Strombolian eruption. *Journal of Volcanology and Geothermal Research*, Volume 180, pp. 81-88.
- James, M. R., Lane, S. R., Chouet, B. & Gilbert, J. S., 2004. Pressure changes associated with the ascent and bursting of gas slugs in liquid-filled vertical and inclined conduits. *Journal of Volcanology and Geothermal Research*, Volume 129, pp. 61-82.
- Jaupart, C., 1996. Physical models of volcanic eruptions. *Chemical Geology*, Volume 128, pp. 217-227.
- Jaupart, C. & Vergnolle, S., 1988. Laboratory models of Hawaiian and Strombolian eruptions. *Nature*, Volume 331, pp. 58-60.

- Jaupart, C. & Vergnolle, S., 1989. The generation and collapse of a foam layer at the roof of a basaltic magma chamber. *Journal of Fluid Mechanics*, Volume 203, pp. 347-380.
- Jeanloz, R., 2000. Mantle of the Earth. In: H. Sigurdsson, et al. eds. *Encyclopedia of Volcanoes (1st Edition)*. s.l.:Academic Press, pp. 41-54.
- Kazahaya, K., Shinohara, H. & Saito, G., 1994. Excessive degassing of Izu-Oshima volcano: magma convection in a conduit. *Bulletin of Volcanology*, Volume 56, pp. 207-216.
- Kemme, H. R. & Kreps, S. I., 1969. Vapor Pressure of Primary n-Alkyl Chlorides and Alcohols. *Journal of Chemical and Engineering Data*, 14(1), pp. 98-102.
- Kliakhandler, I. L., 2002. Continuous chain of bubbles in concentrated polymeric solutions. *Physics of Fluids*, Volume 14, pp. 3375-3379.
- Kočárková, H., Rouyer, F. & Pigeonneau, F., 2013. Film drainage of viscous liquid on top of bare bubble: Influence of the Bond number. *Physics of Fluids*, 25(2).
- Kondo, G. et al., 2019. Gas flux cyclic regime at an open vent magmatic column inferred from seismic and acoustic records. *Scientific Reports*, Volume 9.
- Kusuno H., Yamamoto H. & Sanada T., 2019. Lift force acting on a pair of clean bubbles rising in-line. *Physics of Fluids*, 31(7).
- Ladd, A. J. C., 1993. Dynamical simulations of sedimenting spheres. *Physics of Fluids A: Fluid Dynamics*, 5(2), pp. 299-310.
- Ladd, A. J. C., 1997. Sedimentation of homogeneous suspensions of non-Brownian spheres. *Physics of Fluids*, 9(3), pp. 491-499.
- Landau, L. D. & Lifshitz, E. M., 1966. *Fluid Mechanics (Volume 6 of Course of Theoretical Physics) (Third Edition)*. Oxford: Pergamon Press.
- Lane, S. J., James, M. R. & Corder, S. B., 2013. Volcano infrasonic signals and magma degassing: First-order experimental insights and application to Stromboli. *Earth and Planetary Science Letters*, Volume 377-378, pp. 169-179.
- Le Bas, M., Le Maitre, R., Streckeisen, A. & Zanettin, B., 1986. A Chemical Classification of Volcanic Rocks Based on the Total Alkali-Silica Diagram. *Journal of Petrology*, 27(3), pp. 745-750.
- Legendre, D., Magnaudet, J. & Mougin, G., 2003. Hydrodynamic interactions between two spherical bubbles rising side by side in a viscous liquid. *Journal of Fluid Mechanics*, Volume 497, pp. 133-166.
- Liu, E. J., Cashman, K. V. & Rust, A. C., 2015. Optimising shape analysis to quantify volcanic ash morphology. *GeoResJ*, Volume 8, pp. 14-30.
- Manga, M., 1996. Waves of bubbles in basaltic magmas and lavas. *Journal of Geophysical Research*, 101(B8), pp. 17,457-17,465.
- Manga, M. & Stone, H. A., 1993. Buoyancy-driven interactions between two deformable viscous drops. *Journal of Fluid Mechanics*, Volume 256, pp. 647-683.

- Manga, M. & Stone, H. A., 1994. Interactions between bubbles in magmas and lavas: effects of bubble deformation. *Journal of Volcanology and Geothermal Research*, Volume 63, pp. 267-279.
- Mangan, M. T., Sisson, T. W. & Hankins, W. B., 2004. Decompression experiments identify kinetic controls on explosive silic eruptions. *Geophysical Research Letters*, Volume 31.
- Marsden, L. H., Neuberg, J. W., Thomas, M. E., Mothes, P. A. & Ruiz, M. C., 2019. Combining Magma Flow and Deformation Modeling to Explain Observed Changes in Tilt. *Frontiers in Earth Science*, Volume 7, pp. 219-233.
- Martínez Mercado, J., Chehata Gómez, D., van Gils, D., Sun C. & Lohse, D., 2010. On bubble clustering and energy spectra in pseudo-turbulence. *Journal of Fluid Mechanics*, Volume 650, pp. 287-306.
- Mori, T. & Burton, M., 2009. Quantification of the gas mass emitted during single explosions on Stromboli with the SO₂ imaging camera. *Journal of Volcanology and Geothermal Research*, Volume 188, pp. 395-400.
- Mueller, S., Llewellyn, E. W. & Mader, H. M., 2010. The rheology of suspensions of solid particles. *Proceedings of the Royal Society A*, Volume 466, pp. 1201-1228.
- Mueller, S., Llewellyn, E. W. & Mader, H. M., 2011. The effect of particle shape on suspension viscosity and implications for magmatic flows. *Geophysical Research Letters*, Volume 38, pp. 1-5.
- Munday, E. B., Mullins, J. C. & Edle, D. D., 1980. Vapor Pressure Data for Toluene, 1-Pentanol, 1-Butanol, Water and 1-Propanol and for the Water and 1-Propanol System from 273.15 to 323.15 K. *Journal of Chemical and Engineering Data*, Volume 25, pp. 191-194.
- Neuberg, J. W., Tuffen, H., Collier, L., Green, D., Powell, T. & Dingwell, D., 2006. The trigger mechanism of low-frequency earthquakes on Montserrat. *Journal of Volcanology and Geothermal Research*, Volume 153, pp. 37-50.
- Nguyen, C. T. et al., 2013. Film drainage and the lifetime of bubbles. *Geochemistry Geophysics Geosystems*, 14(9), pp. 3,616-3631.
- Okumura, S. et al., 2013. Couple effect of magma degassing and rheology on silicic volcanism. *Earth and Planetary Science Letters*, Volume 362, pp. 163-170.
- Oliver, D. R., 1961. The sedimentation of suspensions of closely-sized spherical particles. *Chemical Engineering Science*, Volume 15, pp. 230-242.
- Oppenheimer, J., Capponi, A., Cashman, K. V., Lane, S. J., Rust, A. C. & James, M. R., 2020. Analogue experiments on the rise of large bubbles through a solids-rich suspension: A “weak plug” model for Strombolian eruptions. *Earth and Planetary Science Letters*, Volume 531.
- Pan, V., Holloway, J. R. & Hervig, R. L., 1991. The pressure and temperature dependence of carbon dioxide solubility in tholeiitic basalt melts. *Geochimica et Cosmochimica*, Volume 55, pp. 1587-1595.

- Parfitt, E. A., 2004. A discussion of the mechanisms of explosive basaltic eruptions. *Journal of Volcanology and Geothermal Research*, Volume 134, pp. 77-107.
- Parfitt, E. A. & Wilson, L., 1995. Explosive volcanic eruptions—IX. The transition between Hawaiian-style lava fountaining and Strombolian explosive activity. *Geophysical Journal International*, 121(1), pp. 226-232.
- Parfitt, E. A., Wilson, L. & Neal, C. A., 1995. Factors influence the height of Hawaiian lava fountains: implications for the use of fountain height as an indicator of magma gas content. *Bulletin of Volcanology*, Volume 57, pp. 440-450.
- Park, S. H., Park, C., Lee, J. & Lee, B., 2017. A simple parameterization for the Rising Velocity of Bubbles in a Liquid Pool. *Nuclear Engineering and Technology*, Volume 49, pp. 692-699.
- Patrick, M., Swanson, D. & Orr, T., 2019. A review on controls on lava lake level: insights from Halema'uma'u Crater, Kilauea Volcano. *Bulletin of Volcanology*, 81(13).
- Pioli, L., Azzopardi, B. J., Brunet, M. & Kurokawa, A. K., 2017. Outgassing and eruption of basaltic magmas: The effect of conduit geometry. *Geology*, 45(8), pp. 759-762.
- Pistone, M., Cordonnier, B., Caricchi, L., Ulmer, P., & Marone, F., 2015. The Viscous to Brittle Transition in Crystal- and Bubble-Bearing Magmas. *Frontiers in Earth Science*, 3(71)
- Polacci, M., Baker, D. R., Mancini, L., Favretto, S. & Hill, R. J., 2009. Vesiculation in magmas from Stromboli and implications for normal Strombolian activity and paroxysmal explosions in basaltic systems. *Journal of Geophysical Research*, 114(B1).
- Prousevitch, A. A., Sahagian, D. L. & Anderson, A. T., 1993. Dynamics of Diffusive Bubble Growth in Magmas - Isothermal Case. *Journal of Geophysical Research*, 98(B12), pp. 22,283-22,307.
- Richardson, J. F. & Zaki, W. N., 1954. The sedimentation of a suspension of uniform spheres under conditions of viscous flow. *Chemical Engineering Science*, Volume 3, pp. 65-73.
- Ripepe, M., Harris, A. J. L. & Carniel, R., 2002. Thermal, seismic and infrasonic evidences of variable degassing rates at Stromboli volcano. *Journal of Volcanology and Geothermal Research*, Volume 118, pp. 285-297.
- Rogers, N. & Hawkesworth, C., 2000. Composition of Magmas. In: H. Sigurdsson, et al. eds. *Encyclopedia of Volcanoes (1st Edition)*. s.l.:Academic Press, pp. 115-131.
- Rust, A. C. & Cashman, K. V., 2007. Multiple origins of obsidian pyroclasts and implications for changes in the dynamics of the 1300 B.P. eruption of Newberry Volcano, USA. *Bulletin of Volcanology*, Volume 69, pp. 825-845.
- Scriven, L. E., 1959. On the Dynamics of Phase Growth. *Chemical Engineering Science*, Volume 10, pp. 1-13.
- Shea, T., 2017. Bubble nucleation in magmas: A dominantly heterogeneous process?. *Journal of Volcanology and Geothermal Research*, Volume 343, pp. 155-170.

Shea, T., Gurioli, L., Larsen, J. F., Houghton, B. F., Hammer, J. E. & Cashman, K. V., 2010. Linking experimental and natural vesicle texture in Vesuvius 79AD white pumice. *Journal of Volcanology and Geothermal Research*, Volume 192, pp. 69-84.

Sparks, R. S. J., 1978. The Dynamics of Bubble Formation and Growth in Magmas: A Review and Analysis. *Journal of Volcanology and Geothermal Research*, Volume 3, pp. 1-37.

Sparks, R. S. J. et al., 1994. Physical Aspects of Magmatic Degassing .1. Experimental and Theoretical Constraints on Vesiculation. In: M. R. Carroll & J. R. Holloway, eds. *Volatiles in Magmas*. Chantilly, VA: Mineralogical Society of America and Geochemical Society, pp. 413-445.

Spearman, J. & Manning, A. J., 2017. On the hindered settling of sand-mud suspensions. *Ocean Dynamics*, 67(3-4), pp. 465 – 483.

Spelt, P. D. M. & Sangani, A. S., 1998. Properties and Averaged Equations for Flows of Bubbly Liquids. *Applied Scientific Research*, Volume 58, pp. 337-386.

Spera, F. J., 2000. Physical Properties of Magma. In: H. Sigurdsson, et al. eds. *Encyclopedia of Volcanoes (1st Edition)*. s.l.:Academic Press, pp. 171-190.

Spera, F. J. & Stein, D. J., 2000. Comment on "Rheology of bubble-bearing magmas" by Lejeune et al.. *Earth and Planetary Science Letters*, Volume 175, pp. 327-331.

Squires, K. D. & Eaton, J. K., 1991. Preferential concentration of particles by turbulence. *Physics of Fluids A: Fluid Dynamics*, 3(5), pp. 1169-1178.

Stevenson, D. S. & Blake, S., 1998. Modelling the dynamics and thermodynamics of volcanic degassing. *Bulletin of Volcanology*, Volume 60, pp. 307-317.

Swanger, L. A. & Rhines, W. C., 1972. On the Necessary Conditions for Homogeneous Nucleation of Gas Bubbles in Liquids. *Journal of Crystal Growth*, Volume 12, pp. 323-326.

Tallarico, A. & Dragoni, M., 1999. Viscous Newtonian laminar flow in a rectangular channel: application to Etna lava flows. *Bulletin of Volcanology*, Volume 61, pp. 40-47.

Taqieddin, A., Allshouse, M. R., Alshawabkeh, A. N., 2018. Review - Mathematical Formulations of Electrochemically Gas-Evolving Systems. *Journal of The Electrochemical Society*, **165**(13) E694-E711

Tatibouët, J. & Gendron, R., 2004. A study of Strain-induced Nucleation in Thermoplastic Foam Extrusion. *Journal of Cellular Plastic*, Volume 40, pp. 27-44.

Tazieff, H., 1970. New Investigations on Eruptive Gases. *Bulletin of Volcanology*, 34(2), pp. 421-438.

Tilling, R. I., 1987. Fluctuations in Surface Height of Active Lava Lakes During 1972-1974 Mauna Ulu Eruption, Kilauea Volcano, Hawaii. *Journal of Geophysical Research*, 92(B13), pp. 13,721-13,730.

van Wijngaarden, L., 1993. The mean rise velocity of pairwise-interlacing bubbles in liquid. *Journal of Fluid Mechanics*, Volume 251, pp. 55-78.

- van Wijngaarden, L., 1998. On Pseudo Turbulence. *Theoretical and Computational Fluid Dynamics*, Volume 10, pp. 449-458.
- Vergnolle, S. & Japuart, C., 1986. Separated Two-Phase Flow and Basaltic Eruptions. *Journal of Geophysical Research*, 91(B12), pp. 12,842-12,860.
- Vona, A., Romano, C., Dingwell, D. B. & Giordano, D., 2011. The Rheology of crystal-bearing basaltic magmas from Stromboli and Etna. *Geochimica et Cosmochimica Acta*, Volume 75, pp. 3,214-3,236.
- Wacker-Chemie GmbH, nd.. Wacker Silicone Fluids AK. [Online] Available at: http://www.behlke.com/pdf/wacker_silicone_oil.pdf/ [Accessed 23 September 2019]
- Wallace, P. & Anderson, A. T., 2000. Volatiles in Magmas. In: H. Sigurdsson, et al. eds. *Encyclopedia of Volcanoes (1st Edition)*. s.l.:Academic Press, pp. 149-170.
- Webb, S. L. & Dingwell, D. B., 1990. Non-Newtonian Rheology of Igneous Melts at High Stresses and Strain Rates: Experimental Results of Rhyolite, Andesite, Basalt and Nephelinite. *Journal of Geophysical Research*, 95(B10), pp. 15,695-15,701.
- Wilson, L., 1980. Relationships Between Pressure, Volatile Content and Ejecta Velocity in Three Types of Volcanic Explosion. *Journal of Volcanology and Geothermal Research*, Volume 8, pp. 297-313.
- Wilson, L. & Head, J. W., 1981. Ascent and Eruption of Basaltic Magma on the Earth and Moon. *Journal of Geophysical Research*, 86(B4), pp. 2971-3001.
- Ying, H., Puzhen G. & Chaoqun, W., 2019. Experimental and Numerical Investigation of Bubble-Bubble Interactions during the Process of Free Ascension. *Energies*, Volume 12, pp. 1977-1997.
- Young, M. L. & Klima, M. S., 2000. Evaluation of a hindered-settling column for size/density separations. *Minerals and Metallurgical Processing*, 7(3), pp. 194-197.
- Yu, Z., Yang, H. & Fan, L-S., 2011. Numerical simulation of bubble interactions using an adaptive lattice Boltzmann method. *Chemical Engineering Science*, Volume 66, pp. 3441-3451.
- Zenit, R., Koch, D. L. & Sangani, A. S., 2001. Measurements of the average properties of a suspension of bubbles rising in a vertical channel. *Journal of Fluid Mechanics*, Volume 429, pp. 307-342.